NΛSΛ

National Aeronautics and
Space Administration

Turbofan Aft Duct Suppressor Study

by

A.A. Syed
R.E. Motsinger
G.H. Fiske
General Electric Company

M.C. Joshi
R.E. Kraft
Douglas Aircraft Company

prepared for

National Aeronautics and Space Administration
Lewis Research Center
21000 Brookpark Road
Cleveland, Ohio 44135

Contract NAS3-22766

NASA

National Aeronautics and
Space Administration

Turbofan Aft Duct Suppressor Study

by

A.A. Syed
R.E. Motsinger
G.H. Fiske
General Electric Company

M.C. Joshi
R.E. Kraft
Douglas Aircraft Company

prepared for

1. Report No. NASA CR175067	2. Government Accession No.	3. Recipient's Catalog No.
4. Title and Subtitle AFT DUCT SUPPRESSOR STUDY		5. Report Date
		6. Performing Organization Code
7. Author(s) A.A. Syed, R.E. Motsinger, G.H. Fiske, M.C. Joshi, R.E. Kraft		8. Performing Organization Report No. R83AEB566
		10. Work Unit No.
9. Performing Organization Name and Address General Electric Company Aircraft Engine Business Group 1 Neumann Way Cincinnati, Ohio 45215		
		11. Contract or Grant No. NAS3-22766
		13. Type of Report and Period Covered Contract Report
12. Sponsoring Agency Name and Address NASA Lewis Research Center 21000 Brookpark Road Cleveland, Ohio 44135		
		14. Sponsoring Agency Code

15. Supplementary Notes

Program Manager: B. Clark
NASA Lewis Research Center
21000 Brookpark Road
Cleveland, Ohio 44135

16. Abstract

Suppressions due to acoustic treatment in the annular exhaust duct of a model fan have been theoretically predicted and compared with measured suppressions. The predictions are based on the modal analysis of sound propagation in a straight annular flow duct with segmented treatment. Modal distributions of the fan noise source (fan-stator interaction only) were measured using in-duct modal probes. The flow profiles were also measured in the vicinity of the modal probes. The acoustic impedance of the single-degree-of-freedom treatment was measured in the presence of grazing flow. The measured values of mode distribution of the fan noise source, the flow velocity profile and the acoustic impedance of the treatment in the duct were used as input to the prediction program. The predicted suppressions, under the assumption of uniform flow in the duct, compared well with the suppressions measured in the duct for all test conditions.

The interaction modes generated by the rotor-stator interaction spanned a cut-off ratio range from nearly 1 to 7.

The modal probe data and a users' guide to the computer programs are available as separate publications.

17. Key Words (Suggested by Author(s)) Fan exhaust duct noise suppression Acoustic propagation in segmented annular ducts Acoustic spinning mode measurement In-situ acoustic impedance measurement	18. Distribution Statement Unclassified - Unlimited		
19. Security Classif. (of this report) Unclassified	20. Security Classif. (of this page) Unclassified	21. No. of Pages 188	22. Price*

NASA-C-168 (Rev. 10-75)

TABLE OF CONTENTS

TABLE OF CONTENTS (Concluded)

LIST OF FIGURES

LIST OF FIGURES (Continued)

LIST OF TABLES

LIST OF SYMBOLS AND DEFINITIONS

Except when otherwise defined in the text, the following nomenclature is used
in this report.

Symbols

A	complex mode amplitude
c	speed of sound
d	core thickness of the acoustic treatment
E	acoustic energy
f	frequency
H	duct height
H_{xy}	transfer function of two acoustic signals at locations x and y
i	$= \sqrt{-1}$
[I]	unit matrix
I_z	acoustic intensity
k	free space wave number
k_r	radial wave number
k_θ	circumferential wave number
K	axial wave number (propagation constant)
L	segment length
m	spinning mode order
M	mean flow Mach number
n	radial mode order
N	number of segments
p	acoustic pressure
P_r	radial eigenfunction
r	radial coordinate
R	resistance of treatment
T	temperature
v	axial acoustic velocity
X	reactance of treatment
z	axial coordinate
[R]	admittance interface reflection matrix

Symbols (Continued)

$[S]$	stacked system matrix
$[T]$	admittance interface transmission matrix
$[U]$	uniform section transmission matrix
$\{Q\}$	acoustic source vector
$\{A\}$	acoustic mode vector
NEX	Index n in the boundary layer velocity profile. Thus, NEX = 7 is for the 1/7th power boundary lay velocity profile.
θ	angular location in the cylindrical polar coordinate system
ω	angular frequency 2π f/c
β	duct wall acoustic admittance
γ	complex dimensionless eigenvalue $k_r \cdot r_2$, where r_2 is the outer wall radius
δ	Dirac delta
ζ	duct wall acoustic impedance
η	$Hf/c = H/\lambda$ = non-dimensional frequency
κ	K/k = non-dimensional axial wave number
λ	wavelength
$\rho_o c$	characteristic impedance of medium
ρ_o	density of air in the duct

Subscripts/Superscripts

$(J),(K)$	duct segment designation
$j-1, j,$ $k, k+1$	duct plane designation
m	spinning mode order
n	radial mode order
S	"source" plane
T	"termination" plane
z	axial direction
$+$	forward propagation
$-$	backward propagation
$\star$	complex conjugate
eq	equivalent

1.0 SUMMARY

Sound suppressions due to acoustically absorptive treatment in the
annular exhaust duct of a model fan have been theoretically predicted and
compared with measurements.

The predictions were based on the modal analysis of sound propagation
in a straight annular fan exhaust duct with axially segmented treatment.
Measured values of the mode distribution of the fan noise source (rotor-stator
interaction source only) and of the acoustic impedance of the treated segment
in the duct were used as input to the prediction program. The predicted
suppressions obtained with the assumption of uniform flow (no radial or
circumferential shear in the flow) compared well with the measured in-duct
suppressions for all test conditions.

Measurements of the acoustic modes were made on a fan test model
installed in an anechoic chamber at General Electric Company's Corporate
Research and Development Center in Schenectady, New York. The fan exhaust
duct was annular in cross section with a hub-to-tip ratio of 0.5. It
consisted of three axial segments. Acoustic mode probes were located in the
first and the third segments which were hard walled. Initial tests were
conducted with a hard wall second segment. Later measurements were made with
acoustically absorptive inner and outer walls in the second segment. The
suppression of sound due to the treated segment was determined from these data
by computing the difference between the acoustic energy flux at the upstream
and the downstream measurement locations. The quality of the measured modal
data was very good. The acoustic field in the duct at the frequency of
interest was observed to be stationary over the periods of the modal
measurements. This ensured accurate measurement of the modal amplitude and
phase data. Fan speeds for the tests were chosen so that the modes generated
by the fan-stator interaction spanned a cut-off ratio range from just over one
to seven.

The acoustically absorbing wall segments consisted of single-degree-of-freedom (SDOF) treatment with linear characteristics. The measurements of the normal acoustic impedance of the treatment were carried out in General Electric Company's Acoustic Laboratory at Evendale, Ohio. These included measurements under no-flow conditions on the treatment hardware and under grazing flow conditions on a sample of the treatment.

The modal probe data and a users' guide to the computer programs are available as separate publications (see list of references).

2.0 INTRODUCTION

Acoustically absorptive treatment in aircraft engine ducts is an essential part of the overall aircraft noise reduction effort. With the increased emphasis on energy efficiency, it is necessary to maximize the effectiveness of the treatment. Duct treatments must be designed to suppress specific noise sources in short ducts. By maximizing the treatment effectiveness, a reduction in the treatment length required to achieve a given overall engine noise level can be realized. This reduction translates into reduced fan reverser length required and, consequently, results in lower installed engine weight and higher performance consistent with the desired goal of energy efficient noise reduction. In order to achieve this goal, analytical treatment design must be made an integral part of the advanced energy efficient noise reduction technology.

Recognizing the importance of spinning modes in the design of the acoustic treatment, several studies have been conducted to investigate the propagation of acoustic modes in axi-symmetric ducts. These studies, however, are limited to semi-infinite ducts with uniform wall impedance. Zorumski (Reference 1) developed an analysis to account for the axial impedance changes. This analysis also included both the upstream and the downstream travelling modes. Kraft, et. al., (Reference 2) measured the acoustic modal distribution in a laboratory model inlet duct and designed and tested a treatment to verify Zorumski's analysis.

This report contains the results of a study on the propagation of acoustic modes in an annular exhaust duct. It involved the development of a set of computer programs based on the modal analysis (Reference 3) of sound propagation to predict in-duct suppression due to axially segmented acoustic treatment. It also involved an experimental program designed to determine whether the analysis capability was sufficient to describe the physics in turbofan aft duct suppressors. Although simplified, the experiment was designed to contain the first-order physical effects which were thought to govern the far field radiation attenuation due to an exhaust duct suppressor.

3

As the experiment was intended to verify the sound propagation theory in a realistic turbofan exhaust duct, it contained the following features:

1. A realistic fan stage (NASA Lewis model fan--rotor 55) capable of producing well-defined spinning modes.
2. An exhaust nozzle with a realistic contour and contraction ratio.
3. A straight annular section exhaust duct to model the simplified sound propagation analysis.
4. A uniform, linear treatment design to minimize impedance sensitivity to the operating conditions of the text vehicle.

Over the three fan speeds tested, spinning modes were generated with cut-off ratios ranging between just over 1 to 7. The acoustic measurements involved the measurement of (a) modal coefficients upstream and downstream of a treated segment in the exhaust duct, (b) the aft radiated acoustic far field, and (c) the acoustic impedance of the treatment used in the aft duct.

The test vehicle was mounted in an anechoic chamber in order to measure the far field radiated noise under free field conditions.

The measurement of the acoustic impedance involved the use of the in-situ method (References 4, 5, 6) and of the Acoustic Plunker (Reference 7), a non-destructive portable transducer developed by the General Electric Company to measure the normal acoustic impedance of finished treatment panels. A total of 90 measurements on both the inner and the outer treatment sections were made with the Plunker to establish that the normal acoustic impedance of the treatment was uniform over the area of these sections and that both the inner and the outer surfaces had equal impedance within prescribed manufacturing tolerances.

The theory of sound propagation in a uniform duct with fluid flow and its extension to ducts with axial impedance segmentation is described in Section 4.1. Section 4.2 deals with the theoretical aspects of the computation of the modal coefficients from the mode probe data and the

theoretically determined mode eigenfunctions and axial wave numbers in the hardwall segment of the duct. The problem has been considered for the uniform flow and the radially sheared flow cases. It involves the solution of a set of linear simultaneous equations for the complex modal coefficients. In the case of uniform flow the eigenfunction of a downstream propagating (m,n) mode is identical to that of the upstream propagating mode of the same order. This allows decoupling of the problem which makes the solution simpler in that smaller size matrix equations have to be solved. In the case of radially sheared flow, the eigenfunctions of the upstream and the downstream propagating modes of the same (m,n) order are not identical which means that a much bigger size matrix equation has to be handled. As the sensitivity of matrix solutions to small input errors increases with the size of the matrix, redundant measurements were included in the analysis giving a "least squares fit" type of solution from the available data.

The theory of the in situ impedance measurement technique is described in Section 4.3. This method assumes that the treatment is point reacting, and there is no transmission of sound through the walls of the adjacent cavities. The sound field inside the cavity is assumed to consist of plane waves only. The method employs the complex ratio of two acoustic originals--one at the surface of the treatment and the other at a known location in the cavity (usually at the hard back wall). For this reason it has often been referred to as the '2-microphone method.' An error analysis of the technique is included in Appendix B.

The description of the experimental apparatus and a selection of representative test data are included in Section 5. The test vehicle was mounted in the Aeroacoustic Anechoic Facility in the General Electric Corporate Research and Development Center, Schenectady, New York. The airflow and noise source consisted of the 15 bladed NASA Lewis 0.504 m diameter fan designated as Rotor 55. From the original eleven outlet guide vane set, eight vanes were used at a spacing of 0.5 rotor tip chord length from the rotor to generate a rotor stator interaction tone at levels appreciably higher then noise produced by other mechanisms. To prevent rotor turbulence noise

generation, a turbulence control structure was incorporated in the inlet duct of the fan. The annular flow path of the fan exhaust duct consisted of two hardwall sections where in-duct acoustic probes were located, a treated section and a nozzle termination which was representative of typical engine nozzles. The acoustic measurement in the duct involved circumferential traversing of an array of pressure transducers through 360 degrees. Signals were recorded at 18 degree intervals and then analyzed. In order to ensure stationarity of the acoustic field over the time of recording the signals from the two arrays (of twelve tranducers each) used in the measurement, the fan speed was maintained at a constant value during a test.

Aerodynamic measurements were made to determine the velocity profile at each of the in-duct probe locations. This information was necessary for the calculation of the axial wave numbers and radial mode shapes (eigenfunctions). Instrumentation included: three total pressure and total temperature rakes, each with five radial stations. In addition, two pitot tubes which could traverse radially and circumferentially and sixteen static pressure taps mounted in both inner and outer walls were employed. All aerodynamic probes and rakes were removed during acoustic tests.

The effects of grazing flow and of sound intensity on the impedance of the treatment were investigated using laboratory samples constructed from the same materials used in the construction of the annular duct hardware. Steady flow resistance measurements were made first after removing the flexcore (but leaving the bonding agent intact). The sample was then instrumented for in-situ impedance measurements in the Grazing Flow Duct using a thick walled cylindrical cavity to ensure local reaction aspect of the experiment.

The theory-experiment check is fully discussed in Section 6, and the major conclusions drawn from this work are listed in Section 7. The exhaust duct suppression prediction program (Reference 8) based on the modal analysis was used to predict the suppression due to the treatment in the exhaust duct at three fan speeds. The duct was modelled as a three segment straight annular duct with the treated segment placed between the two hardwall

6

segments. Mode coefficients based on the assumption of uniform flow through the duct were first obtained from the in-duct measurements. The mode coefficients of the forward (downstream) traveling modes at the upstream measurement plane (source plane) and of the backward (upstream) traveling modes at the downstream measurement plane (termination plane) were used to specify the source and the termination matrices. With these parameters and the knowledge of the impedance of the treated segment, the duct geometry, the flow conditions and the spinning mode order number, the program (Reference 8) calculates the eigenvalues, the axial propagation constants (both forward and backward), the uniform section transmission matrices for each segment and the reflection and transmission matrices of the segment interfaces. The program then sets up the stacked system matrix equation and solves it to obtain the forward and backward complex mode coefficients in each segment and the modal energy flux at each plane. The net energy flux at each plane and the overall sound power level (PWL) suppression are then calculated. Suppressions predicted in this manner agreed well with the suppressions obtained from the in-duct measurements.

The sensitivity of the predicted suppression to the treatment impedance values was also examined by varying both the resistance and the reactance of the input to the prediction program. The predicted suppression was found to be more sensitive to variations in reactance, particularly at the maximum fan speed tested (1900 Hz) when a variation of 0.1 ρc in reactance resulted in as much as 4 dB change in suppression.

Predictions were also made using the sheared flow mode coefficients. These did not compare as well with the measured values as those obtained with the uniform flow mode coefficients. This is considered to be due to a significant energy mismatch that occurs at the segment interfaces when using the sheared flow option in the prediction routines. This problem has not been resolved.

Based on the theory experiment check presented in Section 6, it can be concluded that the modal analysis for sound propagation in segmented ducts can

7

be used to predict the in-duct suppression due to acoustically absorptive treatment in the exhaust duct of a turbofan. The modal distribution of the acoustic source and the reflection characteristics of the duct termination are required for the prediction. They may be obtained from measurements or from analytical methods.

The acoustic data from the mode probes in terms of the linear amplitude and phase measured at defined (z, r, θ) locations in the hardwall segments of the aft duct are included in the data report (Reference 9).

3.0 OBJECTIVES

The objectives of the work reported in this report are:

1. Development of the analytical tools required for rapid and cost effective evaluation of acoustic treatment designs for fan exhaust ducts using modal propagation analysis.
2. Provide experimental substantiation of the above analytical tools in a realistic turbofan exhaust duct employing a model fan stage and a realistic exhaust nozzle.
3. Study the effect of the selective reflection by the nozzle on the far field suppression.

9

4.0 THEORETICAL CONSIDERATIONS

In this section of the report, the theoretical model of the acoustic
wave propagation in an acoustically lined cylindrical duct of uniform cross
section carrying radially sheared flow and its extension to axial segmentation
of the treatment is described. This theory is the basis of the computer
programs described in Reference 8. In addition, the theoretical bases of the
computations used in the determination of the modal coefficients from the mode
probe data obtained in the hardwall segments of the fan exhaust duct and of
the in-situ impedance measurement technique are described.

4.1 WAVE-FIELD THEORY

The prediction of suppression of sound due to treatment in the exhaust
duct is based on a theoretical analysis of sound propagation in axially
segmented annular ducts (Reference 3). Propagation in the duct is considered
in terms of the treatment and the presence of both hardwall and treated
segments in the duct are incorporated in the analysis by considering the duct
to be axially segmented and by allowing propagation of modes in both forward
and backward directions. Reflection and redistribution of acoustic energy at
segment interfaces and at the exhaust nozzle are also considered. The theory
of sound propagation in a uniform duct with flow and its extension to ducts
with axial impedance segmentation are described in the following paragraphs.

4.1.1 SOUND PROPAGATION IN ANNULAR DUCTS WITH FLOW

The propagation of sound in a duct carrying uniform flow is governed by
the convected wave equation

$$\nabla^2 p = \frac{1}{c^2} \left(\frac{\partial}{\partial t} + V_z \frac{\partial}{\partial z} \right)^2 p \tag{4.1}$$

where V_z is the mean flow velocity in the axial direction, ∇^2 is the
Laplacian operator and p is the acoustic pressure. To solve this equation by

PRECEDING PAGE BLANK NOT FILMED

11

the separation of variables, assume that the acoustic pressure can be represented in cylindrical coordinates (Figure 4.1) as

$$p(r,\theta,z,t) = p_r(r) p_{\theta(\theta)}\, e^{iKz - i\omega t} \qquad (4.2)$$

This reduces the wave equation to two ordinary differential equations, namely

$$\frac{d^2 p_\theta}{d\theta^2} = -k_\theta^2\, p_\theta \qquad (4.3)$$

and

$$\frac{d^2 p_r}{dr^2} + \frac{1}{r}\frac{dp_r}{dr} + \left(k_r^2 - \frac{k_\theta^2}{r^2} \right) p_r = 0 \qquad (4.4)$$

with

$$K^2(1 - M^2) + 2MkK + (k_r^2 - k^2) = 0 \qquad (4.5)$$

k is the wave number in free space and k_r, k_θ, and K are the wave numbers in the radial, circumferential, and axial directions respectively. M is the mean flow Mach number (equal to V_z/c).

Equation (4.3) has a solution of the form

$$p_\theta(\theta) = C_\theta\, e^{im\theta} \qquad (4.6)$$

where values of k_θ are restricted to integers since the coordinate θ is periodic with period 2π and the pressure must be single valued. Physically the integral values of k_θ, to be denoted by m, represent circumferential mode orders. If the duct contains radial splitters that are lined, k_θ may be complex.

Equation (4.4) with $k_\theta = m$ is the standard Bessel equation and has the solution

$$p_r(r) = J_m(k_r r) + C_m Y_m(k_r r) \qquad (4.7)$$

where J_m and Y_m are Bessel functions (of order m) of the first and second kind respectively. The acoustic admittance boundary condition that equation (4.7) must satisfy at the duct walls can be expressed in terms of the continuity of particle displacement as

$$\left.\frac{dp_r}{dr}\right|_{r=r_1} = ik\beta_1 \left(1 - \frac{K}{k} M\right)^2 p_r \Big|_{r=r_1} \qquad (4.8)$$

and

$$\left.\frac{dp_r}{dr}\right|_{r=r_2} = -ik\beta_2 \left(1 - \frac{K}{k} M\right)^2 p_r \Big|_{r=r_2} \qquad (4.9)$$

where β_1 and β_2 are the specific acoustic admittance of the inner wall at radius r_1, and the outer wall at radius r_2. Substitution of equation (4.7) into equations (4.8) and (4.9) yields a set of two simultaneous transcendental complex equations which must be solved for k_r and C_m. For a given circumferential mode order m, these equations have a sequence of roots $(k_r r_2)$ which represent the eigenvalues for a sequence of radial modes. The functions $p_r(r)$ obtained from equation (4.7) represent the corresponding eigenfunctions. Setting $k_r r_2 = \gamma$, $r_1/r_2 = \rho$ and eliminating C_m from the simultaneous equations obtained by the substitution of equation (4.7) into equations (4.8) and (4.9), we get a single equation for the eigenvalue of the form $F(\gamma) = 0$ (see Appendix C).

The eigenvalues can be obtained by solving this equation using the second order Newton-Raphson iteration formula

$$\gamma_{i+1} = \gamma_i - \frac{2F(\gamma_i)F'(\gamma_i)}{2[F'(\gamma_i)]^2 - F(\gamma_i)F''(\gamma_i)} \qquad (4.10)$$

where γ_i is the initial (guessed) value of the root and γ_{i+1} is the iterated value of the root. The primes denote differentiation with respect to the argument. This formula is repeatedly applied until successive iterations give roots (eigenvalues) whose absolute values differ by less than 10^{-5}.

The accurate and reliable determination of these eigenvalues is a critical part of the calculation of sound propagation in ducts. The ability of the solution procedure to converge to the correct sequence of eigenvalues depends critically upon the initial value of each root at the start of the iteration process. In order to assure convergence, the iteration is performed in several steps as indicated below.

Rectangular duct hardwall eigenvalues are used as starting values and the radius ratio is slowly decreased from unity to the annular duct radius ratio in order to obtain annular duct hardwall eigenvalues. The latter are used as starting values to obtain the eigenvalues for the case of hard outer wall and inner wall of admittance β_1. This is done by slowly incrementing the inner wall admittance magnitude from zero to $|\beta_1|$ and iterating along the line of constant phase of β_1. Using the new eigenvalues as the starting values and slowly incrementing the outer wall admittance magnitude from zero to $|\beta_2|$ (along the line of constant phase of β_2) the eigenvalue for the annular duct with inner wall admittance equal to β_1 and outer wall admittance equal to β_2 are determined.

When the inner and outer wall admittances are equal, the two step process described above to obtain softwall eigenvalues from hardwall eigenvalues reduces to a single step process. In this case the inner and outer wall admittance magnitudes are incremented simultaneously and equally in small steps from 0 to $|\beta_w|$ where β_w is the admittance of both walls.

The same iteration procedure is used while the flow Mach number is increased in small steps from zero to M in order to obtain the lined annular duct eigenvalues in the presence of uniform flow.

This careful step-by-step iteration process provides a reasonably reliable eigenvalue routine. However, the method is not totally infallible and occasionally cases of missed modes or modes found more than once are encountered.

An alternate method to determine the eigenvalues is used for cases for which the iteration process is not successful. In this method the eigenvalue equation is set up as a differential equation of the form (see Appendix C for details of the eigenvalue equation)

$$\frac{d\gamma}{dx} = F(m, kr_2, M, \gamma, \beta)\frac{d\beta}{dx} \tag{4.11}$$

where x is an independent parameter in the equation. To obtain the eigenvalues corresponding to wall admittance β_w (for both inner and outer walls), equation (4.11) is integrated, using Runge-Kutta method, from x = 0. The step size (Δx) in the integration process is kept small to obtain good accuracy. Furthermore, in order to minimize the error accumulated in the integration process, a second order Newton-Raphson iteration of the eigenvalue is performed at each step. Use of this eigenvalue solution procedure in combination with the original iterative procedure improves the reliability of the eigenvalue solution especially in identifying a mode that could have been missed by the iterative procedure.

After the soft-wall eigenvalues have been determined, the axial wave number K can be computed from

$$\frac{K}{k} = \frac{-M\pm \sqrt{1 - (1 - M^2)\left(\frac{k_r}{k}\right)^2}}{1 - M^2} \tag{4.12}$$

In the case of a hard wall duct ($\beta_1 = \beta_2 = 0$), when the expression under the radical becomes negative, K becomes complex and causes the mode under consideration to decay exponentially. Under such conditions the mode cannot transport any acoustic energy. The cut-on frequency f* for a mode can thus be defined by setting

$$k^* = k_r \sqrt{1-M^2}$$

and obtaining

$$f^* = \frac{c\gamma \sqrt{1-M^2}}{2\pi r_2} \qquad (4.13)$$

The cut-off ratio ξ, which is the ratio of the modal frequency to the cut-on frequency of the mode, is given by

$$\xi = \frac{f}{f^*} = \frac{2\pi n}{\gamma \sqrt{1-M^2}} \qquad (4.14)$$

where the frequency parameter   . A mode is considered cut off for $\xi<1$ but will be propagating when $\xi>1$. The definition for the cut-off ratio as given in equation (4.14) is valid for a rectangular duct of height r_2 if γ is replaced by the rectangular duct eigenvalue $k_y r_2$, and for a cylindrical duct of radius r_2 with γ equal to $k_r r_2$.

The effects of sheared flow on the wave propagation are evaluated by assuming that the boundary layers at the duct walls are sufficiently thin so that the predominant part of the acoustic energy flux takes place in the uniform flow region. In this case the solution to the differential equation for acoustic pressure in the presence of shear layers is approximated by choosing the eigenfunctions to be of the same form as in the uniform flow case (i.e., equation (4.7), with eigenvalues modified by the effects of the boundary layers. To obtain the eigenvalues in the presence of wall boundary layers, the equation governing the radial variation of acoustic pressure, i.e.,

$$\frac{d^2 p_r}{dr^2} + \frac{1}{r}\frac{dp_r}{dr} + \frac{2\kappa}{1 - M\kappa}\frac{dM}{dr}\frac{dp_r}{dr} + \left(k_r^2 - \frac{m^2}{r^2}\right) p_r = 0 \qquad (4.15)$$

16

(where $\kappa = K/k$ = non-dimensional propagation constant) is rewritten as two simultaneous first order differential equations, namely

$$\frac{dq}{dr} = -(\frac{1}{r} + \frac{2\kappa}{1-M} \frac{dM}{dr})q - (k_r^2 - \frac{m^2}{r^2})p_r$$

and
$$\frac{dp_r}{dr} = q \qquad\qquad (4.16)$$

and solved numerically by a combination of Runge-Kutta integration and Newton-Raphson iteration as outlined below.

The no-flow softwall annular duct eigenvalue ($\gamma = k_r r_2$) and the corresponding propagation constant $\kappa = K/k$, as calculated from equation (4.12), are used as the initial estimates. At the inner wall p_r is assigned a value equal to the uniform flow eigenfunction value and the inner wall boundary condition equation (4.8) is used to calculate $q = dp_r/dr$. These values of p_r and q provide the initial values to integrate equations (4.16) by Runge-Kutta method across the annulus to obtain p_r and q at the outer wall. The values of p_r and q at the outer wall are used to calculate the admittance

$$\beta = \left. \frac{-q}{ik(1-M\kappa)^2 p_r} \right|_{r=r_2} \qquad\qquad (4.17)$$

If this value differs from the specified admittance β_2, then the process must be repeated with a new value of γ until the condition $\beta=\beta_2$ is satisfied. This is done by second order Newton-Raphson iteration. By setting the difference $\beta-\beta_2$ equal to $F(\gamma)$ a revised eigenvalue is defined as

$$\gamma - \frac{2F(\gamma)F'(\gamma)}{2(F'(\gamma))^2 - F(\gamma)F''(\gamma)} \qquad\qquad (4.18)$$

17

where $F'(\gamma) = dF/d\gamma$ and $F''(\gamma) = d^2F/d\gamma^2$ are obtained by
performing Runge-Kutta integration of equations (4.16) with $\gamma \pm \epsilon$ and
$\gamma \pm i\epsilon$ as initial estimates for the eigenvalue. The iteration process
is repeated until an eigenvalue that satisfies the outer wall admittance
boundary condition is obtained. This procedure can be used with any arbitrary
boundary layer flow profile by appropriately specifying the Mach number
gradients dM/dr. The linear or the one-seventh power law boundary layer
profiles are used for most calculations.

In order to obtain good accuracy of the integration process, a variable
step size is used. Logarithmically spaced steps for the power law profile
provide smaller steps in the region of high velocity gradient.

Having determined the eigenvalues and eigenfunctions, the general
solution for acoustic pressure is constructed in terms of a series
representation utilizing the eigenfunctions, i.e.,

$$
p(r,\theta,z) = \sum_m \sum_n \left[A_{mn} \, P_{\theta_m}(\theta) \, x \right.
$$

$$
\left. P_{r_n}(k_{r,mn}r) \, e^{iK_{mn}z} \right]
\tag{4.19}
$$

where the summation is done over all spinning mode orders m and radial mode
orders n. As discussed before, the radial variation can be represented by the
eigenfunction form of equation (4.7). $k_{r,mn}$ and K_{mn} are the eigenvalue
(divided by r_2) and the axial propagation constant respectively for the
(m,n) mode. A_{mn} is designated the mode coefficient and is normally
determined by using the orthogonality property of the eigenfunctions.
Unfortunately, the eigenfunctions in the case of wave propagation in ducts
with flow are not orthogonal in the usual Sturm-Liouville sense. A
generalized definition of orthogonality developed by Kraft and Wells
(Reference 10) can, however, be used to evaluate the mode coefficients.

4.1.2 MODAL ANALYSIS FOR SEGMENTED DUCT

The solution for wave propagation in a duct with multiple treatment
elements utilizes a transfer matrix principle (References 1 and 2) to connect
the solution at one end of the duct with the other. The duct is assumed to be
composed of axially uniform sections which adjoin at planes where a
discontinuity in wall admittance ocurs (Figure 4.1). Modal reflections and
redistributions at admittance discontinuity planes and the consequent
existence of forward and backward traveling waves in the uniform sections are
taken into account in the solution.

Based on the modal expansion of equation (4.19) the acoustic pressure
at an arbitrary axial position z in section J (see Figure 4.2) in the presence
of forward and backward traveling waves is given by

$$
p^{(J)}(r,\theta,z) = \sum_m \sum_n \left[A_{mn}^{+(j-1)} e^{iK_{mn}^{+(J)}(z-z_{j-1})} p_{\theta_m}(\theta) p_{r_n}(k_{r_{mn}}^{+(J)} r) \right.
$$
$$
\left. + A_{mn}^{-(j)} e^{-iK_{mn}^{-(J)}(z_j-z)} p_{\theta_m}(\theta) p_{r_n}(k_{r_{mn}}^{-(J)} r) \right] \quad (4.20)
$$

When the duct and liner geometries are axisymmetric, the spinning modes are
not coupled. The analysis can then be simplified by restricting attention to
one spinning mode order (m), i.e.,

$$
p^{(J)}(r,\theta,z) = p_{\theta_m}(\theta) \sum_n \left[A_n^{+(j-1)} \times \right.
$$
$$
e^{iK_n^{+(J)}(z-z_{j-1})} p_{r_n}(k_{r_n}^{+(J)} r)
$$
$$
\left. + A_n^{-(j)} e^{-iK_n^{-(J)}(z_j-z)} p_{r_n}(k_{r_n}^{-(J)} r) \right] \quad (4.21)
$$
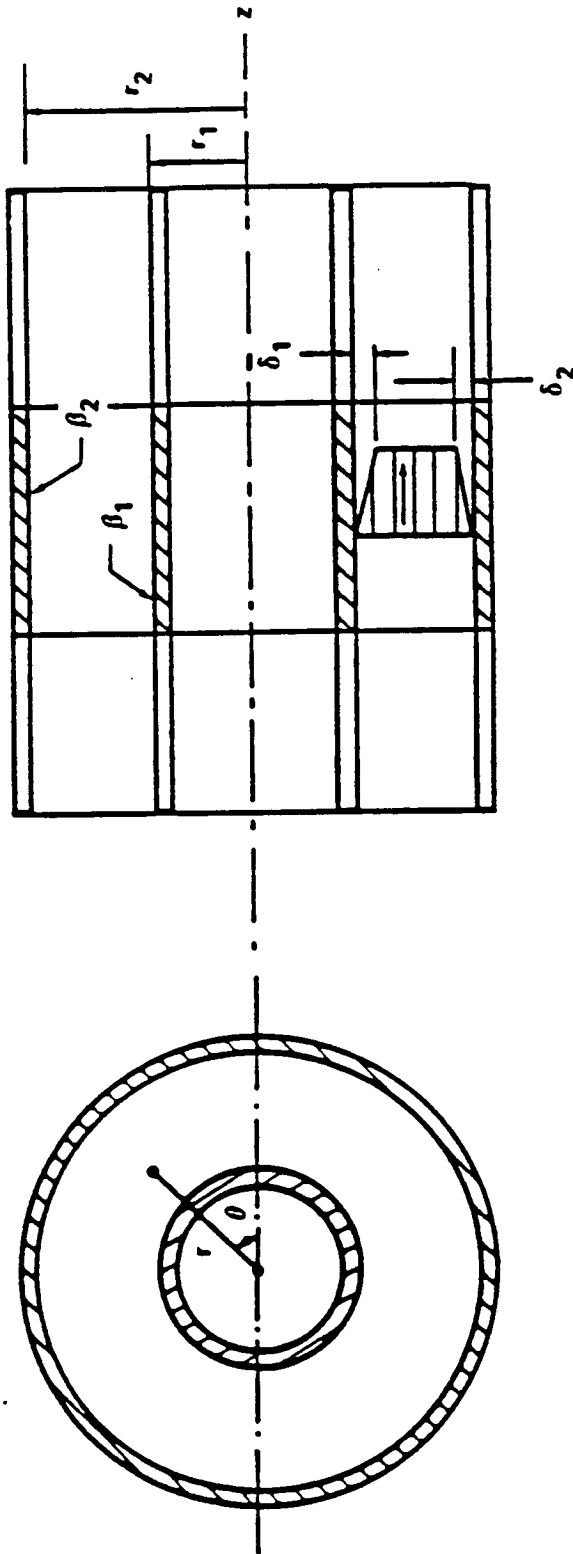
Figure 4.1. The Annular Duct Geometry
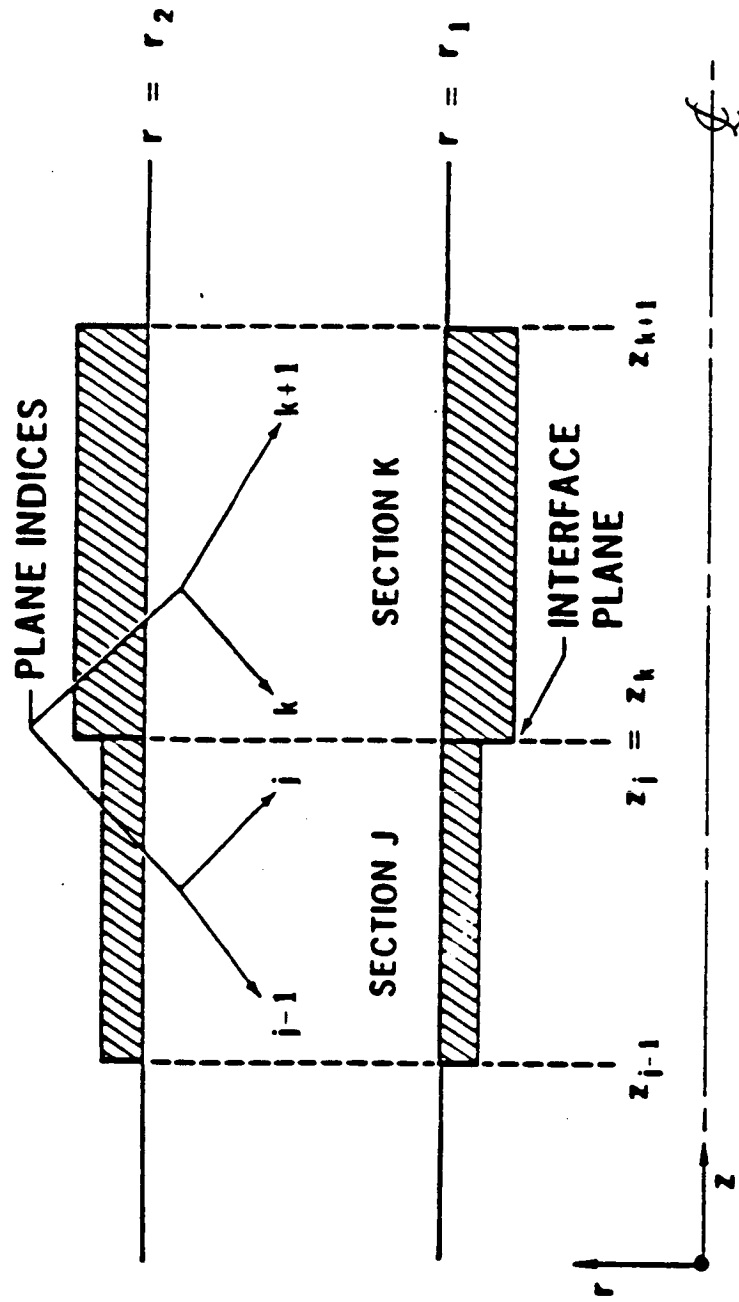
Figure 4.2. Plane and Section Designation Convention for Two Adjacent Duct Treatment Segments

where the spinning order subscript m has been dropped from A, K and k_r for brevity. In equations (4.20) and (4.21) the lower case superscripts are used to indicate values at duct admittance discontinuity planes while the upper case superscripts indicate values in uniform duct sections. The plus (+) and minus (−) superscripts indicate forward and backward propagation respectively. A completely analogous equation holds in section K and other sections of the duct.

In any uniform section of the duct, since each mode propagates independently, the mode coefficients at the end planes of the section are related by the axial propagation constant and the section length. Thus, for the radial mode n,

$$
\left.\begin{aligned}
A_n^{+(j)} &= A_n^{+(j-1)}\, e^{iK_n^{+(J)} L_J} \\[2em]
A_n^{-(j-1)} &= A_n^{-(j)}\, e^{-iK_n^{-(J)} L_J}
\end{aligned}\right\}
\tag{4.22}
$$

By representing the mode coefficients for the radial modes as elements of a column matrix, the above equations can be written in the following matrix form

$$
\left\{A^{+(j)}\right\} = \left[U^{+(j),+(j-1)}\right] \left\{A^{+(j-1)}\right\}
\tag{4.23a}
$$

for forward propagation, and

$$
\left\{A^{-(j-1)}\right\} = \left[U^{-(j-1),-(j)}\right] \left\{A^{-(j)}\right\}
\tag{4.23b}
$$

22

for backward propagation. Here [U] is the uniform section transmission matrix, with elements

$$
\left.
\begin{aligned}
U_{sn}^{+(j),+(j-1)} &= \delta_{sn}\, e^{iK_n^{+(J)}\,(z_j - z_{j-1})} \\[2em]
U_{sn}^{-(j-1),-(j)} &= \delta_{sn}\, e^{-iK_n^{-(J)}\,(z_j - z_{j-1})}
\end{aligned}
\right\}
\tag{4.24}
$$

Across an axial admittance discontinuity, such as that from plane j to plane k, solutions with different eigenfunction bases are related by requiring the acoustic pressure and the axial component of acoustic velocity to remain continuous across the discontinuity. The pressure continuity condition

$$
p(r,\ z_j) = p(r,\ z_k)
\tag{4.25}
$$

is written, using the modal expansion of pressure, in the matrix form

$$
\begin{aligned}
\left\{ p^{+(J)} \right\}^T \left\{ A^{+(j)} \right\} &+ \left\{ p^{-(J)} \right\}^T \left\{ A^{-(j)} \right\} \\
= \left\{ p^{+(K)} \right\}^T \left\{ A^{+(k)} \right\} &+ \left\{ p^{-(K)} \right\}^T \left\{ A^{-(k)} \right\}
\end{aligned}
\tag{4.26}
$$

where the superscript T represents the transpose of a column matrix. The axial acoustic velocity is expressed in terms of the acoustic pressure (using the momentum equation) as

$$
v_{z_n}(r) = \frac{K_n}{\rho_o c (k - M\,K_n)}\, p_{r_n}(r)
\tag{4.27}
$$

so that the velocity continuity equation

$$
v_z(r, z_j) = v_z(r, z_k)
\tag{4.28}
$$

can be written as

$$\{p^{+(J)}\}^T \left[\beta_z^{+(J)}\right] \{A^{+(j)}\}$$

$$+ \{p^{-(J)}\}^T \left[\beta_z^{-(J)}\right] \{A^{-(j)}\}$$

$$= \{p^{+(K)}\}^T \left[\beta_z^{+(K)}\right] \{A^{+(k)}\}$$

$$+ \{p^{-(K)}\}^T \left[\beta_z^{-(K)}\right] \{A^{-(k)}\} \tag{4.29}$$

where $[\beta_z]$ is the axial admittance matrix with elements

$$\beta_z^{+(J)}(m,n) = \delta_{mn} \frac{K_n^{+(J)}}{k - M K_n^{+(J)}} \tag{4.30}$$

After some lengthy matrix algebra equations (4.26) and (4.29) can be solved to obtain

$$\{A^{+(k)}\} = \left[T^{+(k),+(j)}\right] \{A^{+(j)}\} + \left[R^{+(k),-(k)}\right] \{A^{-(k)}\} \tag{4.31}$$

and

$$\{A^{-(j)}\} = \left[T^{-(j),-(k)}\right] \{A^{-(k)}\} + \left[R^{-(j),+(j)}\right] \{A^{+(j)}\} \tag{4.32}$$

where [T] and [R] represent the transmission and reflection matrices for the admittance discontinuity plane under consideration. The determination of [T] and [R] matrices requires several matrix algebraic operations as shown in the following equations

24

$$[T^{+(K),+(j)}] = [H_1^{+(K),+(K)}]^{-1}[H_1^{+(K),+(J)}]$$

with

$$[H_1^{+(K),+(J)}] = [G_1][G^{+(K),+(J)}] - [G^{+(K),+(J)}][\,\beta_z^{+(J)}]$$

$$[G_1] = [G^{+(K),-(J)}][\,\beta_z^{(J)}][G^{+(K),-(J)}]^{-1}$$

and

$$G^{+(K),+(J)}(n,m) = \int_{r_1}^{r_2} r\, p_{r_n}\left(k_{r_n}^{+(K)}\, r\right) \times p_{r_m}\left(k_{r_m}^{+(J)}\, r\right) dr \qquad (4.33)$$

where p_r is the eigenfunction represented in equation (4.7). Similar equations hold for other transmission and reflection matrix elements. Since the eigenfunctions are expressed in terms of the Bessel functions of the first and second kind, calculation of the reflection and transmission matrix elements requires the evaluation of the integrals of the products of the Bessel functions.

Equations (4.23a) and (4.23b), involving the uniform section matrix [U], along with equations (4.31) and (4.32), involving the transmission matrix [T] and the reflection matrix [R], when written for each uniform section and discontinuity in the duct, are sufficient to relate the forward and backward wave solutions at one end of the duct with those at the other. Use of this method to calculate the propagation of waves in a laboratory exhaust duct of finite length would require specification of the axial admittances at the end planes to establish the transmission and reflection matrices. (The axial admittance at the duct termination depends on the method of flanging the duct and the location of the boundaries in the free field. It is further complicated by the nonuniform exhaust flow field. At the source location, the axial admittance must be related to the internal impedance of the source.) An

alternate approach is to choose the two end planes at arbitrary stations in hardwall sections of the duct upstream and downstream of treated sections and specify the overall modal participation (i.e., the sum of the forward and backward traveling waves) at these planes. The modal participation can be obtained from in-duct modal measurements.

The equation which relates the forward and backward modal vectors in the source plane is

$$\left[\diagdown_I \diagdown \right] \left\{ A^{+(S)} \right\} - \left[R_S^{+(S),-(S)} \right] \left\{ A^{-(S)} \right\} = \left\{ Q_S \right\} \qquad (4.34)$$

and at the termination plane is

$$\left[\diagdown_I \diagdown \right] \left\{ A^{-(T)} \right\} - \left[R_T^{-(T),+(T)} \right] \left\{ A^{+(T)} \right\} = \left\{ Q_T \right\} \qquad (4.35)$$

where

$[R_S]$ = reflection matrix at source plane

$[R_T]$ = reflection matrix at termination plane

$[I]$ = unit matrix

and $\{Q_S\}$ and $\{Q_T\}$ are the generalized source and termination vectors. If, as suggested above, the source and termination planes are chosen as planes in hardwall sections of the duct then

$$[R_S] = -[I] = [R_T] \qquad (4.36)$$

and the source and termination vectors become the sum of the forward and backward waves which can be obtained from measurement for input to the program. Equations (4.34) and (4.35) along with equations (4.23a), (4.23b) for each uniform admittance section of the duct and equations (4.31) and (4.32) for each axial admittance discontinuity form a completely determined system. This system of equations is written as a stacked system matrix equation

26

$$[S] \, \{A\} = \{Q\} \qquad\qquad (4.37)$$

where [S] is the stacked system matrix and [Q] is the generalized source vector. Equation (4.37) is solved by a double-back substitution routine to obtain

$$\{A\} = [S]^{-1}\{Q\} \qquad\qquad (4.38)$$

The stacked system matrix is shown in Figure 4.3 for a three segment duct.

Equations (4.34) and (4.35), along with (4.36), cannot be used for the source and termination planes when the duct walls at these planes are lined or when the presence of boundary layer is to be considered. Under these conditions, the eigenvalues of the forward and backward modes are different and the forward and backward mode coefficients cannot, therefore, be added simply to obtain the complex pressure field. A separation of forward and backward traveling modes at the source and termination planes can, however, be obtained experimentally. This will define the mode content incident from the source, i.e., the forward traveling mode coefficients at Plane 1, $\{Q_S^+\}$, and the mode content reflected from the nozzle; i.e., the backward traveling mode coefficients at Plane 6, $\{Q_T^-\}$. The stacked system matrix equation shown in Figure 4.3 can then be modified by setting $[R_S] = 0 = [R_T]$ and substituting $\{Q_S^+\}$ and $\{Q_T^-\}$ for $\{Q_S\}$ and $\{Q_T\}$, respectively. Thus, by using the measured forward traveling mode distribution at Plane 1; i.e., $\{Q_S^+\}$ and the backward traveling mode distribution on Plane 6; i.e., $\{Q_T^-\}$, the stacked system matrix (Equation 4.37) can be solved for the forward and backward mode coefficients at all planes.

Once the modal solution vector $\{A\}$ is obtained, the acoustic energy (E_z) at the end planes of all segments is obtained from the following expression of the axial acoustic intensity due to Cantrell and Hart (Reference 11)

Planes

§1   §2   §3

1 2 3 4 5 6
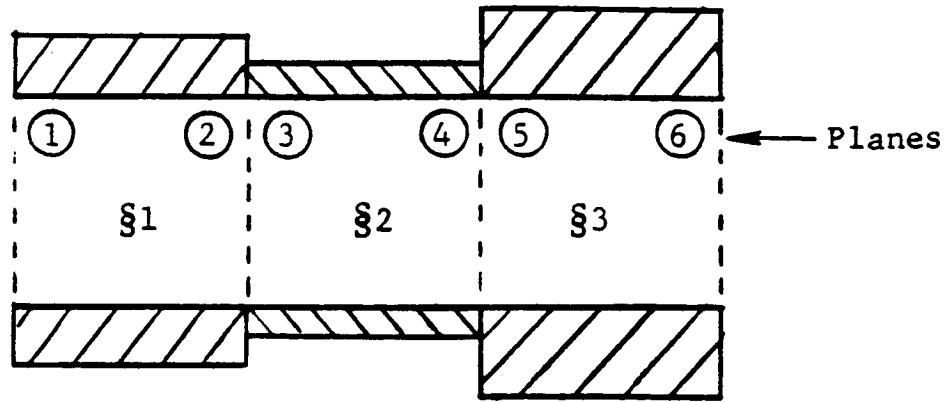
$$
\begin{bmatrix}
[\mathbf{I}] & 0 & 0 & 0 & 0 & 0 & -[R_S] & 0 & 0 & 0 & 0 & 0 \\
-[U^{+2+1}][\mathbf{I}] & 0 & 0 & 0 & 0 & 0 & 0 & 0 & 0 & 0 & 0 \\
0 & -[T^{+3+2}][\mathbf{I}] & 0 & 0 & 0 & 0 & 0 & -[R^{+3-3}] & 0 & 0 & 0 \\
0 & 0 & -[U^{+4+3}][\mathbf{I}] & 0 & 0 & 0 & 0 & 0 & 0 & 0 & 0 \\
0 & 0 & 0 & -[T^{+5+4}][\mathbf{I}] & 0 & 0 & 0 & 0 & 0 & -[R^{+5-5}] & 0 \\
0 & 0 & 0 & 0 & -[U^{+6+5}][\mathbf{I}] & 0 & 0 & 0 & 0 & 0 & 0 \\
0 & 0 & 0 & 0 & 0 & 0 & [\mathbf{I}] & -[U^{-1-2}] & 0 & 0 & 0 & 0 \\
0 & -[R^{-2+2}] & 0 & 0 & 0 & 0 & 0 & [\mathbf{I}] & -[T^{-2-3}] & 0 & 0 & 0 \\
0 & 0 & 0 & 0 & 0 & 0 & 0 & 0 & [\mathbf{I}] & -[U^{-3-4}] & 0 & 0 \\
0 & 0 & -[R^{-4+4}] & 0 & 0 & 0 & 0 & 0 & 0 & [\mathbf{I}] & -[T^{-4-5}] & 0 \\
0 & 0 & 0 & 0 & 0 & 0 & 0 & 0 & 0 & 0 & [\mathbf{I}] & -[U^{-5-6}] \\
0 & 0 & 0 & 0 & 0 & -[R_T] & 0 & 0 & 0 & 0 & 0 & [\mathbf{I}]
\end{bmatrix}
\begin{Bmatrix}
A^{+1} \\ A^{+2} \\ A^{+3} \\ A^{+4} \\ A^{+5} \\ A^{+6} \\ A^{-1} \\ A^{-2} \\ A^{-3} \\ A^{-4} \\ A^{-5} \\ A^{-6}
\end{Bmatrix}
=
\begin{Bmatrix}
Q_S \\ 0 \\ 0 \\ 0 \\ 0 \\ 0 \\ 0 \\ 0 \\ 0 \\ 0 \\ 0 \\ Q_T
\end{Bmatrix}
$$

Figure 4.3.   Stacked System Matrix Equation for Three-Segment Duct

$$I_z (r,z) = (1+M^2) \, \text{Re} \, [pv_z^*] + \frac{M}{\rho_0 c} pp^* + \rho_0 c \, Mv_z v_z^* \qquad (4.39)$$

and

$$E_z (z) = 2\pi \int_{r_1}^{r_2} I_z(r,z) \, r dr \qquad (4.40)$$

The energies at the first and the last planes in the segmented duct can be used to calculate the total attenuation due to the treatment in the duct.

4.1.3 NOZZLE REFLECTION COEFFICIENT

If the termination plane of the fan duct analytical model is represented by a plane in the hard wall section of the duct right at the entrance to the nozzle, the stacked matrix [S] of the stacked system equation (4.37) can be completely determined only if the nozzle reflection matrix $[R_T]$ is specified. The matrix $[R_T]$ relates the backward propagating wave just upstream of the nozzle (and due to reflection from the nozzle) to the forward propagating wave at the same location by the relation.

$$\{A^{-(T)}\} = [R_T^{-(T),+(T)}] \, \{A^{+(T)}\} \qquad (4.41)$$

No theory adequate for the purposes of this study is currently available for the prediction of the nozzle reflection coefficients for multimodal propagation. $[R_T]$ can, however, be determined experimentally.

The experimental determination of the nozzle reflection matrix $[R_T]$ can be complicated due to the fact that the axisymmetric nozzle contraction causes a scattering of acoustic modes among radial modes of the same spinning mode order, i.e., a mode incident onto the nozzle can be reflected as a combination of several modes. The difficulty in determining the elements of

29

the reflection matrix in the presence of cross-mode scattering among multiple modes lies in the determination of the off-diagonal terms. Separating forward and backward modes upstream of the nozzle gives a system of n equations (for n modes) in the form of equation 4.41 in which the reflection coefficient matrix $[R_T]$ is unknown; i.e., there are n equations in n^2 unknowns. One hypothetical method of determining the nozzle reflection matrix would be to generate a radial mode in isolation which, upon incidence to the nozzle, is scattered as a distribution of radial modes. The reflection coefficients for the incident mode, i.e., R_{n1}, R_{n2}, R_{n3} . . . etc., can then be determined from the forward-backward modal separation of the complex pressure profile measured just upstream of the nozzle. Each mode, in turn, would have to be generated individually. It is, however, impossible to generate an isolated radial mode in a fan-duct system.

An alternate approach is to use the measured complex pressure profile at a station just upstream of the nozzle for several different distributions of the incident modes and separate the forward and backward mode coefficients. The measurements made for each distribution of incident modes will produce an independent equation, provided that these incident distributions are not linearly related. If a total of n modes are participating in the propagation and scattering phenomena, n different distributions of incident modes must be generated. This can be achieved by introducing axisymmetric phasing effects in the duct system, i.e., varying treatment length, using liners of unequal admittance on opposite duct walls, using mode-scattering obstacles, Helmholtz cavities, etc., to alter the source radial mode distribution. For each distribution of incident modes, n equations represented by a matrix equation like equation (4.41) is obtained, so that for n different distributions of incident modes n x n equations will be obtained which can be solved for the n x n elements of the reflection matrix $[R_T]$. To solve these equations, it is required that the incident modal distributions are not equal or linearly related, to avoid numerical problems caused by determinants with two proportional rows or columns.

When the nozzle reflection matrix is determined as suggested above, Equation (4.41) can be written as

$$[R_T^{-(T),+(T)}]\{A^{+(T)}\} - \{A^{-(T)}\} = 0 \qquad (4.42)$$

Equation 4.42 can then be used to replace Equation 4.35 so that the stacked system matrix equation in Figure 4.3 will have $\{Q_T\}=0$. Then, with $[R_S]$ set to zero, the matrix equation can be solved upon specification of the forward traveling source vector $\{Q_S^+\}$. As discussed before, the source vector is specified by the measured separation of forward and backward modes just downstream of the fan plane.

It should again be mentioned that in the case of an annular exhaust duct-nozzle system where spinning modes propagate, scattering of modes by the nozzle can be assumed to occur among radial modes only if the nozzle retains the axisymmetry of the duct.

4.2   MATHEMATICAL DETAILS OF MODAL DECOMPOSITION

Starting with the equation that describes the pressure field in a duct with flow,

$$P(r, \theta, z, t) = \sum_{m=-M}^{M} \sum_{n=0}^{N} [A_{mn}^+ P_{r_{mn}}^+ (r)\ e^{ik_{mn}^+ z}$$

$$+ A_{mn}^- P_{r_{mn}}^- (r)\ e^{-ik_{mn}^- z}]\ e^{i(m\theta - \omega t)} \qquad (4.43)$$

consider measurement of the acoustic pressure amplitude and phase (relative to a reference signal $e^{i(\phi - \omega t)}$). The measurement is made at a number of circumferential positions, $\theta_j = (j\pi/M)$, j = 0, 1, 2 . . . ., (2 M - 1), where M = M + 1. Applying the discrete Fourier transform [Reference 4] to the

measurements, we obtain the order m coefficient of the measured circumferential pressure distribution (for fixed values of r and z)

$$\tilde{p}_m(r,\ z) = \frac{1}{2\tilde{M}} \sum_{j=0}^{2\tilde{M}-1} \tilde{p}(r,\ \theta_1,\ z)\ \bar{e}^{i(km\pi/\tilde{M})} \qquad (4.44)$$

$$m = 0,\ \pm\ 1,\ \ldots,\ \pm\ M$$

Applying the discrete Fourier transform to equation (4.43) and comparing with equation (4.44), we obtain

$$\sum_{n=0}^{N}\ [A_{mn}^+ p_{r_{mn}}^+ (r)\ e^{i(k_{mn}^+ z)}$$

$$+ A_{mn}^- p_{r_{mn}}^- (r)\ e^{i(-k_{mn}^- z)}\ ] = \tilde{p}_m(r,z) \qquad (4.45)$$

The radial and axial mode separation will be considered next. When the radial mode shapes, $p_{r_{mn}}^+(r)$ and $p_{r_{mn}}^-(r)$ are equal, then the radial mode separation can be obtained by measuring $p_m(r,\ z)$ at $(N + 1)$ values of r, for a fixed z. The results are then used to form the following matrix equation

$$\underline{A}\ \underline{x} = \underline{a} \qquad (4.46a)$$

where

$$\underline{A} = \begin{bmatrix} p_{r_{mo}}(r_1) & p_{r_{m1}}(r_1) & \cdots & p_{r_{mN}}(r_1) \\ p_{r_{mo}}(r_2) & \cdot & \cdot & \cdot \\ \cdot & \cdot & \cdot & \cdot \\ \cdot & \cdot & \cdot & \cdot \\ p_{r_{mo}}(r_{N+1}) & \cdot & \cdot & p_{r_{mN}}(r_{N+1}) \end{bmatrix} \qquad (4.46b)$$

$$\underline{x} = \left\{ \begin{array}{l} A_{mo}^{+} \, e^{ik_{mo}^{+}z} \quad + \quad A_{mo}^{-} \, e^{-ik_{mo}^{-}z} \\[2em] A_{m1}^{+} \, e^{ik_{m1}^{+}z} \quad + \quad A_{m1}^{-} \, e^{-ik_{m1}^{-}z} \\[1em] \qquad \cdot \qquad\qquad\qquad \cdot \\[0.3em] \qquad \cdot \qquad\qquad\qquad \cdot \\[1em] A_{mN}^{+} \, e^{ik_{mN}^{+}z} \quad + \quad A_{mN}^{-} \, e^{-ik_{mN}^{-}z} \end{array} \right\} \qquad (4.46c)$$

and

$$\underline{a} = \left\{ \begin{array}{l} P_{m}(r_1, \, z) \\[1em] P_{m}(r_2, \, z) \\[0.5em] \qquad \cdot \\[0.3em] \qquad \cdot \\[0.5em] P_{m}(r_{n+1}, \, z) \end{array} \right\} \qquad (4.46d)$$

This matrix equation is then solved for the unknown vector, $\underline{x}$. Note that the value of $\underline{x}$ is a function of the axial coordinate, z.

To separate the order (m, n) forward and backward propagating modes, the circumferential and radial mode separation described above is performed at two axial locations, z_1 and z_2. Denoting the components of $\underline{x}$ corresponding to the (m, n) mode by $X_{mn}(z_1)$ and $X_{mn}(z_2)$, the following matrix can be formed for the desired unknowns A_{mn}^{+} and A_{mn}^{-}.

$$\underline{B} \, \underline{y} = \underline{b} \qquad (4.47a)$$

33

$$\underline{B} = \begin{bmatrix} e^{ik_{mn}^{+} z_1} & e^{-ik_{mn}^{-} z_1} \\ e^{ik_{mn}^{+} z_2} & e^{-ik_{mn}^{-} z_2} \end{bmatrix} \tag{4.47b}$$

$$\underline{y} = \left\{ \begin{array}{c} A_{mn}^{+} \\ A_{mn}^{-} \end{array} \right\} \tag{4.47c}$$

and

$$\underline{b} = \left\{ \begin{array}{c} X_{mn}(z_1) \\ X_{mn}(z_2) \end{array} \right\} \tag{4.47d}$$

This matrix equation can be solved explicitly, with the results

$$A_{mn}^{+} = \frac{e^{-ik_{mn}^{+}z_1}[X_{mn}(z_1) - X_{mn}(z_2) e^{ik_{mn}^{-}\Delta z}]}{1 - e^{i(k_{mn}^{+} + k_{mn}^{-})\Delta z}} \tag{4.48a}$$

and

$$A_{mn}^{-} = \frac{e^{-ik_{mn}^{-}z_2}[X_{mn}(z_2) - X_{mn}(z_1) e^{ik_{mn}^{+}\Delta z}]}{1 - e^{i(k_{mn}^{+} + k_{mn}^{-})\Delta z}} \tag{4.48b}$$

where

$$\Delta z = z_2 - z_1 \tag{4.48c}$$

If we examine the uncertainties in the measurement of A_{mn}^{+} and A_{mn}^{-}, we see that it is sensitive to the factor $[1 - \cos(k_{mn}^{+} + k_{mn}^{-})\Delta z]$ in the denominator. In order to avoid this problem, two things can be done. First, careful

spacing can be chosen such that $[(k^+_{mn} + k^-_{mn})\Delta z]$ does not equal an integral multiple of 2π. Secondly, redundant measurements can be introduced, which will significantly improve the modal decomposition accuracy. The procedure for using redundant data to effect a least squares matrix solution will now be explained. Consider the general matrix equation

$$\underline{D}\ \underline{\xi} = \underline{\sigma} \tag{4.49}$$

Here $\underline{D}$ is a square matrix of order q whose elements may be complex. $\underline{\xi}$ is the vector containing q complex unknowns, and $\underline{\sigma}$ is the (complex) input data vector of order q. For matrices $\underline{D}$, whose determinant is non zero, there is a unique solution for $\underline{\xi}$. However, when σ is determined from experimental measurements, small measurement errors may lead to significant inaccuracies in $\underline{\xi}$.

To increase the accuracy in the calculation of $\underline{\xi}$, additional independent measurements may be added to the system. Assume that s additional independent measurements are added to the system. The size of the matrix $\underline{D}$ is then (q + s) by q, and $\underline{\sigma}$ is of order (q + s), while $\underline{\xi}$ remains of order q. The system is now overdetermined, and no exact solution for $\underline{\xi}$ is possible. The approach used is then to define the remainder $\underline{\gamma}$, where

$$\underline{\gamma} = \underline{D}\ \underline{\xi} - \underline{\sigma} \tag{4.50}$$

We now search for the value of $\underline{\xi}$ which minimizes the magnitude of $\underline{\gamma}$. Noting that $\underline{\gamma}$ is complex, we define the magnitude squared of $\underline{\gamma}$ by γ, where

$$\gamma = \gamma_i\gamma^*_i = D_{ij}\ D^*_{ik}\ \xi_i\xi^*_k$$

$$\tag{4.51}$$

$$- \sigma_i\ D_{ik}\xi^*_k - D_{ij}\ \xi_j\ \sigma^*_i + \sigma_i\sigma^*_i$$

where the * denotes the complex conjugate. We now minimize γ by setting $\partial\gamma/\partial\xi_i$ and $\partial\gamma/\partial\xi^*_i$ equal to zero. The resulting equations can be written in matrix form as

$$\underline{D}^{*T}\,\underline{D}\,\underline{\xi} = \underline{D}^{*T}\,\underline{\sigma} \tag{4.52}$$

where T indicates the transpose. Equation (4.52) is the generalization of the least-squares fit for matrix equations, and can be applied to either equations (4.46a) or (4.47a).

For ducts with sheared flow, $P^{+}_{r_{mn}}(r)$ and $P^{-}_{r_{mn}}(r)$ are not identical. Under these conditions, the radial and axial mode separation cannot be decoupled in the manner discussed above, but must be carried out simultaneously. With only two axial locations, this would lead to inverting a matrix of the order 2 (N + 1) as opposed to order (N + 1) when decoupling was possible (N = q + s). As the sensitivity of matrix solutions to small input errors increases with an increase of matrix size, redundant measurements should be used in this case also. The resulting matrix equation is

$$\underline{C}^{*T}\,\underline{C}\,\underline{\sigma} = \underline{C}^{*T}\,\underline{c} \tag{4.53a}$$

where

$$
\underline{C} = \begin{bmatrix}
P^{+}_{r_{mo}}(r_1)e^{ik^{+}_{mo}z_1} & P^{-}_{r_{mo}}(r_1)e^{-ik^{-}_{mo}z_1} & P^{+}_{r_{m1}}(r_1)e^{ik^{+}_{m1}z_1} & \cdots & P^{-}_{r_{mN}}(r_1)e^{-ik^{-}_{mN}z_1} \\[2ex]
P^{+}_{r_{mo}}(r_1)e^{ik^{+}_{mo}z_2} & P^{-}_{r_{mo}}(r_1)e^{-ik^{-}_{mo}z_2} & \cdot & \cdot & P^{-}_{r_{mN}}(r_1)e^{-ik^{-}_{mN}z_2} \\[2ex]
P^{+}_{r_{mo}}(r_1)e^{ik^{+}_{mo}z_3} & P^{-}_{r_{mo}}(r_1)e^{-ik^{-}_{mo}z_3} & \cdot & \cdot & P^{-}_{r_{mN}}(r_1)e^{-ik^{-}_{mN}z_3} \\[2ex]
P^{+}_{r_{mo}}(r_2)e^{ik^{+}_{mo}z_1} & \cdot & \cdot & \cdot & \cdot \\[2ex]
\cdot & \cdot & \cdot & \cdot & \cdot \\[1ex]
\cdot & \cdot & \cdot & \cdot & \cdot \\[1ex]
\cdot & \cdot & \cdot & \cdot & \cdot \\[2ex]
P^{+}_{r_{mo}}(r_{N+1})e^{ik^{+}_{mo}z_3} & \cdots & \cdot & \cdot & P^{-}_{r_{mN}}(r_{N+1})e^{ik^{-}_{mN}z_3}
\end{bmatrix}
$$

$$(4.53b)$$

$$(4.53b)$$

$$\underline{\sigma} = \left\{ \begin{array}{c} A_{mo}^{+} \\ A_{mo}^{-} \\ A_{m1}^{+} \\ \cdot \\ \cdot \\ \cdot \\ A_{mN}^{-} \end{array} \right\}$$

$$(4.53c)$$

and

$$\underline{c} = \left\{ \begin{array}{c} P_m \ (r_1, \ z_1) \\ P_m \ (r_1, \ z_2) \\ P_m \ (r_1, \ z_3) \\ P_m \ (r_2, \ z_1) \\ \cdot \\ \cdot \\ P_m \ (r_{N+1}, \ z_3) \end{array} \right\}$$

$$(4.53d)$$

As before, the * denotes the complex conjugate and T implies the transpose of the matrix.

4.3   THE IN-SITU IMPEDANCE MEASUREMENT TECHNIQUE

The In-Situ method (References 4, 5, 6) has been used for the measurement of the Normal Acoustic Impedance of locally reacting treatment panels. Dean[4] and Kooi and Sarin[5] used this technique on single degree of freedom (SDOF) panels while Zandbergen[6] measured the impedance of 2 degrees of freedom (2DOF) samples using this method. Zandbergen, et. al.,[12] also measured the impedance of the inlet acoustic treatment of a Fokker F28 aircraft power plant during flight.

The theory of this method is illustrated here for an SDOF liner. The sketch below shows a single cavity with an acoustically hard backwall at $x = o$ and a porous face sheet at $x = d$. The walls of the cavity are assumed to be

37

rigid so that no transmission of sound between cavities is allowed. The width
of the cavity is sufficiently small to allow only plane wave propagation
between the backwall and the face sheet.
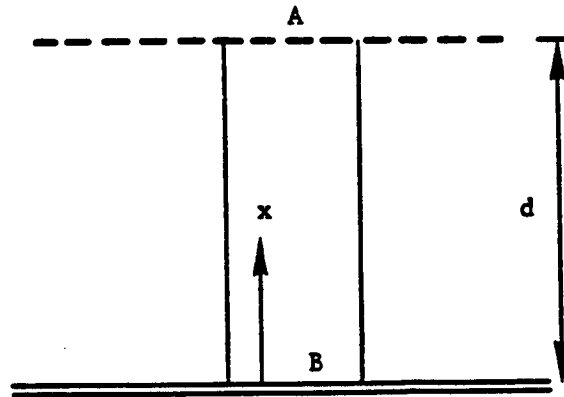
The acoustic pressure at any position x in the cavity and frequency f
is given by

$$p(x,f) = p_0 e^{i(\omega t + \phi_B)} \cos(kx) \tag{4.54}$$

where k is the acoustic wave number ω/c, c is the speed of sound in the air
filling the cavity and the space outside it, $\omega = 2\pi f$ and $i = \sqrt{-1}$.

The acoustic particle velocity u in the x direction is related to the
acoustic pressure by the linearized momentum equation:

$$\frac{\partial}{\partial t} u(x,f) = \frac{-1}{\rho} \frac{\partial}{\partial x} p(x,f) \tag{4.55}$$

where ρ is the density of the air.

From equations (4.54) and 4.55)

$$u(x,f) = -i \frac{\sin(kx)}{\rho c} p_0 e^{i(\omega t + \phi_B)}$$

$$= -i \frac{\sin(kx)}{\rho c} p_B(f) \tag{4.56}$$

where $p_B(f) = p_o e^{i(\omega t + \phi_B)}$, the acoustic pressure at the back wall.

It is assumed that the acoustic particle velocity is continuous across the thin porous face sheet. That is

$$u_A^+(f) = u_A^-(f) = -i \, \frac{\sin(kd)}{\rho c} \, p_B(f) \tag{4.57}$$

Thus the normal impedance at the face sheet is given by

$$\zeta_A(f) = \frac{p_A(f)}{-u_A^+(f)\rho c} = -i \, \text{cosec}(kd) \, \frac{p_A(f)}{p_B(f)} \tag{4.58}$$

where $p_A(f)$ is the acoustic signal at the surface of the face sheet just outside the cavity.

As illustrated by Equation (4.58), the In-Situ method requires the measurement of the complex ratio of two acoustic signals. For this reason, it is often referred to as the Two Microphone Method.

In the presence of grazing flow, the face sheet transducer signal $p_A(f)$ may contain flow noise which may be regarded as random in nature and uncorrelated with the acoustic signal. In order to remove this contamination of the face sheet signal, Equation (4.58) is modified to

$$\zeta_A(f) = -i \, \text{cosec}(kd) \, . \, \overline{H_{AB}(f)} \tag{4.59}$$

where

$\overline{H_{AB}(f)} = \overline{p_A(f)p_B^*(f)} \, / \, \overline{p_B(f)p_B^*(f)}$, the time averaged complex transfer function of the two signals at locations A and B.

5.0 EXPERIMENTAL PROGRAM AND RESULTS

This section describes the critical experiment conducted to obtain the data necessary to test the validity of the theory described in Section 4.1. This experiment consisted of measurement of the necessary information required to calculate the suppression achieved by an acoustically treated section in the exhaust duct of a fan vehicle.

The vehicle was designed for a strong blade-vane interaction tone, making use of Rotor 55 with only 8 outlet guide vanes closely spaced against the 15 bladed rotor. An inlet turbulence control structure was incorporated into the anechoic-chamber test facility so as to reduce the production of other acoustic modes.

The treatment section was designed to be as linear as possible in order to establish the value of the wall admittance with minimum uncertainty. Impedance measurements were made on the actual treatment panels used in the test vehicle. Laboratory measurements were made to determine quantitatively the effects of flow velocity and sound pressure level upon the acoustic impedance.

Acoustic "Mode" probes were incorporated upstream and downstream of the treated section (of the fan exhaust duct) to establish the acoustic modes propagating in both directions at two axial cross-sectional planes, one upstream and the other downstream of the treated section. These probes were designed to measure the modes expected for the vane-blade interaction as well as all other cut-on modes at the tone frequency of the rotor blades.

Aerodynamic measurements were made at the same axial planes (by the same probe actuators) to establish the mean flow profiles, both radially and circumferentially, and to determine the boundary layer profiles incident upon and leaving the treated sections.

The data from the acoustic probes were used in conjunction with the aerodynamic measurements to establish the composition of the amplitudes and

relative phases of the acoustic modes for use in the analytical prediction of the acoustic suppression of the treated section, as discussed in the section, "Theory-Experiment Comparison".

5.1   TEST APPARATUS

5.1.1 TEST FACILITY

The vehicle was tested in an anechoic-chamber 10.668 m wide by 7.62 m long by 3.048 m high, measured from the tips of the foam wedges. The wedges, .71 m deep polyurethane foam, provide less than ±1 dB standing wave ratio down to 200 Hz. Far-field noise measurements were made by an array of twelve, 6.35mm-diameter, far-field microphones (B&K 4135) located on a 5.182 m radius arc. The microphones were arranged at 10° intervals from 20° to 110° relative to the fan exhaust. Table 5.1 summarizes the positions relative to the nozzle. Calibration was by piston phone, B&K Model 4220, prior to each far-field measurement.

The far field microphone levels were recorded on a Sangamo Sabre IV tape recorder at 152 cm per second (60 ips) tape speed. Power spectra were generated by processing the microphone signals through an HP 5451C Fourier analyzer system. Power spectrum levels at blade passing frequency were integrated for overall acoustic power levels. Fan operation was stabilized to steady state before initiating any data recording.

The fan was driven in the exhaust mode as shown in Figure 5.1. Figure 5.2 shows Rotor 55 as it was installed in the chamber. The air is inducted through a vertical stack and turned through 90° as illustrated in Figure 5.3; an inlet turbulence control device was included.

The effectiveness of the 90° turn at the base of the vertical inlet stack and the TCS structure was determined. Kiel probe data are shown in Figure 5.4. Losses across the TCS and the flow contouring were found to be small, and varied by less than 0.5% at any location except at the top of the

42

Table 5.1. Far Field Microphone Distances and Angles

Relative to Fan		Relative to Nozzle	
Distance Meters	Angle Degrees	Distance Meters	Angle Degrees
5.18	20	3.54	36
5.18	30	3.73	44
5.18	40	3.97	57
5.18	50	4.25	69
5.18	60	4.56	80
5.18	70	4.87	90
5.18	80	5.18	100
5.18	90	5.49	109
5.18	100	5.77	118
5.18	110	6.04	126
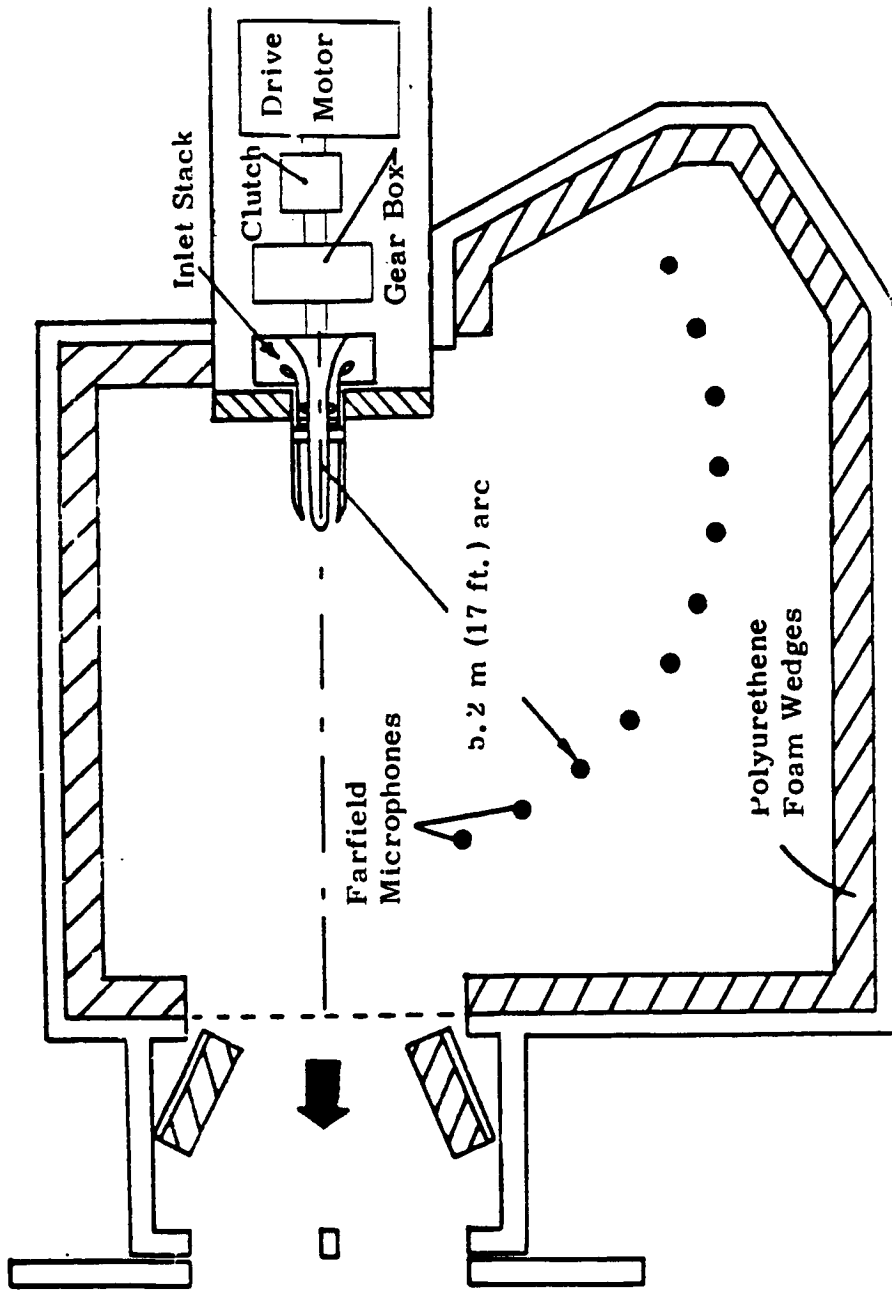
Figure 5.1. Schematic of the General Electric-Schenectady Anecholc Chamber, Fan Exhaust Test Configuration
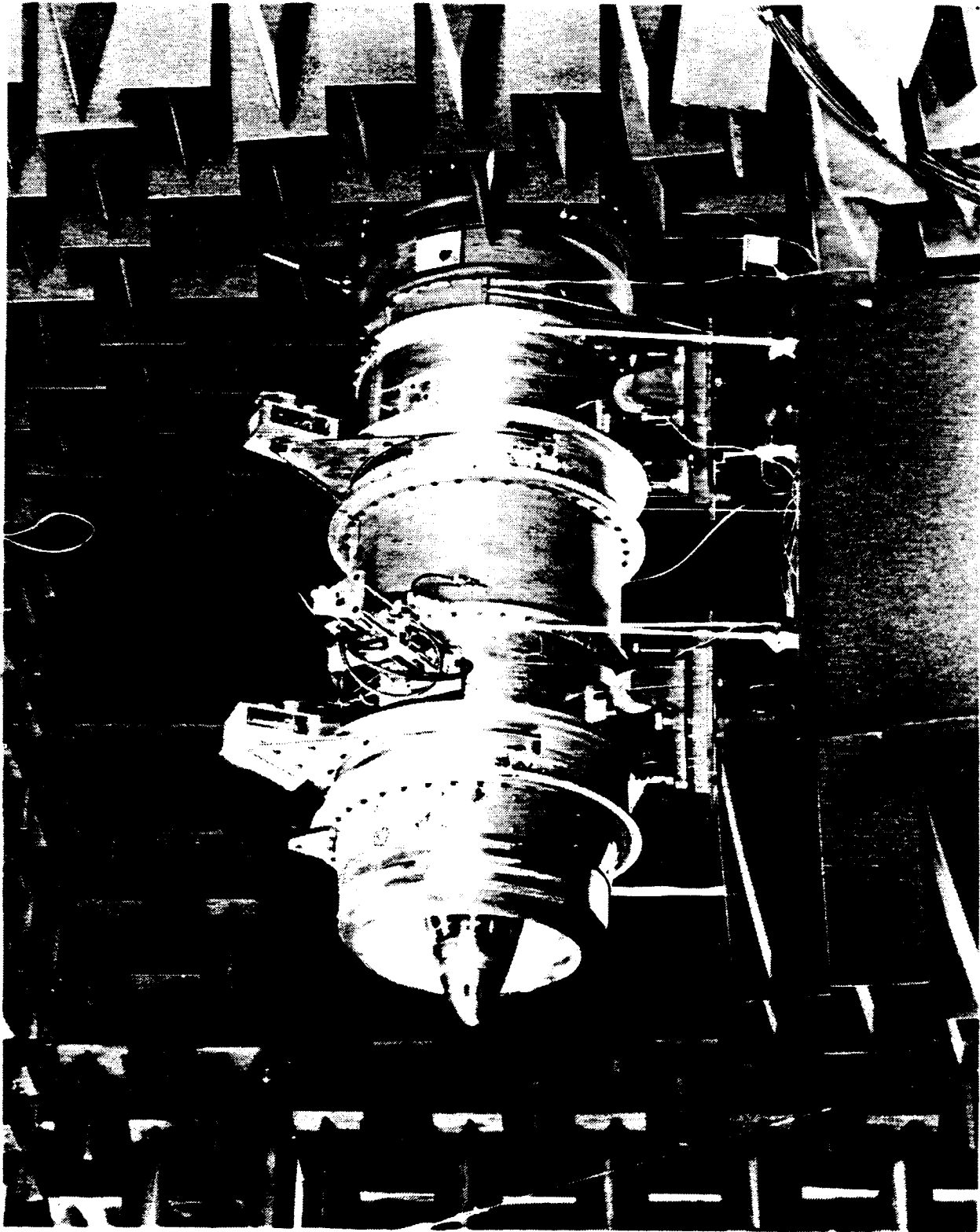
Figure 5.2. Installed Test Vehicle in the Exhaust Mode

45

See Insert Above

TURBULENCE CONTROL STRUCTURE

ANECHOIC CHAMBER WALL

FAN FLOW

ROTARY ACTUATORS/
MODAL PROBES

SUPPORT STRUT

NOZZLE

ROTOR 55

OGV

ACOUSTIC
TREATMENT
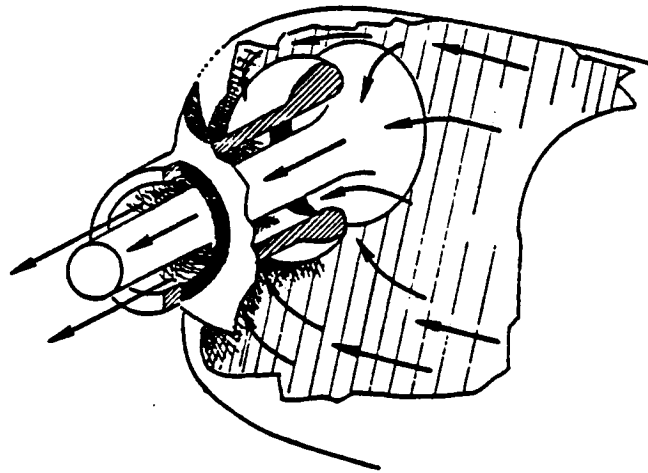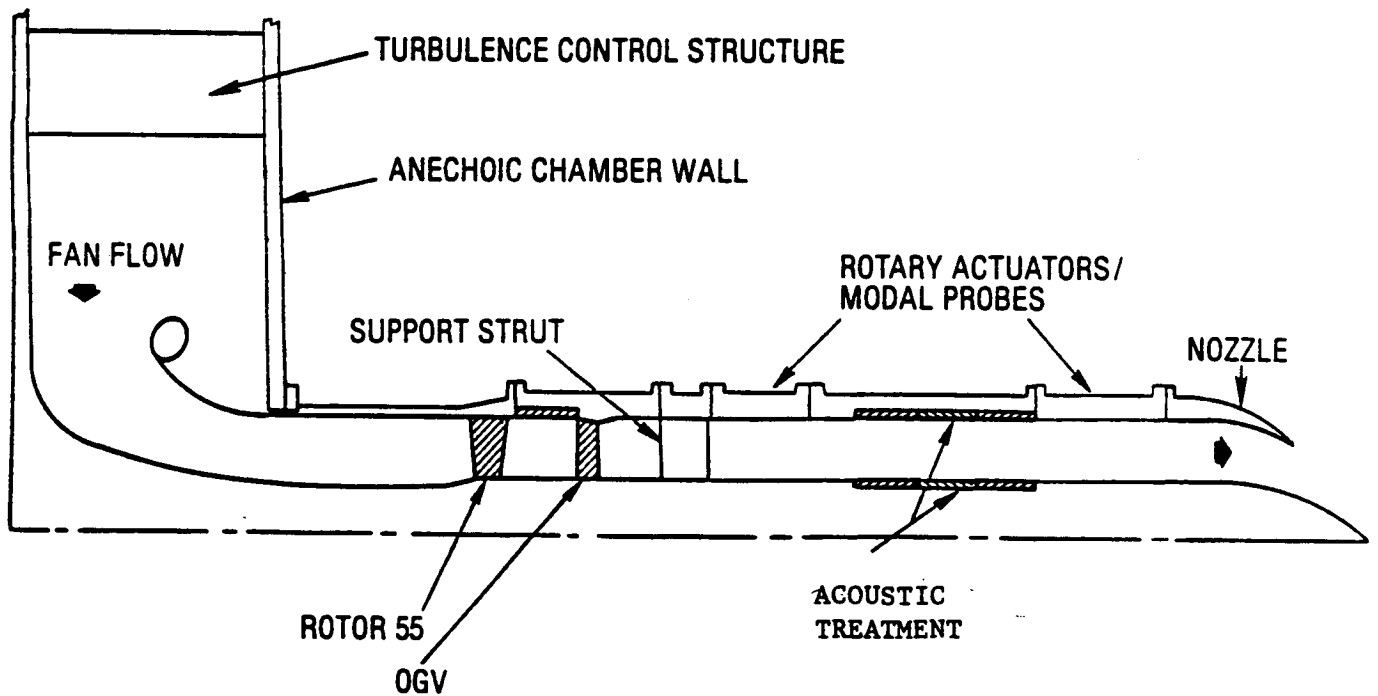
Figure 5.3. Schematic Diagram of the Test Vehicle Showing Rotor 55 as
Operated in the Exhaust Mode
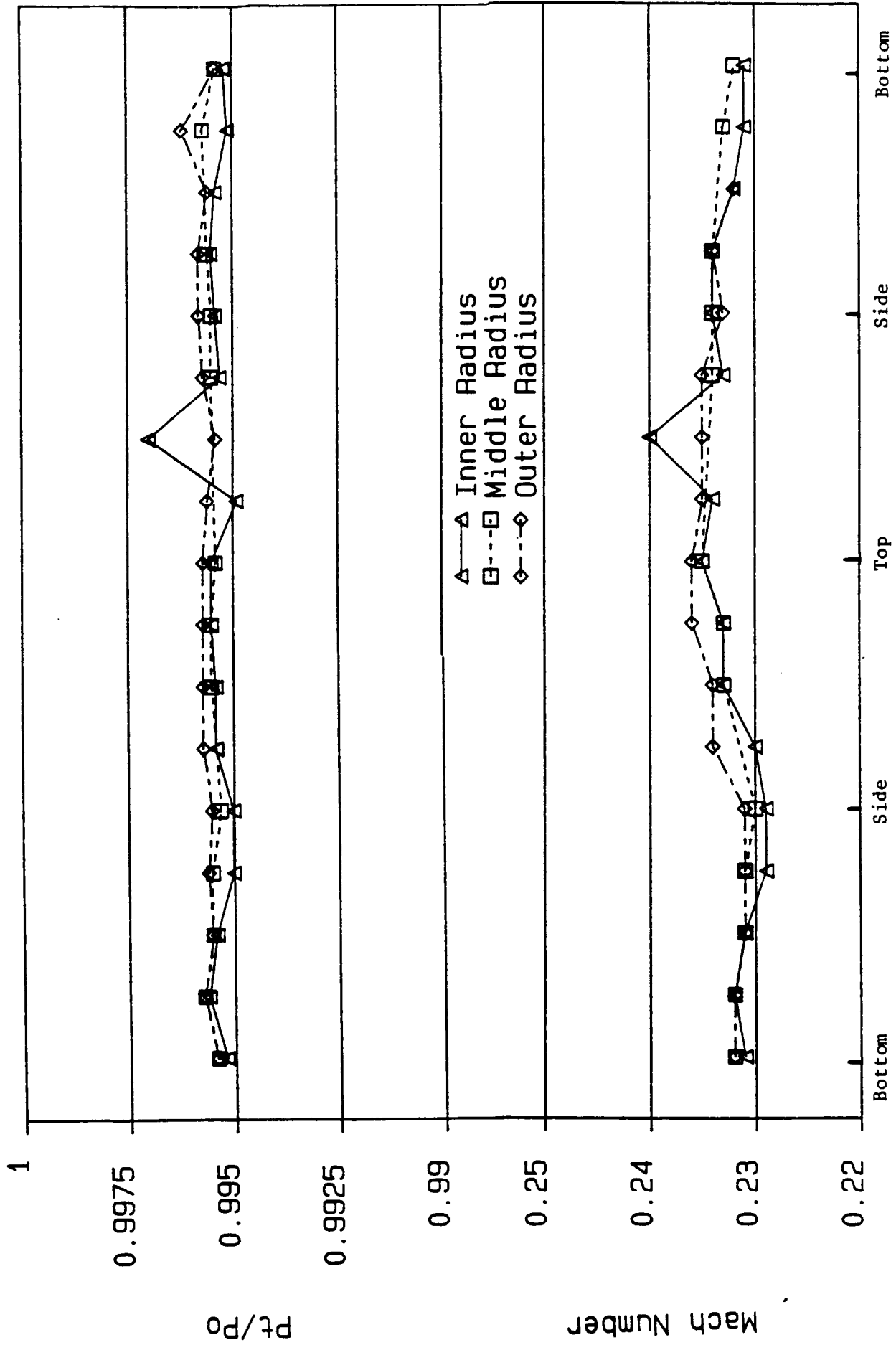
Figure 5.4.   Kiel Probe Data at the Inlet to the Fan. Circumferential Variation of the Mean Axial Flow Mach Number and Pressure Ratio (P_t/P_0) at Three Radial Locations

47

duct towards the outer wall. Mach numbers were calculated by using static pressures that corresponded to the weighted average of the two closest static wall taps. The flow was uniform at the measurement locations. The only point of significant variation is at the top of the duct towards the outer wall where the flow is about 3% above the mean.

5.1.2 FAN VEHICLE

The vehicle used in this program was the NASA Lewis Research Center fan Rotor 55 modified for this program to a close-spaced rotor-OGV configuration as shown in Figure 5.5. Rather than the original eleven outlet guide vane set spaced at 1.5 chord length eight vanes were used at a spacing of 0.5 rotor tip chord length. The annular exhaust duct consisted of two hardwall sections where in-duct acoustic probes were located, a treated section, and a nozzle termination. Test variations included a hardwall section in place of the treated section.

Pertinent design characteristics of the vehicle are summarized in Table 5.2.

Table 5.2. Rotor 55 Design Characteristics

Fan Diameter....................... 50.8 cm (20 in.)
Radius Ratio....................... 0.46
Number of Fan Blades............... 15
Inlet Guide Vanes.................. None
Number of Stators.................. 8
Design Tip Speed (100%) N/√θ).... 213 m/sec (700 fps)
Design Fan Speed (100% N/√θ)..... 8021 rpm
Stage Pressure Ratio............... 1.16
Weight Flow........................ 27.0 kg/sec (59.5 lbm/sec)

48

5.1.3 AERODYNAMIC INSTRUMENTATION

Velocity profile measurements were made both upstream and downstream of the treatment section by means of two traversing pitot tubes (radial and circumferential traverse), three total-pressure (and total-temperature) pitot tubes each with five radial locations, and sixteen wall static taps. Boundary layer profiles were determined at both locations, up and downstream, by means of two radially traversing boundary layer probes in conjunction with the sixteen wall static taps.

All aerodynamic instrumentation information concerning type and location is summarized in Figure 5.6.

Pressure data were individually sampled through two 48 channel scanivalve systems. Temperature data were sampled though an HP scanner and digital voltmeter. The data reduction program included corrections for compressible flow, taking into account specific heat variation with temperature and humidity.

5.1.4 ACOUSTIC "MODE" PROBES

In general, to determine modal coefficients the in-duct sound field needs to be determined. The easiest quantity to measure in a duct is the acoustic pressure, which for rotor/stator interaction can be written as

$$P(r, \theta, z, t) = \sum_{m=-M}^{M} \sum_{n=0}^{N} [A_{mn}^+ p_{mn}^+(r) e^{iK_{mn}^+ z}$$

$$+ A_{mn}^- p_{mn}^-(r) e^{-iK_{mn}^- z}] e^{i(m\theta - \omega t)} \qquad (5.1)$$

$P_{barometric}$

Inlet: $\begin{cases} T_{wet}, T_{dry} \\ T_{static}, P_{total}, P_{static} \end{cases}$

*Removed Prior to Acoustic Testing

16 Kiel Probes
at 22.5° Spacing*

r_{inner} = 127.0mm
r_{middle} = 177.8mm
r_{outer} = 228.6mm

TURBULENCE
CONTROL
STRUCTURE

FAN FLOW

1) Radially Traversing
   Boundary Layer Probes

2) Three Radial Rakes
   (5 radial positions)

3) Traversing Pitots
   (radial and circumferential)

Static Wall Taps (16)
8 outer wall
8 inner wall

Sta. 0.0   Sta. 27.26   Sta. 56.26
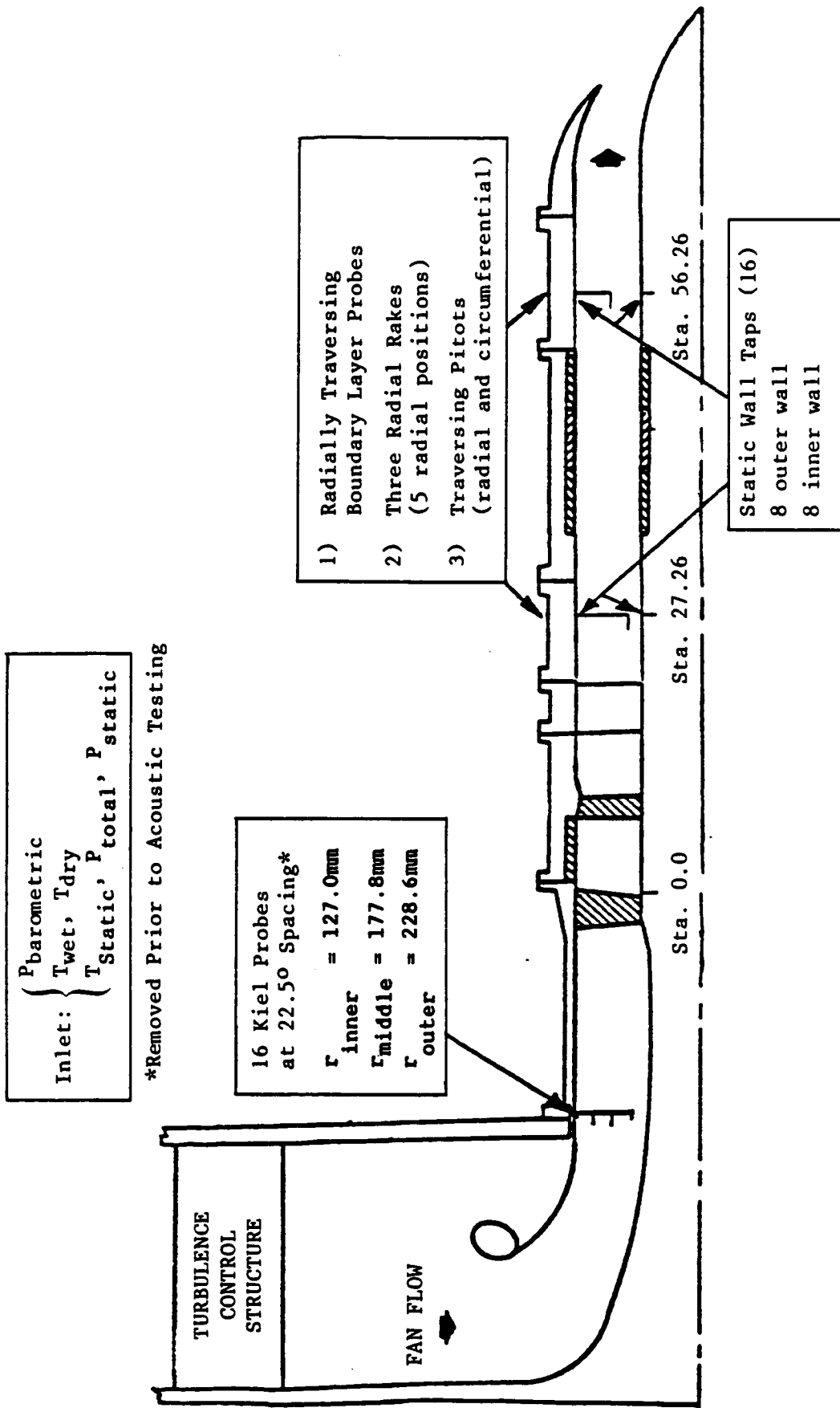
Figure 5.6. Schematic Diagram of the Fan Exhaust Duct Showing Instrumentation Locations
for Aerodynamic Measurements

This expression is a solution of the convected wave equation using separation of variables. Here the complex constants A_{mn}^+ and A_{mn}^- are the modal coefficients of the forward and backward propagating (m, n) modes. $p_{mn}(r)$ and K_{mn} are the radial mode shape functions and axial wave numbers, with the superscripts + and − corresponding to forward and backward propagation, respectively. The other variables are r, θ, z, t, and ω, which refer to radial location, angular location, axial location, time, and blade passing angular frequency, respectively.

Determination of the complex modal coefficients (amplitude and phase) requires that the complex pressure (amplitude and phase) be measured. In the case where primarily coherent noise is present, as was the case here, the signal processing technique of phase averaging can be used [Reference 13]. This signal processing technique selects from a given input signal only that portion which is coherent with a specified reference signal, and the random or noncoherent portion of the input signal is ignored (average approaches zero). A phase lock amplifier, which uses this technique, can be used to measure in-duct acoustic pressure amplitude and phase.

In the case of uniform flow in either cylindrical or annular ducts with hard walls, the radial mode shapes are Bessel functions of the radial order n, the circumferential mode order m, and of argument $(k_r r)$. Also the forward and backward propagating values $p^+(r)$ and $p^-(r)$ are equal. When radially sheared flow is present, then the radial mode shape is also a function of the velocity profile, and forward and backward values $p^+(r)$ and $p^-(r)$ are not equal.

When pressure, radial mode shapes, axial wave numbers, probe position, and blade passing fequency are all known, the modal coefficients are determined by the discrete Fourier transform and matrix manipulation. The details of this modal decomposition are discussed in Section 4.2. An important limitation of this process is that the use of only two axial measurement positions can lead to large measurement inaccuracies [References 14, 15]. As is shown in Section 4.2, a third axial measurement position significantly improves the modal decomposition accuracy.

Probe Description

Two in-duct mode probe arrays were designed and fabricated so that all cut-on circumferential and radial modes including forward and backward propagating modes, could be determined. A sketch of the probe design and geometry is given in Figure 5.7. Each array consisted of four radially located probes, each probe included three axial Kulite pressure transducers, in order to provide a redundant measurement at each radial location. Two probes mounted to a strut are shown in Figure 5.8. Each probe had three slots containing recessed Kulite transducers (Model LQ-080-5). Each transducer is connected by five wires (0.13 mm diameter) routed through the probe shell and grooves in the support struts. Both the probe and strut were made as small as possible based on transducer size and on the acoustic considerations discussed below. The Kulite model used was chosen not only because of its small size (1.29 mm on each side) but also because of its linearity, stability, and relatively high sensitivity. Each array was mounted on a circumferential traversing actuator, as can be seen in Figure 5.9.

Disturbance of the sound field due to the presence of the strut and probe was of primary concern. Probe scattering can alter the transducer readings significantly when an acoustic wave is traveling in a direction perpendicular to the probe axis. This scattering problem has been previously considered [Reference 16]. Also, scattering effects from the strut arise both from the blocking of the acoustic motion by the body surface and from the mean flow nonuniformity due to the strut thickness. This problem was treated using the Taylor transformation [Reference 17], which reduces the low Mach number problem to an equivalent stationary medium problem. Based on an analysis using that approach, the probe diameter was selected to be 4.76 mm and the strut thickness 6.35 mm. With these values the error in phase measurement was expected to be less than 4.5° and in magnitude, less than 1.0%.

Vortex shedding off the probe support strut was considered, and a thickness of 6.35 mm was selected to assure that the frequency was at least twice the blade-passing-frequency.
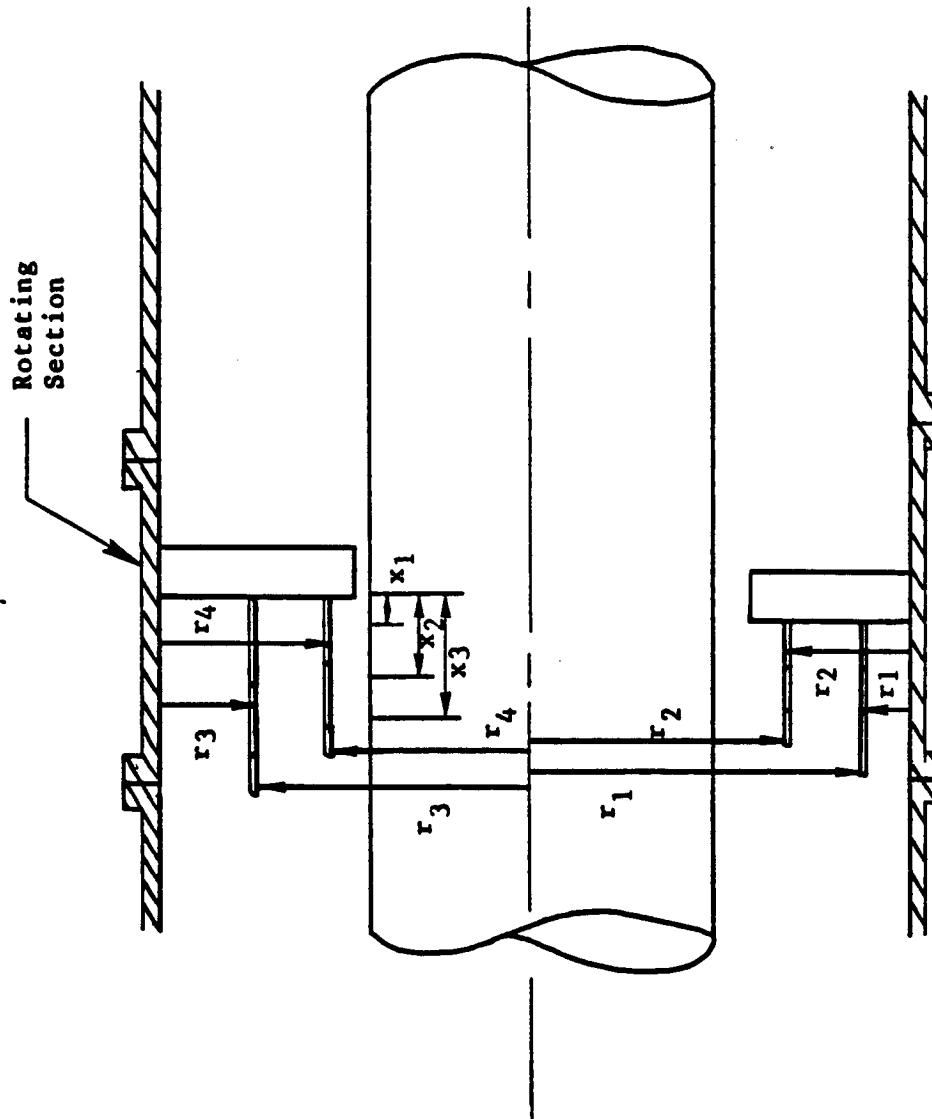
Probe Number	Radial Position (mm)	Axial Transducer Separations (mm)	
		(x_2-x_1)	(x_3-x_2)
1	$r_1 =$	47.62	28.57
	$r_2 =$	47.62	28.57
2	$r_3 =$	47.62	28.57
	$r_4 =$	47.62	28.57

Rotating Section

Figure 5.7. Schematic Diagram Showing the Radial Locations of the Mode Probes and the Axial Separations Between the Acoustic Pressure Transducers on Each Axial Probe

54
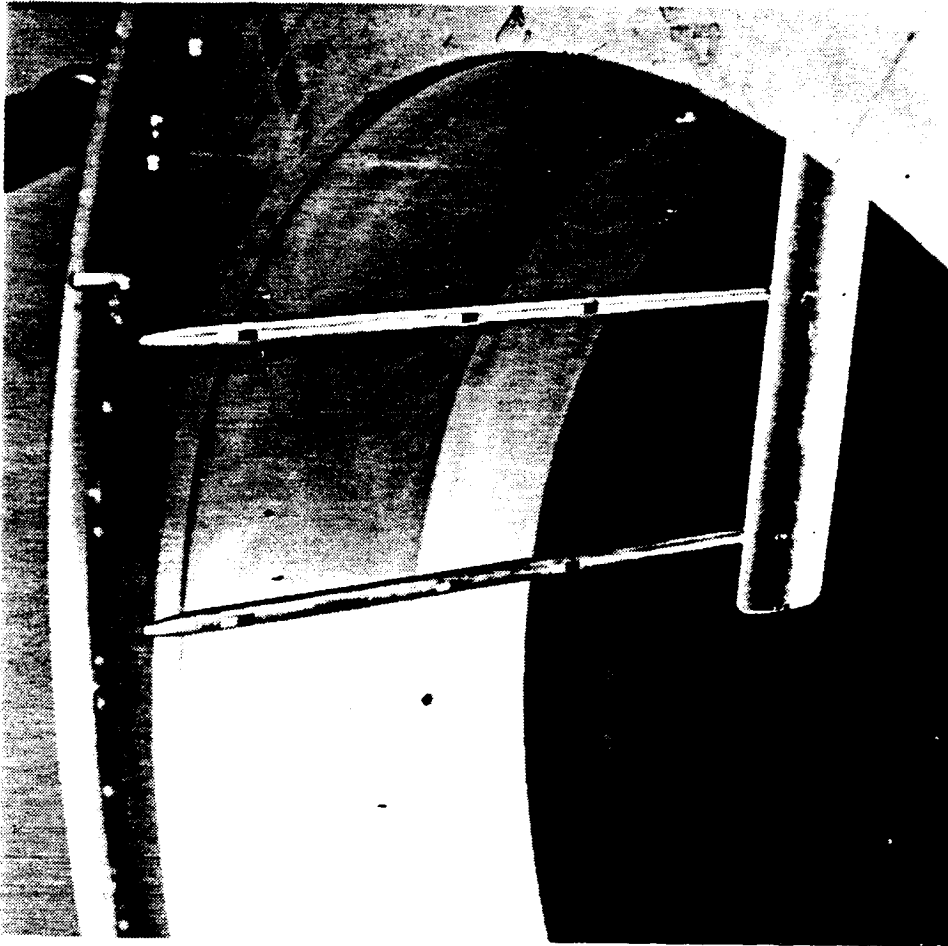
Figure 5.8. Photograph Showing Two Axial Probes Mounted on a Radial Strut
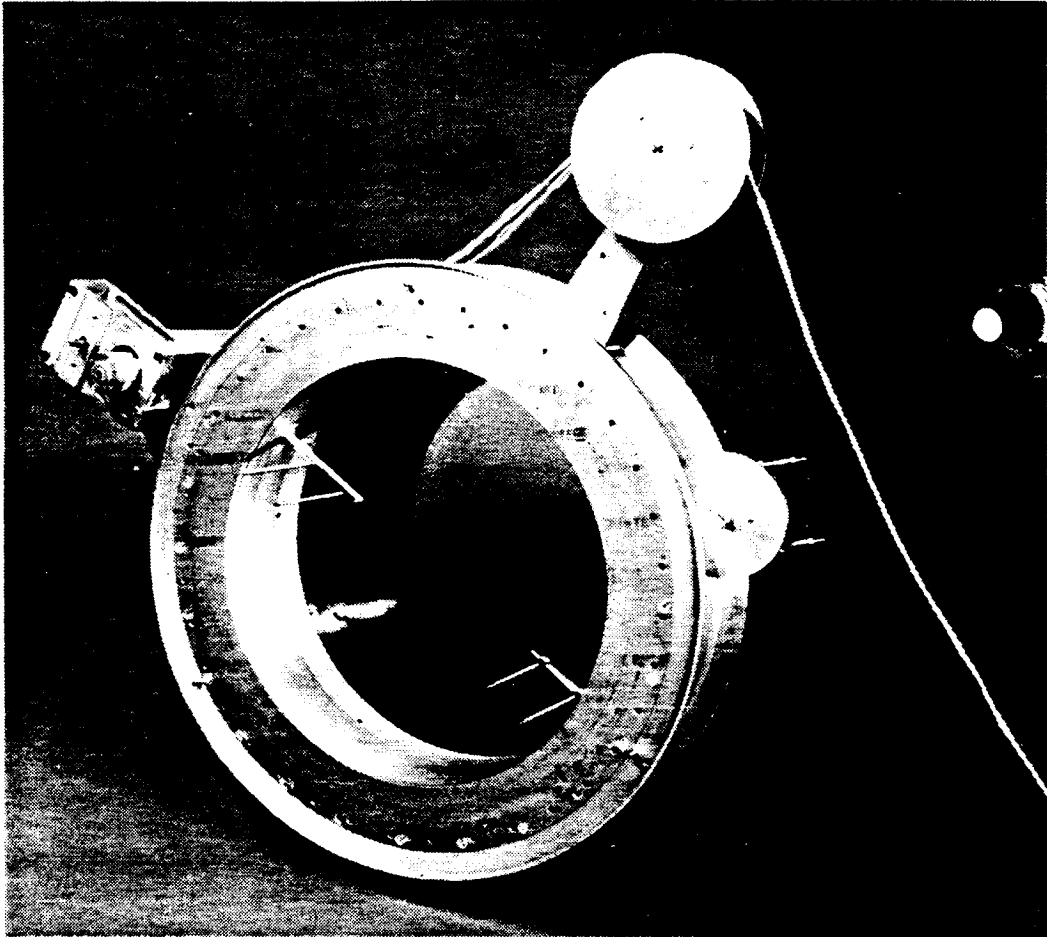
Figure 5.9. Photograph of a Complete Set of "Mode Probes" Showing the Circumferential
Traversing Actuator and Axial Probes at Four Radial Locations Mounted on
Two Diametrically Opposed Radial Struts

The probe and supporting strut were designed to withstand the stress at velocities in excess of 0.4 Mach number and to withstand regular handling during calibration of the probes. In order to meet these requirements the machine screws and the probe shell were made of tempered 403 SS with a yield strength of 150,000 psi. The natural frequencies of the probe and strut were determined to be well out of range of blade passing frequency.

A schematic of the measurement system is given in Figure 5.10. Data acquisition was controlled by an HP 1000 computer that sampled pressure and temperature data, and stored in-duct acoustic phase and magnitude measurements. Two microprocessors assisted in this task under direction of the HP 1000. One microprocessor controlled the actuator and directed a multi-channel scanning amplifier (GR 1566) to sample each mode probe transducer signal through a phase-lock amplifier (Brookdeal Model Ortholoc-SC 9505). The phase-lock amplifier passes only that portion of the signal which is coherent with the blade passing frequency. The blade passing frequency was measured by optically sensing the passage of each blade tip to trigger a square wave generator. Both the phase and the magnitude of the coherent portion of the mode probe signal were determined in this manner. The second microprocessor controlled the operation of the phase-lock amplifier and transferred phase quadrant information to the HP 1000. The HP 1000 also applied calibration corrections. The acoustic signals were recorded on a Sangamo IV tape recorder.

The mode probes were rotated in 18° increments around the entire circumference of the duct, so that data were measured at 20 circumferential positions for each test point. After a test point was completely surveyed, the data files of phase and magnitude measurements were supplied to the computer program which then calculated the individual modal coefficients, using the method for modal decomposition described in Section 4.

The probes were calibrated for both magnitude and phase. The calibration included all wiring and support equipment up to the phase lock amplifier. The probes were calibrated by mounting each probe in an impedance
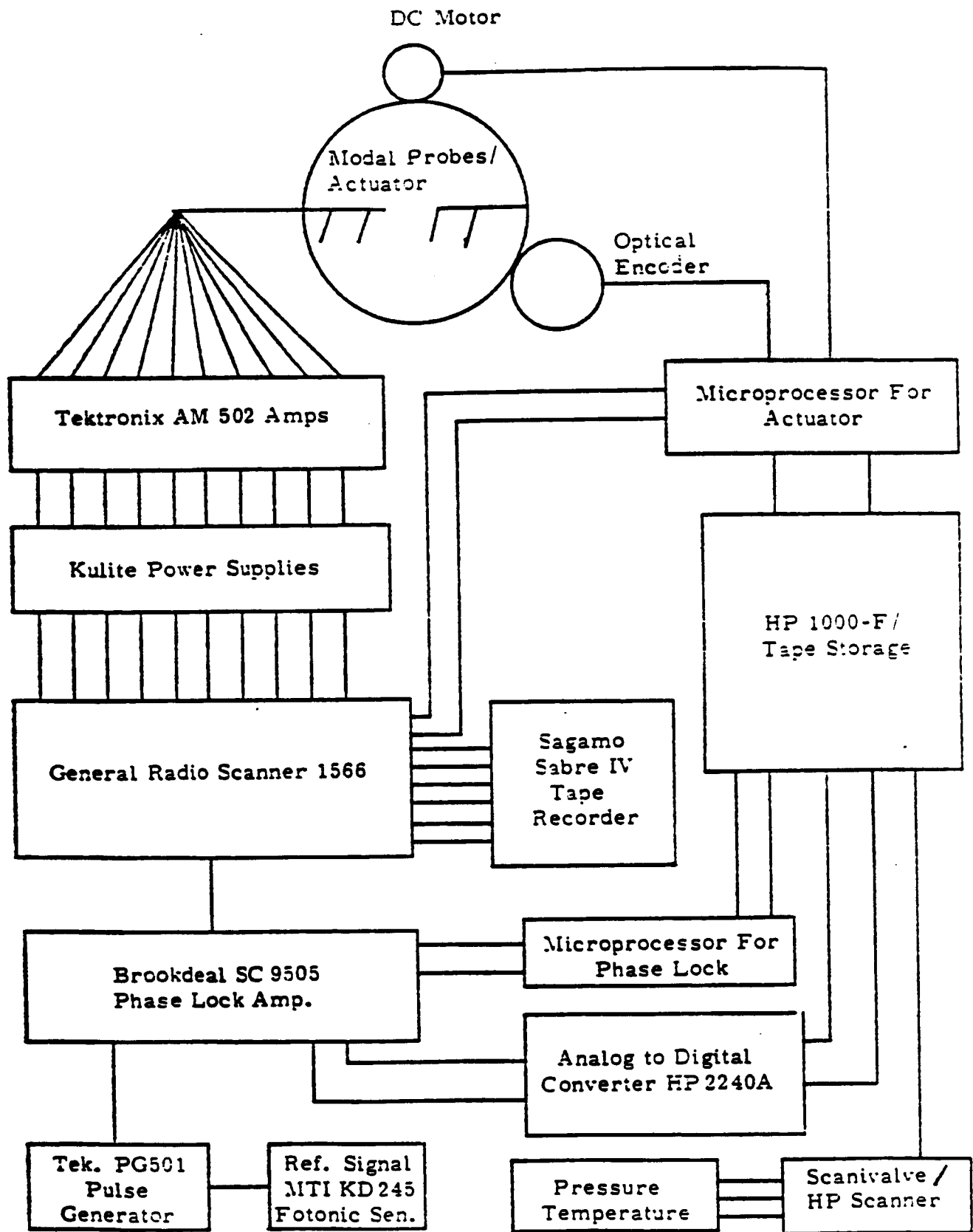
Figure 5.10. A Schematic Diagram of the Data Acquisition and Analysis System Used in the Modal Measurements

tube in the same axial plane as a previously calibrated 6.35 mm (0.25 in.) Bruel and Kjaer model 4135 microphone and then using a speaker at the other end of the tube to generate a plane wave at blade passing frequency. Because only a plane wave was generated, the calibration was valid for both level and phase. With the speaker set at a fixed level, the magnitude of each transducer as read with the phase lock amplifier was matched by use of variable gain amplifiers for each transducer. Any difference in phase between each transducer and the microphone was recorded and included as a correction in the data reduction program.

The rotary actuator was used to locate the modal probes circumferentially. The actuator consists of a stationary section and a rotating section. The stationary section, mounted on the adjacent ducting, provides the support for the motor drive, optical locating devices, and transducer wire guides. The rotating section, actuated by a motor driven chain, contains the probes. As can be seen in Figure 5.9, the transducer wires feed over a rotating disk and wrap around the rotating section of the actuator as it moves. A microprocessor for each actuator controls the motor to drive the rotating section to a predetermined location. The location is determined by a rotary optical encoder (Teledyne Gurley Model 8625). Although the microprocessor controls the actuator, a visual check and manual adjustment of the angular location of the Mode Probe was carried out.

5.2   VEHICLE AERO-ACOUSTIC RESULTS

This section presents the results of the vehicle testing, including: aerodynamic parameters, measured modal amplitudes, and farfield acoustic data. Results from measurements of the treatment impedance, both statically and with grazing sound and flow, are presented in the following section (5.3).

5.2.1 SELECTION OF FAN SPEED POINTS

The fan was operated at three speed points in order to vary the cut-off ratio of the blade-vane-interaction tones. It was varied from a minimum value

59

near unity (near cut-off) to a relatively high maximum value, over seven, so
as to have a range of values between these two extremes that would provide
experimental data for a severe test of the validity of the analytic method
presented in Section 4. The interaction-tone modes were established by the 8
outlet guide vanes chosen for the 15 bladed rotor:

$$m = 15 \pm 8k; \quad k = 0, 1, 2....$$

The cut-off ratios (defined as the frequency divided by the hardwall cut-off
frequency of the mode) for the propagating interaction modes at the speed
settings selected are summarized in Table 5.3.

Table 5.3. Acoustic Modes Generated by Rotor 55 With an Eight Vane
Stator With Associated Cut-Off Frequencies and Ratios

Mode	Cut-Off Freq. (Hz)	Hardwall Cut-Off Ratios at:		
		1900 Hz (7600 rpm)	1500 Hz (6000 rpm)	1000 Hz (4000 rpm)
-1, 0	270	7.04	5.56	3.70
-1, 1	1305	1.46	1.15	--
7, 0	1695	1.12	--	--

5.2.2 FAN PERFORMANCE

The operating map for Rotor 55 is shown in Figure 5.11a. The data in
this plot shows the repeatability of the performance when three different vane
designs were used under the QCSEE Program [Reference 18]. In the current
program, the aerodynamic data incorporated for use in determining the flow
field into and from the test section was used to obtain an approximate
confirmation that the flow from the fan stage was representative of a typical
fan vehicle. The test section aerodynamic data are presented and discussed in
the next section (5.2.3). Data points determined from the upstream and the
downstream locations are shown in Figure 5.11b, for a fan speed of 7600 rpm
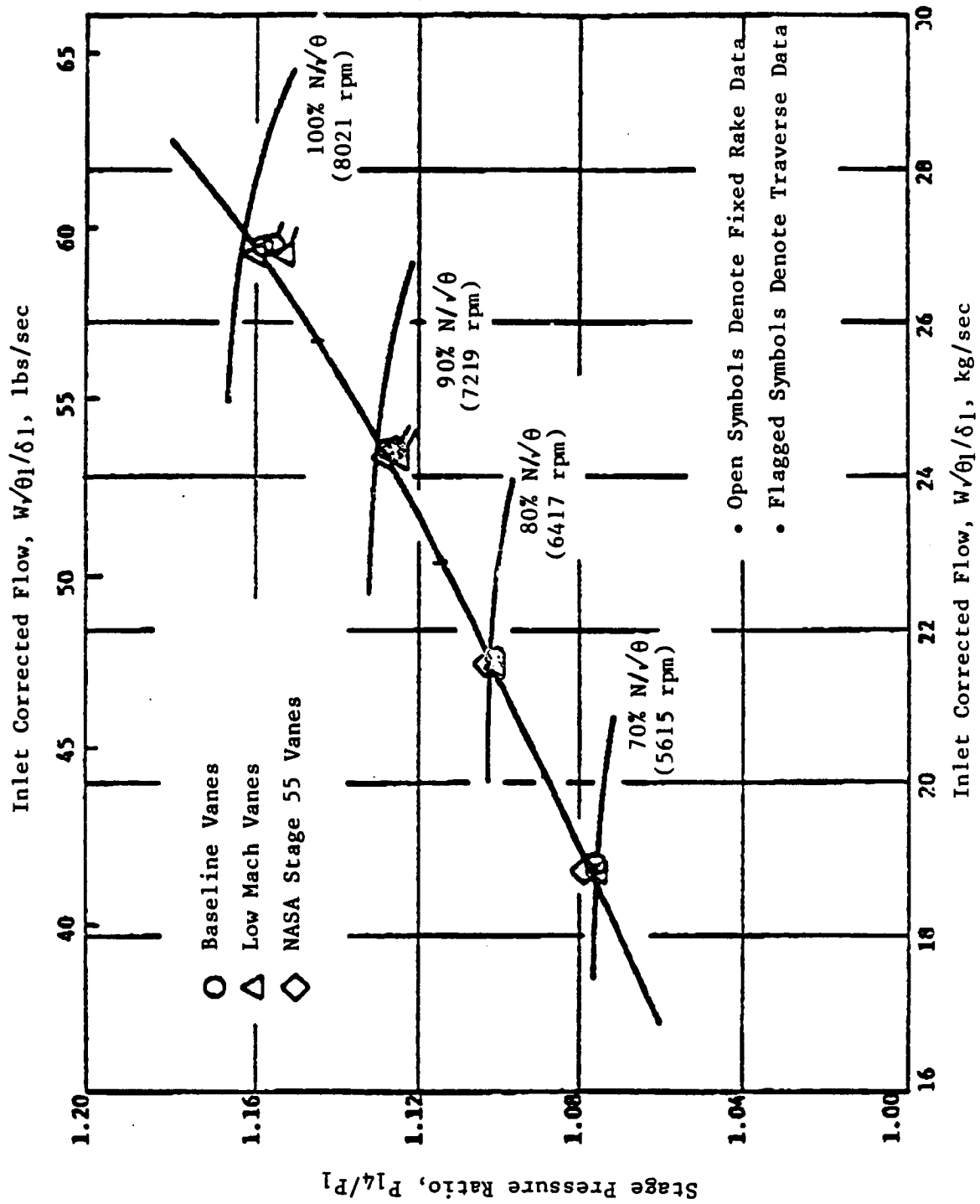
Figure 5.11a. Operating Map for the Rotor 55
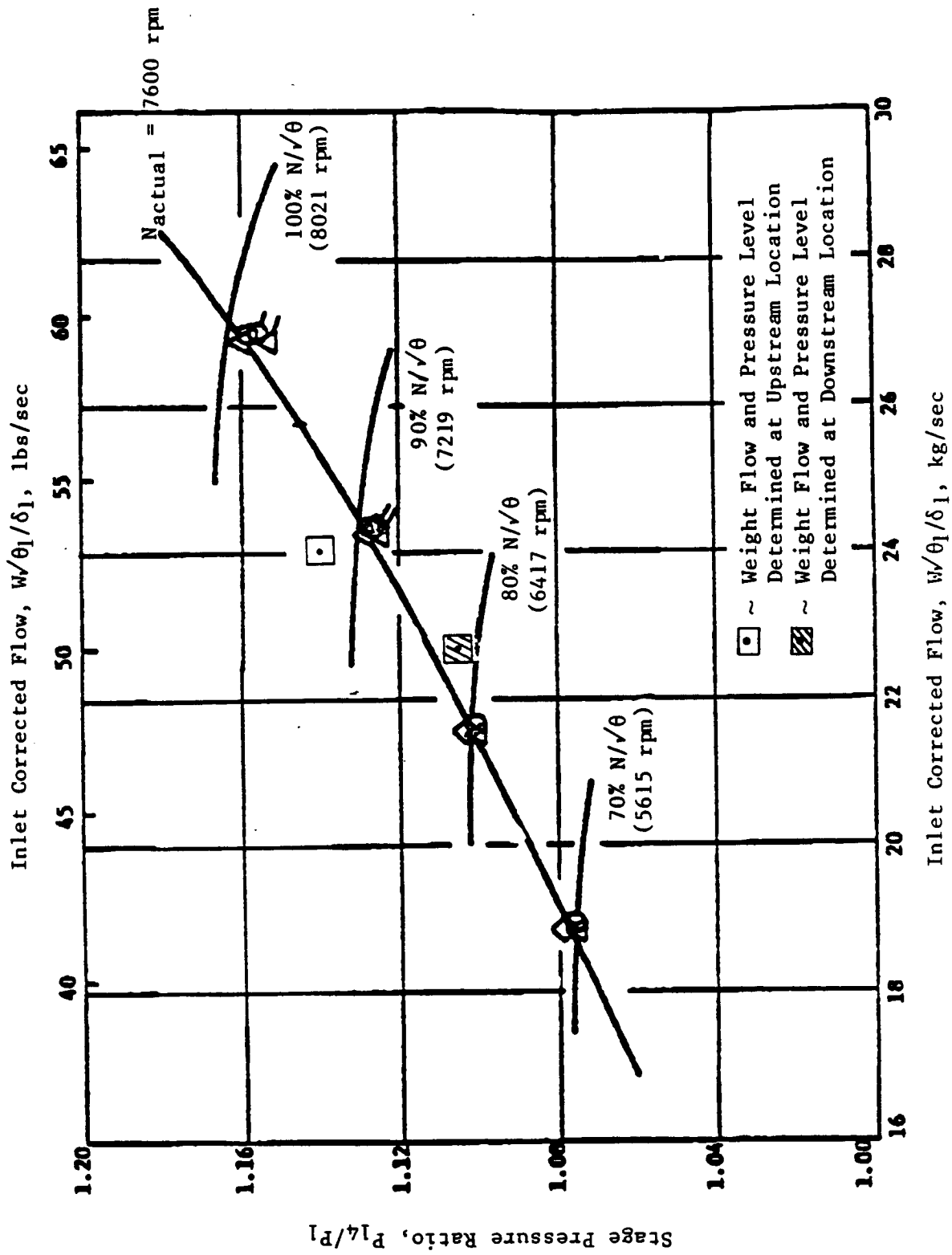
Figure 5.11b. Data Points Determined from the Upstream and Downstream Locations
for This Program at 7600 Physical RPM.

(95%). As noted on the figure, the two locations gave different values; this was because of the radial velocity profiles used (see Figure 5.12) which made the result dependent upon the particular circumferential location of the instrumentation. These data were concluded to be sufficient for the purposes needed, that is: the modified fan assembly was sufficiently close to design values of pressure-ratio and air-flow-rate to be a representative turbofan noise and airflow source.

As an interesting sidelight, these same type of data in the original fan buildup assembly, revealed serious deficiencies that were traced to inadvertant misalignment of the outlet-guide-vane angles. This condition was detected and corrected, thereby resulting in the successful measurement of the acoustic modal amplitudes and phases as described in the theory-experiment comparison (Section 6).

5.2.3 TEST SECTION AERODYNAMIC DATA

Typical radial velocity profiles at the upstream and downstream locations are shown in Figure 5.12; these profiles were determined by the traversing boundary-layer rakes which were restricted to a single circumferential position. There was sufficient difference in the mean values of velocities to cause concern about the validity of the data.

Therefore, circumferential traverses were then also made with the results shown in Figures 5.13 and 5.14, at radial insertion depths of .067 and .102 m, respectively. These data reveal periodic velocity defects around the circumference. At the upstream station the peaks and valleys show a circumferential offset between the two radii. The defects also shift in the circumferential direction as they move downstream.

Swirling wakes off the outlet guide vanes were the cause. The mixing-out of these defects resulted in the more uniform circumferential profile at the downstream location. The particular circumferential location chosen for the radial profile measurement was responsible for the discrepancy

63
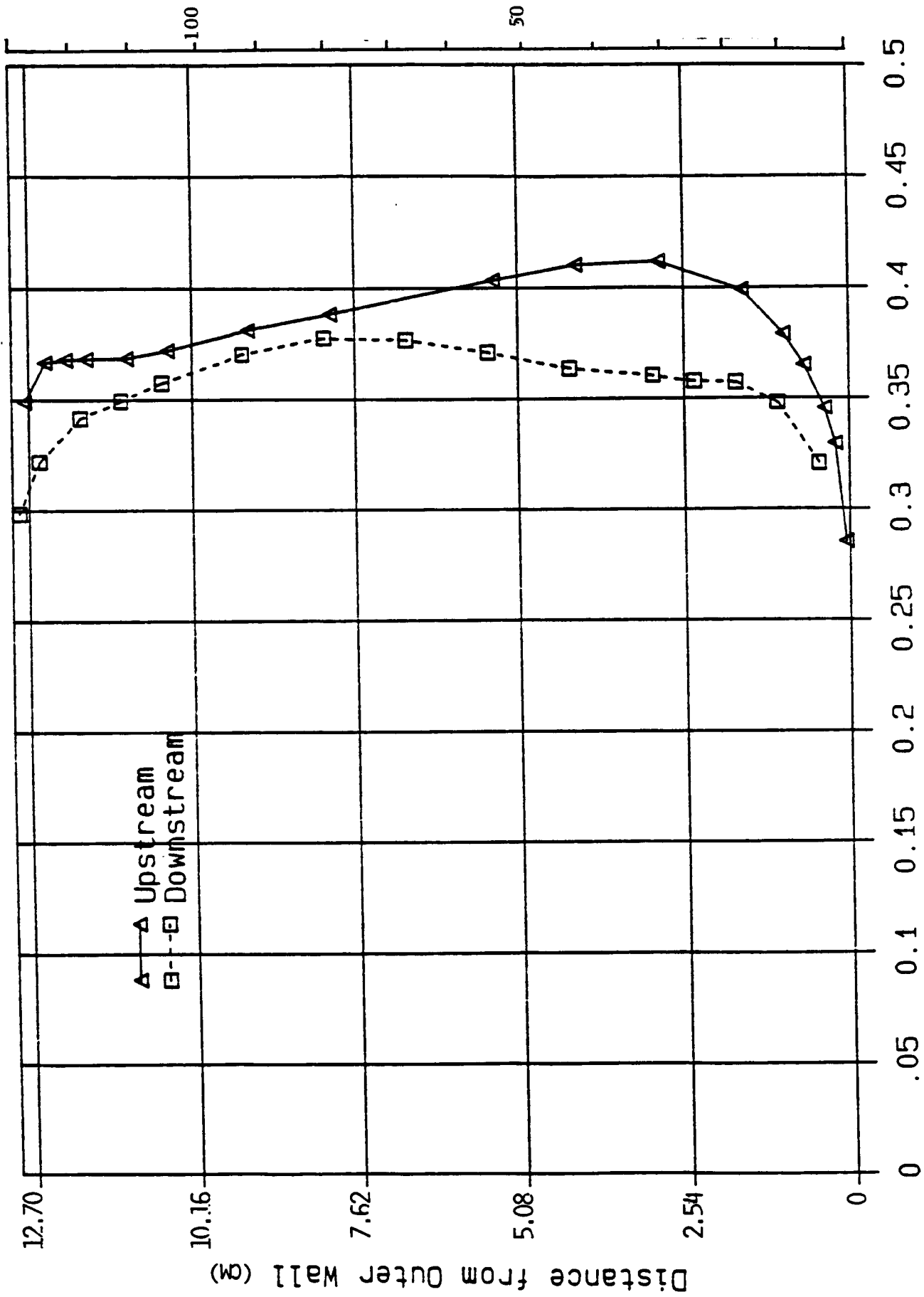
Figure 5.12. Radial Profiles of the Mean Axial Flow Mach Number Measured at the Same Circumferential Location; 7600 rpm
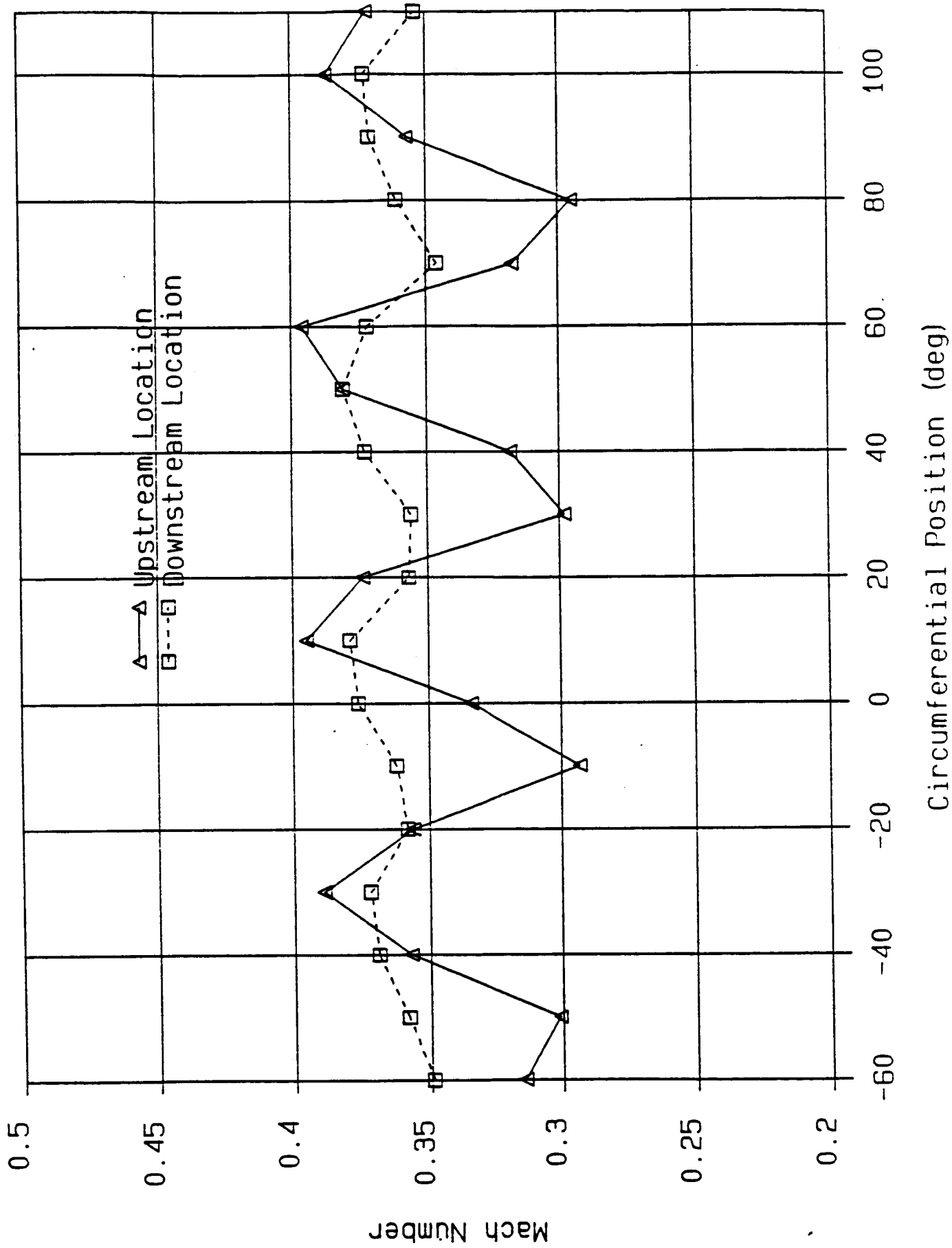
Figure 5.13. Circumferential Variations of the Mean Axial Flow Mach Number at 67.3 mm (2.65 Inch) From the Outer Wall; 7600 rpm
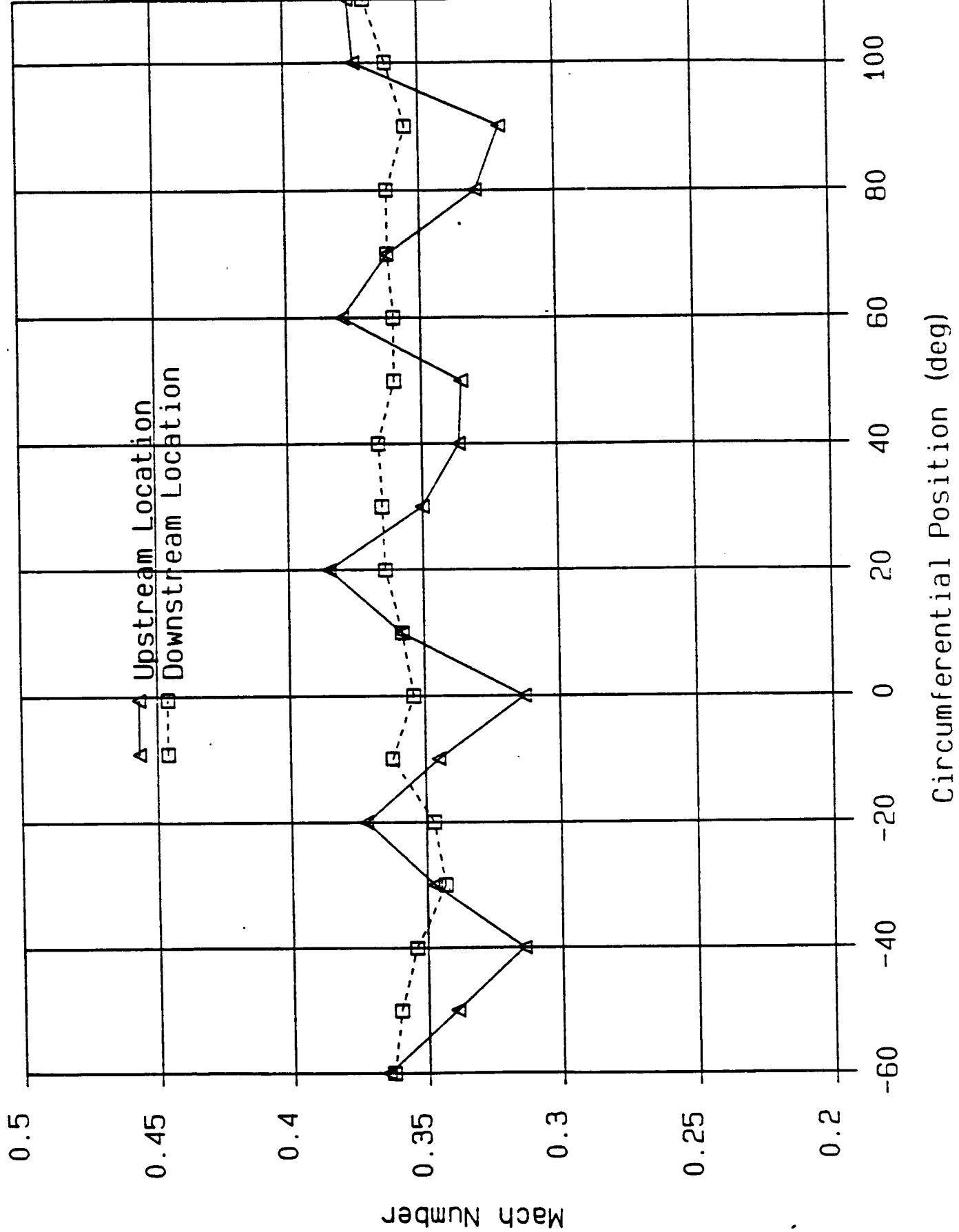
Figure 5.14. Circumferential Variations of the Mean Axial Flow Mach Number at 101.6 mm (4.0 inch) From the Outer Wall; 7600 rpm

66

initially of concern in Figure 5.12. Finer resolution of the two
circumferential traverses is shown in Figure 5.15 which reveals that there
were no smaller scale defects.

The circumferential velocity non-uniformity is of concern because the
theory of Section 4 only accounts for radial velocity gradients. Averaged
Mach numbers were used for calculation of axial wave numbers and radial mode
shapes.

Most aerodynamic measurements were made at 7600 rpm, although enough at
6700 rpm and 2800 rpm were made to assure that the fan performance matched
previous tests (Figure 5.11b). Figures 5.16 and 5.17 show the similarity of
the profiles both upstream and downstream at 7600 rpm and 6700 rpm.

During acoustic runs, all probes were removed from the airstream. Wall
static taps and recessed boundary-layer probes were monitored to assure that
the flow field was the same during the acoustic measurements as with the more
thorough aerodynamic surveys. Figure 5.18 shows a typical comparison between
the results from the boundary layer probe and earlier results with a
traversing pitot tube.

5.2.4 ACOUSTIC DATA

This section presents the results of the acoustic modal measurements in
the test section, at both upstream and downstream locations; measurements were
made at each of the three fan speeds for the test section with the treatment
in place and with the treatment replaced by a hardwall (zero admittance).

Modal Measurement Results

For the hardwall case, the results from the two separate mode probes
(upstream and downstream location) provided a quantitative measure of the
effect of the non-uniformity of the circumferential flow profile (e.g., per
Figures 5.13 and 5.14) and of the nozzle reflections upon the resolution of
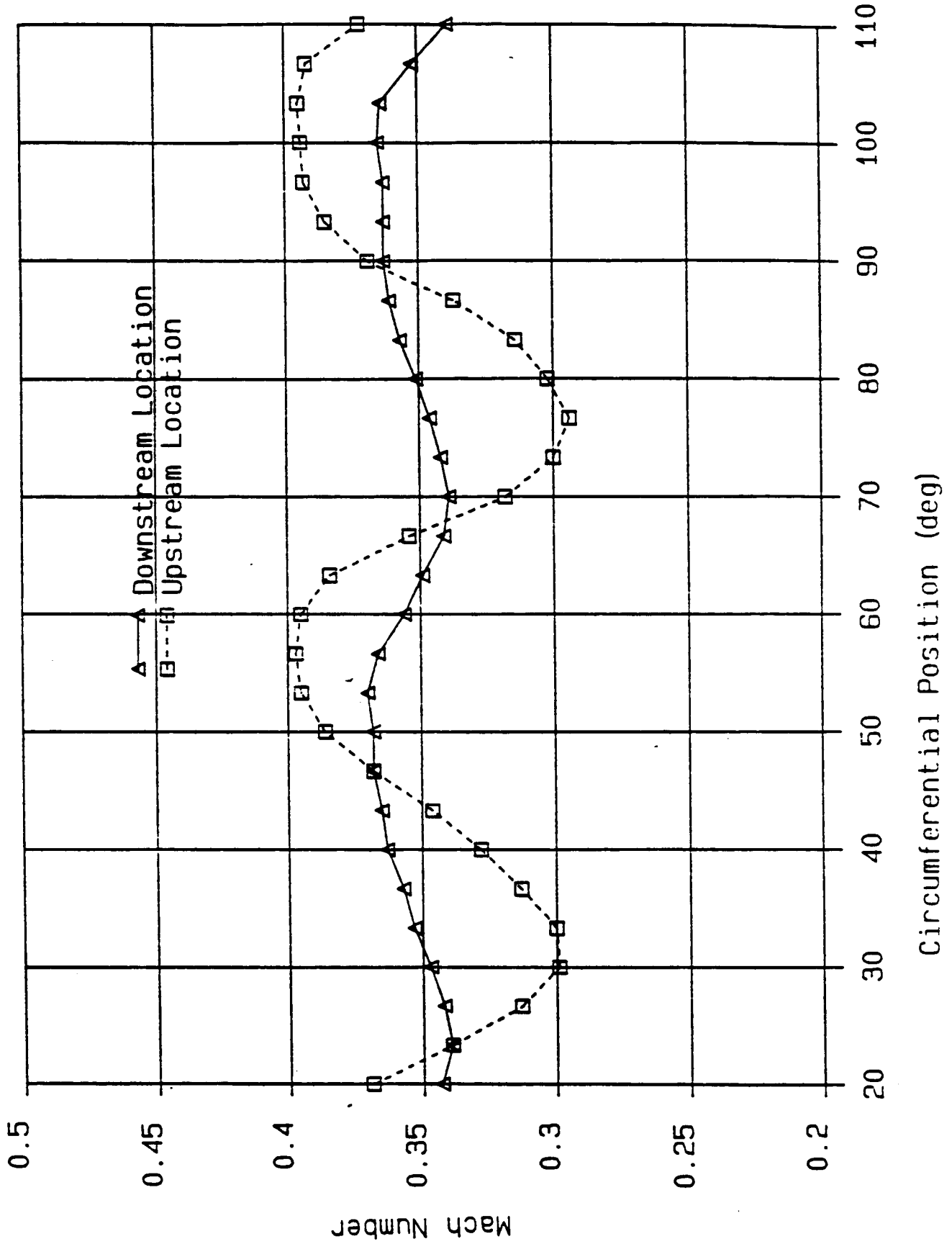
Figure 5.15. Circumferential Variations of the Mean Axial Flow Mach Number at 63.5 mm (2.5 Inch) From the Outer Wall; 7600 rpm
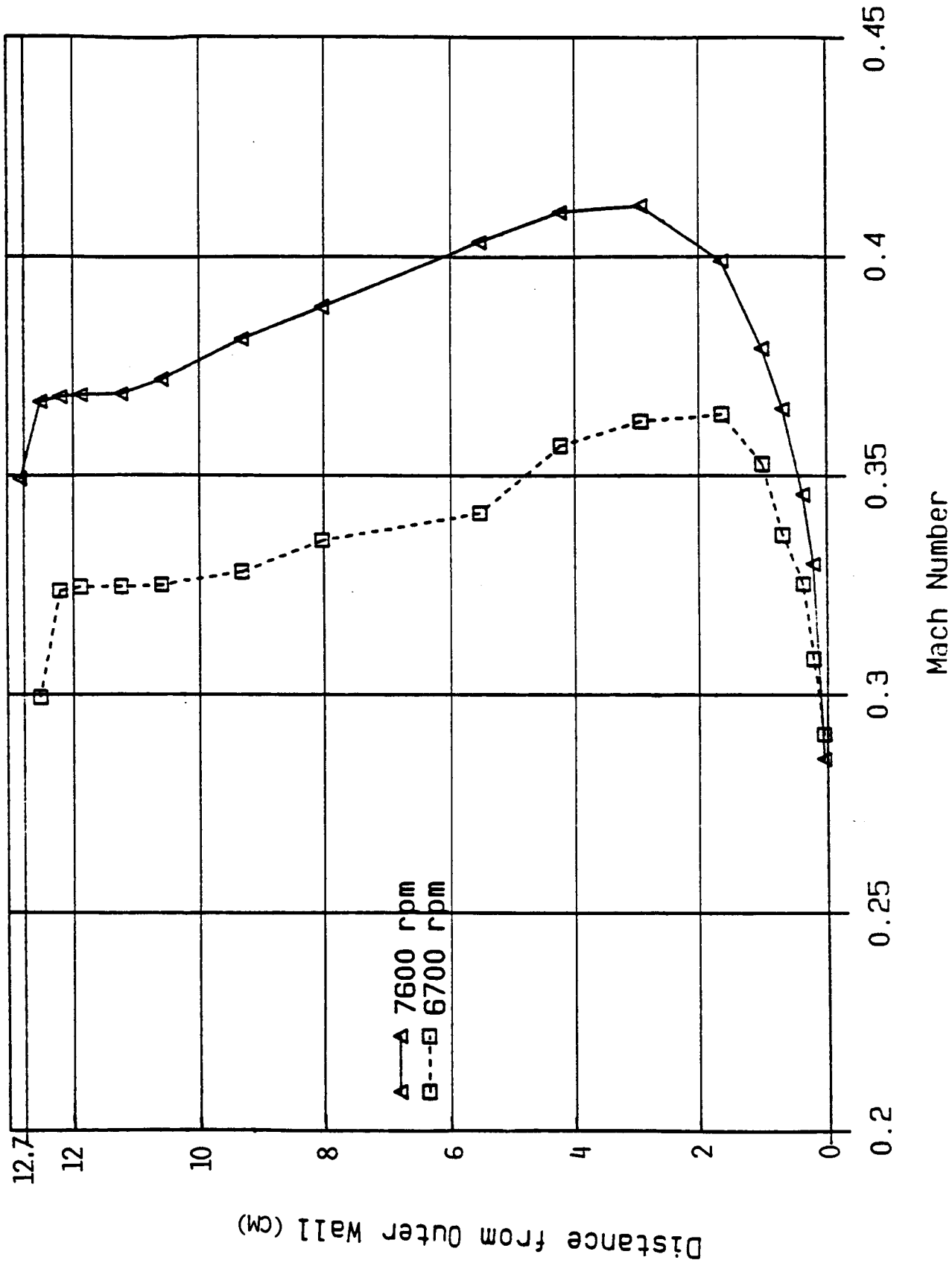
Figure 5.16. Radial Profiles of the Mean Axial Flow Mach Number Measured in the Upstream Location at 7600 and 6700 rpm Values

69
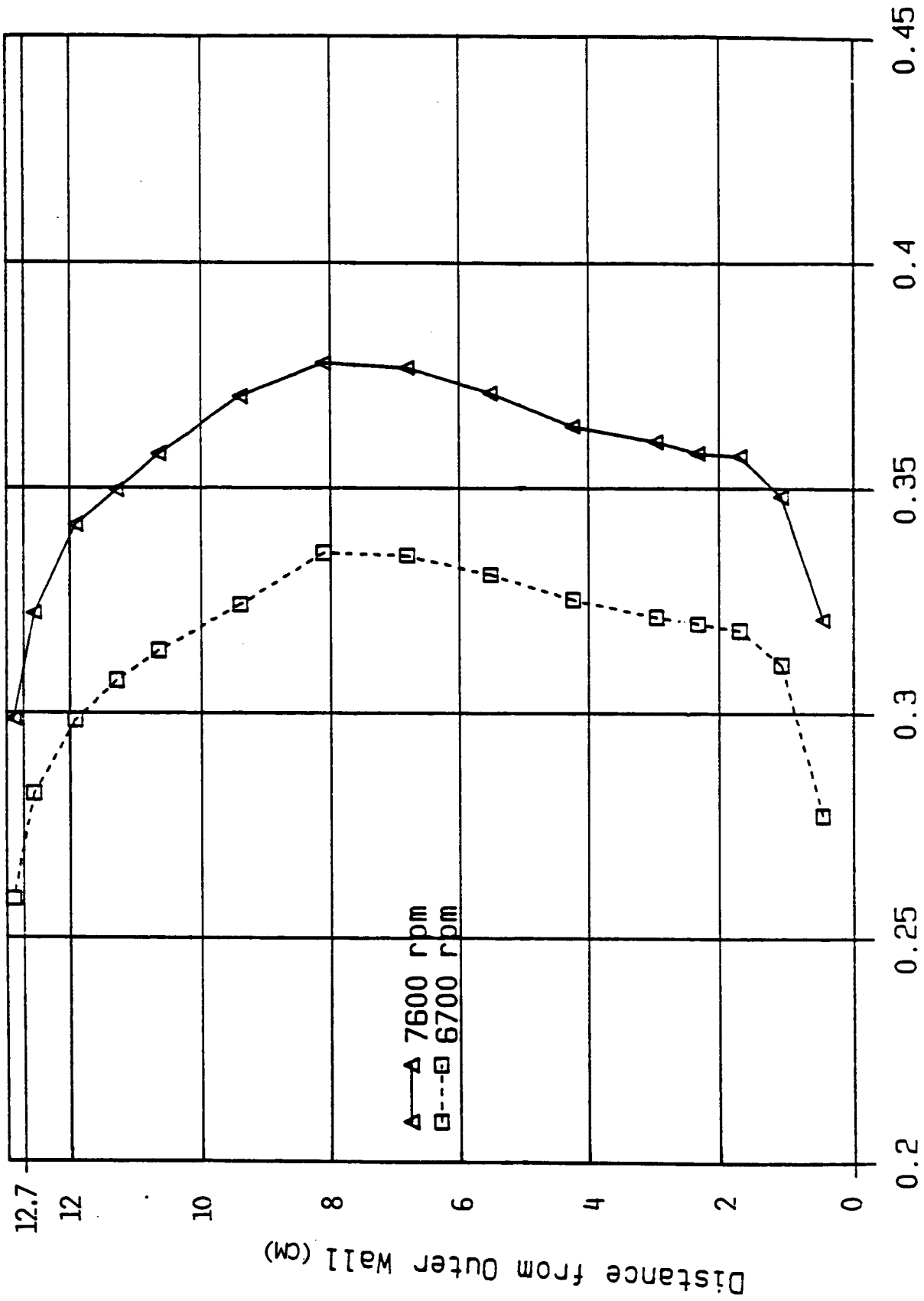
Figure 5.17. Radial Profiles of the Mean Axial Flow Mach Number Measured in the Downstream Location at 7600 and 6700 rpm Values
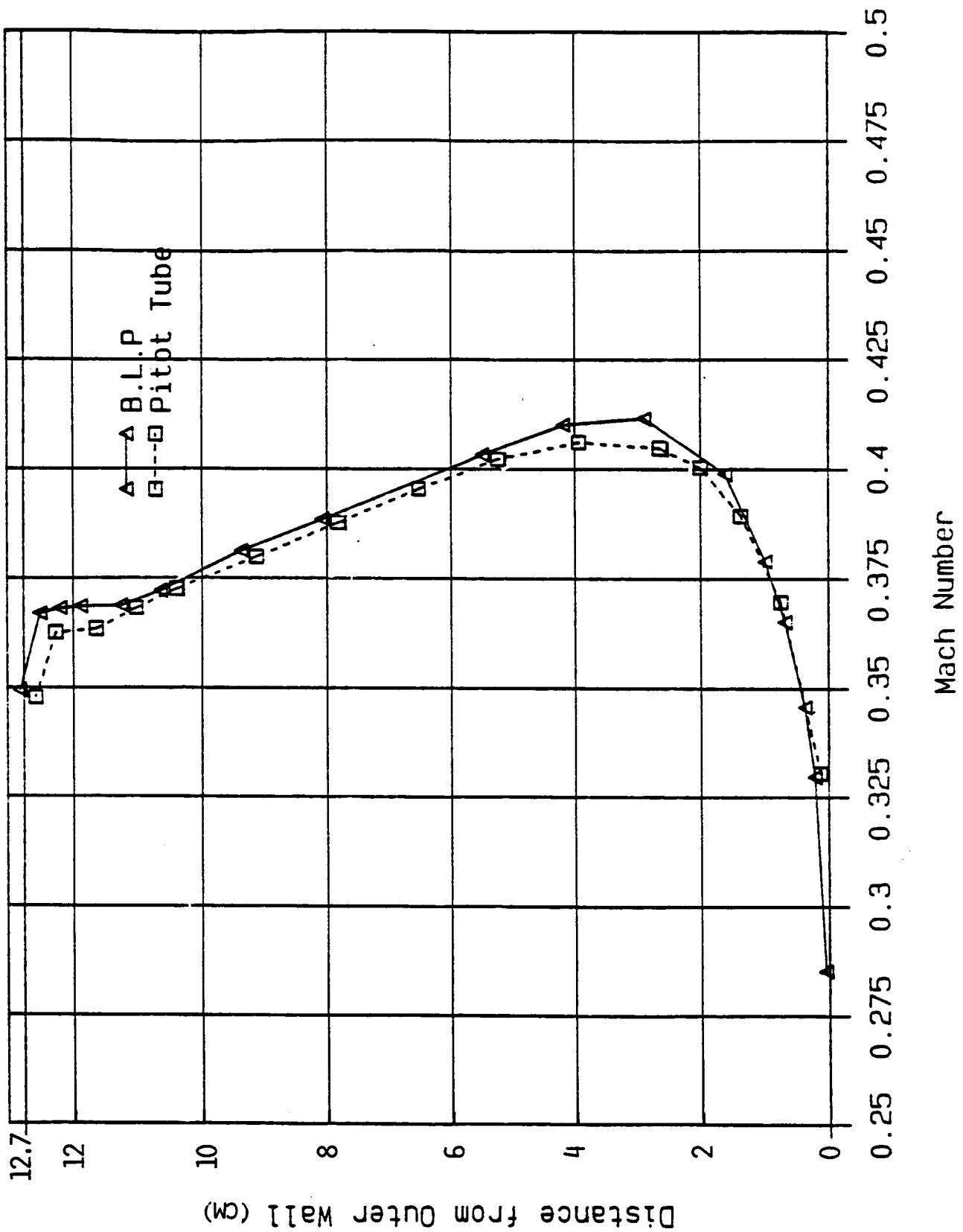
Figure 5.18. A Typical Comparison of Radial Profiles of Mean Axial Flow Mach Number Obtained by a Boundary Layer Probe and a Traversing Pitot-Tube

the modal coefficients. A typical result of this check is summarized in Table 5.4 in terms of the relative forward propagating energy (dB). The table shows two cases, one considering only cut-on modes in the modal coefficient determination and the other considering, in addition, cut-off modes up through m = 9 circumferential modes (maximum obtainable from 20 circumferential measurement locations) and n = 3 radial modes (maximum obtainable from four radial measurement locations).

Table 5.4. Comparison of Computed Propagating Energy Flux, Upstream and Downstream, for Hardwall Test Section

Fan Speed (RPM)	Blade Passing Freq. (Hz)	Mode Index (M,n)	Cut-off Ratio	Relative Energy Flux* (dB)	
				Allowing Cut-on Only	Allowing Cut-on and Cut-off
7600	1900	-1,0	7.04	1.2	2.1
		-1,1	1.46	0.8	0.1
		7,0	1.12	0.1	0.5
6000	1500	-1,0	5.56	0.4	0.2
		-1,1	1.15	0.7	0.3
4000	1000	-1,0	3.70	2.3	3.4

*Relative energy flux is the difference between energy flux measured upstream and that measured downstream.

The agreement, in general, is very good at the two higher fan speeds, and within about 3 dB at the lowest speed; the agreement is best for the modes nearest cut-off. (Further discussion of the effects of flow on acoustic pressure profiles ratio modal components is given in the theory/experiment comparison, Section 6).

The results of the modal decomposition (using maximum values of m and n of 9 and 3, respectively, and eigenvalues for uniform flow with thin boundary layer) are presented in Figures 5.19 through 5.24. The cases are listed in Table 5.5.

Table 5.5. Index of Figures Showing Modal Amplitudes and Phases

Figure Number	Case Freq. (Hz)	Test Section	Modal Definition
5.19a	1900	Hardwall	Amplitude
5.19b	1900	Hardwall	Phase
5.20a	1900	Treated	Amplitude
5.20b	1900	Treated	Phase
5.21a	1500	Hardwall	Amplitude
5.21b	1500	Hardwall	Phase
5.22a	1500	Treated	Amplitude
5.22b	1500	Treated	Phase
5.23a	1000	Hardwall	Amplitude
5.23b	1000	Hardwall	Phase
5.24a	1000	Treated	Amplitude
5.24b	1000	Treated	Phase
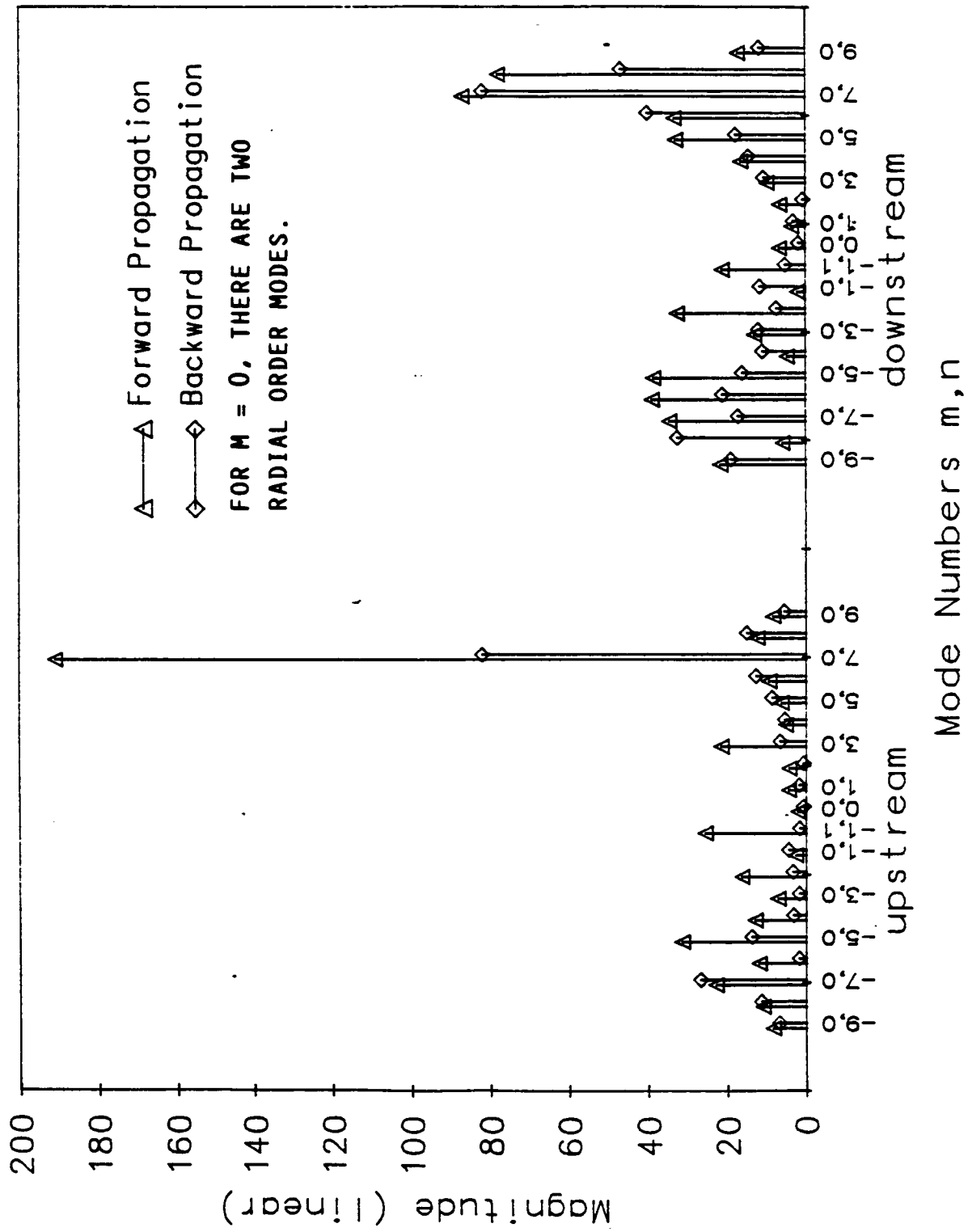
Figure 5.19a. Modal Coefficient Amplitudes Measured at the Upstream and the Downstream Locations in the Hardwall Configuration; 7600 rpm, 1900 Hz
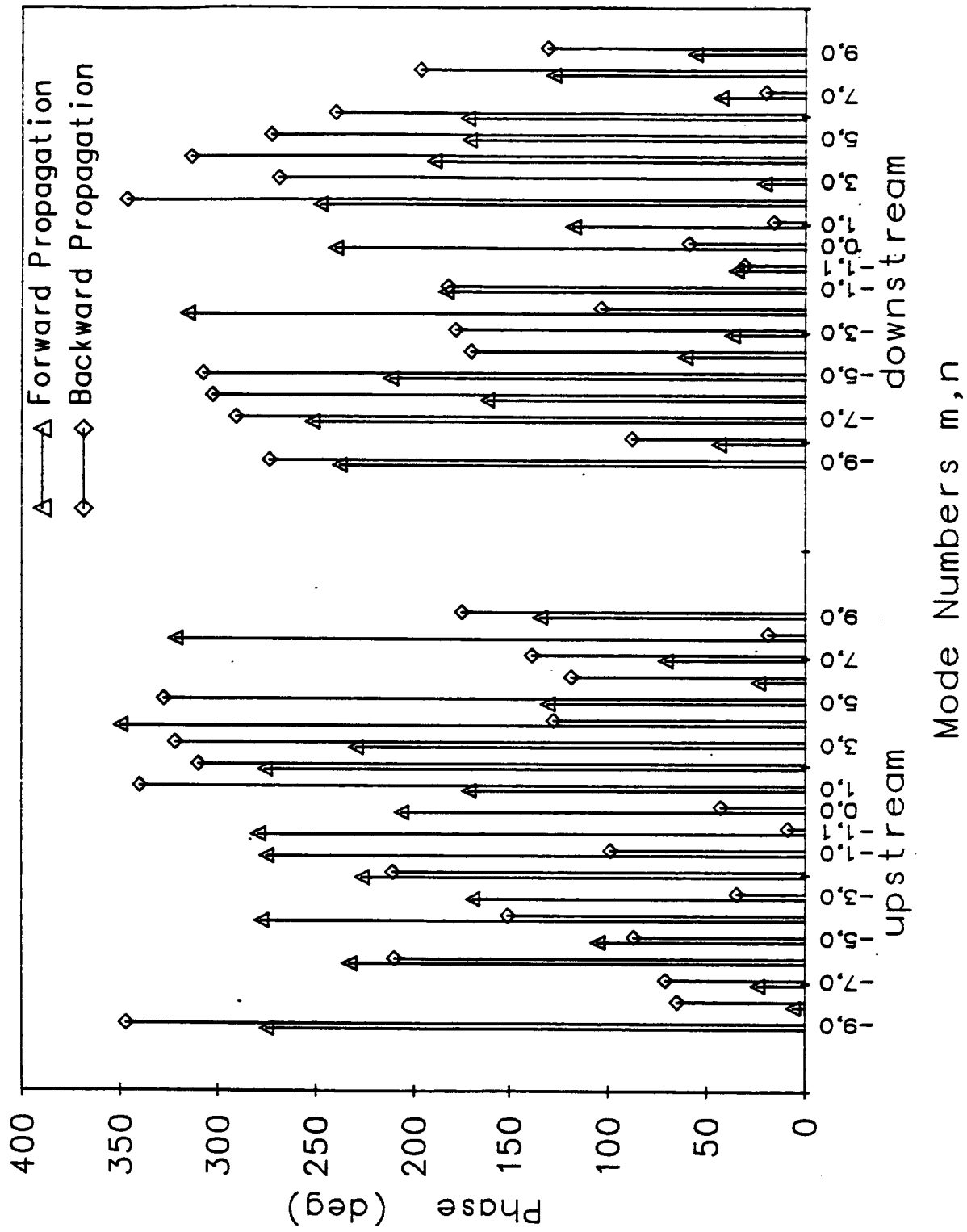
Figure 5.19b. Phase Values Corresponding to the Amplitude of Modal Coefficients in Figure 5.19a; 7600 rpm, 1900 Hz
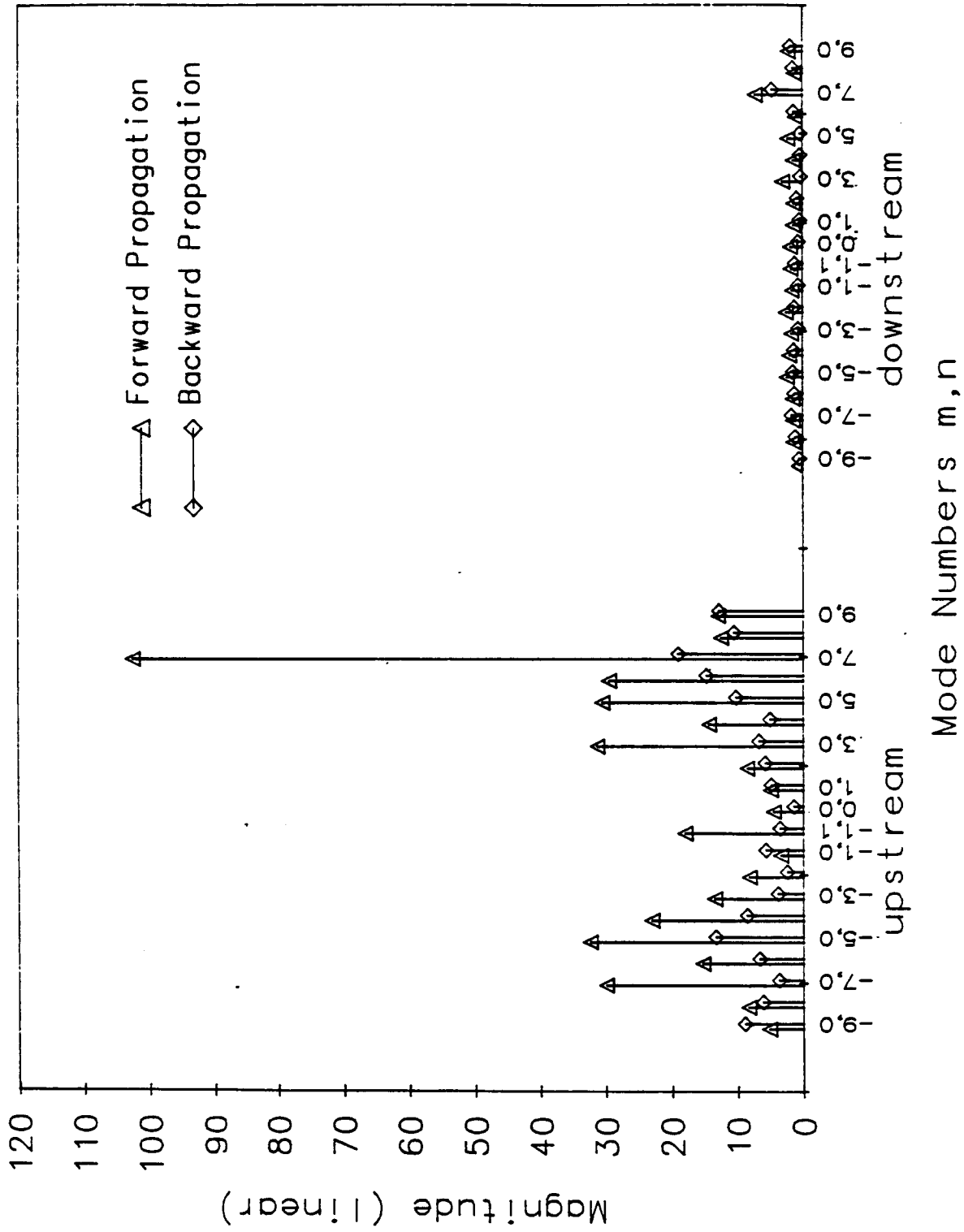
Figure 5.20a. Modal Coefficient Amplitudes at the Upstream and Down stream Locations in the Treated Configuration; 7600 rpm, 1900 Hz
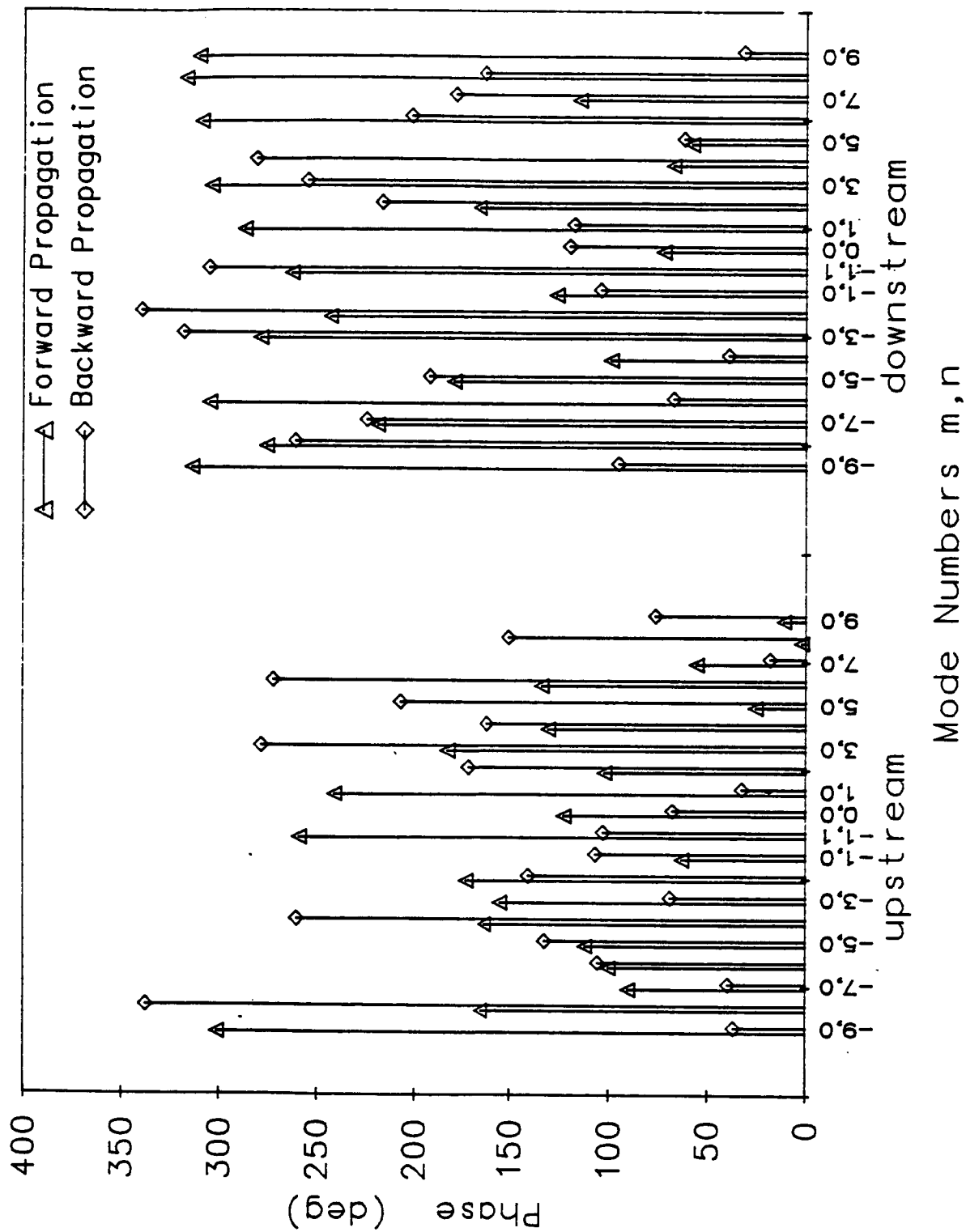
Figure 5.20b. Phase Values Corresponding to the Amplitudes of Modal Coefficients in Figure 5.20a; 7600 rpm, 1900 Hz
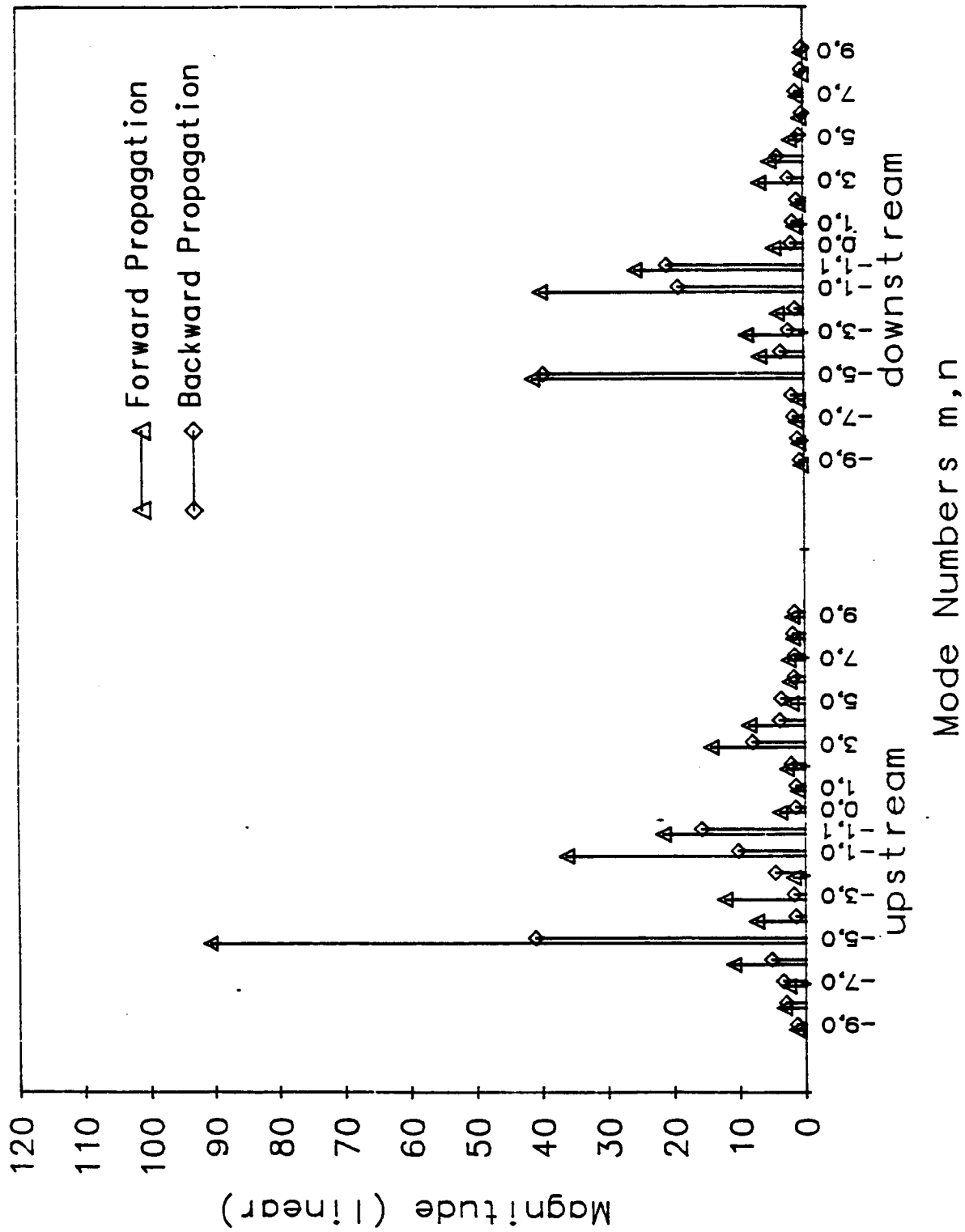
Figure 5.21a. Modal Coefficient Amplitudes at the Upstream and the Downstream Locations in the Hardwall Configuration; 6000 rpm, 1500 Hz

78
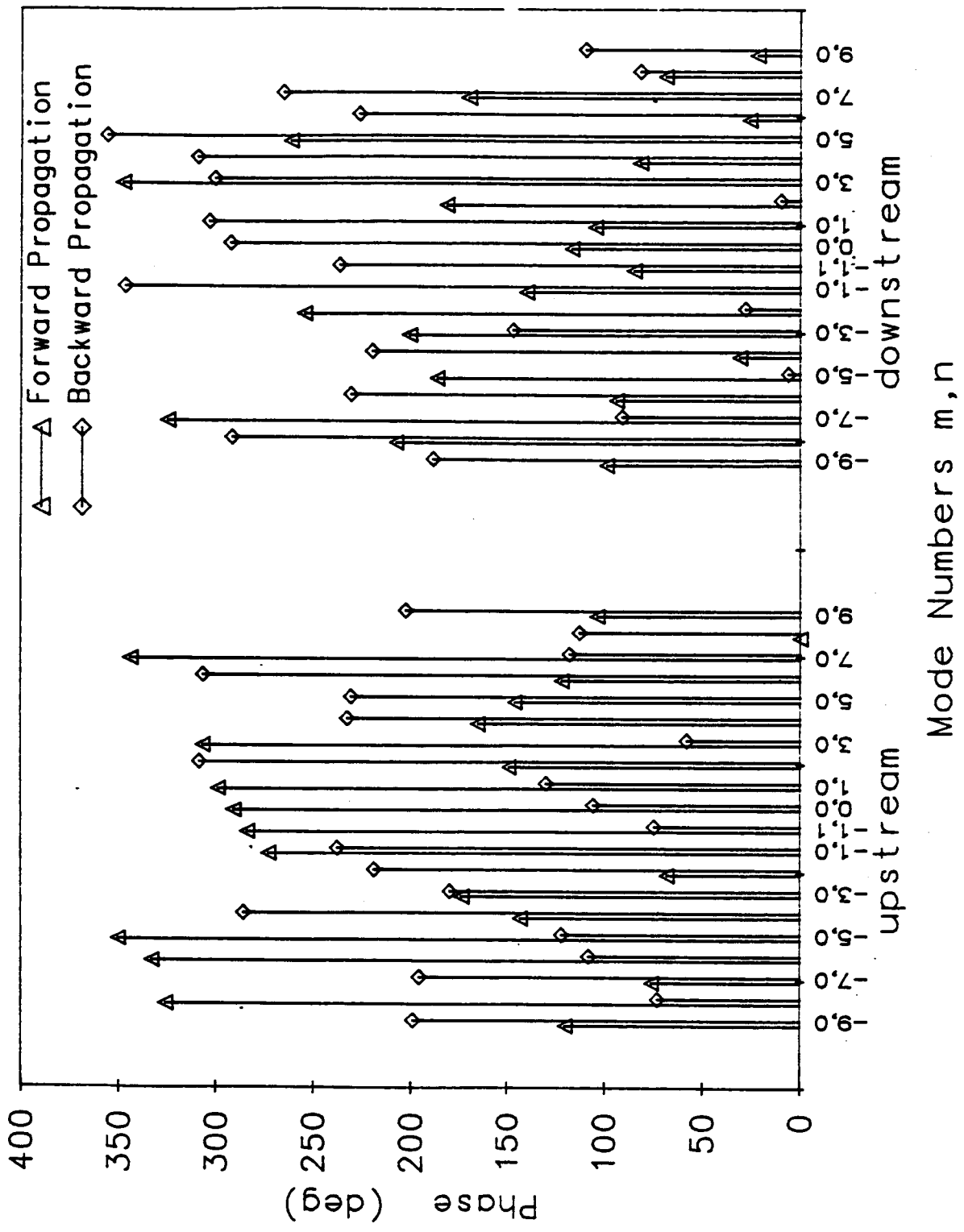
Figure 5.21b.   Phase Values Corresponding to the Amplitude of Modal Coefficients in Figure 5.21a; 6000 rpm, 1500 Hz
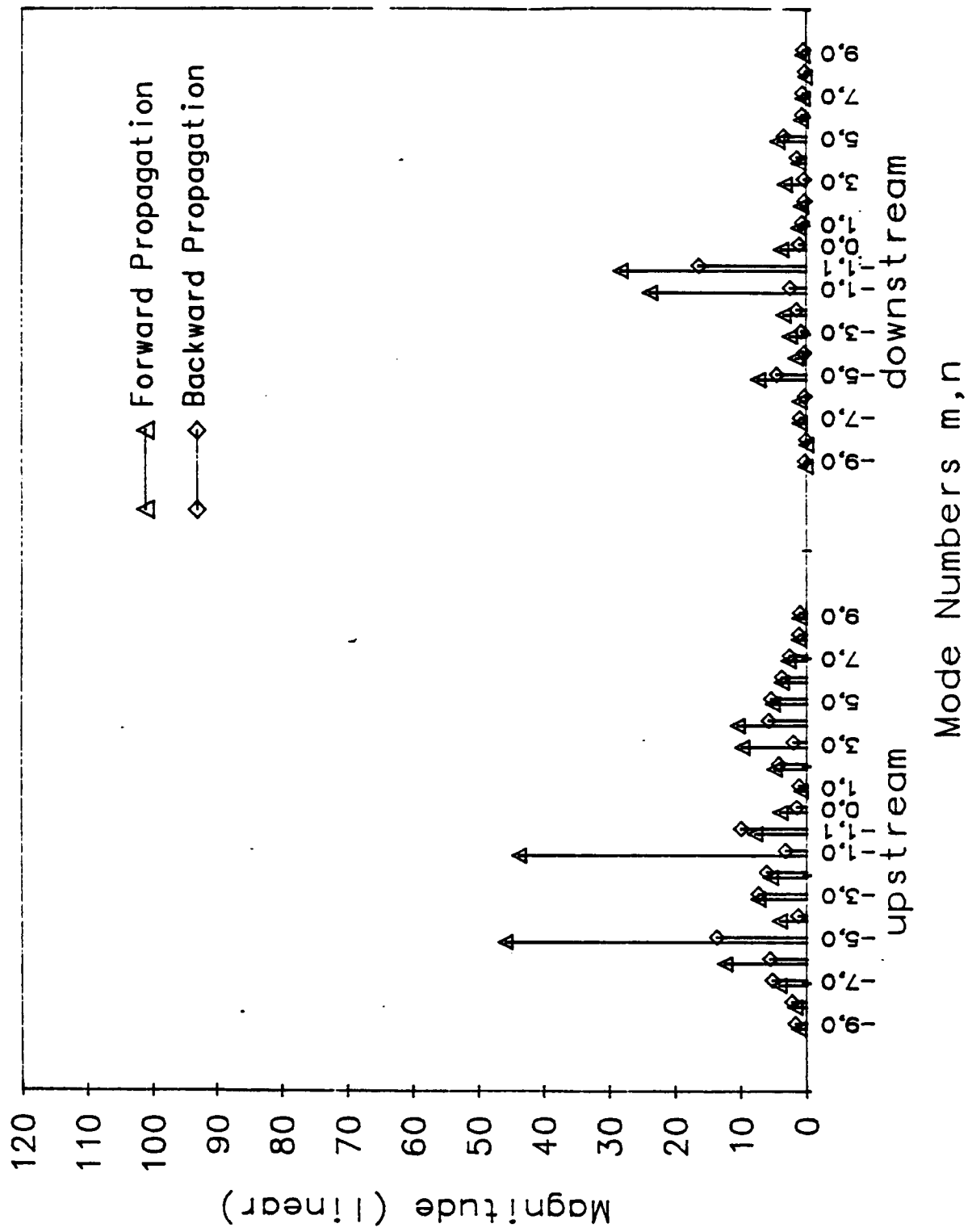
Figure 5.22a. Modal Coefficient Amplitudes Measured at the Upstream and the Downstream Locations in the Treated Configuration; 6000 rpm, 1500 Hz
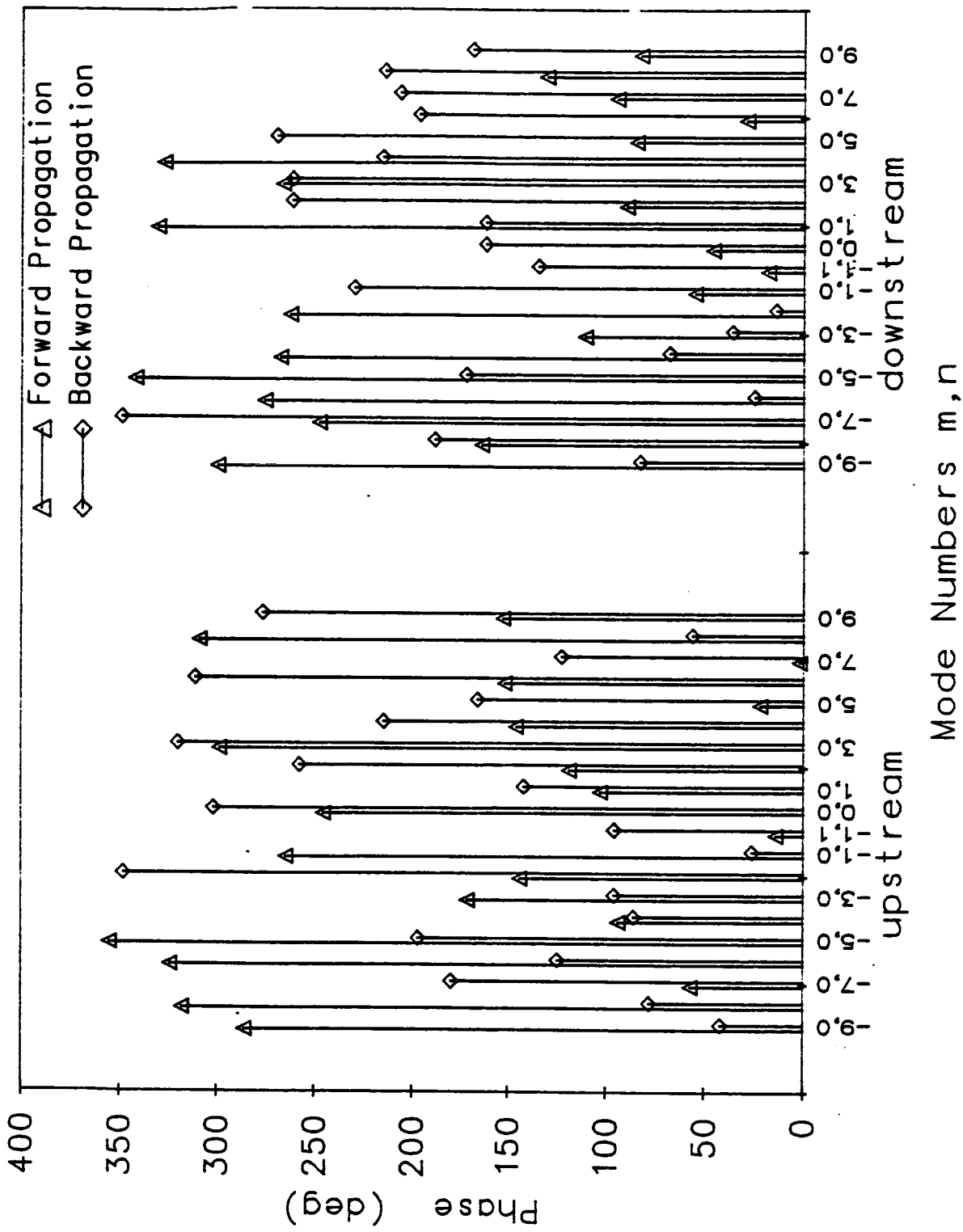
Figure 5.22b. Phase Values Corresponding to the Amplitudes of the Modal Coefficients in Figure 5.22a; 6000 rpm, 1500 Hz
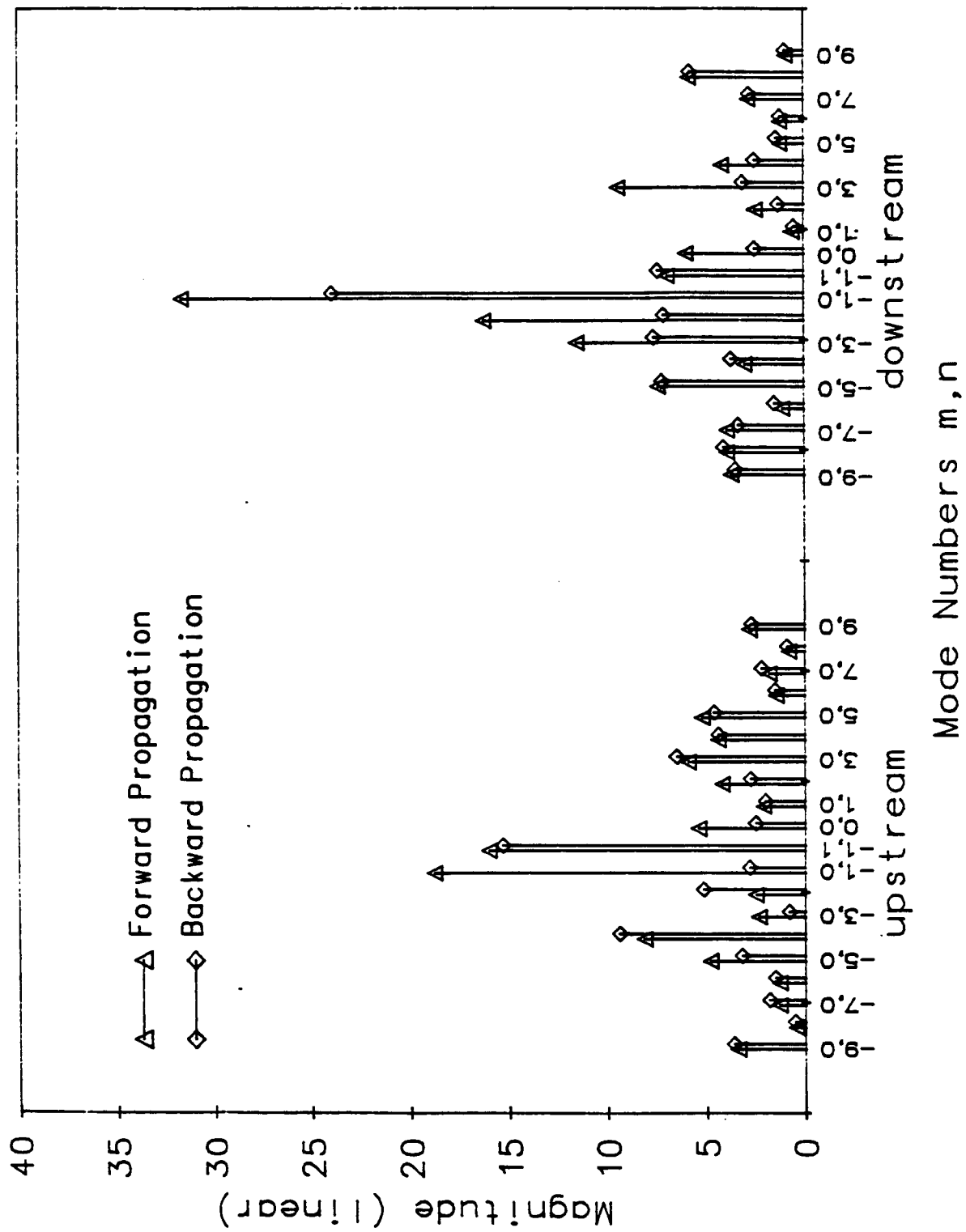
Figure 5.23a. Modal Coefficient Amplitudes Measured in the Upstream and the Downstream Locations in the Hardwall Configuration; 4000 rpm, 1000 Hz
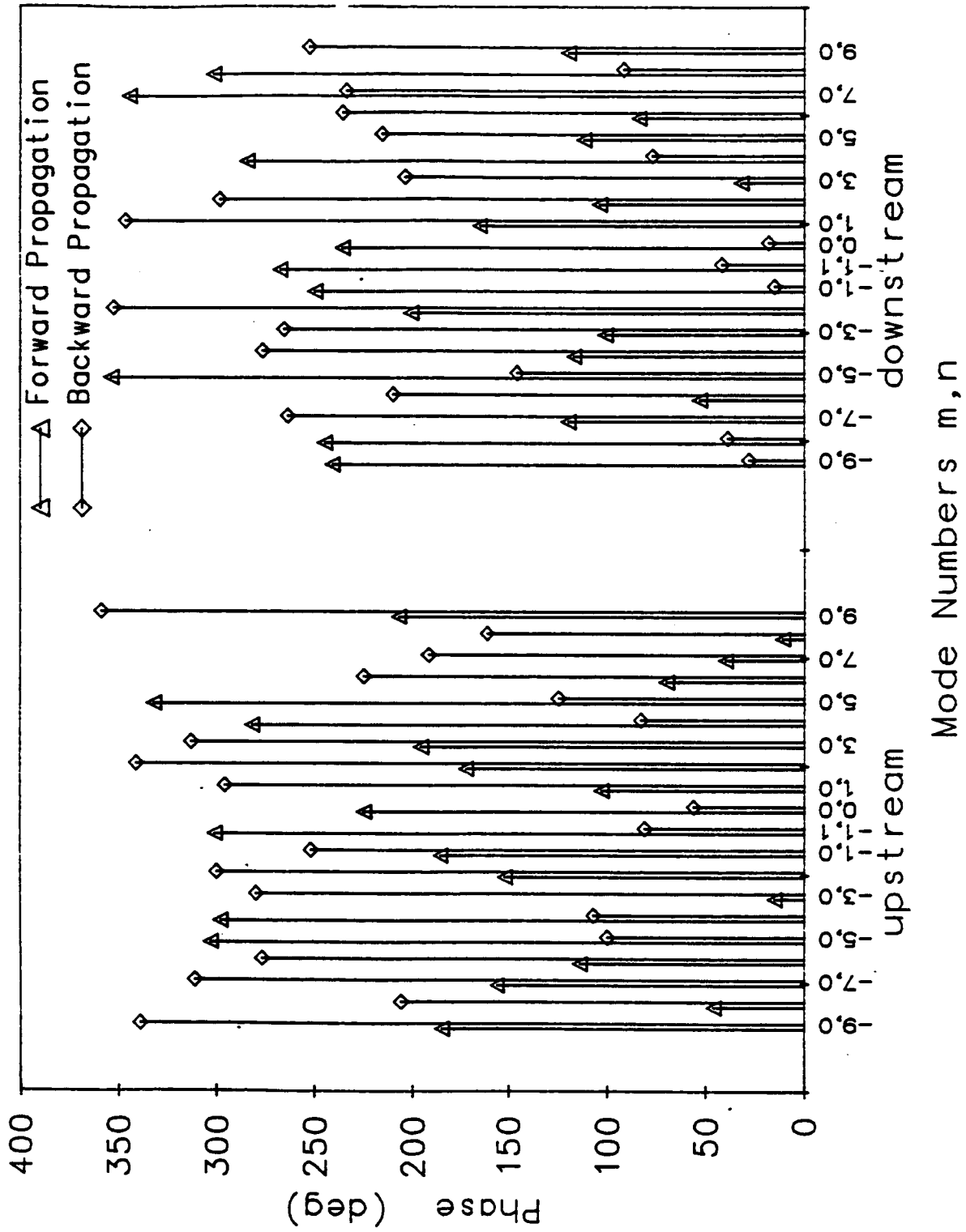
Figure 5.23b. Phase Values Corresponding to the Modal Coefficients in Figure 5.23a; 4000 rpm, 1000 Hz
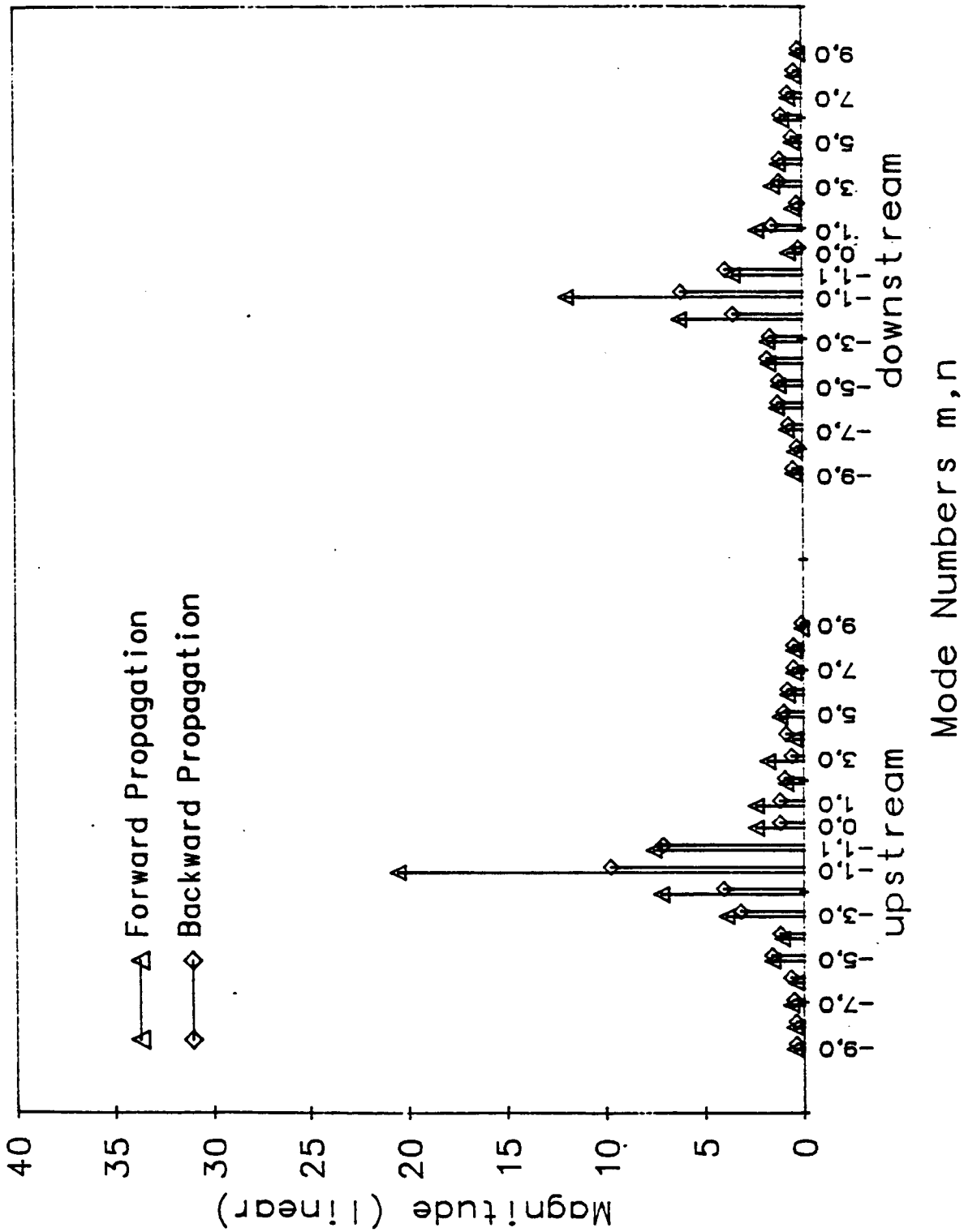
Figure 5.24a. Modal Coefficient Amplitudes Measured in the Upstream and the Downstream Locations in the Treated Configuration; 4000 rpm, 1000 Hz
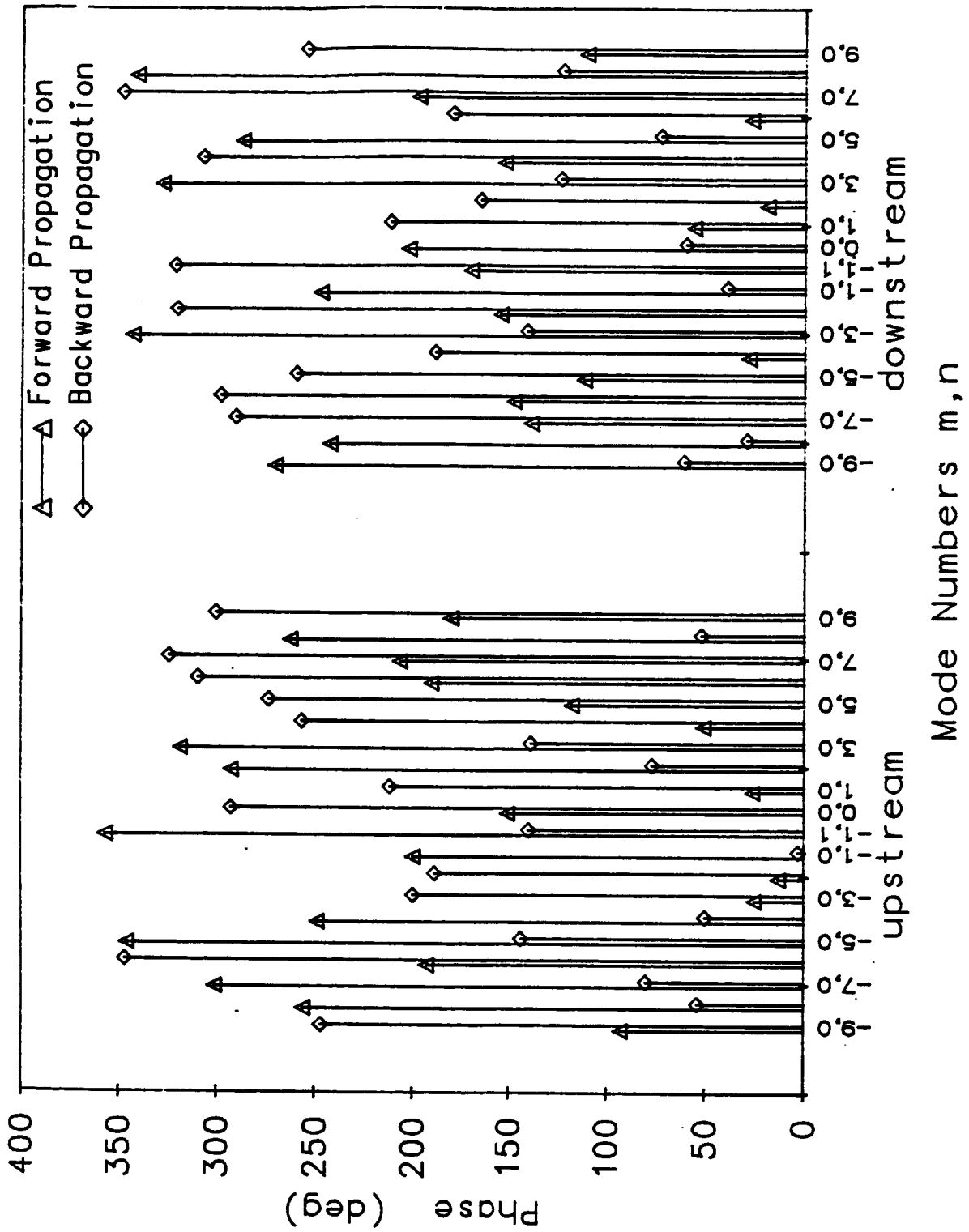
Figure 5.24b. Phase Values Corresponding to the Modal Coefficients in Figure 5.24a; 4000 rpm, 1000 Hz

The figures show the modes expected from rotor/stator interaction, although other modes are present also. For the 1500 Hz case only the (-1, 0) and (-1, 1) should be present. Figure 5.21a shows these modes were indeed measured but there was also a strong (-5, 0) mode. This would be possible if the inlet flow were not uniform, and may in fact be the result of interaction between the one high velocity zone near the top of the duct (Figure 5.4) and the fan. The fact that this mode is so strong is due to the fact it is just cut-on. Also because it is just cut-on it exhibits large reflections, which may explain its drop in level from upstream to downstream. In other cases the expected rotor/stator modes were stronger. For example, the forward propagating (7, 0) mode was about 7 dB stronger than any other mode in the 1900 Hz hardwall case.

Figure 5.22a (1500 Hz) is a typical case with treatment. As expected, the upstream forward propagating coefficients are about the same as in the hardwall case, but the downstream coefficients are lower, due to the treatment. Figures 5.20 and 5.24 show similar results for the 1900 Hz and 1000 Hz cases. As is evident, the treatment proved to be optimally designed for 1900 Hz. As expected, in the 1900 Hz case the (7, 0) mode which is just cut-on is the dominant mode, although in the 1000 Hz case the (-1, 1) mode which also is just cut-on is weak and the (1, 0) mode dominates.

Treatment was expected to have no effect on the upstream forward propagating modal coefficients. Figure 5.25 shows the effects of treatment and temperature on these coefficients. Run A66 was a 7600 rpm hardwall case. Run A67 was the same as A66 except for the fact the upstream and downstream modal instrumentation was switched. When run A67 was carried out the outside temperature was lower and because of this temperature change the (7, 0) mode is less cut-on for A66 and therefore stronger, while the other modes are in relatively good agreement. Run A71 was the 7600 rpm treatment run with temperatures similar to A67 and it shows good agreement with the hardwall cases except the A66 (7, 0) mode as would be expected. It should be noted that the A67 downstream coefficients did not make sense and as far as can be determined the only possible cause was calibration drift. Run A67 was the only run where the probes were not calibrated the day of the run and the downstream probes had a different set of calibration trim potentiometers. This could explain why the upstream probes still gave good results.
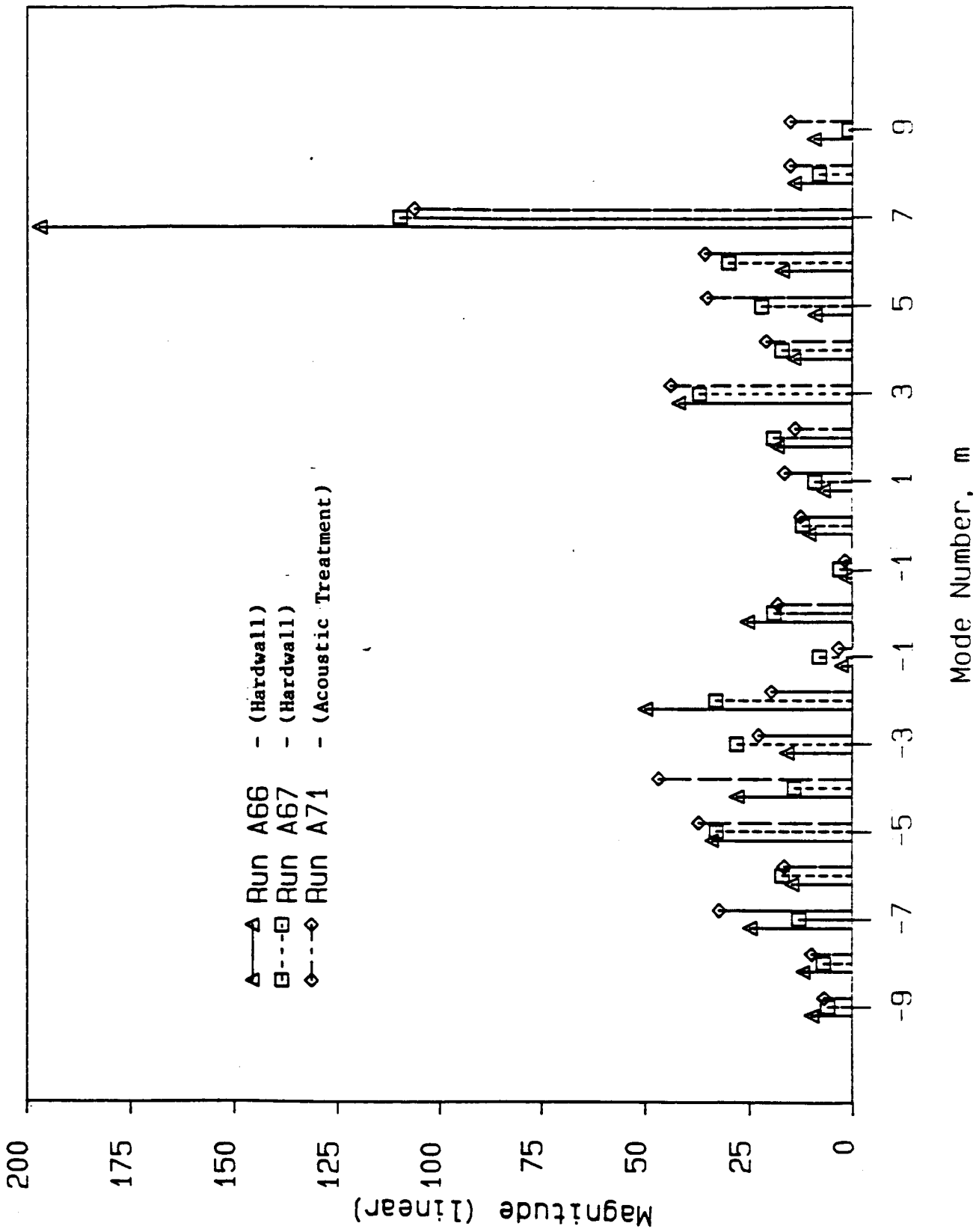
Figure 5.25. Modal Coefficient Amplitudes of Forward (Downstream) Propagating Modes
Measured at the Upstream Location; 7600 rpm, 1900 Hz

C-2

In general, the differences between carrying out the modal decomposition using sheared flow values of $p_{r,mn}$ and K_{mn} or uniform values were small, although the 1000 Hz case did show a difference of 1.5 dB in the (-1, 0) mode. The same could be said whether the modal decomposition was solved for cut-on modes only or for all modes.

Far-Field Measurement Results

Table 5.6 shows the sound power levels for both hardwall and treatment cases along with the resultant suppression at each running speed. The integration for acoustic power level was done using the nozzle exhaust as the acoustic source and the revised distances and angles from Table 5.1.

Table 5.6. Sound Power Levels From Far Field Data
(Power Spectrum Bandwidth = 4 Hz)

Blade Passing Freq. (Hz)	PWL (dB) Hardwall	PWL (dB) Treatment	Treatment Suppression
1000	120.0	118.8	1.2
1500	129.2	125.0	4.2
1900	126.8	116.6	10.2

Figures 5.26 through 5.28 show the directivity patterns of the narrow band SPLs. The lack of suppression in the 30° microphone position could well be the result of the directivity shifting, which would be expected. In general, the SPL at blade passing frequency was 5 to 10 dB higher than its harmonics for 7600 rpm and 6000 rpm, while for 4000 rpm the difference was at least 15 dB.

5.3 ACOUSTIC TREATMENT IMPEDANCE

In the theory experiment check of Section 6, an accurately determined value of the acoustic impedance of the treatment sections was required.
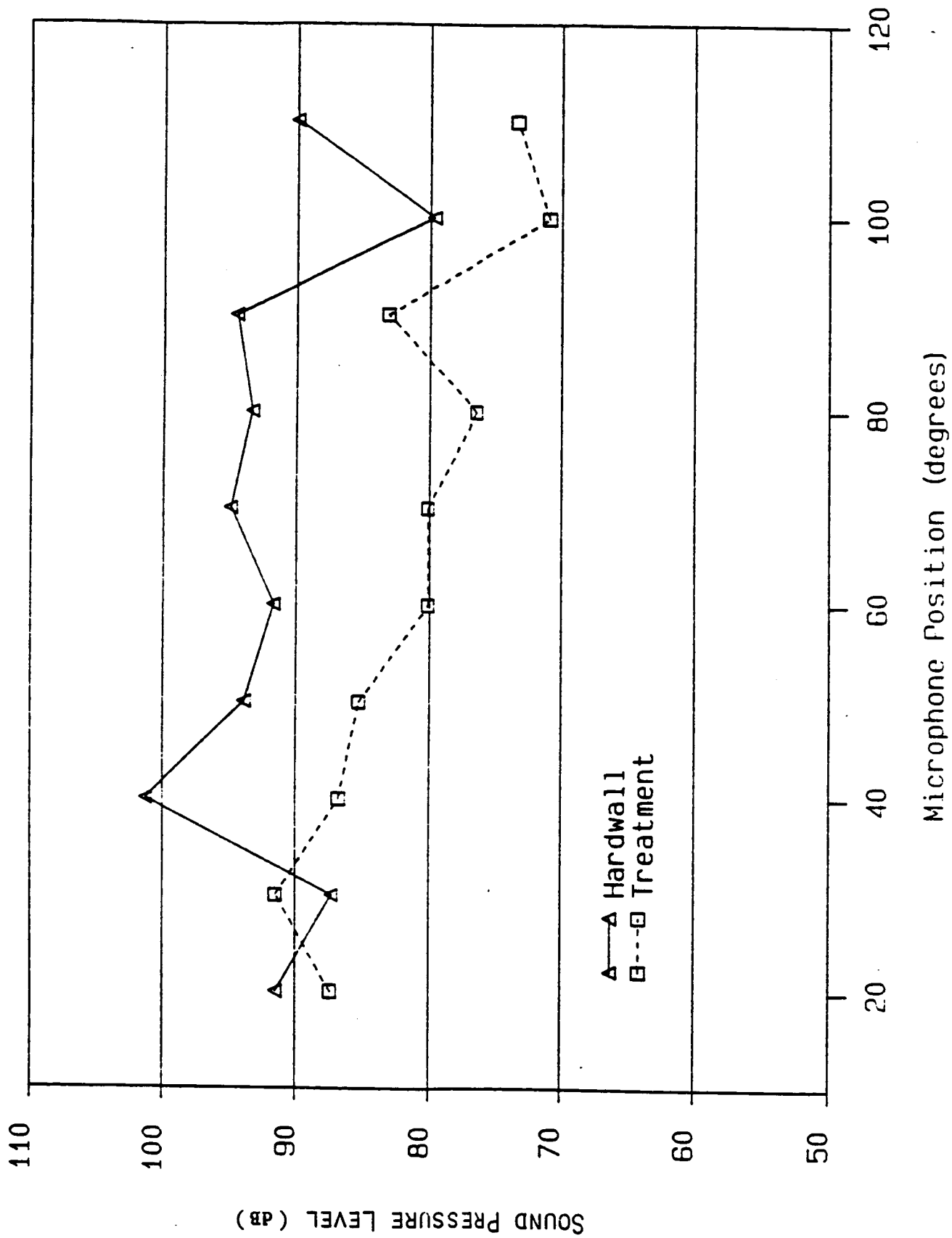
Figure 5.26. Plots of the Far Field (Narrow Band) Sound Pressure Level (SPL dB) Against Microphone Angular Position Relative to the Nozzle Axis for Hardwall and Treated Configurations at 7600 rpm (1900 Hz)
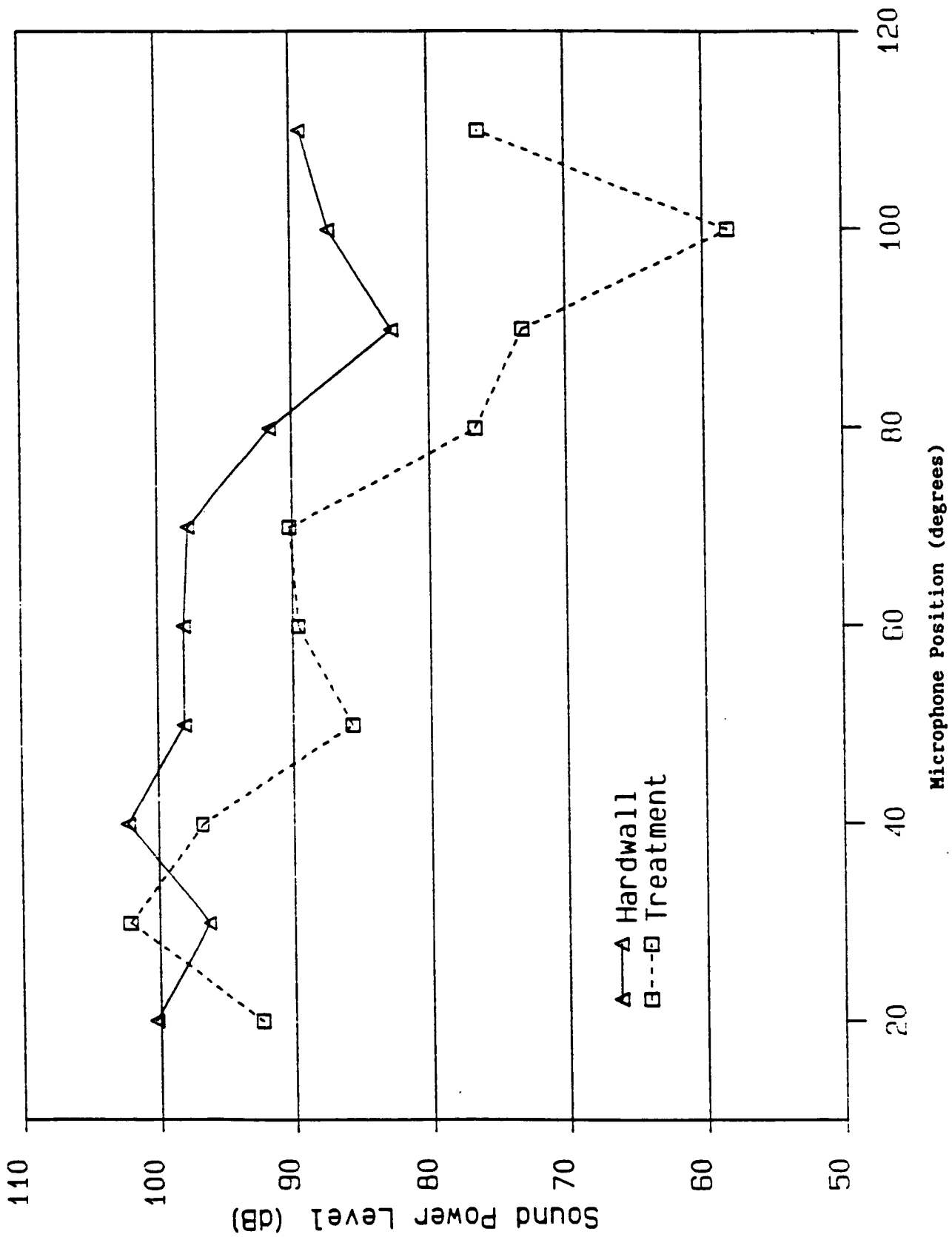
Figure 5.27. Plots of the Far Field (Narrow Band) SPL Against Microphone Angular Position Relative to Nozzle Axis for Hardwall and Treated Configurations at 6000 Hz (1500 Hz)
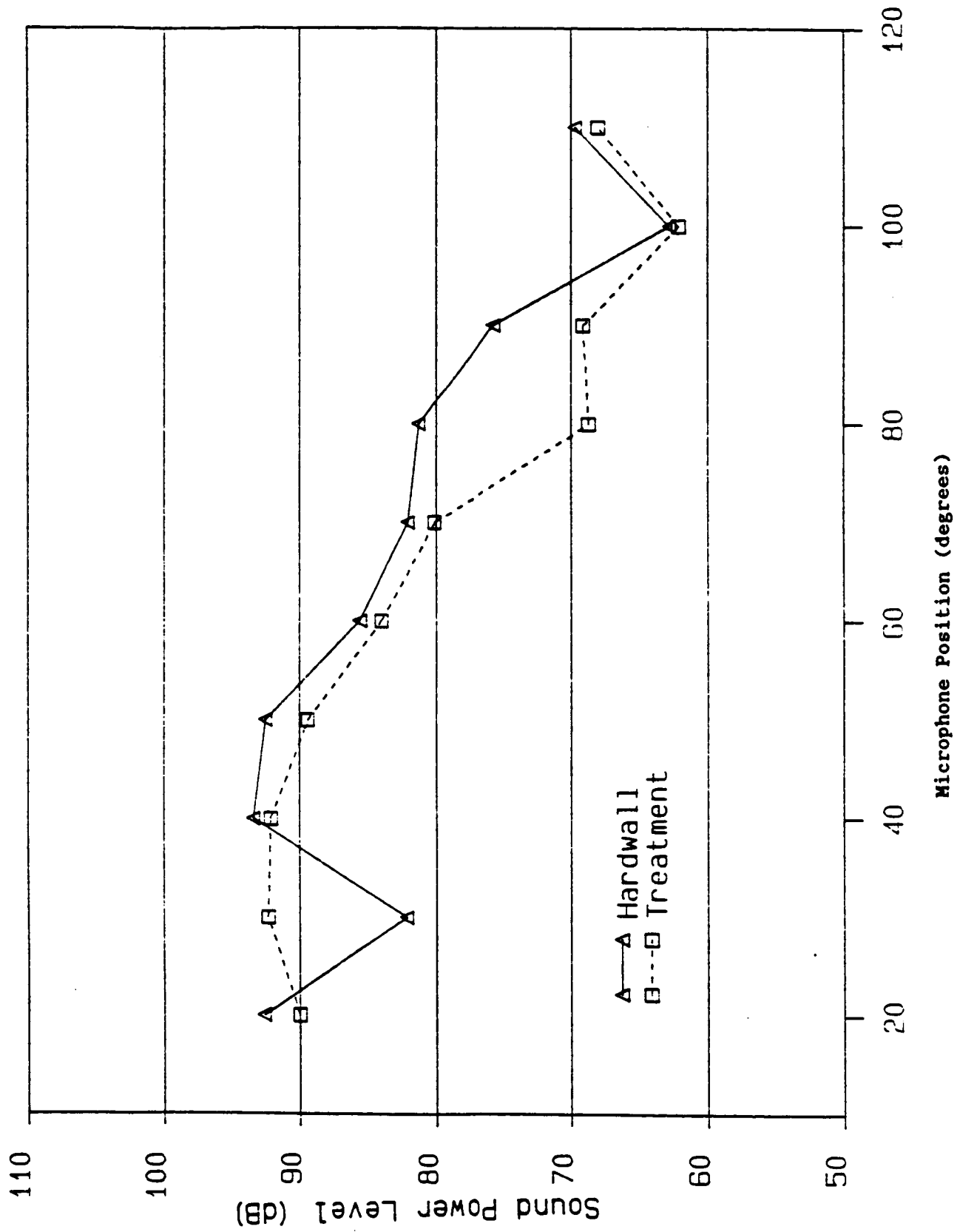
Figure 5.28. Plots of the Far Field (Narrow Band) SPL Against Microphone Angular Position Relative to Nozzle Axis for the Hardwall and Treated Configurations at 4000 rpm (1000 Hz)

Although the treatment was designed to be linear, measurements were carried out to establish the effects of sound intensity variation and grazing flow. In addition a comprehensive survey of the impedance was made over the surface of both the inner and the outer treatment sections to ensure that (a) the acoustic impedance of the two surfaces was equal and (b) the treatment impedance was uniform over the entire surface. The details of the design of the treatment, the measurement techniques and apparatus used and impedance data obtained are presented below.

5.3.1 TREATMENT DESIGN

The acoustic treatment was designed to be locally reacting and to have equal impedance on the inner and the outer walls of the treated section of the aft duct. A single degree of freedom (SDOF) design was chosen consisting of a 25.4 mm thick Flex Core bonded to a 1.143 mm porous face sheet and the wooden back wall of the treatment sections. The Flex Core used is made from 0.063 mm thick aluminum sheet. The geometry of the cells is illustrated in Figure 5.29a.

The face sheet consisted of a 200 x 400 wire mesh bonded onto a 30% porosity aluminum perforate (.83 mm hole size) sheet. The purpose of the wire mesh was to make the treatment linear; that is, the effects of flow and sound intensity on the impedance of the treatment were expected to be small as a consequence of the wire mesh.

From previous experience of the blockage due to bonding the core to face sheets, the resistance of the treatment was expected to be approximately 1.0 ρc ($\simeq$ 41.6 cgs Rayls). The resistance actually measured on the finished treatment sections and on the laboratory samples was approximately 0.5 ρc.

The geometry of the treated segment of the aft duct is schematically shown in Figure 5.29b.

200 x 400 Wiremesh
on Perforate Face Sheet

Flex Core

25.4 mm.

Hardwood Casing

Cross Section of Flexcore
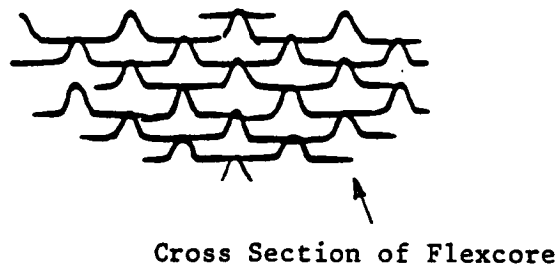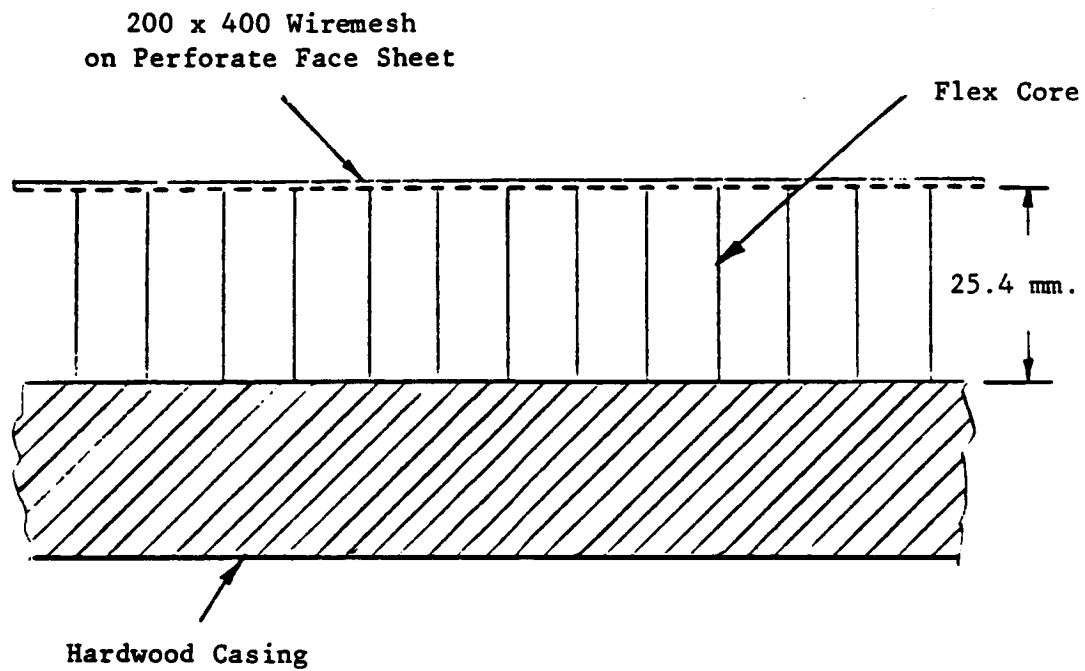
Figure 5.29a. Schematic Diagram of the Acoustic Treatment Used in the Treated Segment
of the Aft Duct

25.4 mm deep SDOF with 200 x 400
Wiremesh on 30% Porosity Perforate
as the Resistive Face Sheet

254 mm φ

508 mm φ

Flow

266.7 mm
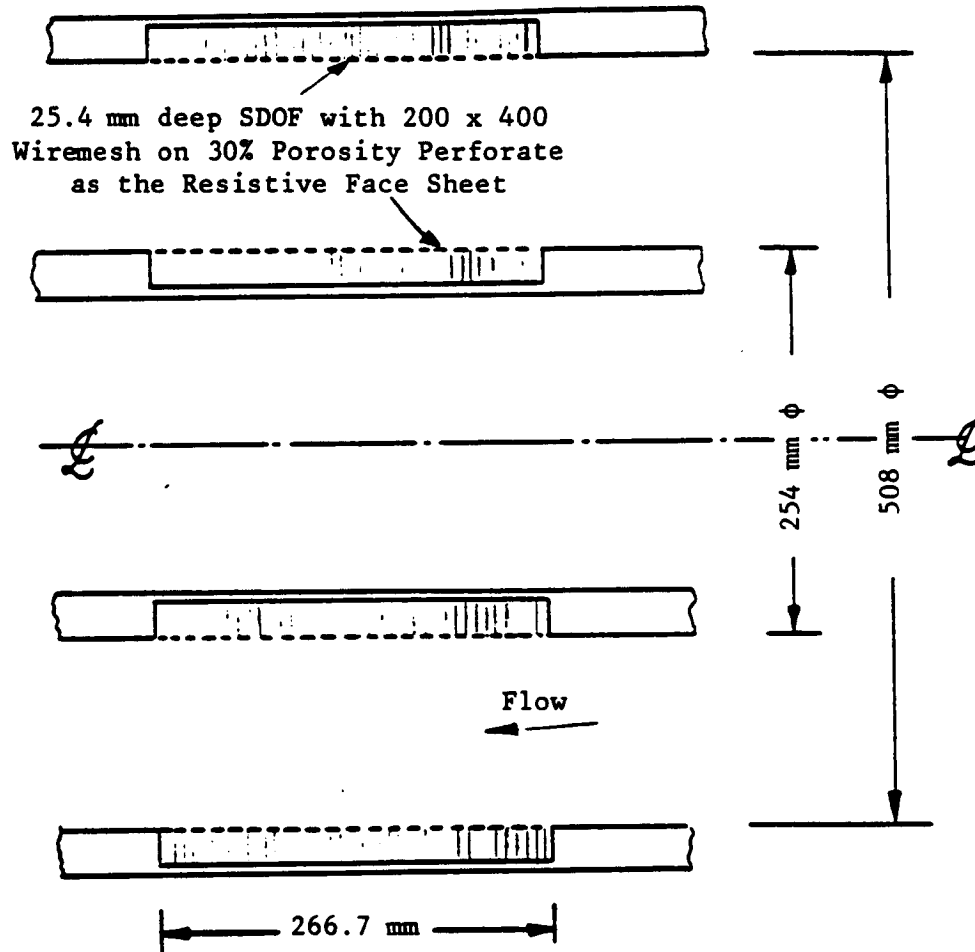
Figure 5.29b.   Schematic Diagram Showing the Acoustic Treatment
in the Straight Annular Part of the Fan Exhaust Duct

5.3.2 IN-SITU IMPEDANCE MEASUREMENTS

● **Measurement Apparatus**

The effects of grazing flow and sound intensity were studied in the Grazing Flow Duct using a sample of the face sheet of the treatment. The sample was prepared using the same materials and procedures as used in the manufacture of the treatment sections for the aft duct. The Flex Core was removed while ensuring that the blockage of the face sheet due to the bonding resin was preserved on the sample. A steady (dc) flow measurement on the sample was made prior to its preparation for In-Situ measurements.

Figure 5.30 shows the test sample. The cavity consists of a thick brass cylinder with inside diameter of 17.78 mm. The depth of the cavity could be varied between 25.4 mm and 45.72 mm. Endevco pressure transducers (Model 8514-10) were used to measure the acoustic signals at the face sheet and the back wall. These transducers are of 1.587 mm diameter. The range of these is 0-68950 pascals (0-10 psi) with a sensitivity of .004569 ± .0013 mV/pascal (31.5 ± 9.0 mV/psi). The size and the sensitivity of these transducers made them suitable for the In-Situ measurements.

Figure 5.31 shows the data acquisition and analysis hardware used in the measurements. The signals from the transducers were amplified by Tektronix amplifiers (Model AM 502). These are DC-coupled differential amplifiers with good common-mode rejection capabilities (rejection ratio of 50 dB DC to 50 kHz) and high gain for low voltage measurements. The amplified signals were sampled and analyzed by the Time Data Analysis system based on a 12 bit, 2 channel A to D converters and a DEC PDP 1135 minicomputer. The A to D converter of the Time Data Analysis system has amplifiers and antialiasing filters for each data channel which can be selected through software. This ensures that spectral information is uncontaminated by higher frequency signal and that the best use of the dynamic range of the A to D converter is made.

95
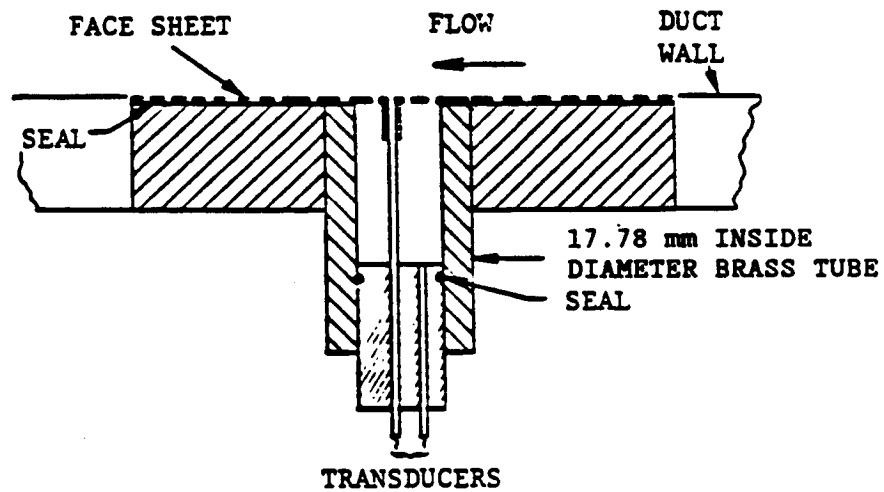
Figure 5.30. Schematic Diagram of the Apparatus Used for In-Situ Impedance Measurements in the Grazing Flow Duct
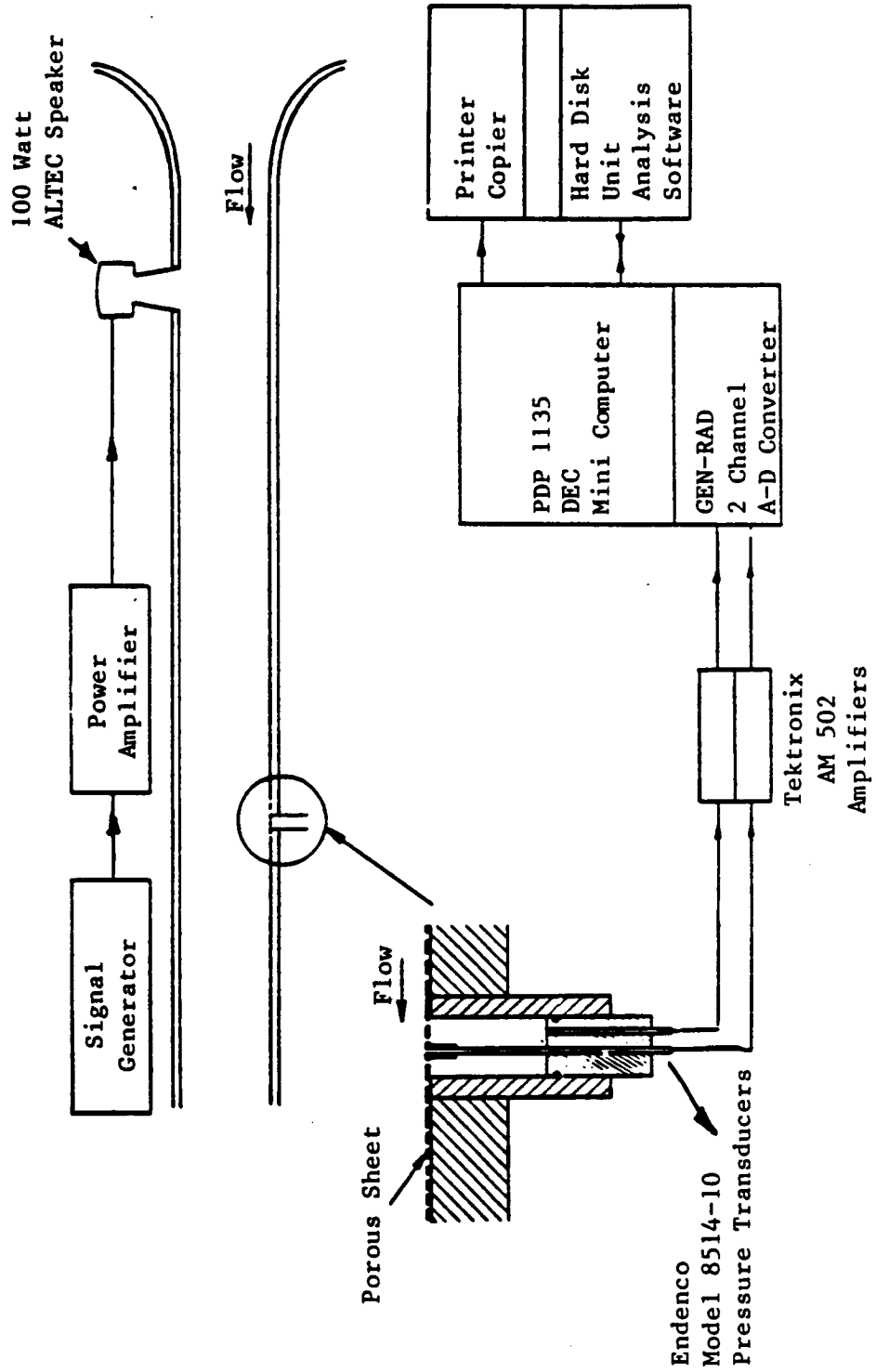
Figure 5.31. Schematic Diagram of the Data Acquisition and Analysis Hardware Used in the In-Situ Impedance Measurements

In-Situ impedance measurements were also made on the treatment sections prior to their installation in the vehicle. The outer treatment section was made up from six circumferential segments and the inner section was made up from three segments (see Figure 5.32). A single In-Situ measurement was made in each segment. The purpose of these measurements was to establish an averaged impedance value (without grazing flow) for the treatment to be tested in the aft duct. The experimental arrangement used in these measurements is shown in Figure 5.33. Broadband noise was used for these measurements. The measurements on the inner section were done using a sampling rate of 12,800 Hz and a bandwidth of 12.5 Hz while those on the outer section were carried out with a sampling rate of 25,600 Hz and band width of 50 Hz.

- Impedance Data From the Treated Sections of the Aft Duct - No Flow

Resistances and reactances from the measurements on the outer treatment section are presented in Figure 5.34. The narrowband spectra of the signals measured at the face sheet and the back wall of the cavity at location A are shown in Figure 5.35.

The coherence of the two signals and the phase difference between them is shown in Figure 5.36.

The quality of the data in Figures 5.35 and 5.36 is typical of these measurements.

With the exception of the impedance measured at cavity E, these measurements look good. They show that the resistance varies by a small amount between these cavities. For example at 1900 Hz, the resistance measured at cavity A is 0.48 ρc while that measured at cavity B is .67 ρc.

As the inner treatment section is made up of three circumferential segments, only three In-Situ measurements were made on it. The data from these measurements is shown in Figures 5.37. The reactances do not vary from

Figure 5.32. Photograph of the Inner Treatment Section of the Acoustically Treated
Segment of the Aft Duct

99

SOUND
SOURCE

FACE-SHEET
TRANSDUCER

DIAMETER OF PERFORATIONS
WAS 1.59 mm

BACK WALL TRANSDUCER
(1.59 mm DIAMETER)
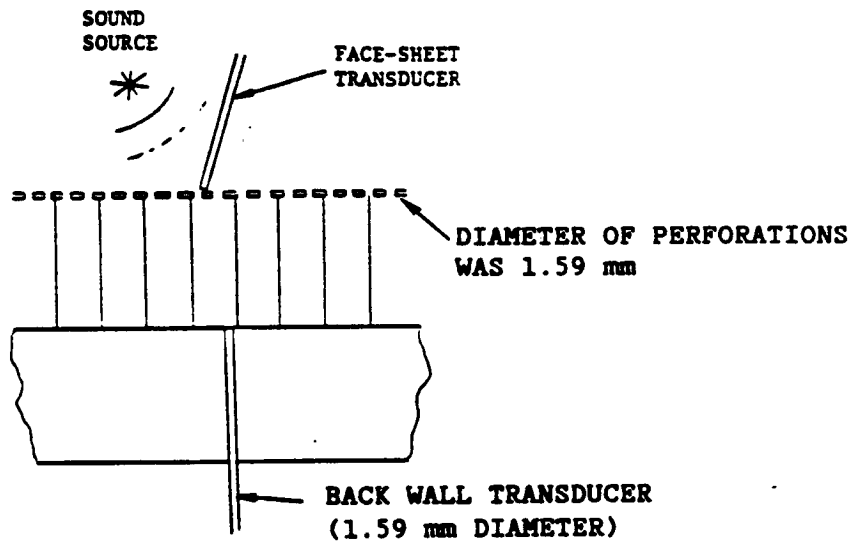
Figure 5.33.   Experimental Arrangement Used in the In-Situ Impedance Measurements
on the Outer and the Inner Treatment Sections of the Aft Duct
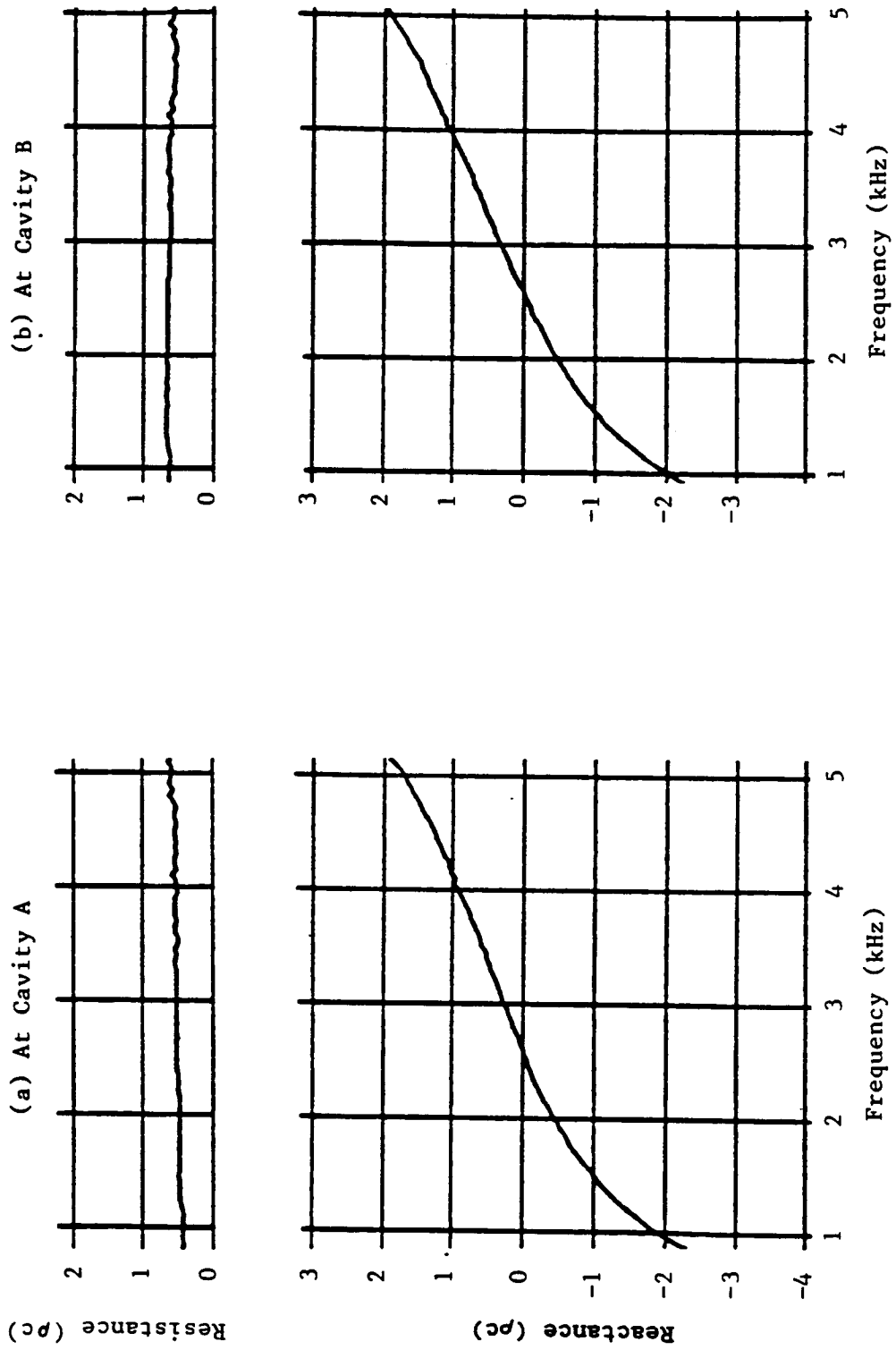
Figure 5.34. In-Situ Impedance Measurements at Six Different Circumferential Locations on the Outer Treatment Section of the Aft Duct
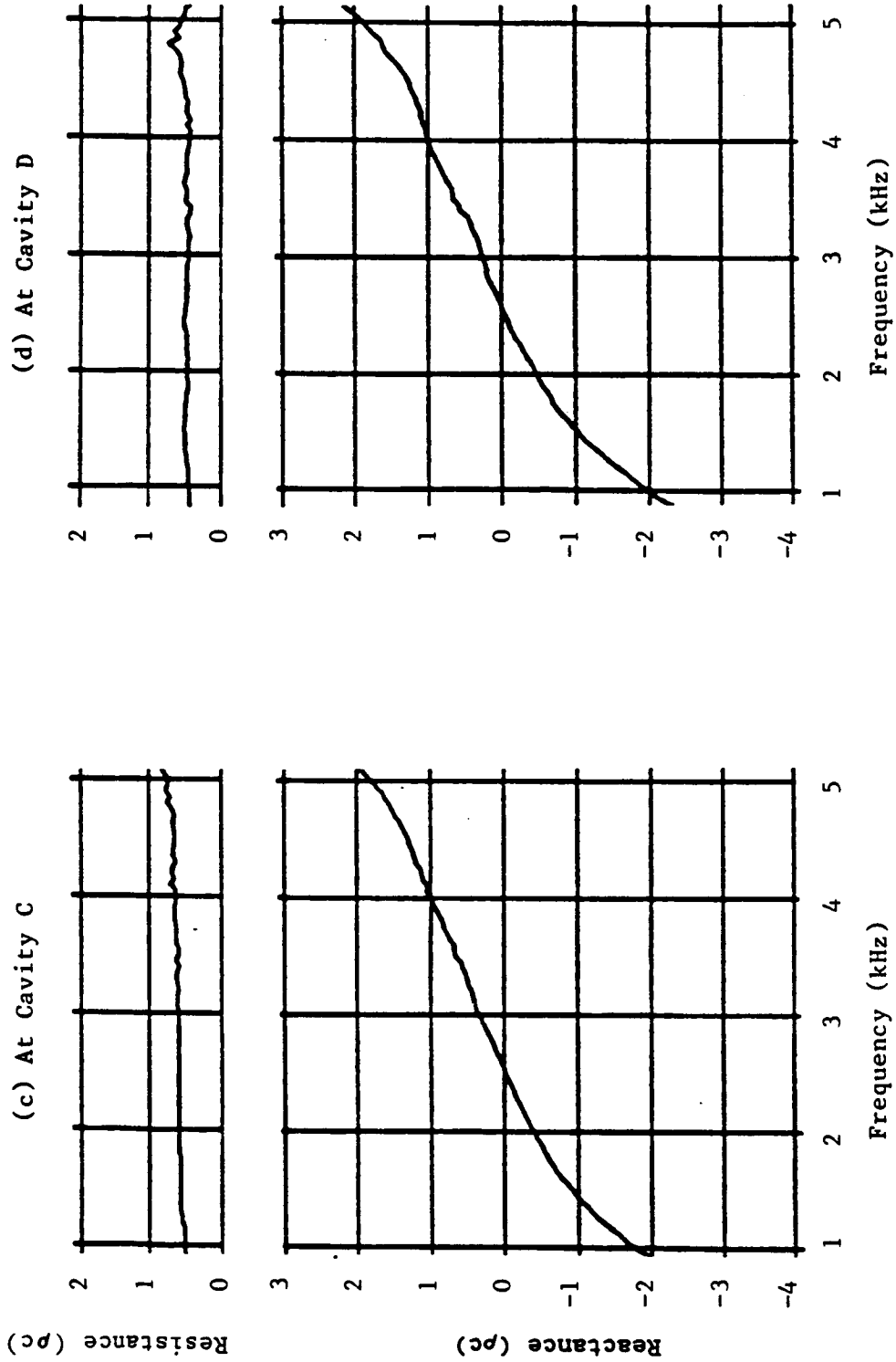
Figure 5.34. In-Situ Impedance Measurements at Six Different Circumferential Locations on the Outer Treatment Section of the Aft Duct (continued)

Figure 5.34. In-Situ Impedance Measurements at Six Different Circumferential Locations on the Outer Treatment Section of the Aft Duct (continued)

Figure 5.36. The Coherence of Two Signals of Figure 5.35 and the Phase Difference $(\phi_A - \phi_B)$ as Functions of Frequency
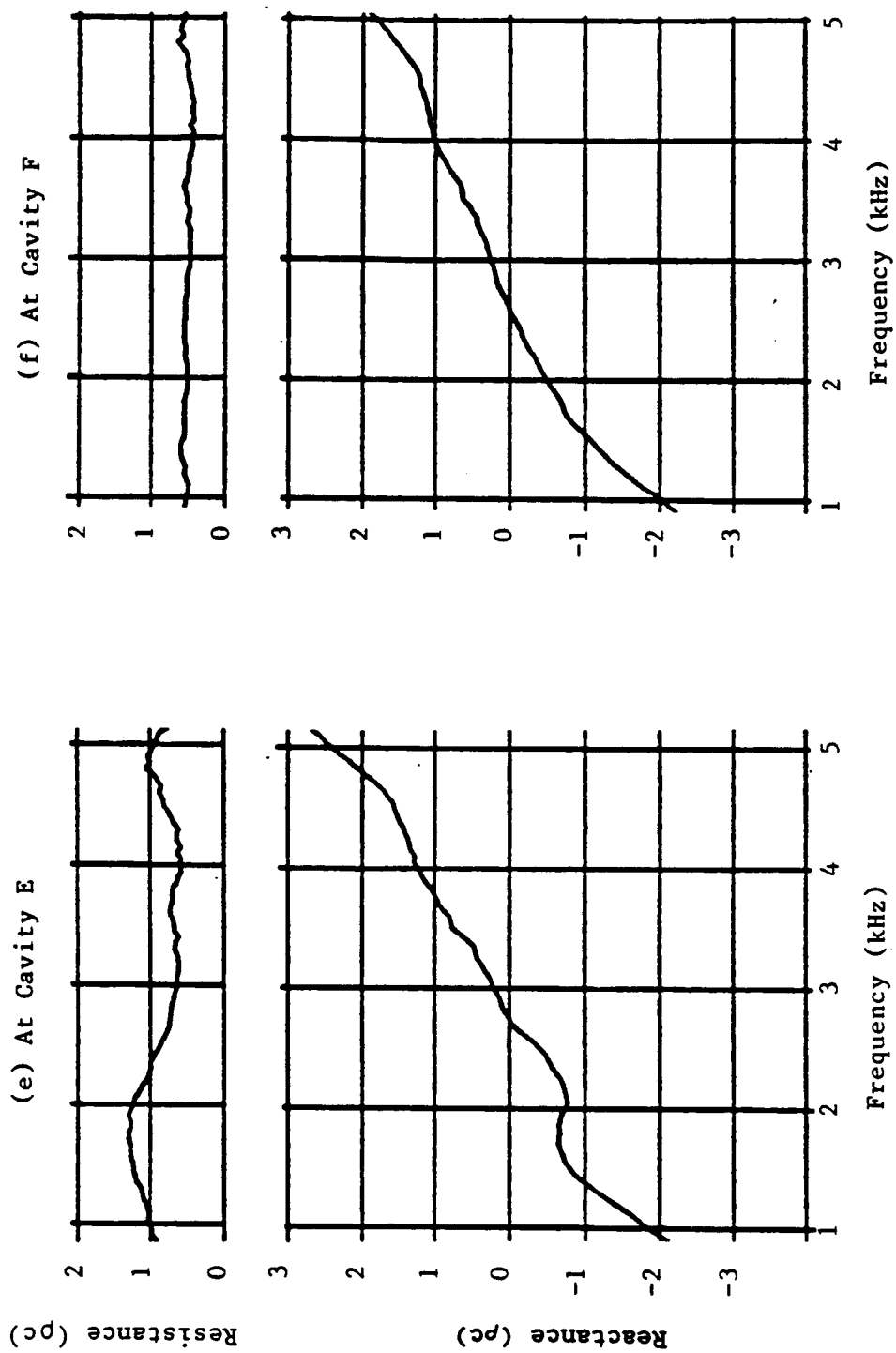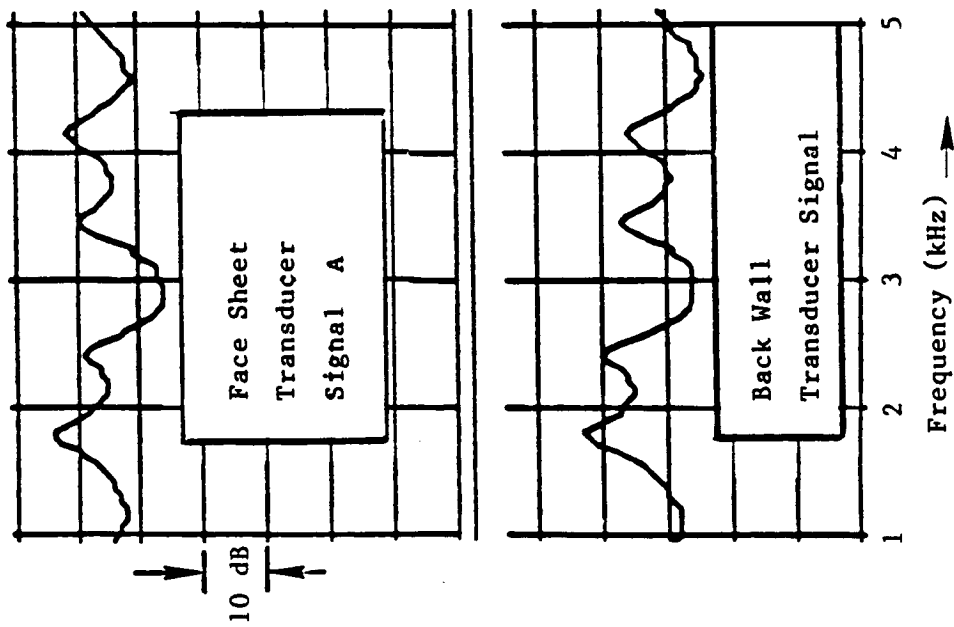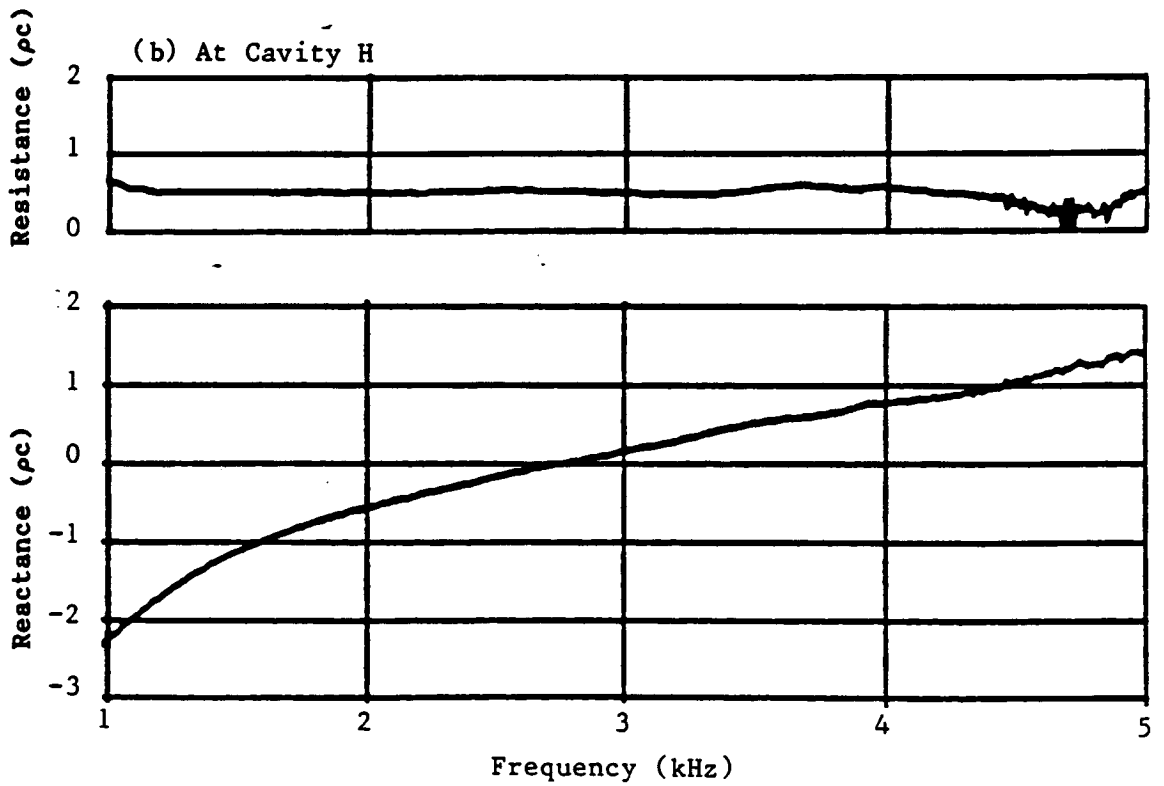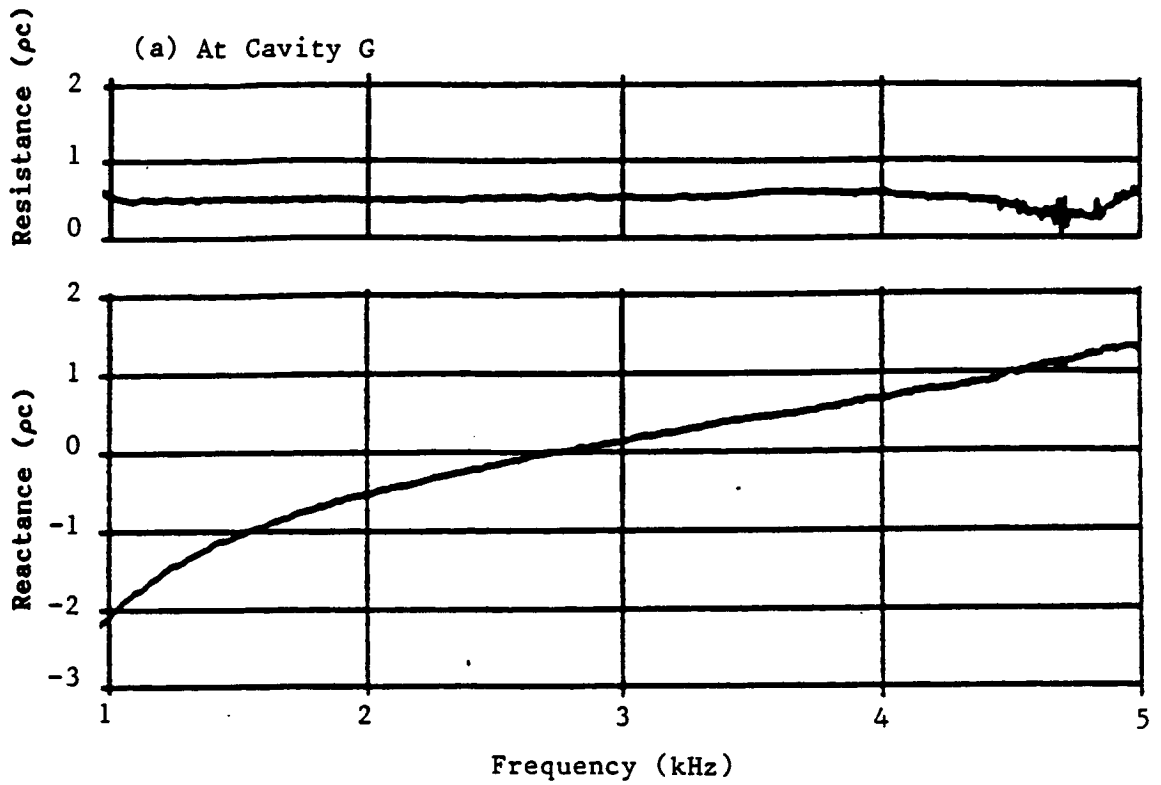
Figure 5.35. Auto Correlation Spectra of the Acoustic Signals in the In-Situ Measurement of Cavity A of Figure 5.34

Figure 5.37. In-Situ Measurements at Three Different Circumferential Locations on the Inner Treatment Section

105
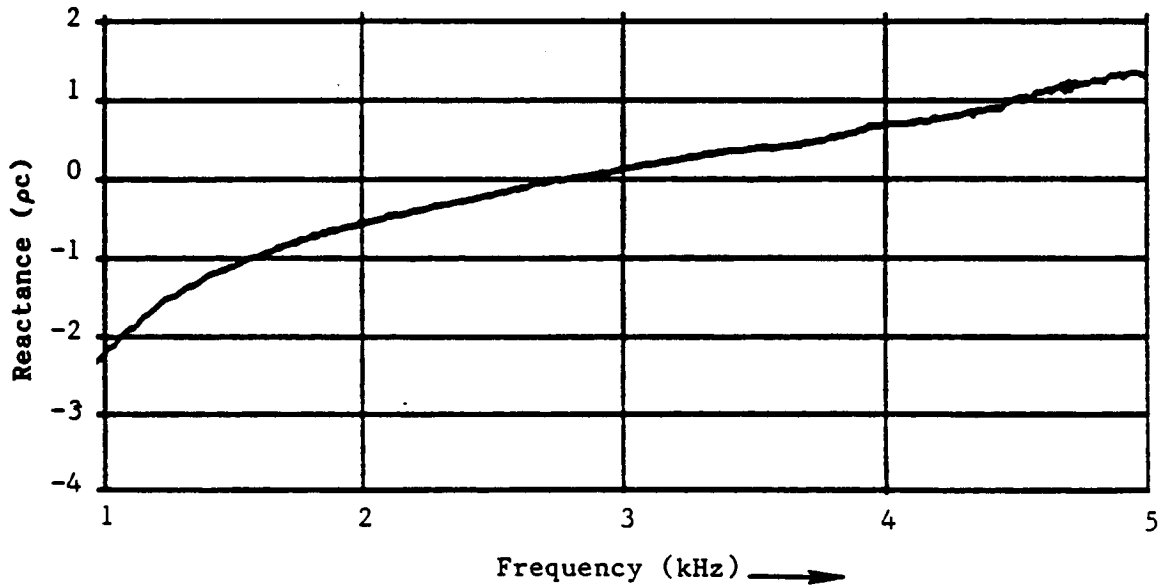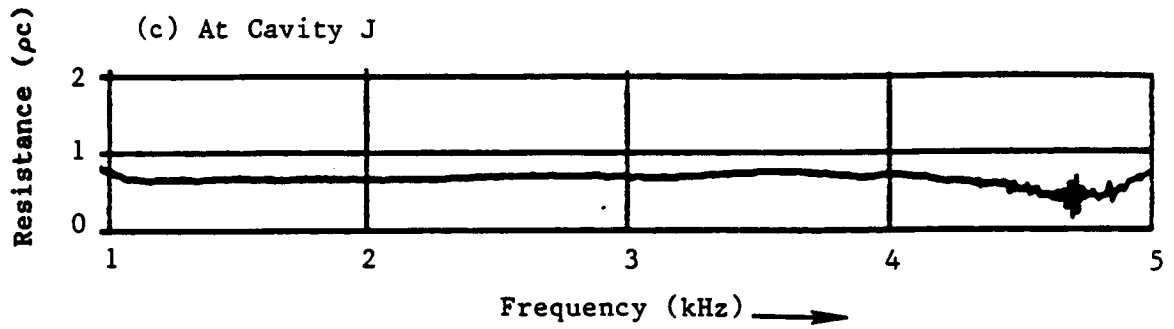
(c) At Cavity J

Figure 5.37.   In-Situ Measurements at Three Different Circumferential Locations
on the Inner Treatment Section (continued)

point to point, but the resistance at cavity c is appreciably higher than at cavities a or b. This observation raised the question as to how representative the measurements at a, b and c were of the impedance of the panels on which they were located. There was a need to make several additional measurements to get a good statistical measure of the averaged impedance value of the treatment and the standard deviation from it. To do this by the In-Situ method would be tedious and time consuming. Consequently it was decided to carry out a comprehensive survey of the treatment impedance using the Acoustic Plunker (See 5.3.3). It should be noted however that at any point the acoustic resistance measured by the In-Situ method is virtually constant between 1000 Hz and 2000 Hz, the range of interest in this study.

- ## Impedance Measurements in the Grazing Flow Duct (GFD)

These measurements were carried out on a laboratory sample of the treatment. First the effects of sound intensity were measured without grazing flow. Then the effects of grazing flow on the impedance were measured. It was assumed that the correlations obtained from these measurements would accurately represent the grazing flow and sound intensity effects occurring on the treatment in the aft duct during modal measurements.

- ## The Effects of Sound Intensity

Figure 5.38 shows the increase in acoustic resistance relative to the value measured at 125 dB plotted against the sound pressure level at the three frequencies of interest. At 1000 Hz, the effect of increasing SPL on the acoustic resistance was much lower than that measured at 1500 Hz and 1900 Hz. Negligible effects of sound intensity changes were observed on the reactance of the sample.

The above data was obtained with discrete frequency sound field in the duct.
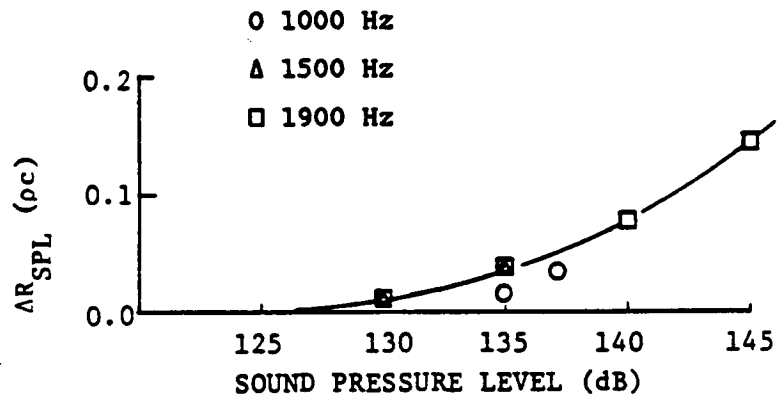
Figure 5.38. Increase in Acoustic Resistance With Sound Pressure Level (SPL, dB) of the Discrete Acoustic Signal; No-Flow

● <u>The Effects of Grazing Flow</u>

A cavity depth of 4.572 cm instead of 2.54 cm was chosen for these measurements because an error analysis (see Appendix B) had shown that the magnitude of the error in the measured resistance would depend on the magnitude of impedance at the frequency of interest. By increasing the cavity depth, the magnitude of the reactance of the sample was reduced significantly between 1000 Hz and 2000 Hz to yield more accurate measurements of the acoustic resistance in this frequency range. It was assumed that the reactance of the cavity did not influence the effects of grazing flow on the lump impedance of the porous face sheet.

The effects of grazing flow on the resistance of the sample are shown in Figure 5.39a. As expected, the increase in the resistance with increasing mean flow Mach number is roughly the same at the three frequencies of interest. The data correspond to roughly 140 dB (OASPL) at the surface of the sample.

Figure 5.39b shows the corresponding plots of reactance against the mean flow Mach number.

Figure 5.40 shows typical narrowband spectra of the signals sensed by the transducers at the face sheet and the back wall of the cavity at Mach 0.4.

The effect of sound intensity on the impedance in the presence of grazing flow was found to be much less than that measured under no flow conditions. In view of this the sound intensity effects under test conditions in the aft duct may be neglected.

5.3.3 PLUNKER MEASUREMENTS ON THE TREATMENT SECTIONS OF THE AFT DUCT

As a considerable amount of variation in the impedance of the treatment sections was revealed by the In-Situ measurements (as illustrated in Section 5.3.2). A much larger number of impedance measurements on these sections was made using the Acoustic Plunker which is described below.
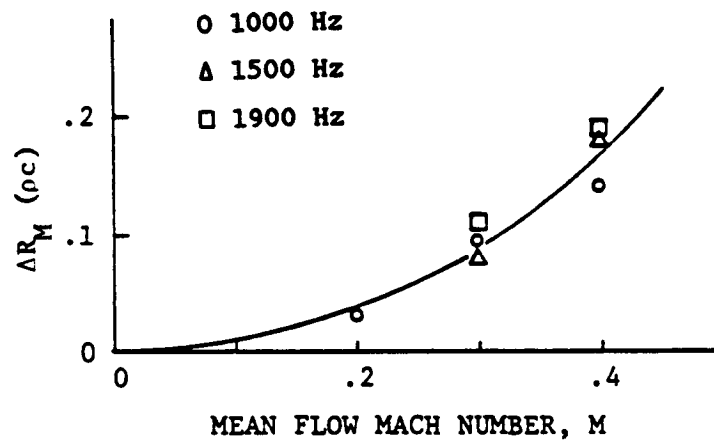
$$\Delta R_M = (R_M - R_{M=0}), \quad SPL = 140 \text{ dB}$$

Figure 5.39a. Increase in Acoustic Resistance With the Mean Flow Mach Number in the Grazing Flow Duct

110
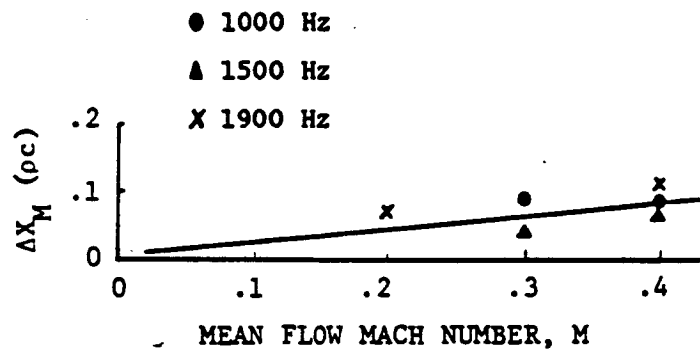
Figure 5.39b. Increase in the Acoustic Reactance With the Mean Flow Mach Number in the Grazing Flow Duct
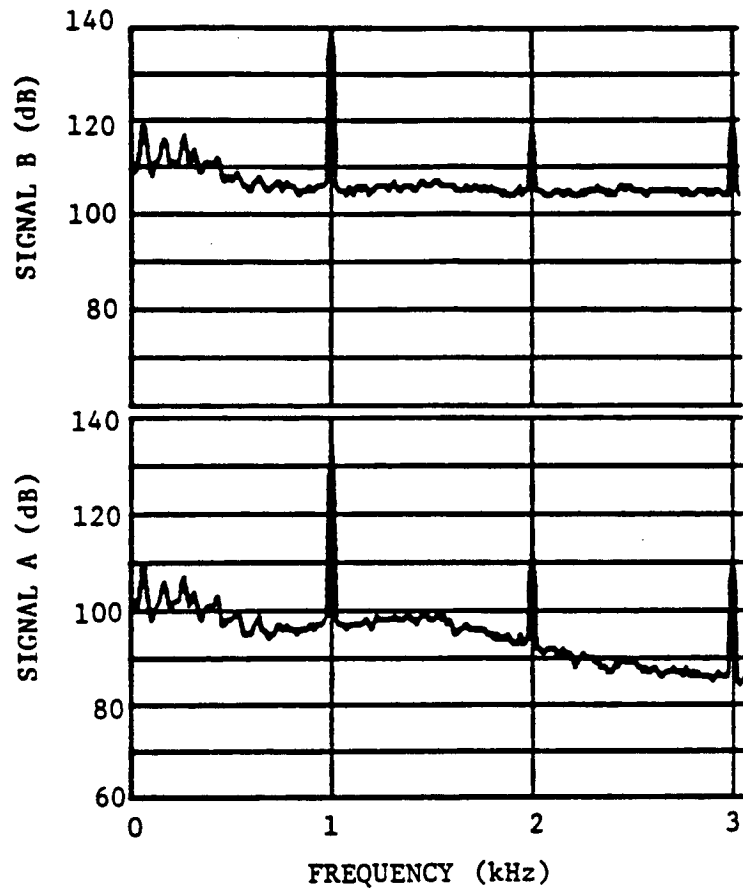
Figure 5.40. Auto Correlation Spectra of the Face Sheet Signal A and Backwall Signal B During an In-Situ Impedance Measurement at M = 0.4

The Acoustic Plunker [Reference 7] is a transducer developed by the General Electric Company for the measurement of the normal acoustic impedance of finished treatment panels. It is a portable and nondestructive device. It has to be calibrated to measure the normal impedance of treatment panels of a particular design. It has sufficient sensitivity to measure small variations of the normal impedance on a given panel at a given OASPL as well as to sense impedance changes with sound intensity.

The Plunker is schematically illustrated in Figure 5.41a. It consists of a tube of circular cross section. The walls of the tube are acoustically hard and smooth. A sound source is located at one end of the tube. The other end is placed against the surface of the treatment panel such that the tube is at right angles to the surface. The rubber flange is designed to minimize sound leakage. The diameter of the Plunker tube is such that over the frequency range of interest, only plane waves can propagate in it. Two transducers located at distances x_1 and x_2 from the treatment surface sense the stationary sound field in the Plunker tube. The signals from the Plunker transducers are analyzed to yield the time averaged values of the complex transfer function:

$$H_{21}(f) = \overline{P_2(f) \, P_1^*(f)} \; / \; \overline{P_1(f) \, P_1^*(f)} \tag{5.2}$$

The apparent impedance measured by the Plunker using the above transfer function is given by:

$$\zeta_p(f) = -i \; \frac{\left\{ \mathrm{Sin}(kx_2) - H_{21}(f)\mathrm{Sin}(kx_1) \right\}}{\left\{ \mathrm{Cos}(kx_2) - H_{21}(f)\mathrm{Cos}(kx_1) \right\}} \tag{5.3}$$

If a sample of the treatment is cut out of the panel at the location where the plunker measurement $\zeta_p(f)$ is made and its normal impedance $\zeta(f)$ is measured in the Impedance Tube schematically illustrated in Figure 5.41b, then the calibration of the Plunker is computed from the above data as follows:

$$\xi_p(f) = \frac{\zeta(f)}{\zeta_p(f)} \tag{5.4}$$

113
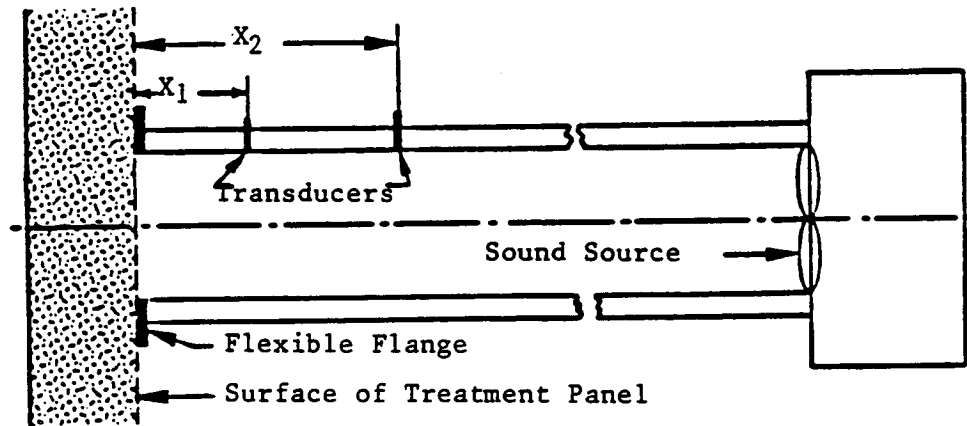
Figure 5.41a.   Schematic Diagram of the Acoustic Plunker
                Placed Against the Surface of a Flat Treatment Panel
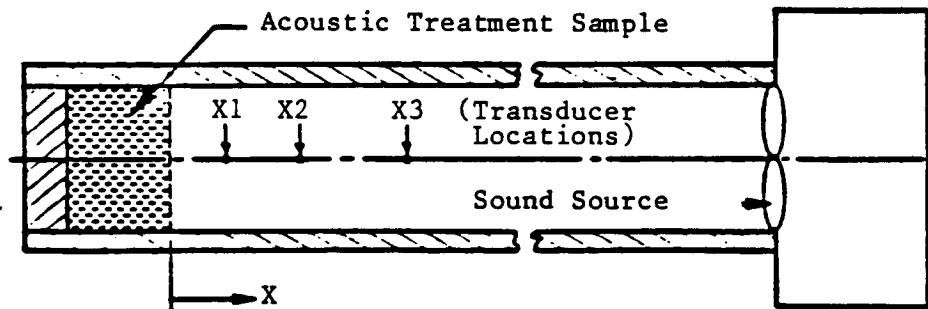
Figure 5.41b.   Schematic Diagram of a Normal Impedance Tube

The calibration of the Plunker as defined above for a given design of treatment is needed because the apparent impedance $\zeta_p(f)$ measured by the Plunker is different from the Impedance Tube data for the following reasons:

1. The absorber volume behind the panel surface in the Plunker measurement is significantly larger than in the equivalent Impedance Tube measurement.

2. Some sound leakage may occur due to imperfect seal between the Plunker and the panel surface due to the curvature of the treatment surface. The effect of this leakage can be calibrated out only if the Plunker axis is always perfectly normal to the surface and that the radius of curvature of the surface is constant everywhere.

3. There may be transmission of sound in the core of the panel at right angles to the sound field in the tube due to

   (a) non rigid cavity walls
   (b) drainage holes between cavities
   (c) imperfect bonding of core to the face sheet and back wall.

Once the calibration $\xi_p(f)$ for a particular panel design is obtained in the manner described above, the normal impedance of any other panel of that design can be measured by simply measuring $\zeta_p(f)$ with the Plunker and then multiplying it with $\xi_p(f)$.

As it was not desirable to cut out a sample from the treatment sections for the aft duct, the Plunker calibration was carried out using an In-Situ measurement of impedance. It was established that this measurement was similar to an Impedance Tube measurement on a laboratory sample of the treatment. The inside diameter of the Plunker tube used in these measurements was 17.78 mm. This size was regarded sufficiently large to give a measurement of impedance on a statistically significant area of the panel. It was also sufficiently small compared to the radius of curvature of the treatment

115

surfaces which could be regarded essentially flat over the area of the tube. It also ensured minimum leakage of sound between the Plunker and the face sheet due to imperfect seal caused by the curvature of the treatment surface. Separate calibrations of the Plunker were required for the outer and the inner sections due to significant differences in the curvatures of their surfaces which affected the extent of leakage between the plunker and the treatment surface.

On each of the six segments of the outer and the three segments of the inner treatment sections, at least ten impedance measurements were obtained with the Plunker. During each measurement the plunker was simply placed on the location. Apart from its own weight, no additional pressure was applied. Care was taken that the axis of the plunker was normal to the surface of the treatment. Because of the curvature of the treatment surface the leakage of sound was a problem. A very small tilting of the axis of the Plunker from the normal caused significant leakage. This problem was particularly severe in the case of the inner treatment section. This leakage of sound affected the accuracy of the impedance data at lower frequencies (below 1500 Hz).

Figure 5.42 shows the results of the impedance survey of the outer treatment section. It is based on sixty different measurements. The standard deviation of the impedance data is quite small at 1500 Hz and 1900 Hz but at 1000 Hz the deviation in the data is much larger due to reasons mentioned above.

Figure 5.43 shows the results of the Plunker measurement on the inner section. As expected, the standard deviation of the resistance values measured on the inner section is larger than that on the outer section. Moreover the resistance values below 1500 Hz are lower than expected due to sound leakage.

Plunker measurements also confirmed that the In-Situ measurement on cavity J of the inner treatment section is representative of the impedance of
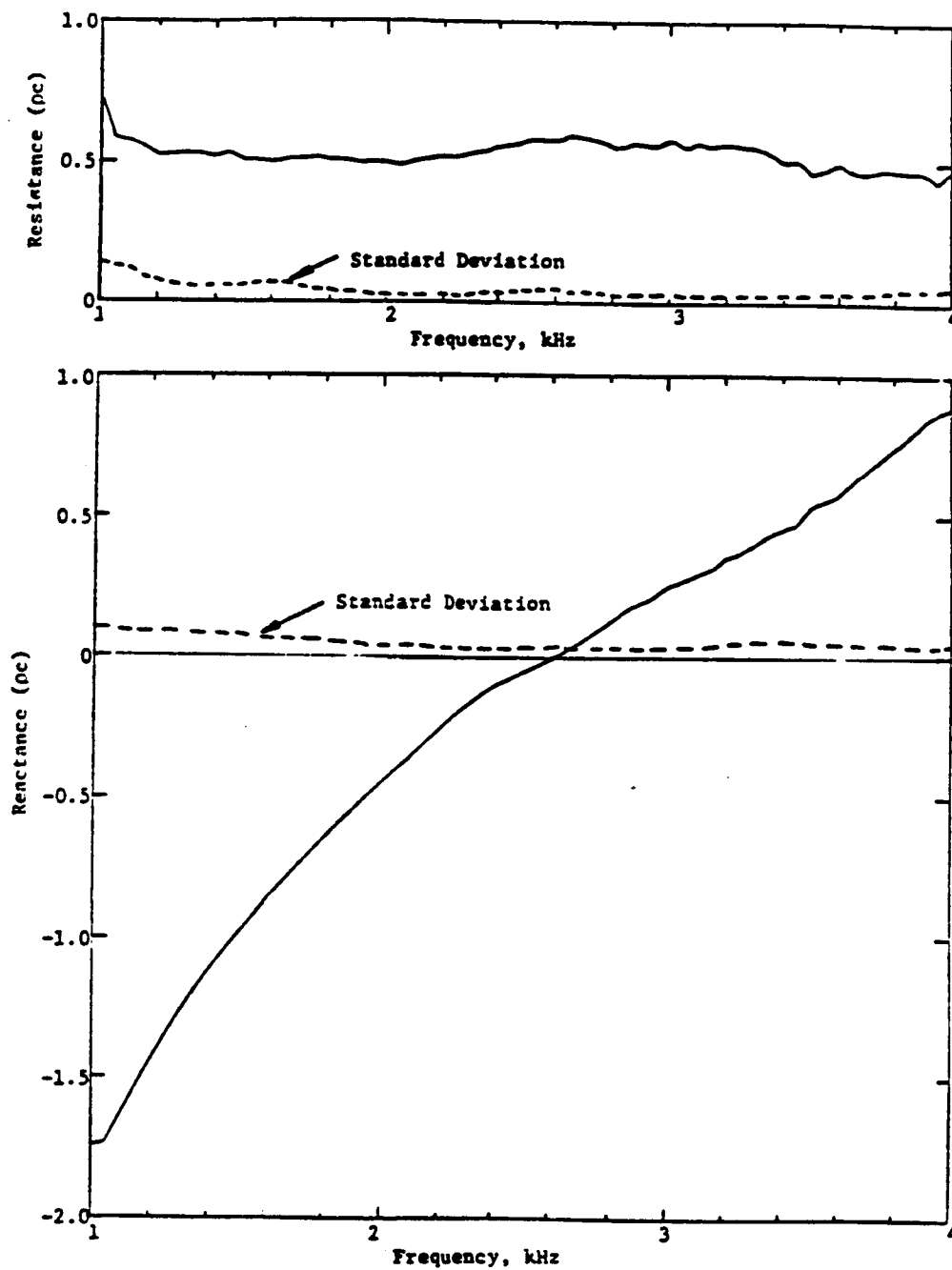
Figure 5.42. Impedance Survey of the Outer Treated Section of the Aft Duct Based on 60 Different Plunker Measurements Over Its Surface

TABLE 5.7

Average Normal Impedance of the Acoustic
Treatment Hardware
(OASPL ≈ 140 dB)

Frequency Hz	Resistance (ρc)	Reactance (ρc)
1000	.51	-1.82
1500	.51	-1.0
1900	.51	- .55
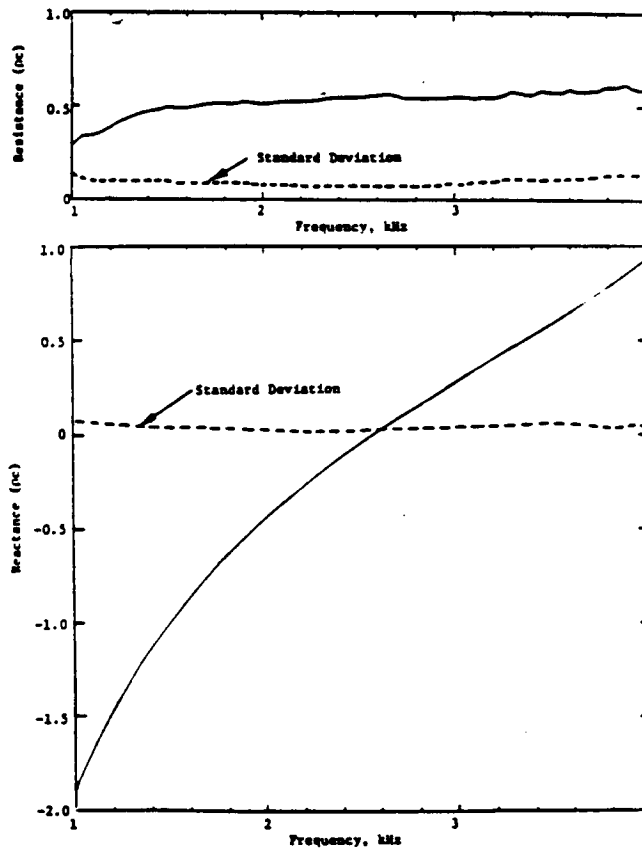
Figure 5.43. Impedance Survey of the Inner Treated Section of the Aft Duct Based on 30 Different Measurements Over Its Surface

118

the entire panel and is midway between the In-Situ measurement results on cavities H and J. The Plunker results show lower frequency dependence than the In-Situ data.

In the light of the Plunker measurements the following conclusions may be drawn.

1. The averaged impedance of the outer treatment section is approximately equal to that of the inner section.

2. The treatment impedance is uniform over the entire surface within the limits of manufacturing tolerances.

It was decided that the averaged acoustic impedance values obtained by the Plunker at the frequencies of interest should be used in the theory-experiment check. These values are presented in Table 5.7. The In-Situ measurements had shown that the resistance of the treatment was essentially constant between 1000 Hz and 2000 Hz. In view of this, the resistance at 1000 Hz was assumed to be the same as that at 1500 Hz. It should also be noted that the Plunker measurements were obtained with an OASPL of 140 dB (approximately) at the treatment surface. As the in-duct sound levels during the tests at Schenectady were significantly lower, appropriate corrections to the resistance values would be required.- In addition corrections should be made for the effects of grazing flow. The following approach is suggested: Using the sound intensity correlation of Figure 5.38 and the average impedance at 140 dB from Table 5.7, the no-flow resistance at 130 dB is approximatey 0.44 ρc. To this should be added the grazing flow effect from Figure 5.39a. The reactance values of Table 5.7 should only be corrected for flow effects using Figure 5.39b.

6.0 THEORY-EXPERIMENT COMPARISON

The annular duct suppression prediction program based on the modal analysis described in Section 4.1 was used to predict the suppression due to the treatment in the Rotor-55 exhaust duct for all three test RPMs. The theoretical predictions are compared with the measurements in this section. The physical phenomenon of propagation in segmented ducts is discussed with reference to this theory-experiment comparison.

6.1   INPUT TO PREDICTION PROGRAM

The exhaust duct was modeled as a three segment straight annular duct with the treated segment placed between two hardwall segments. The lengths of the hardwall segments were taken to be the distances of the mode measurement planes from the treated segment. The effective length of the treated segment was found to be 0.23 meters (L/H = 1.8) after accounting for the hole blockage at segment ends and treatment panel interfaces.

The principal input parameters for the program are the duct geometry, the mean flow conditions, the acoustic frequency, the inner and outer wall impedances (or admittances) for all segments, the spinning mode order, the radial mode distribution of the acoustic source and the reflection characteristics of the duct termination. The mode coefficients of the forward traveling modes measured at the upstream plane (or the "source" plane) and the mode coefficients of the backward traveling modes measured at the downstream plane (or the "termination" plane) were used to specify $\{Q_s\}$ and $\{Q_T\}$ respectively. As mentioned in Section 4.1.2 this required that $[R_s] = 0 = [R_T]$. For the blade passage frequencies corresponding to the rotor RPMs in the test, a maximum of two radial modes (i.e., n=0 and n=1) were expected to be cut-on in the hardwall segment of the duct. While utilizing the prediction program, however, a minimum of four radial modes (i.e., n=0, 1, 2, 3) were considered to participate in the transmission and redistribution of acoustic energy in the duct. The acoustic impedance of the treatment in the duct was initially assumed to be equal to the average normal impedance measured in the absence of flow using the acoustic Plunker (Section 5.3.3).

With these input parameters the program calculates the eigenvalues, the axial propagation constants (for both forward and backward propagating modes), the uniform section transmission matrices for each duct segment, and the reflection and transmission matrices of the segment interfaces. The program then sets up the stacked system matrix equation and solves it to obtain the forward and backward complex mode coefficients and modal energy fluxes at each plane. The net energy flux at each plane and the overall PWL suppression are then calculated.

6.2   IN-DUCT SUPPRESSIONS

Mode coefficients obtained from the in-duct measurements and based on the assumption of uniform mean flow in the duct were first used in the predictions.

Table 6.1 lists the measured and predicted in-duct suppressions for the fan-stator interaction modes at the three blade passage frequencies corresponding to the test conditions. These suppression values represent the difference in the forward energy fluxes between the downstream and upstream measurement planes. The effect of reflections from the nozzle is taken into account by specifying the backward traveling mode coefficients at the downstream plane. The predicted suppressions can be seen to be in good agreement with the measured suppressions for all three frequencies and for both spinning mode orders. The largest difference between the predicted and measured suppressions is 2.7 dB which is not large compared to the measured suppression of 16.8 dB at that condition. Notice that six radial modes were used in the prediction for m = 7 case (for reasons discussed later in this section) while only 4 radial modes were used for m = 0-1.

The predicted and measured mode coefficient distributions of forward propagating acoustic energy at the downstream plane are compared in Figures 6.1 through 6.4 for the four cases listed in Table 6.1. The magnitude as well as the phase of the measured mode coefficients can be seen to be in good

122

Table 6.1. Comparison of Measured Suppressions With Theoretical Predictions

Uniform Flow

FREQUENCY (Hz)	SPINNING MODE (m)	NO. OF RADIAL MODES	TREATMENT IMPEDANCE	IN-DUCT SUPPRESSION, ΔdB_f	
				MEASURED	PREDICTED
1,000	-1	4	0.51-1.82i	2.18	1.40
1,500	-1	4	0.51-1.00i	3.72	4.29
1,900	-1	4	0.51-0.55i	16.83	14.10
1,900	7	6	0.51-0.55i	22.587	24.32

Figure 6.1. Measured and Predicted Complex Mode Amplitudes at the Downstream Plane – Forward Propagating Modes – 1000 Hz, m = -1, M = 0.21, Uniform Flow, Soft Wall
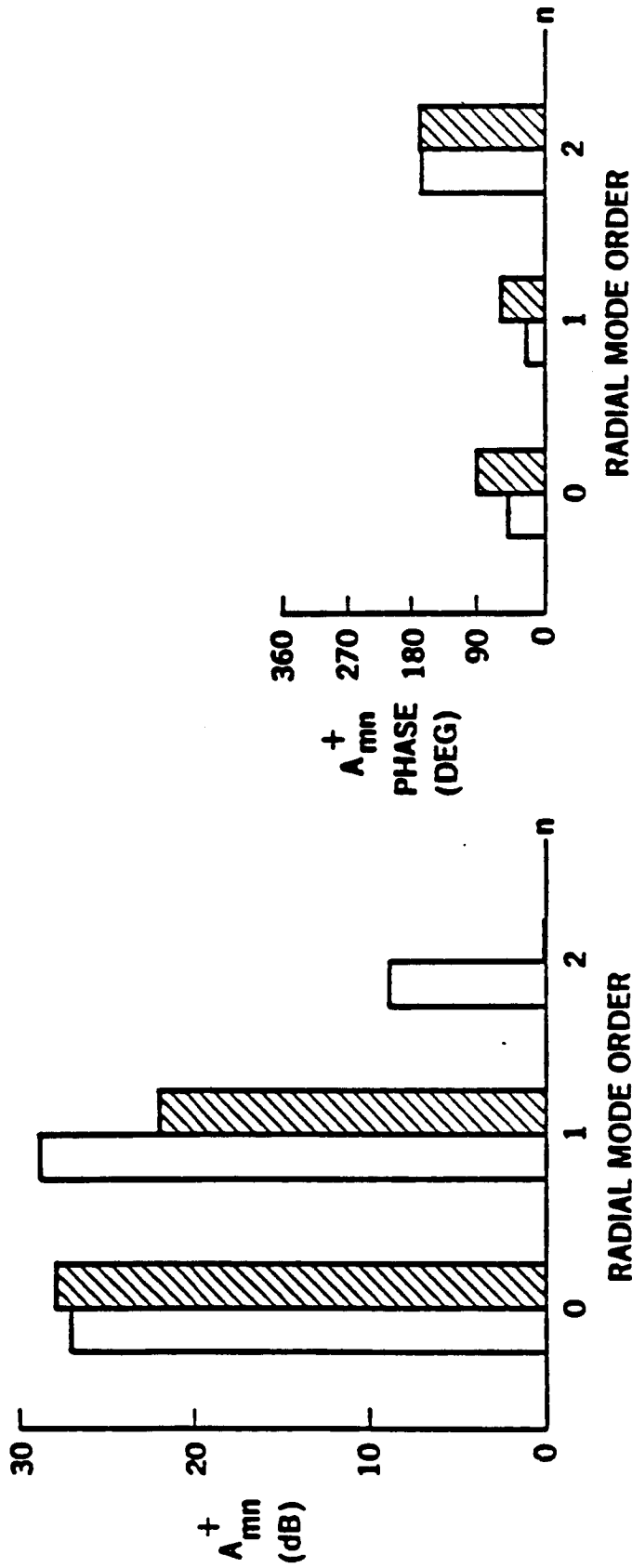
Figure 6.2. Measured and Predicted Complex Mode Amplitudes at the Downstream Plane –
Forward Propagating Modes – 1500 Hz, m = -1, M = .32, Uniform Flow, Soft Wall
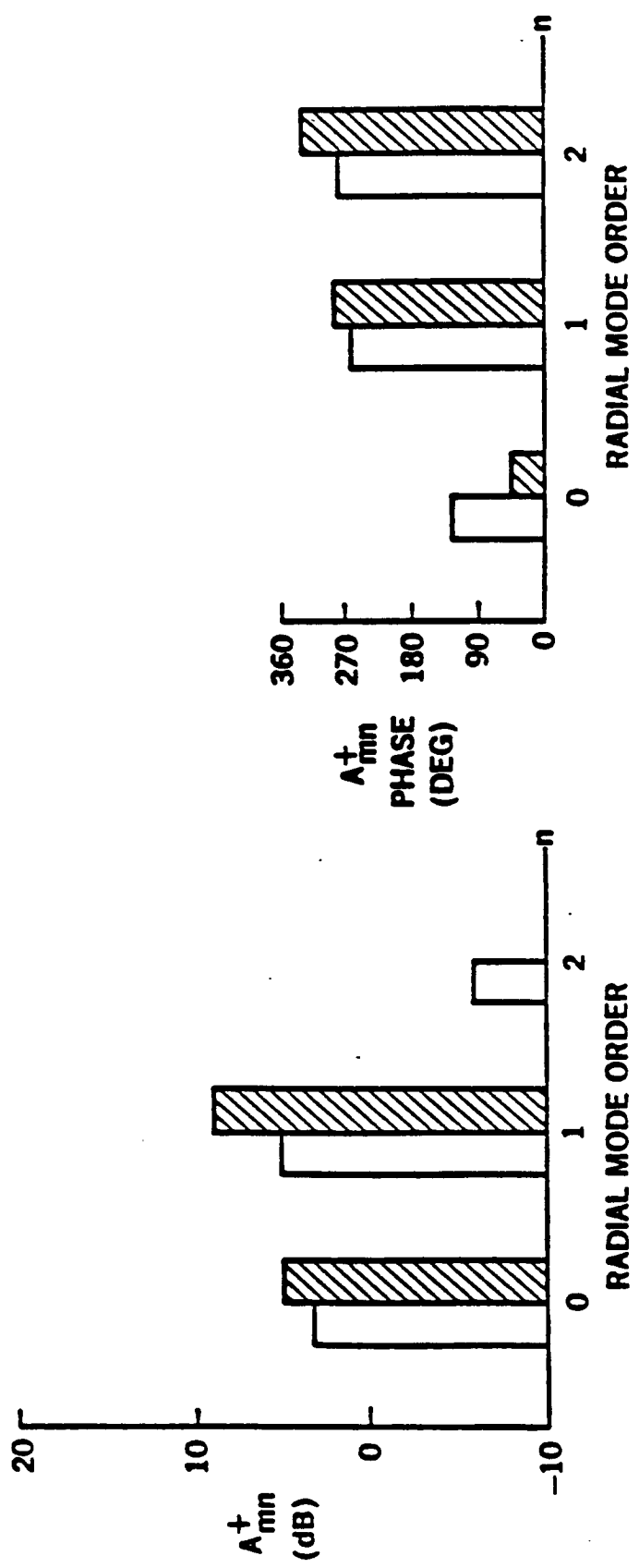
Figure 6.3. Measured and Predicted Complex Mode Amplitudes at the Downstream Plane – Forward Propagating Modes – 1900 Hz, m = -1, M = 0.4, Uniform Flow, Soft Wall
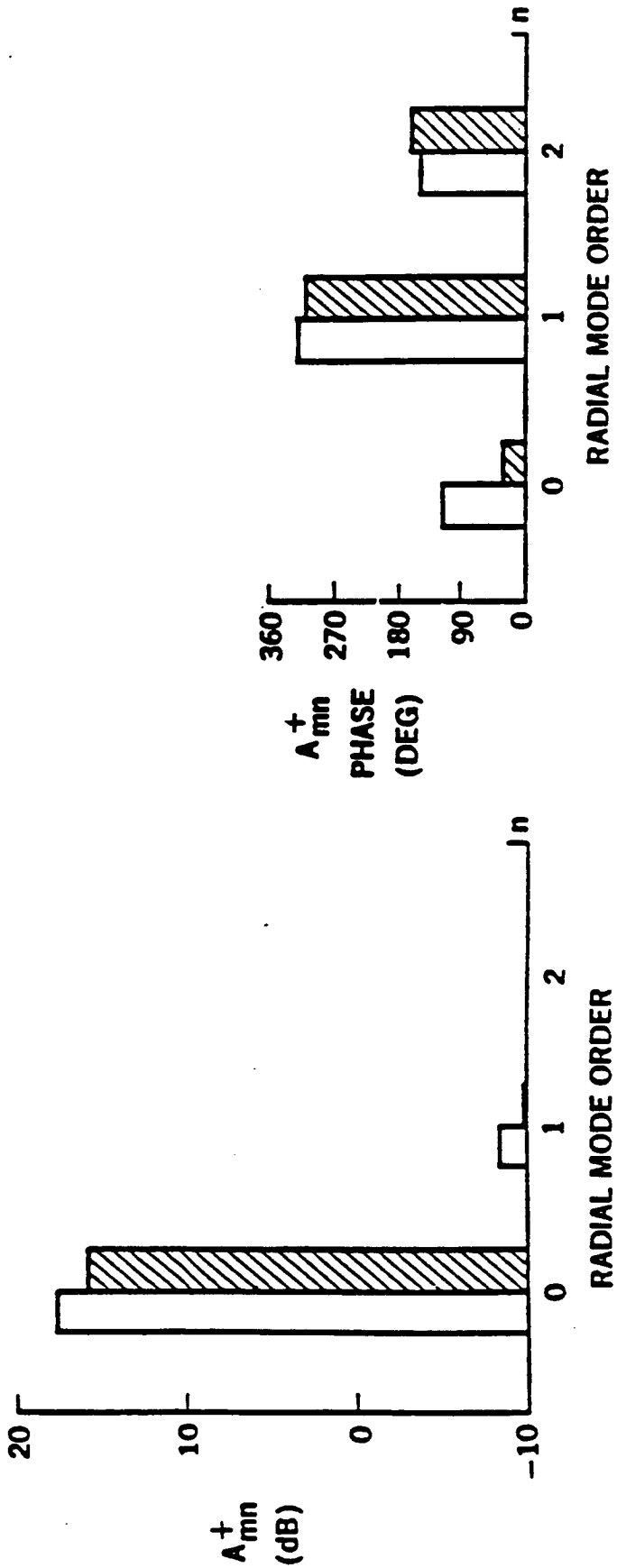
Figure 6.4. Measured and Predicted Complex Mode Amplitudes at the Downstream Plane – Forward Propagating Modes – 1900 Hz, m = 7, M = 0.4, Uniform Flow, Soft Wall

agreement with the predicted values for the cut-on modes. For m = -1 at 1000 Hz and for m = 7 at 1900 Hz the higher order radial modes (n > 0) are theoretically cut-off in the hardwall duct. This causes the predicted amplitudes of these modes at the downstream location to be several dB lower than the predicted amplitude of the first radial mode. The measurements also show the amplitudes of the higher order modes to be at least 10 dB lower than the amplitude of the cut-on mode. The difference in the measured and predicted values of the mode coefficients for cut-off modes will therefore have only a small effect on the total suppression in the duct.

Figures 6.5 through 6.8 compare the predicted values of the mode coefficients for the backward traveling modes at the upstream plane with the corresponding measured values. The comparison for the backward traveling modes is not as good as that for the forward traveling modes. For m = -1 at 1900 Hz (Figure 6.7), the predicted mode amplitude for the second radial mode (n=1) is much higher than the amplitude for the first radial mode (n=0). The measurements, however, show the n=0 mode to be slightly higher than the n=1 mode.

In utilizing the suppression prediction program, it is essential to check that the total acoustic energy is conserved across segment interfaces. The modal analysis requires the acoustic pressure and velocity at all radial locations to be continuous across segment interfaces. However, the pressures (and consequently the velocities) on the two sides of the interface are represented as expansions in sets of eigenfunctions which can be completely different on either side. If the set of eigenfunctions used is not mathematically complete, then the expansions, the pressure matching, and consequently the acoustic energy matching, can be in error. For the first three conditions listed in Table 6.1 the predicted acoustic energy across the segment interfaces in the rotor 55 duct was conserved within 0.1 dB. For the m = 7 mode at 1900 Hz, however, an energy mismatch of 2.5 dB was observed at the downstream segment interface. This mismatch was reduced to 1.2 dB and 1.0 dB by including 6 and 8 radial modes respectively in the analysis. Assessment of the effects of including radial modes of order higher than this was prevented by limitations in the size of the computer program.
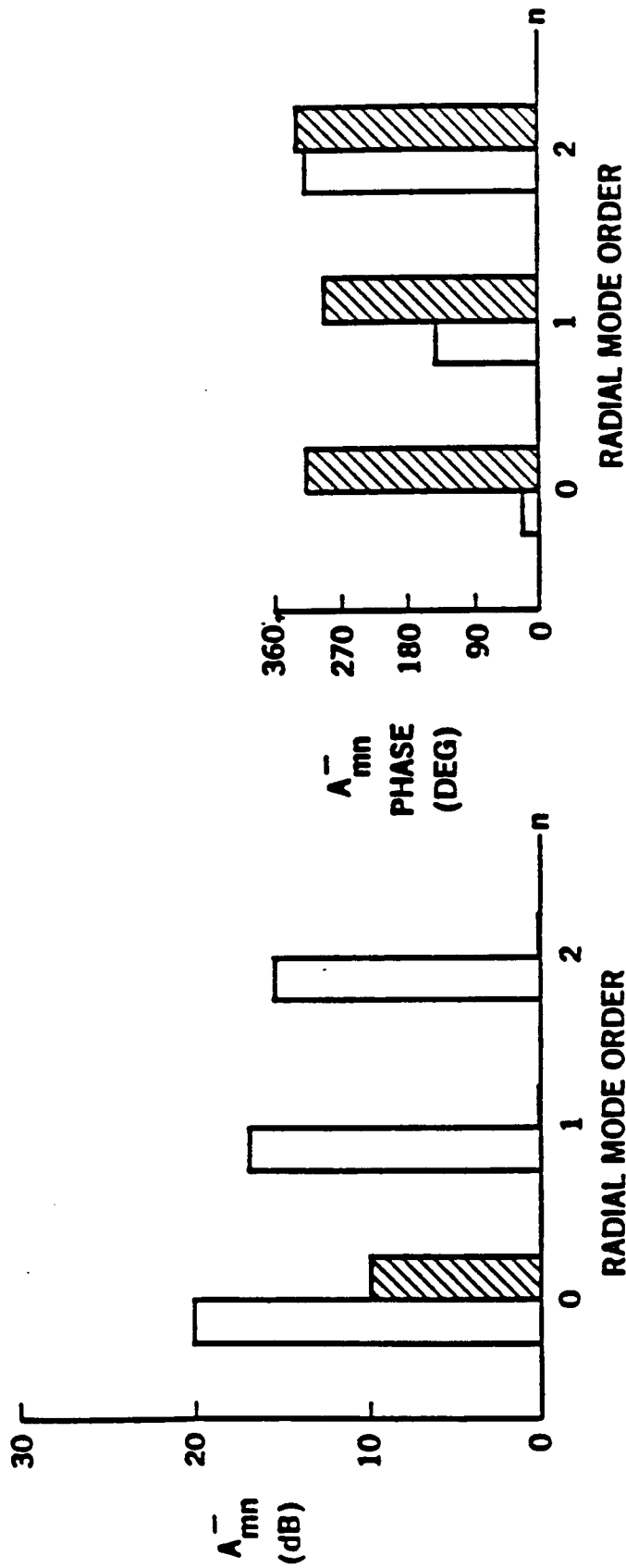
Figure 6.5. Measured and Predicted Complex Mode Amplitudes at the Upstream Plane -
Backward Propagating Modes - 1000 Hz, m = -1, M = .21, Uniform Flow, Soft Wall

129
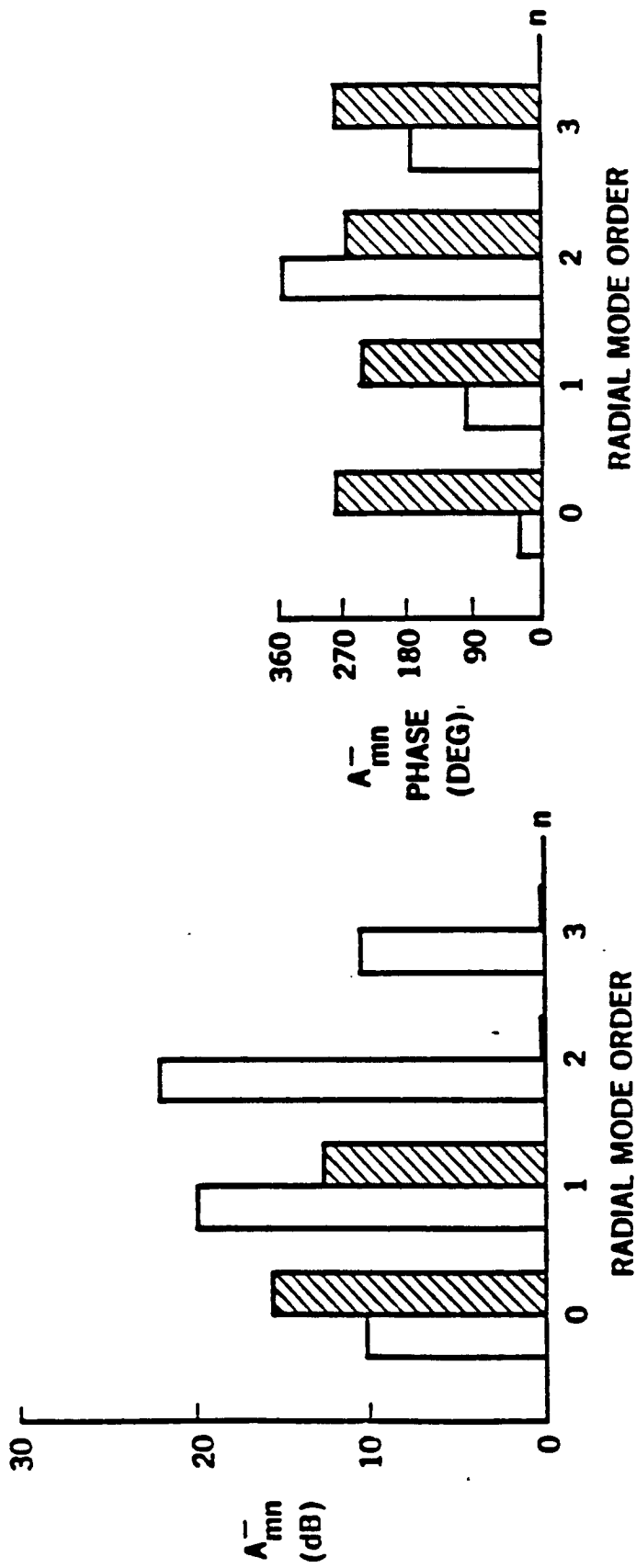
Figure 6.6. Measured and Predicted Complex Mode Amplitudes at the Upstream Plane – Backward Propagating Modes – 1500 Hz, m = -1, M = .32, Uniform Flow, Soft Wall
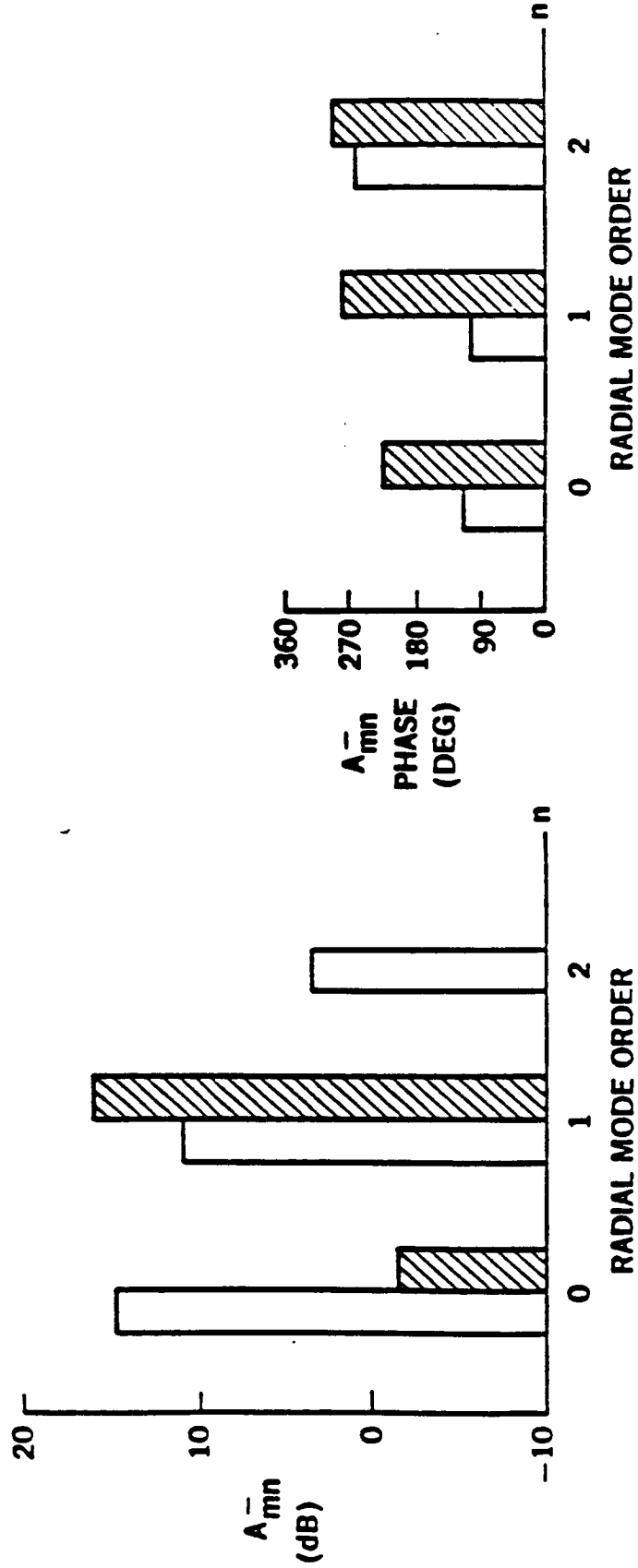
Figure 6.7. Measured and Predicted Complex Mode Amplitudes at the Upstream Plane — Backward Propagating Modes — 1900 Hz, m = -1, M = .4, Uniform Flow, Soft Wall

131
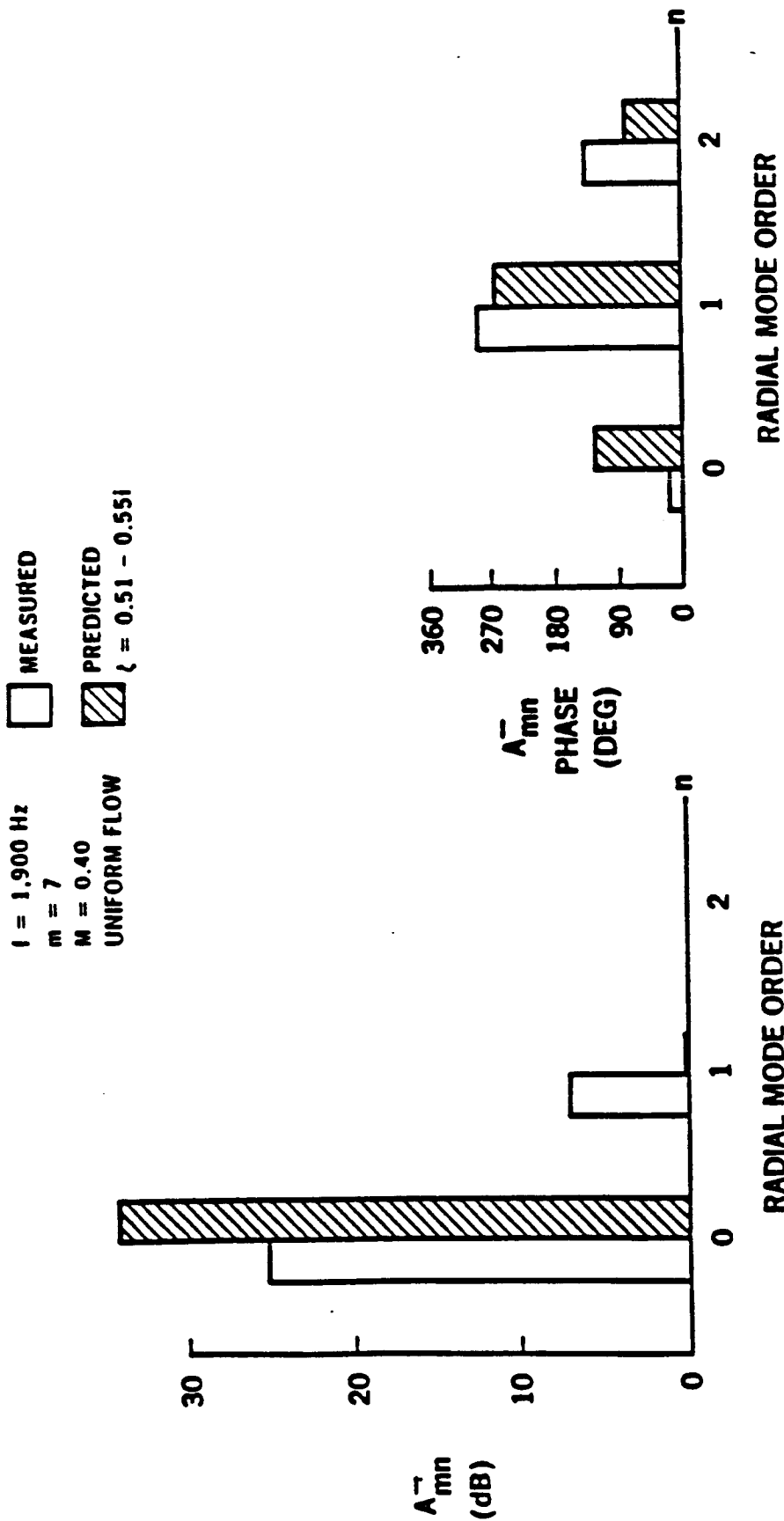
Figure 6.8. Measured and Predicted Complex Mode Amplitudes at the Upstream Plane —
Backward Propagating Modes, 1900 Hz, m = 7, M = 0.4, Uniform Flow, Soft Wall

Figure 6.9 shows the predicted mode coefficients (for both forward and backward propagating modes) at the end planes of the hardwall and treated segments for m = -1 modes at 1000 Hz. At this frequency only the lowest order radial mode (n=0) is cut-on in the hardwall duct. Consequently the forward propagating higher order modes (n > 0) at the "source" plane i.e., plane 1, are suppressed to very low values at plane 2 just upstream of the treated segment. Downstream of the hardwall/treatment interface i.e., at plane 3, the mode coefficient distributions shown are required to match the energy at plane 2. Notice that a combination of forward modes n = 0, 1, 2 and backward modes n = 0, 1 at plane 3 in the treated segment is able to match the energy carried by the combination of forward mode n = 0 and backward modes n = 0 and n = 2 at plane 2 in the hardwall segment. Thus a redistribution of mode coefficients takes place at the segment interface. This is due to the fact that the radial profiles of acoustic pressure and velocity at the interface are expressed as a summation of hardwall eigenfunctions at plane 2 and as a summation of softwall eigenfunctions at plane 3. A similar mode coefficient redistribution takes place at the downstream treatment/hardwall interface.

For m = 7 at 1900 Hz most of the incident energy is contained in only one radial mode (n = 0) that is close to cut-off (see Figure 6.10). This mode has a cut-off ratio equal to 1.1. Upon incidence to the upstream hardwall/treatment interface this mode is reflected into several higher order backward traveling modes. The backward modes at plane 2 in the hardwall can be identified as due to reflection of forward modes at the same plane and not as redistribution of backward modes at plane 3 in the treated segment because the latter have near zero amplitudes as shown. Thus the acoustic energy carried by the combination of the n = 0 forward mode and the backward modes of several higher orders in the hardwall segment must be matched by distribution of energy mostly in the forward modes in the treated segment. The backward modes at plane 3 are small in amplitude because of the high suppression in the treatment. At the downstream treatment/hardwall interface the reflection of the n = 0 forward mode in the treated segment into several higher order backward traveling modes can be observed.
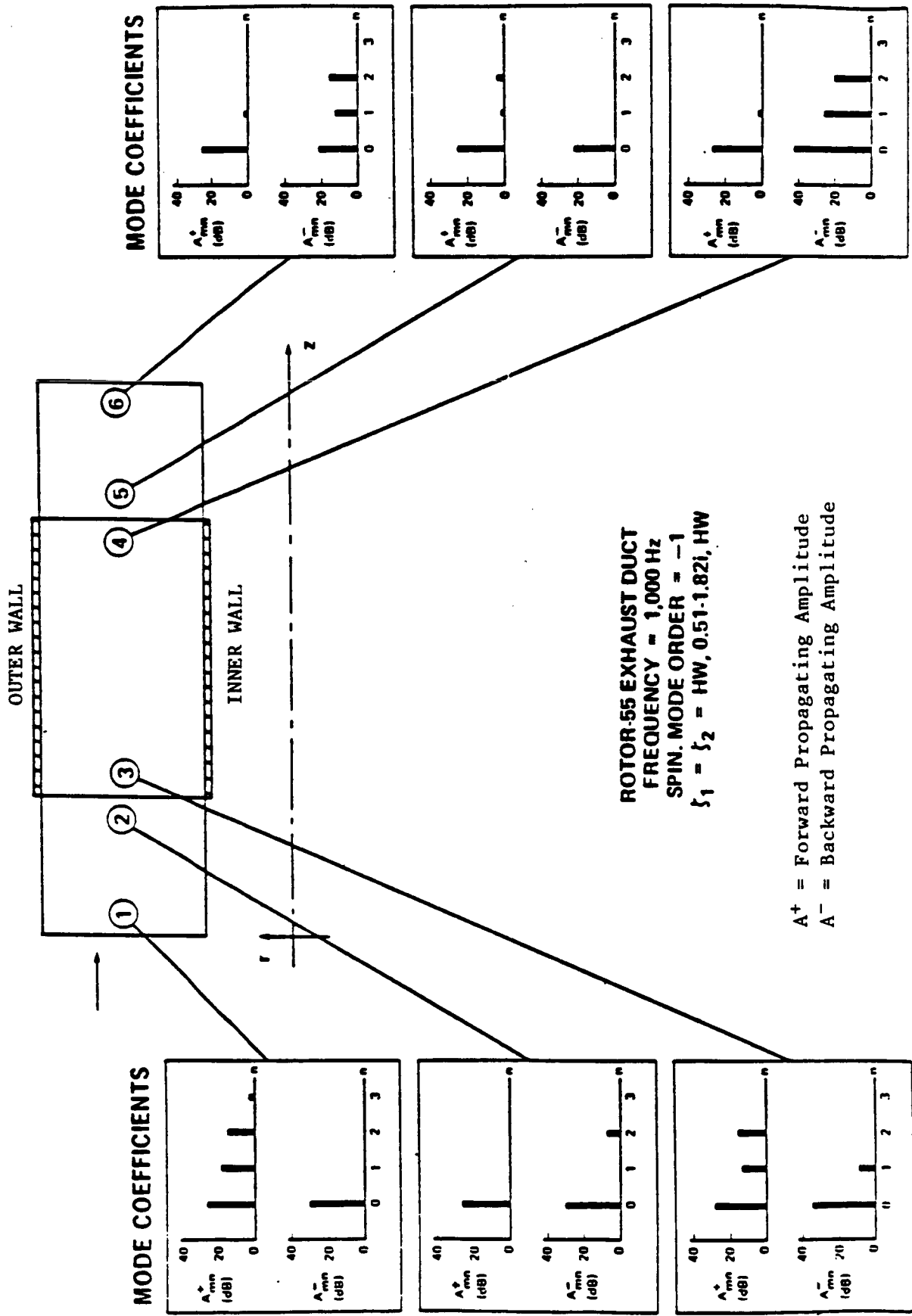
Figure 6.9. Predicted Mode Distributions at Segment End Planes – 1000 Hz. $m = -1$, $M = 0.21$

134

Figure 6.10. Mode Distribution at Segment End Planes – 1900 Hz, m = 7, M = 0.4

135

It is felt that this combination of high reflection and suppression of the near cut-off mode causes the problem of energy mismatch at segment interfaces. The mismatch is reduced by including higher order radial modes in the analysis. Since these modes are "cut-off" they are highly suppressed even in the hardwall segments of the duct. Their contribution to the total acoustic energy at the "source" and "termination" planes is therefore negligible and the in-duct suppression based on the forward energies at these planes does not change much.

6.3   EFFECTS OF SHEARED FLOW

As mentioned in Section 5.2.3, the mean flow in the Rotor 55 exhaust duct was far from uniform. In addition to the radial variation of velocity due to the thick boundary layers at the duct walls, a periodic circumferential variation of the mean velocity due to the persistent stator wakes was also observed. It is not possible to account for the circumferential variations in the prediction of suppression without considerably modifying the analysis. An attempt was, however, made to account for the thick boundary layers by using the analysis described earlier for thin boundary layers. Sheared flow eigenvalues were determined by using the measured velocity profile in the integration of the governing differential equation across the duct annulus. The eigenvalues and the acoustic pressure mode shapes obtained during this integration process were used to obtain the sheared flow mode coefficients from the mode probe measurements. These mode coefficients were used in the suppression prediction program to obtain estimates of the suppressions due to the treatment in the duct.

Table 6.2 compares the measured in-duct suppressions with the suppressions predicted using the sheared flow mode coefficients for the same conditions as in Table 6.1. For the m = -1 mode at 1500 and 1900 Hz the two suppression values can be seen to be in good agreement. Furthermore, the measured values differ from the corresponding values in Table 6.1 by at most 3.2 dB. For the spinning mode m = 7 at 1900 Hz the in-duct measured suppression based on the sheared flow mode coefficients is very similar to the measured suppression based on the uniform flow mode coefficients. The predicted and the measured suppressions based on the sheared flow mode

136

Table 6.2. Comparison of Measured and Predicted In-Duct Suppressions
Based on Sheared Flow Mode Coefficients

FREQUENCY (Hz)	SPINNING MODE (m)	NO. OF RADIAL MODES	TREATMENT IMPEDANCE	IN-DUCT SUPPRESSION, ΔdB_f	
				MEASURED	PREDICTED
1,000	-1	4	0.51-1.82i	5.36	1.60
1,500	-1	4	0.51-1.00i	5.32	5.28
1,900	-1	4	0.51-0.55i	18.96	17.10
1,900	7	6	0.51-0.55i	22.29	28.08

coefficients for this case, however, do not compare as well as those based on the uniform flow mode coefficients. This is due to the large mismatch of energy in the prediction routine at segment interfaces for the sheared flow case. In fact even for the cases where the measurement and prediction agree (i.e., m = -1 mode at 1500 Hz and 1900 Hz), the energy conservation at the segment interfaces is off by up to 0.8 dB. It is believed that this is due to the assumption in the analysis that the complex acoustic pressure profile in the duct in the presence of non-uniform flow can be expanded in terms of the uniform flow eigenfunctions. This assumption is valid only for thin boundary layers and can introduce large errors in highly sheared flows. Furthermore the expression for acoustic intensity (equation 4.39) is valid only for uniform flow.

In an attempt to improve the energy conservation at segment interfaces in the presence of sheared flow, the program was modified so that the acoustic pressure mode shapes generated numerically during the determination of sheared flow eigenvalues are used in the modal analysis instead of the uniform flow eigenfunctions. This modification did not introduce a consistent improvement in the energy conservation at segment interfaces. It was, therefore, not pursued further.

6.4 SENSITIVITY OF SUPPRESSION TO TREATMENT IMPEDANCE

All the predicted suppressions presented so far are based on the average normal acoustic impedance of the treatment panels measured at 140 dB in the absence of flow (see Section 5.3.3). Treatment impedance is known to change due to the presence of flow (and boundary layer) over the treatment and also with changes in sound pressure level in the duct (see References 19 and 4). Results of the experimental attempts to assess the flow and SPL effect on the acoustic impedance of the treatment used in Rotor-55 exhaust duct are described in Section 5.3.2. The average SPL in the Rotor-55 exhaust duct was in the range 125-135 dB. This will cause the resistance of the treatment to be lowered relative to the value at 140 dB. However, the grazing flow over the treatment will cause the resistance to increase. The treatment reactance

was observed to become less negative due to the presence of flow. It was estimated that the treatment resistance and reactance under the test conditions will be within 0.1 ρc of the average normal impedance values. Table 6.3 (for uniform flow condition assumptions) shows that by varying the treatment impedance within this limit the predicted in-duct suppression can be brought into excellent agreement with the measured suppression.

The sensitivity of the predicted suppression to the treatment impedance was established by changing the resistance and reactance over a range of values close to the averaged measured value. The results for m = -1 mode in the presence of sheared flow are plotted in Figures 6.11, 6.12 and 6.13 for f = 1000, 1500 and 1900 Hz respectively. At 1000 Hz the suppression is almost equally sensitive to changes in resistance and reactance, varying by about 1 dB over 0.4 ρc. At 1900 Hz the predicted suppression is extremely sensitive to the reactance and even a change of 0.1 ρc in reactance can change the suppression by 4 dB. The sensitivity to resistance is not that high, but greater than the sensitivity at 1000 and 1500 Hz. In Figure 6.13 there is also an indication of a local peak in the suppression curve at R = 0.45 ρc.

6.5   FAR FIELD SUPPRESSION

The acoustic field radiated from the exhaust duct was measured in the far field at all three rotor speeds for the two cases: a) all hardwall segments in the duct and b) one treatment segment in the duct. By integrating the SPL directivities (at the blade passage frequency) for the treated duct and the hardwall duct and taking the difference we can obtain a power level (PWL) suppression due to the treatment. Table 6.4 lists the power level suppressions and the uniform-flow in-duct suppressions for all three frequencies. At 1000 Hz and 1500 Hz, m = -1 is the only rotor-stator interaction mode generated in the duct. At these frequencies significant energy is carried by the (-1,0) mode. This mode is well cut-on at both frequencies and will have a peak lobe of radiation in a direction close to the duct axis. The jet flow exhausting from the duct termination (i.e., nozzle), however, will introduce refraction effects and cause the peak lobe to move

Table 6.3. Sensitivity of Predicted Suppressions To Treatment Impedance

Uniform Flow

FREQUENCY (Hz)	SPINNING MODE (m)	NO. OF RADIAL MODES	TREATMENT IMPEDANCE	IN-DUCT SUPPRESSION, ΔdB_f	
				MEASURED	PREDICTED
1,000	-1	4	0.51-1.82i	2.18	1.40
			0.51-1.65i	2.18	1.77
			0.60-1.82i	2.18	1.60
1,500	-1	4	0.51-1.00i	3.72	4.29
			0.40-1.00i	3.72	3.73
1,900	-1	4	0.51-0.55i	16.83	14.10
			0.51-0.45i	16.83	16.71
			0.60-0.55i	16.83	14.54
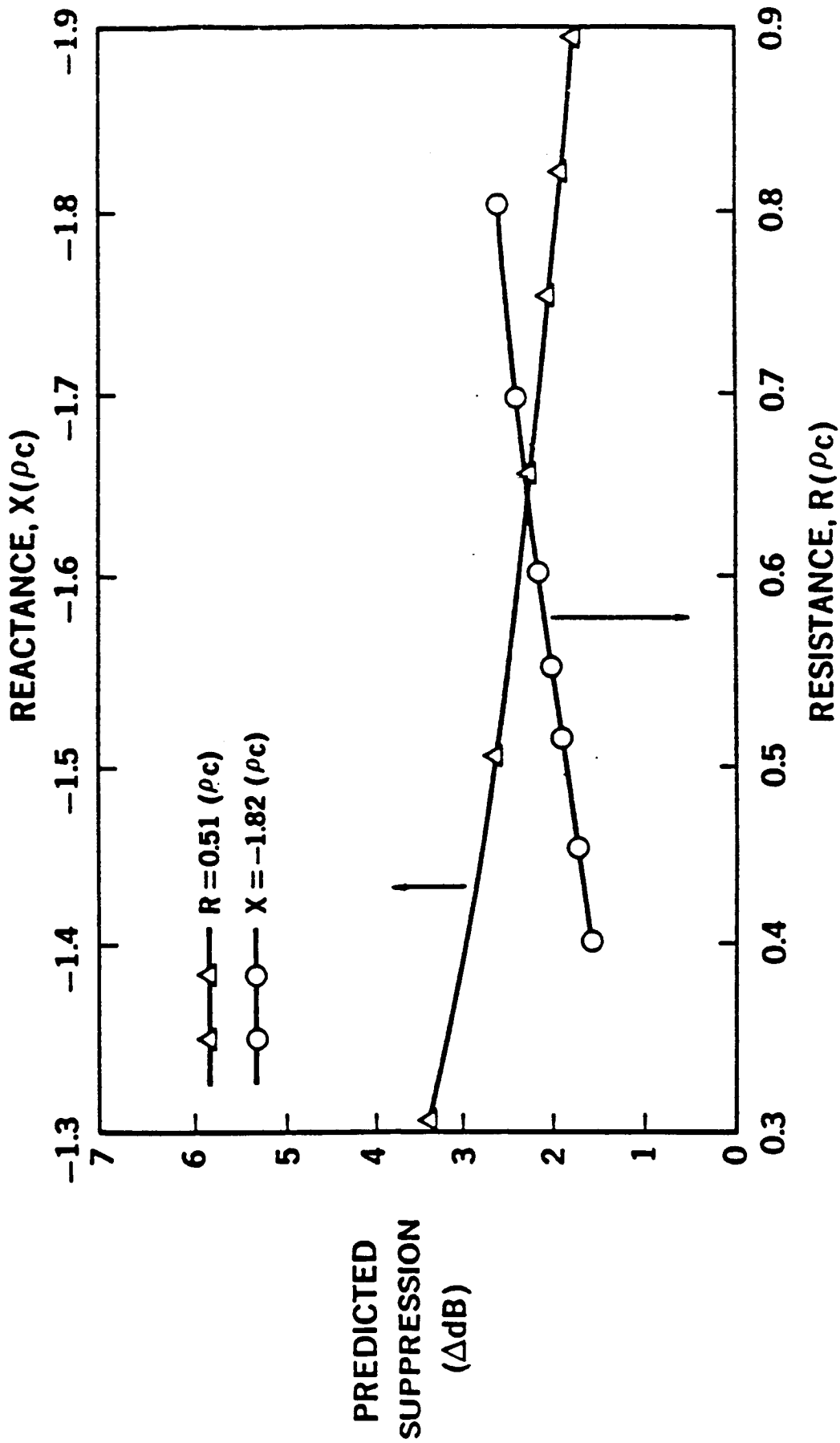
Figure 6.11. Sensitivity of Suppression to Treatment Resistance and Reactance – 1000 Hz; m = -1, n = 0,1,2,3; M = .21 Sheared Flow
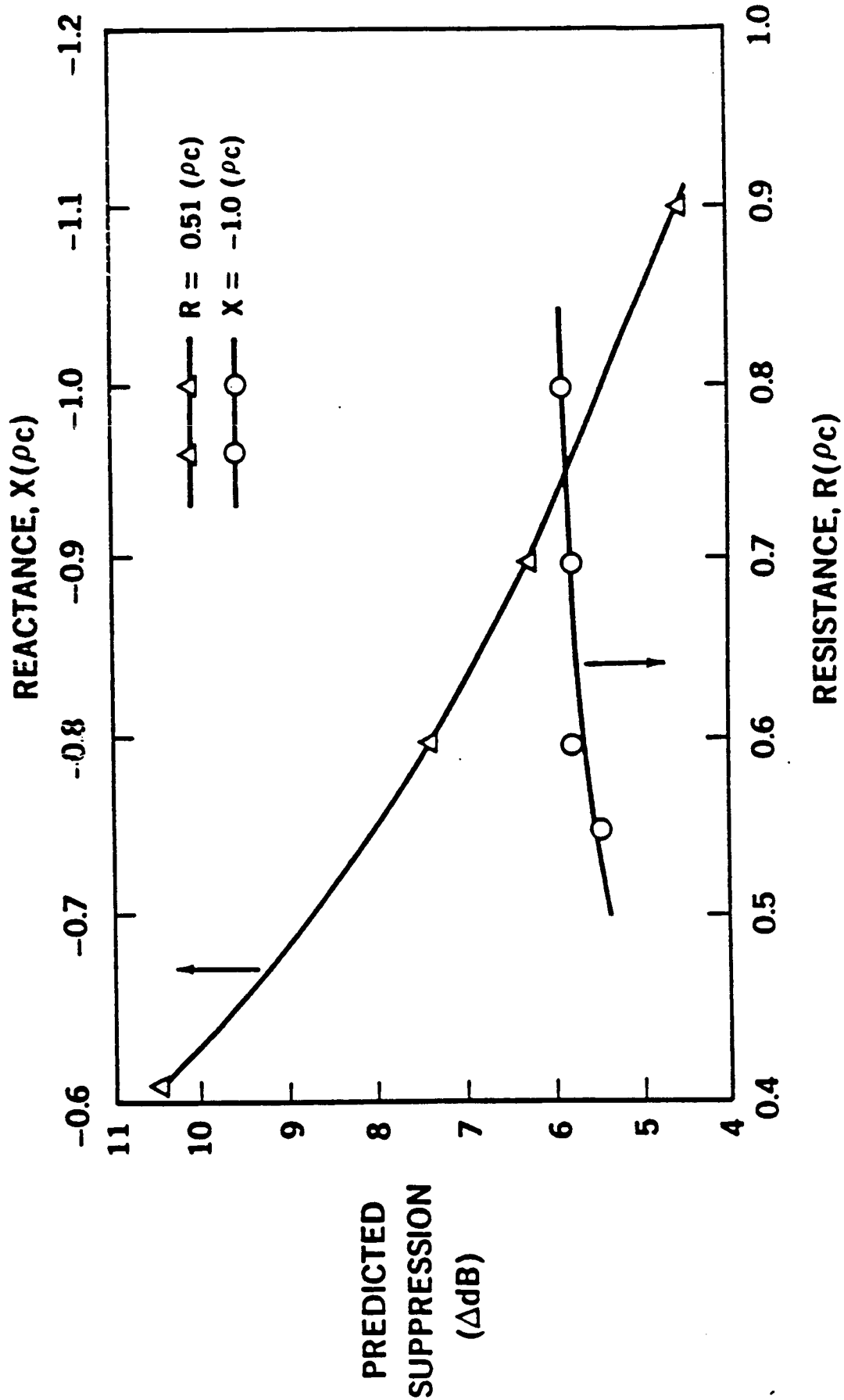
Figure 6.12. Sensitivity of Suppression to Treatment Impedance – 1500 Hz; m = -1; n = 0,1,2,3; M = .32; Sheared Flow
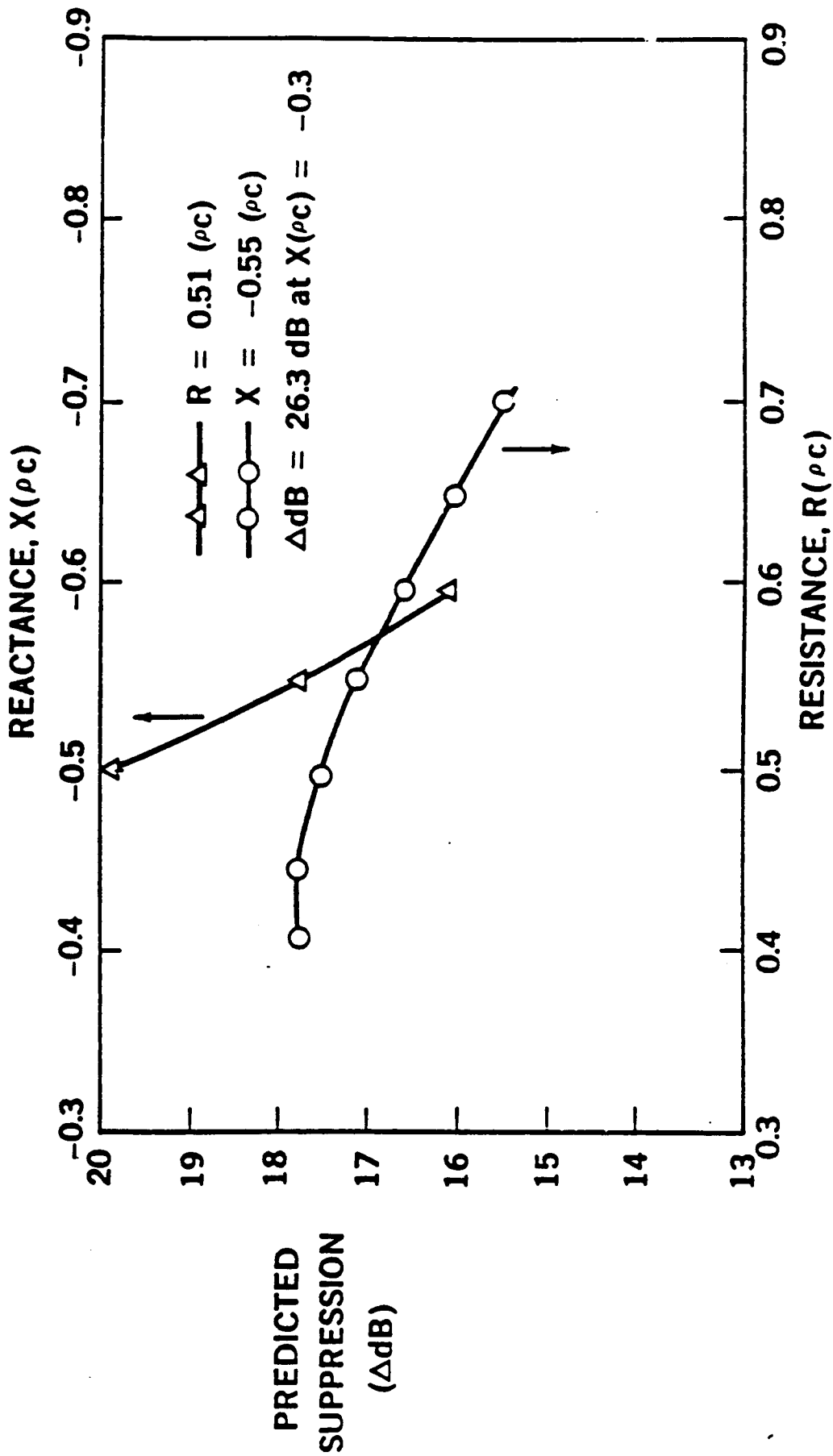
Figure 6.13. Sensitivity of Suppression to Treatment Resistance and Reactance – 1900 Hz; m = -1, n = 0,1,2,3; M = .4; Sheared Flow

Table 6.4. Comparison of In-Duct Suppressions With PWL
Suppressions From Far-Field Data

Uniform Flow

FREQUENCY (Hz)	SPINNING MODE	SUPPRESSION, ΔdB		
		IN-DUCT PREDICTED	IN-DUCT MEASURED	ΔPWL FROM FAR-FIELD DATA
1,000	-1	1.40	2.18	1.2
1,500	-1	4.29	3.72	4.2
1,900	-1	14.10	16.83	
1,900	7	24.32	22.58	10.3

away from the duct axis. Far-field measurements in the sector covering 20° through 110° should be able to capture the peak lobe of radiation and PWL suppressions based on far-field radiation pattern should be representative of the in-duct suppression due to the treatment (assuming the reflection at the nozzle to be of the same order for both hardwall and treatment cases). In Table 6.4, the PWL suppression (based on far-field data) can be seen to be of the same order as the in-duct suppression at 1000 and 1500 Hz.

At 1900 Hz, the interaction modes $m = 0-1$ and $m = 7$ coexist, with the latter carrying a greater part of the energy. A good percent of this energy is, however, reflected back into the duct at the nozzle termination. Measurements in the downstream hardwall section showed the backward energy in the m=7 modes to be only 4 dB below the forward energy. For the $m = -1$ modes this difference was found to be nearly 10 dB. The (7,0) mode has a cut-off ratio near 1.1 and a peak lobe of radiation almost normal to the duct axis. The refractive effects of the jet will move the peak lobe to even higher angles. This can cause the far-field measurement field (20° thru 110°) to miss part of the radiated energy. The $m = -1$ mode will, as in the case of lower frequencies, radiate at a smaller angle to the duct axis. The multi-modal PWL suppression (from far-field data) is 10.3 dB compared to the measured in-duct suppression values of 16.8 and 22.5 dB for the $m = -1$ and $m = 7$ modes respectively. Further examination of the causes for the variations in these numbers is required.

6.6   NOZZLE REFLECTION CHARACTERISTICS

In Section 4.1.3 a method for measuring the reflection matrix of the nozzle $[R_T]$ was outlined. It was pointed out that all the elements of the reflection matrix (including the off-diagonal terms representing the mode scattering) can be determined by measuring the forward and backward mode distributions just upstream of the nozzle for different distributions of the incident modes. For the rotor-55 exhaust duct, in-duct measurements were made with and without the treatment segments in the ducts. The mode distribution incident to the nozzle for the all hardwall segment configuration is different

from the mode distribution for the one treated segment configuration. Mode coefficients measured in these two cases can be used to solve equation 4.41 and determine four elements (namely R_{00}, R_{01} R_{10} and R_{11}) for the nozzle reflection matrix. The first subscript of R represents the radial mode order of the reflected mode and the second subscript refers to the radial mode order of the incident mode.

Table 6.5 lists the nozzle reflection matrix elements based on the measured mode coefficients in the rotor-55 exhaust duct. No clear trend is evident from these numbers. For $m = 7$ modes at 1900 Hz, the reflection matrix element R_{01} can be seen to be very high. This points to the strong $n = 0$ backward mode near the nozzle for these conditions (Figure 6.10).

Theoretical prediction of the suppression due to treatment in the exhaust duct required the inclusion of higher order radial modes (at least four) in the analysis. This resulted in a nozzle reflection matrix with at least 16 elements. The larger matrix cannot be calculated from the available measurements. The nozzle reflection effects were therefore taken into account by setting $[R_T] = 0$ and specifying the backward mode coefficient vector for the "termination" vector $\{Q_T\}$.

6.7   MODE SHAPES AND EQUIVALENT IMPEDANCE

The predicted in-duct suppressions using the measured mode coefficients based on sheared flow eigenvalues and eigenfunctions were compared with the measured suppressions in Section 6.3. The calculations on which these predictions were based showed discontinuity of total acoustic energy across segment interfaces. It is believed that this is due to the assumption in the analysis that the complex acoustic pressure profile in the duct in presence of non-uniform flow can be expanded in terms of the uniform flow eigenfunctions.

Figure 6.14 shows a comparison of the acoustic pressure profile in the presence of sheared flow in the hardwall segment of the duct with the uniform flow eigenfunction shape based on the sheared flow eigenvalue. This and the

Table 6.5. Nozzle Reflection Coefficients (From Hardwall and
Treatment Case Data)

Freq. (Hz)	Spinning Mode Order	RT(0,0)	Reflection Matrix Elements		
			RT(0,1)	RT(1,0)	RT(1,1)
1000	-1	-0.635+0.583i	0.958-0.111i	-0.021+0.049i	-0.723+0.535i
1500	-1	-0.900-0.131i	0.544+0.525i	-0.278+0.469i	0.135+0.319i
1900	-1	0.544+0.491i	-0.394+0.308i	-0.628-0.151i	0.186+0.003i
1900	7	0.344+0.282i	-1.040-8.863i	-0.008-0.002i	0.379+0.599i
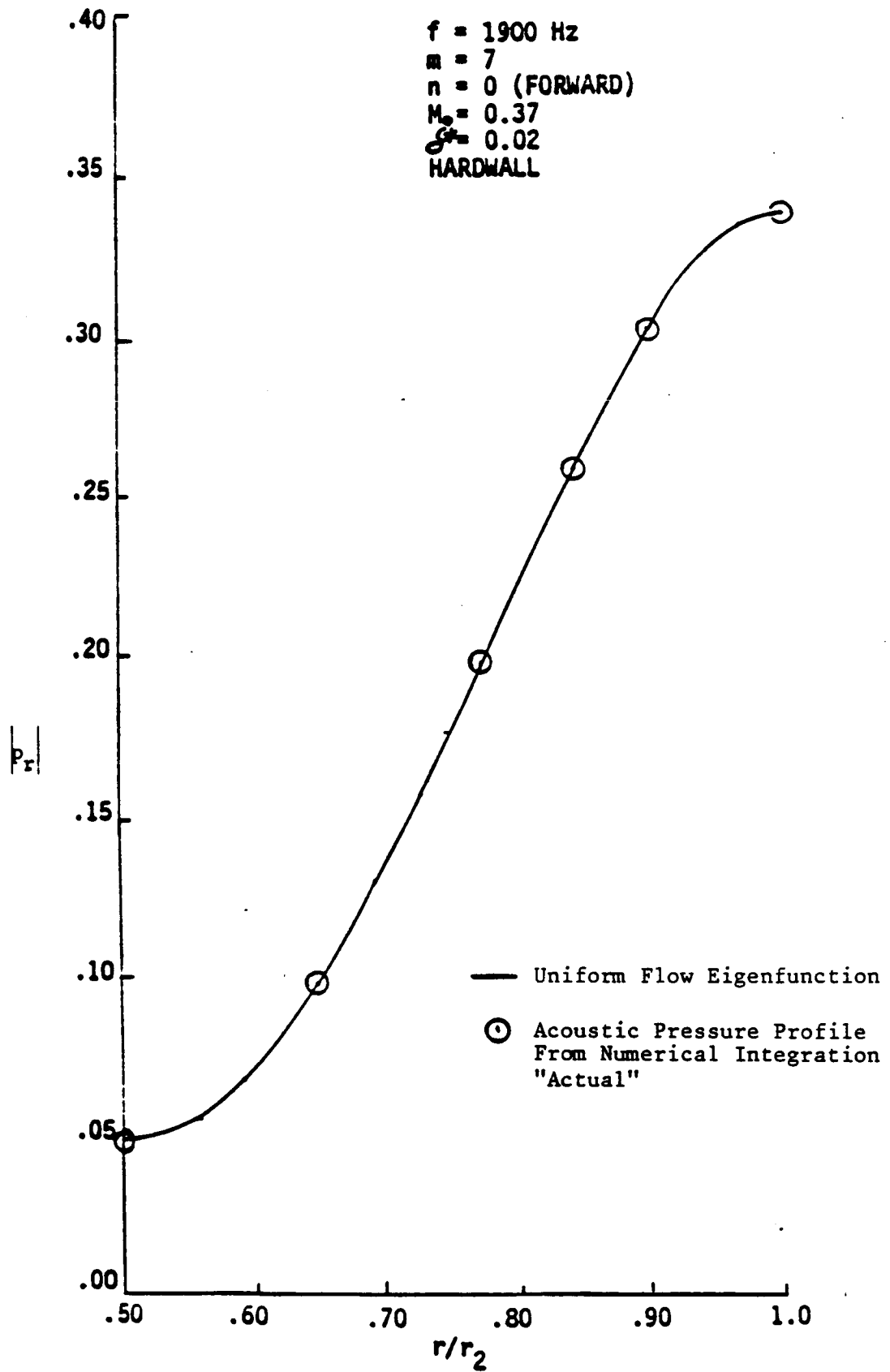
Figure 6.14. Comparison of the Uniform Flow Eigenfunction With the Actual Acoustic Mode Shape in Hardwall Duct – 1900 Hz, m = 7, n = 0, M_o = .37, δ* = 0.02, Forward Propagation

following five figures (i.e., Figures 6.14 through 6.19) are for the m = 7 modes at 1900 Hz. The flow through the duct is assumed to have boundary layers with 2 percent thickness and one-seventh power law velocity profile. The uniform flow eigenfunction for the hardwall duct can be seen to be in excellent agreement with the "actual" pressure profile (obtained by numerical integration).

For the lowest order mode (n=0) propagating backward in the hardwall segment (see Figure 6.15), the uniform flow eigenfunction accurately represents the complex pressure profile in a region of the duct annulus away from the walls. Near the inner wall it overpredicts the actual acoustic pressure while at the outer wall it underpredicts. The differences are, however, small.

In contrast to the hardwall segment cases, the uniform flow eigenfunctions in a treated segment are considerably different from the "actual" acoustic pressure profiles for both forward and backward propagating modes (see Figures 6.16 and 6.17). For the forward mode there is good similarity between the two pressure profiles in the outer half portion of the duct annulus. But near the inner wall even the shapes of the two pressure profiles are different.

These figures show that the uniform flow eigenfunctions can be used to represent the acoustic pressure profile in the hardwall segment of a duct in the presence of thin boundary layers at the walls. In treated segments with sheared flow, however, the uniform flow eigenfunction representation of the acoustic pressure profile is not accurate.

In an attempt to improve the representation of acoustic pressure profile (in ducts carrying sheared flow) by uniform flow eigenfunctions the concept of treating the boundary layer as equivalent wall impedance was studied. As discussed in Section 4.1.1 the radial dependence of acoustic pressure (p_r) in an annular duct carrying uniform flow is

$$p_r(r) = J_m(k_r r) + C_m Y_m(k_r r) \tag{6.1}$$
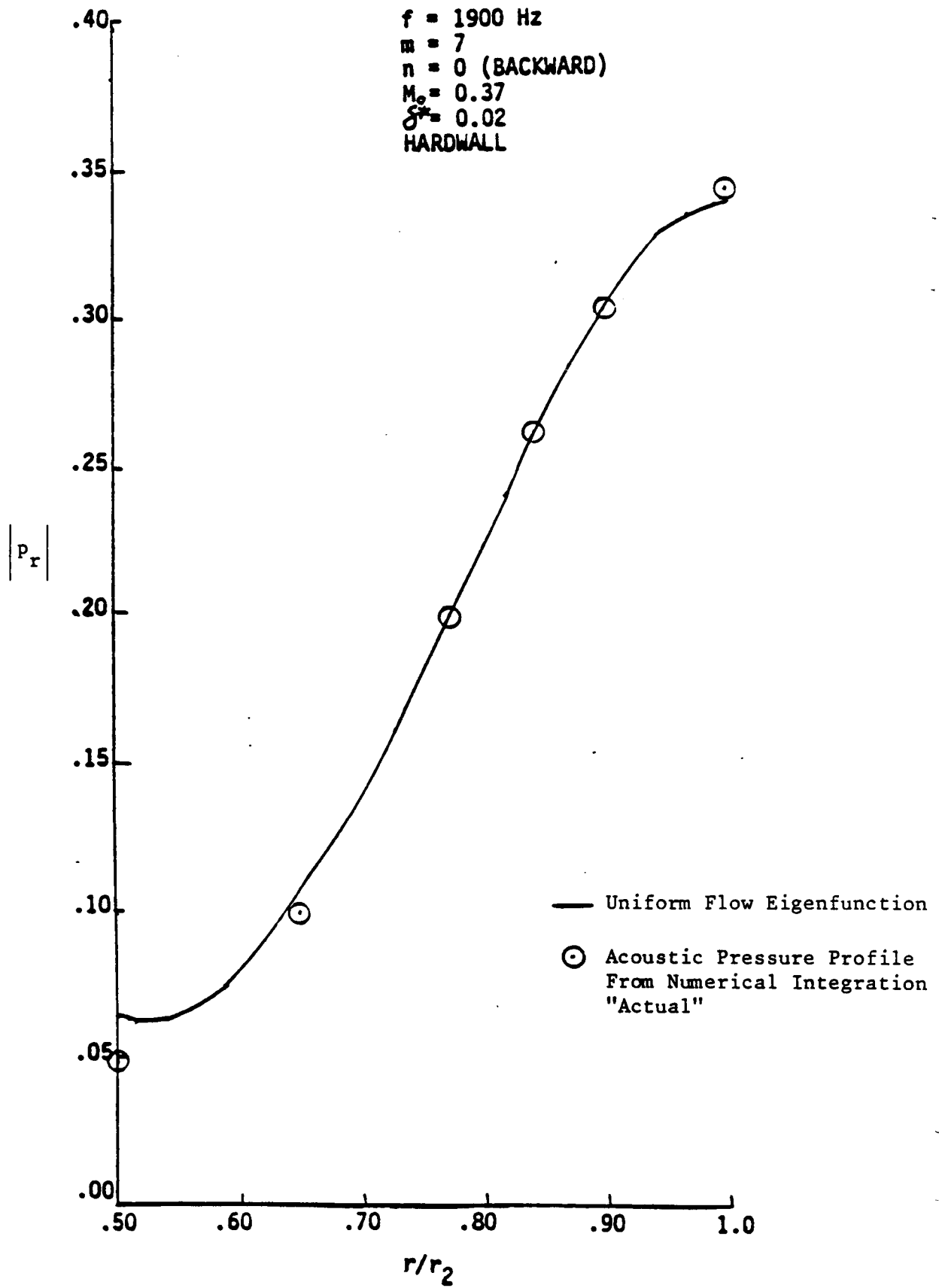
Figure 6.15. Comparison of the Uniform Flow Eigenfunction With the Actual Acoustic Mode Shape in Hardwall Duct – f = 1900 Hz, m = 7, n = 0, M_o = .37, δ^* = .02, Backward Propagation
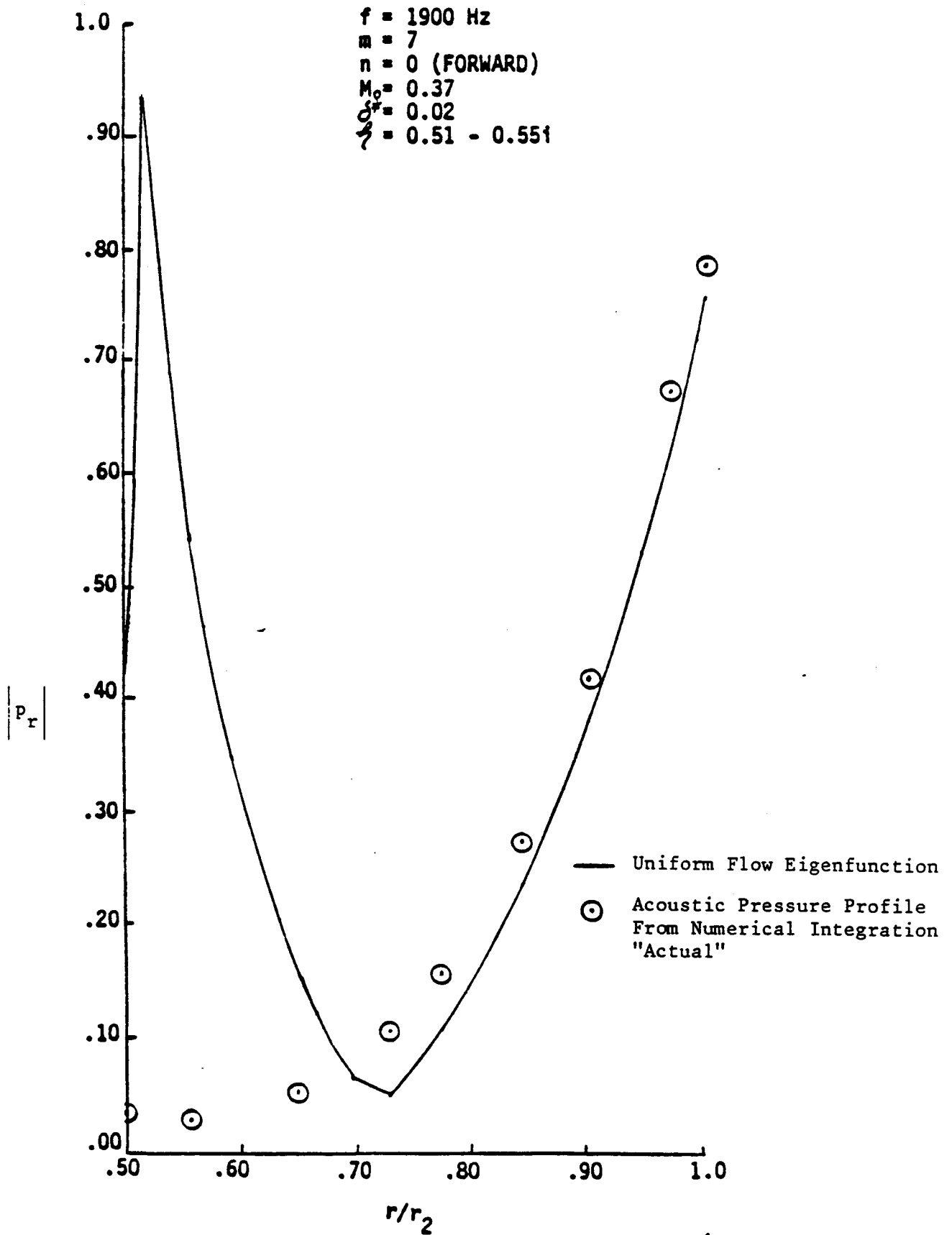
Figure 6.16. Comparison of the Uniform Flow Eigenfunction With the Actual Acoustic Mode Shape in the Treated Duct – 1900 Hz, m = 7, n = 0, M_0 = .37, δ^* = .02, ζ = (.51 – .55i), Forward Propagation
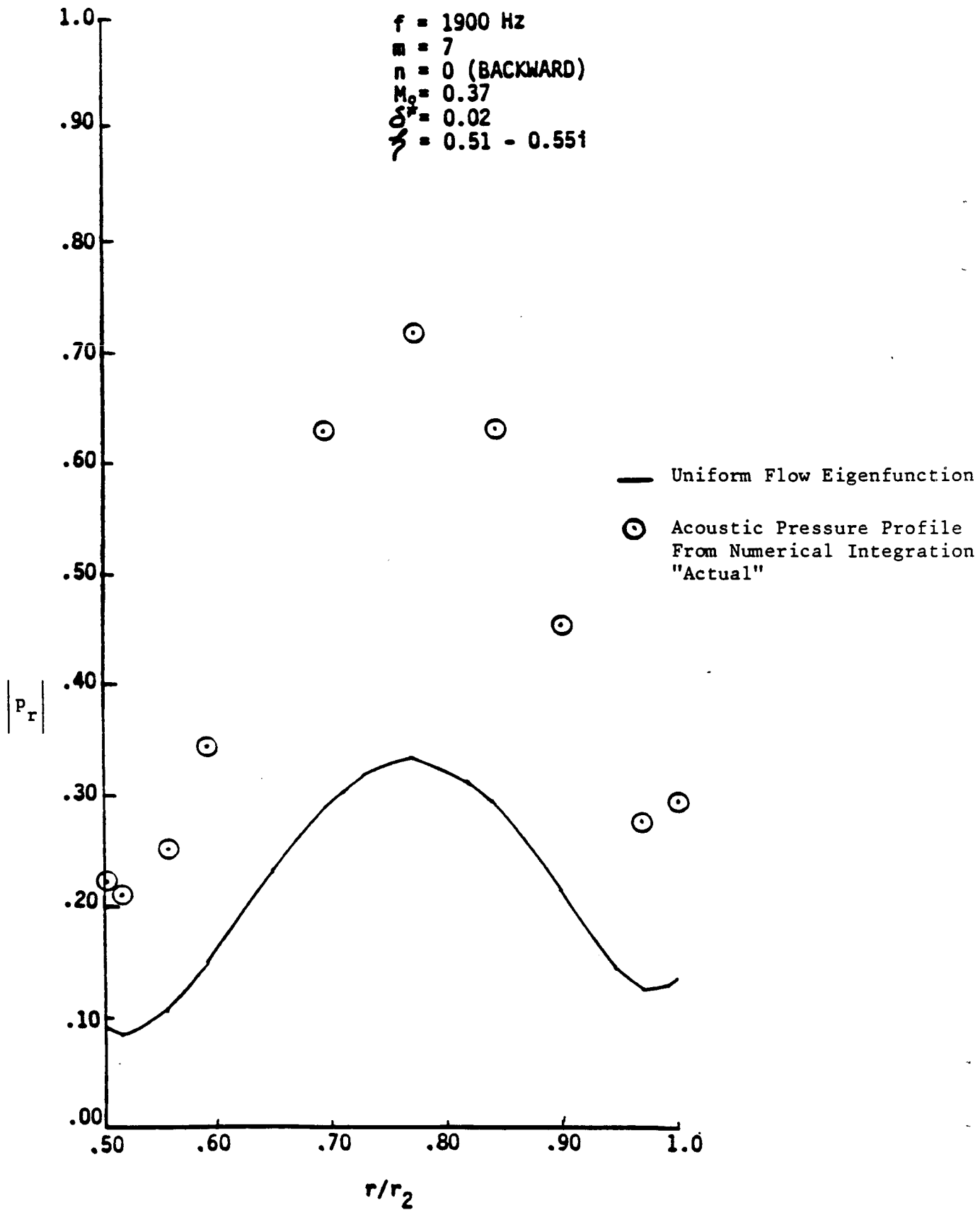
Figure 6.17.   Comparison of the Uniform Flow Eigenfunction With the Actual
Acoustic Mode Shape in the Treated Duct – 1900 Hz, m = 7, n = 0,
M_O = .37, δ^* = 0.02, ζ = (.51 – .55i), Backward Propagation
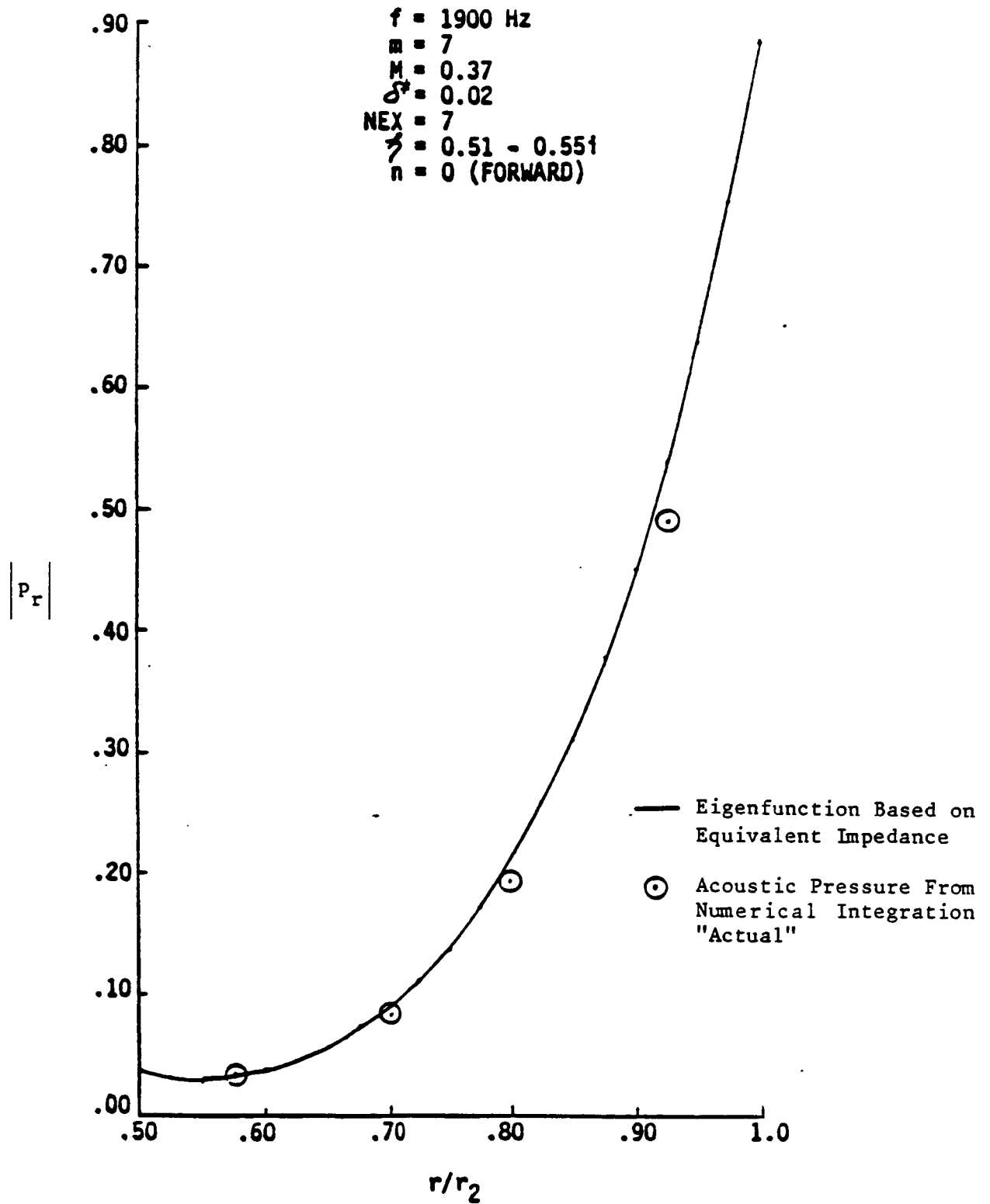
Figure 6.18. Comparison of the Uniform Flow Eigenfunction Based on the Equivalent Impedance With Actual Mode Shape in the Treated Duct – f = 1900 Hz, m = 7, n = 0, M = .37, δ* = .02, NEX = 7, ζ = (.51 − .55i), Forward Propagation
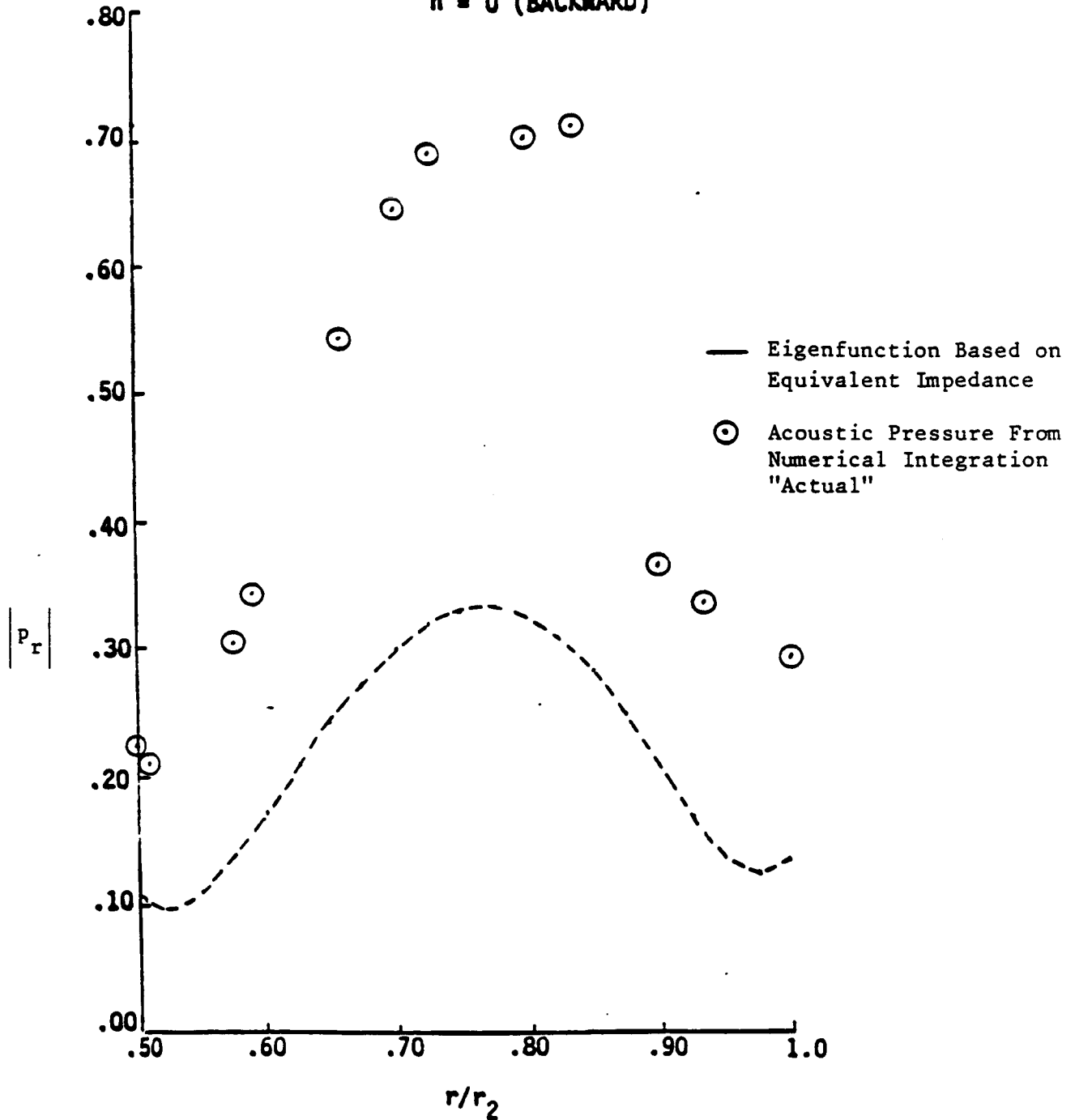
Figure 6.19. Comparison of the Uniform Flow Eigenfunction Based on the Equivalent Impedance With the Actual Mode Shape in the Treated Duct - 1900 Hz, m - 7, n = 0, M = .37, δ* = .02, NEX = 7, ζ = (.51 - .55i), Backward Propagation

and satisfies the admittance boundary conditions at the walls

$$\frac{\partial p_r}{\partial r}\bigg|_{r=r_1} = ik\beta \ (1-\kappa M)^2 p_r \bigg|_{r=r_1} \tag{6.2}$$

and

$$\frac{\partial p_r}{\partial r}\bigg|_{r=r_2} = ik\beta \ (1-\kappa M)^2 p_r \bigg|_{r=r_2} \tag{6.3}$$

These equations can be combined (by eliminating C_m) and rearranged in the form.

$$A_1(\beta kH)^2 + A_2(\beta kH) + A_3 = 0 \tag{6.4}$$

where H is the duct height and A_1, A_2 and A_3 are functions of the eigenvalue, axial propagation constant, duct geometry and flow Mach number. The eigenvalues calculated for the boundary layer cases can be used to evaluate the coefficient A_1, A_2 and A_3 and equation (6.4) can then be solved to obtain the equivalent uniform flow admittance, i.e.,

$$B_{eq} = \frac{-A_2 \pm \sqrt{A_2^2 - 4A_1A_3}}{2A_1 kH} \tag{6.5}$$

This value of the equivalent uniform flow admittance can then be used with the uniform flow eigenvalues corresponding to it (or equivalently with the sheared flow eigenvalues corresponding to the actual wall admittance) and

$$C_m = - \frac{(m - i\beta_{eq} kr_2\Lambda) \ J_m(k_r r_2) - (k_r r_2) J_{m+1}(k_r r_2)}{(m - i\beta_{eq} kr_2\Lambda) \ Y_m(k_r r_2) - (k_r r_2) Y_{m+1}(k_r r_2)} \tag{6.6}$$

with $\Lambda = (1-\kappa M)^2$

in equation (6.1) to obtain the radial acoustic pressure profile.

Figure 6.18 and 6.19 show comparisons of the actual mode shapes with the uniform flow eigenfunctions based on the calculated equivalent impedance. For the forward mode in the treated segment the uniform flow eigenfunction based on the equivalent impedance is in good agreement with the acoustic pressure profile. This is in contrast to the comparison of Figure 6.16. For the backward mode, however, the use of equivalent impedance does not improve the representation of the acoustic pressure profile by the uniform flow eigenfunction. Further investigation is needed to seek ways of improving the eigenfunction representation.

6.8 EFFECT OF AFT-DUCT TREATMENT ON FAN NOISE GENERATION

Recent analysis [Reference 20] on the generation of fan tones has suggested that the fan noise characteristics (both mode distribution and acoustic power) could change when the wall impedance of any section of the duct (at or away from the fan plane) is changed. In the present study the source characteristics were determined from measurements in the duct. For the prediction of the in-duct suppression the source characteristics obtained from measurements with the treatment sections in place were used. The effects of the duct treatment on the fan noise characteristics are thus taken into account in the predicted suppressions.

By comparing the mode coefficients at the upstream measurement plane for the cases of the hardwall duct and the duct with the treatment sections, we should be able to assess the effect of the duct treatment on the fan noise generation. The measured mode distributions of the fan noise in the hardwall duct and in the duct with a treatment section (downstream of the fan plane) are shown in Figures 6.20 thrugh 6.23 for the four test conditions of Table 6.1. The mode coefficients of the lowest order radial mode (n=0) for the m = -1 modes (Figures 6.20, 6.21 and 6.22) in the case of the hardwall duct differ by at most 2 dB from the mode coefficients in the presence of the treatment in the duct. This suggests that the treatment in the exhaust duct of the fan does not have a significant effect on the fan noise generation. For the (7,0) mode (Figure 6.23) the difference in mode coefficients is of the
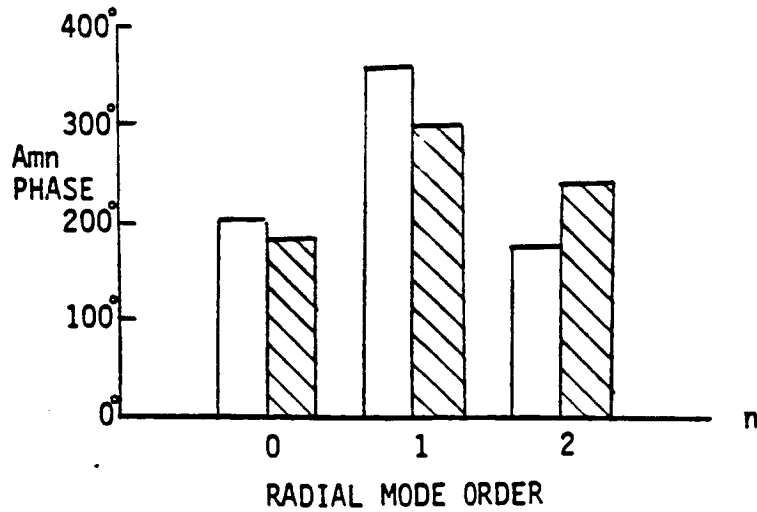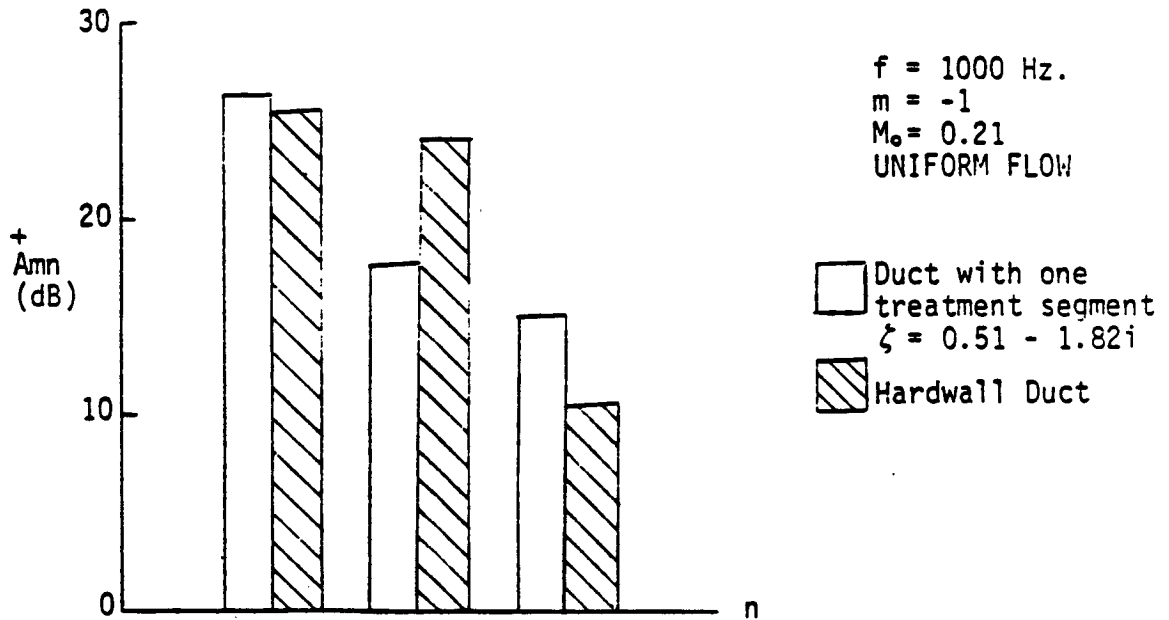
Figure 6.20. Complex Mode Amplitudes and Phase Values at Upstream Plane –
1000 Hz, m = -1, M = .21, Uniform Flow, Forward Propagation
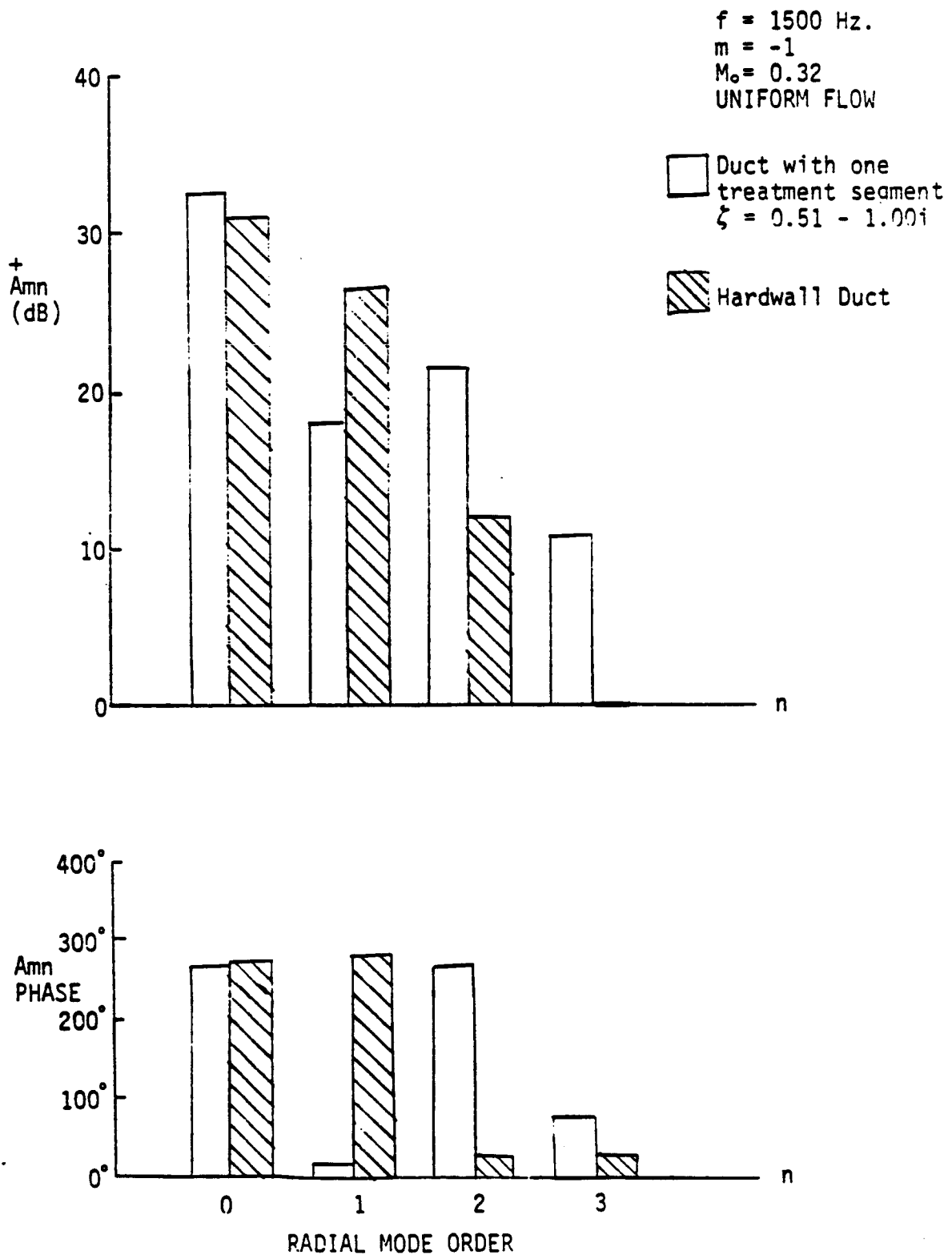
Figure 6.21. Complex Mode Amplitudes and Phase Values at the Upstream Plane – 1500 Hz, m = -1, M = .32, Uniform Flow, Forward Propagation

158
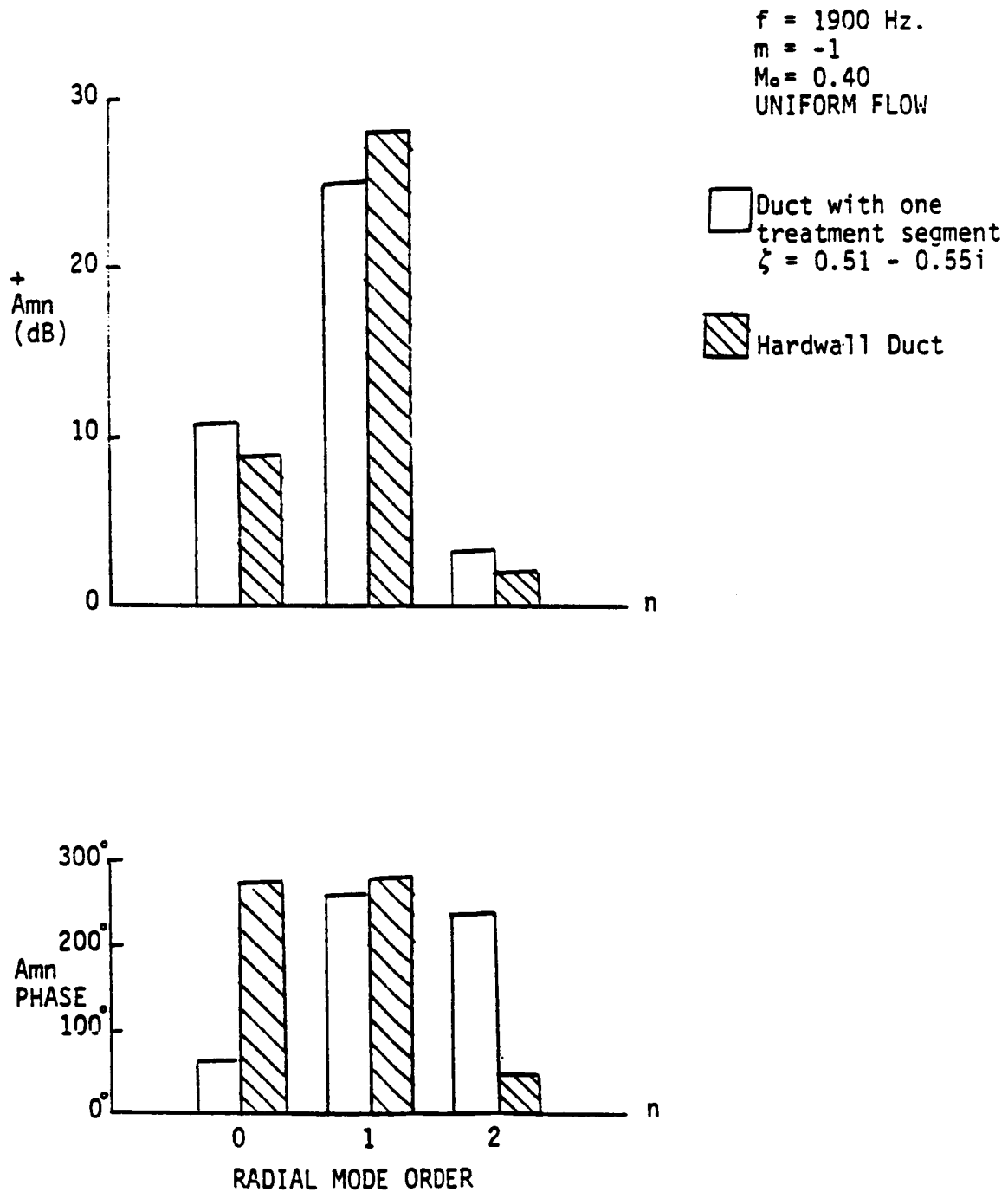
Figure 6.22. Complex Mode Amplitudes and Phase Values at the Upstream Plane – 1900 Hz, m = -1, M = 0.4, Uniform Flow, Forward Propagation
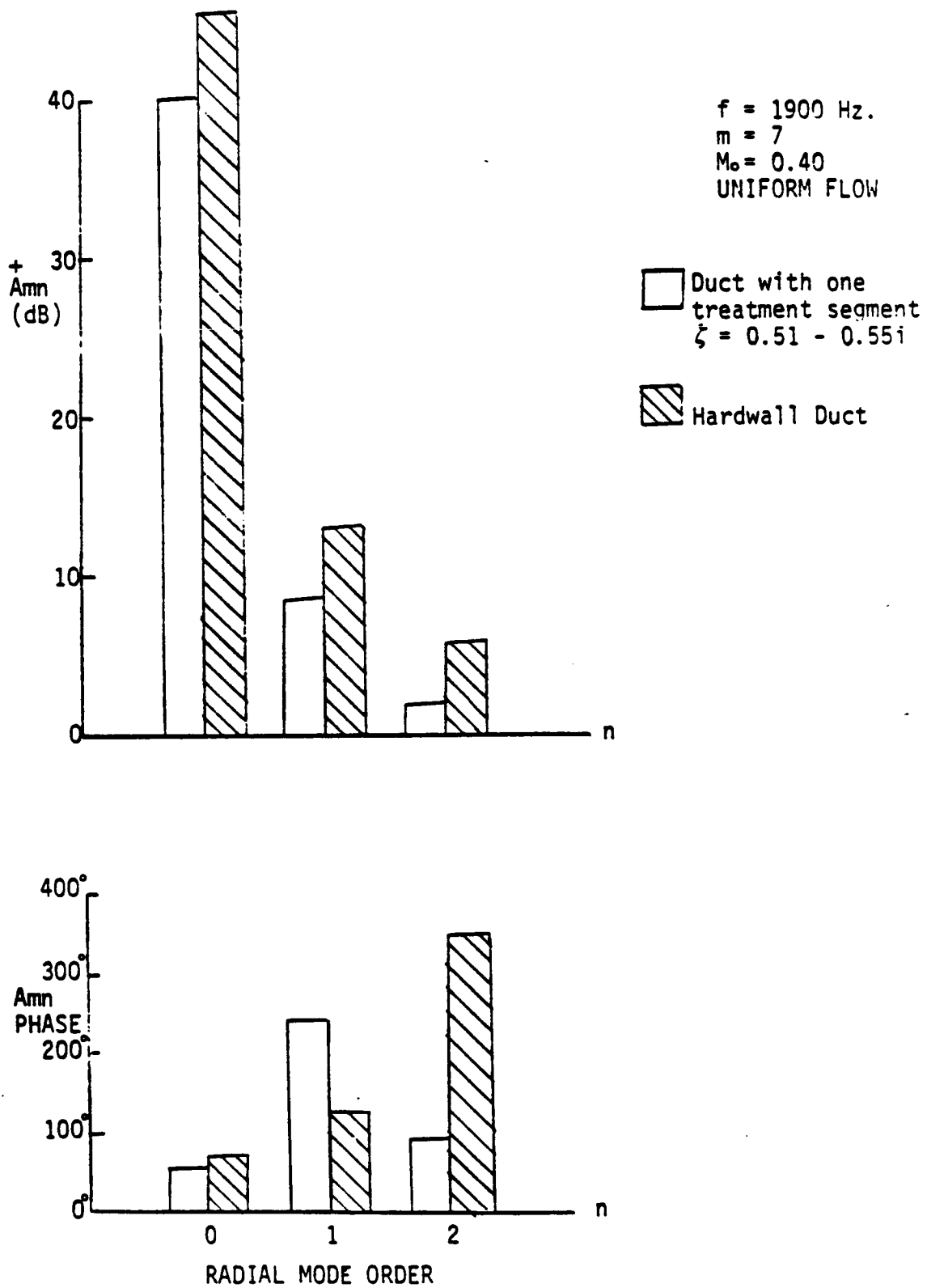
Figure 6.23. Complex Mode Amplitude and Phase Values at the Upstream Plane – 1900 Hz, m = 7, M = 0.4, Uniform Flow, Forward Propagation

order of 5 dB. The differences in mode coefficients for the (7,1) and 7,2) modes are also of the same order thus indicating a change in the ambient or fan operating conditions.

It should be mentioned that the data for the hardwall duct and the duct with the treatment section were obtained on different days and the operating conditions were not identical (except for the fan rpm). The comparisons of the mode coefficients in Figures 6.20 through 6.23 are thus appropriate for qualitative analysis only. Notice that the treatment in the duct was located a few duct heights downstream of the fan OGV plane and therefore may not have a significant effect on the fan noise generation.

7.0 CONCLUDING REMARKS

Based on the theory-data comparisons presented above it can be concluded that the modal analysis for sound propagation in segmented annular ducts can be used to predict the in-duct suppression due to treatment in the exhaust duct of a turbomachine. The modal distribution of the acoustic source and the reflection characteristics of the duct termination are required for the prediction. These can be obtained from measurements (at least in a laboratory duct) or from analytical methods.

The predicted values of the in-duct suppressions based on measured source characteristics and treatment acoustic impedance were found to be in good agreement with the measured suppressions. This is true in spite of the presence of thick boundary layers and circumferential flow variation in the test duct, two effects not fully accounted for in the theory. The presence of thick boundary layers did, however, cause numerical problems in the calculations manifested as energy mismatches at duct segment interfaces. This problem will require further investigation. The predicted suppression was found to be quite sensitive to treatment impedance indicating the importance of accurately determining this parameter.

The analysis should include at least two radial modes above those theoretically "cut-on" in the hardwall segment of the duct. This permits a valid expansion of the acoustic pressure in terms of the mode eigenfunctions and maintains conservation of acoustic energy across segment interfaces. More modes may be required when a significant amount of energy is carried by a mode that is close to cut-off.

PRECEDING PAGE BLANK NO

PRECEDING PAGE BLACK NOT FILMED

REFERENCES

1. Zorumski, W., "Acoustic Theory of Axisymmetric Multisectional Ducts," NASA TR R-419, May 1974.

2. Kraft, R.E., "Theory and Measurement of Acoustic Wave Propagation in Multi-Segmented Rectangular Flow Ducts," Ph.D Dissertation, University of Cincinnati, June 1976.

3. Joshi, M.C., Kraft, R.E., and Son, S.Y., "Analysis of Sound Propagation in Annular Ducts With Segmented Treatment and Sheared Flow," AIAA Paper 80-0123, January 1982.

4. Dean, D.P., "An In-Situ Method of Wall Impedance Measurement in Flow Ducts, Journal of Sound and Vibration, Vol. 34(1), pp. 97-130, 1974.

5. Kooi, J.W. and Sarin, S.L., "An Experimental Study of the Acoustic Impedance of Helmholtz Resonator Arrays Under a Turbulent Boundary Layer," AIAA Paper 81-1998, October 1981.

6. Zandbergen, T., "On the Practical Use of Three-Microphone Technique for In-Situ Acoustic Impedance Measurements on Double Layer Flow Duct Liners", AIAA Paper 81-2000, October 1981.

7. Syed, Asif A, "Acoustic Impedance Measurement, Patent Application, No. 499, 641 filed on May 31, 1983.

8. Joshi, M.C. and Kraft, R.E., "Turbofan Aft Duct Suppressor Study - Program Listing and User's Guide."

9. Fiske, G.H., Syed, A.A., Motsinger, R.E., Joshi, M.C., Kraft, R.E., "Contractors Data Report of Mode Probe Signal Data', NASA Contract No. NAS3-22766.

10. Kraft, R.E., and Wells, W.R., "Adjointness Properties of Differential Systems with Eigenvalue Dependent Boundary Conditions With Application to Flow Duct Acoustics," J. Acoustical Society of America, Vol. 61, No. 4, April 1977.

11. Cantrell, R.H. and Hart, R.W., "Interaction Between Sound and Flow in Acoustic Cavities: Mass, Momentum and Energy Considerations," J. Acoustical Society of America, Vol. 36, No. 4, 1964, pp. 694-706.

12. Zandbergen, T., Logan, J.N., Zeemans, H.J., and Sarin, S.L., "In-Flight Acoustic Measurements in the Engine Intake of a Fokker F28 Aircraft", AIAA Paper No. 83-0677, April 1983.

13. Moore, C.J., "In-Duct Investigation of Subsonic Fan 'Rotor Alone' Noise," Journal of Acoustical Society of America, Vol. 51, No. 5 (Part 1), 1972.

14. Kline, S.J. and McClintock, "The Description of Uncertainties in Single Sample Experiments," Mechanical Engineering, January, 1958.

15. Moore, C.J., "Measurements of Radial and Circumferential Modes in Annular and Circular Fan Ducts," Journal of Sound and Vibration, Vol. 62(2), pp. 235-256, 1979.

16. Morse, M.M. and Ingard, K.U., Theoretical Acoustics, McGraw-Hill, New York, 1968.

17. Taylor, K., "A Transformation of the Acoustic Equation With Implications for Wind-Tunnel and Low-Speed Flight Tests", Proceedings of the Royal Society, 363, 271-281, 1978.

18. Tyler, J.M. and Sofrin, T.G., "Axial Flow Compressor Noise Studies," SAE Trans., 70, pp. 309-332, 1962.

19. Hersh, A.S. and Walker, B., "The Acoustic Behavior of Helmholtz Resonators Exposed to High Speed Grazing Flows," AIAA Paper 76-563, July 1976.

20. Mungur, P. and Gliebe, P.R., "Acoustic Analysis of Fan Tone Generation and Propagation", AIAA Paper 83-0769, AIAA 8th Aeroacoustics Conference, Atlanta, GA, April 1983.

21. Fiske, G.H., Syed, A.A., Motsinger, R.E., Joshi, M.C. and Kraft, R.E., "Measurement of Acoustic Modes and Wall Impedance in a Turbofan Exhaust Duct", AIAA Paper No. 83-0733, April 1983.

22. Joshi, M.C., Kraft, R.E., Fiske, G.H., Syed, A.A. and Motsinger, R.E., "Sound Propagation in Segmented Exhaust Ducts - Theoretical Prediction and Comparison with Measurementss", AIAA Paper No. 83-0734, April 1983.

APPENDIX A

SCATTER IN MODAL COEFFICIENT FILES

Extensive work was done to determine the reliability of a particular probe through the elimination of that probe in the modal decomposition scheme and its subsequent effect on the results. This could be done by eliminating one or two probes from the input data to the modal decomposition program and solving for less radial mode orders. This was done for all probes and then the modal coefficient files were examined for scatter. To determine the degree of scatter, all modal coefficient files that were generated without a particular probe were combined and each mode had its average value and standard deviation calculated. The reasoning was that if a probe was not functioning properly its elimination from the data would result in reduced scatter (lower standard deviation) assuming all the other probes were functioning well. In the case where a probe was calibrated to read high as was the case in the 7600 rpm hardwall run, this proved to be an excellent mode of detecting a bad probe. However, in the case where a probe was slightly miscalibrated or reading low, this method was not as effective. For example, in the case where a broken diaphragm gave no reading, as was the case in all downstream treatment runs, the scatter was less by leaving out this probe but only slightly less. Figure A1 shows a comparison of scatter versus probe elimination for these two cases. Since the degree of confidence in using this method was low for low reading probes, it was not utilized in these cases.

In summary, modal decomposition was carried out using all functioning probes, except in the case of the 7600 rpm hardwall run. In that case, the cause of miscalibration was known before the scatter techniques were applied, and the scatter techniques confirmed that fact. In the downstream treatment cases the probe with the defective transducer was eliminated from modal decomposition. That is, the scatter criteria was not used in the data reduction process.
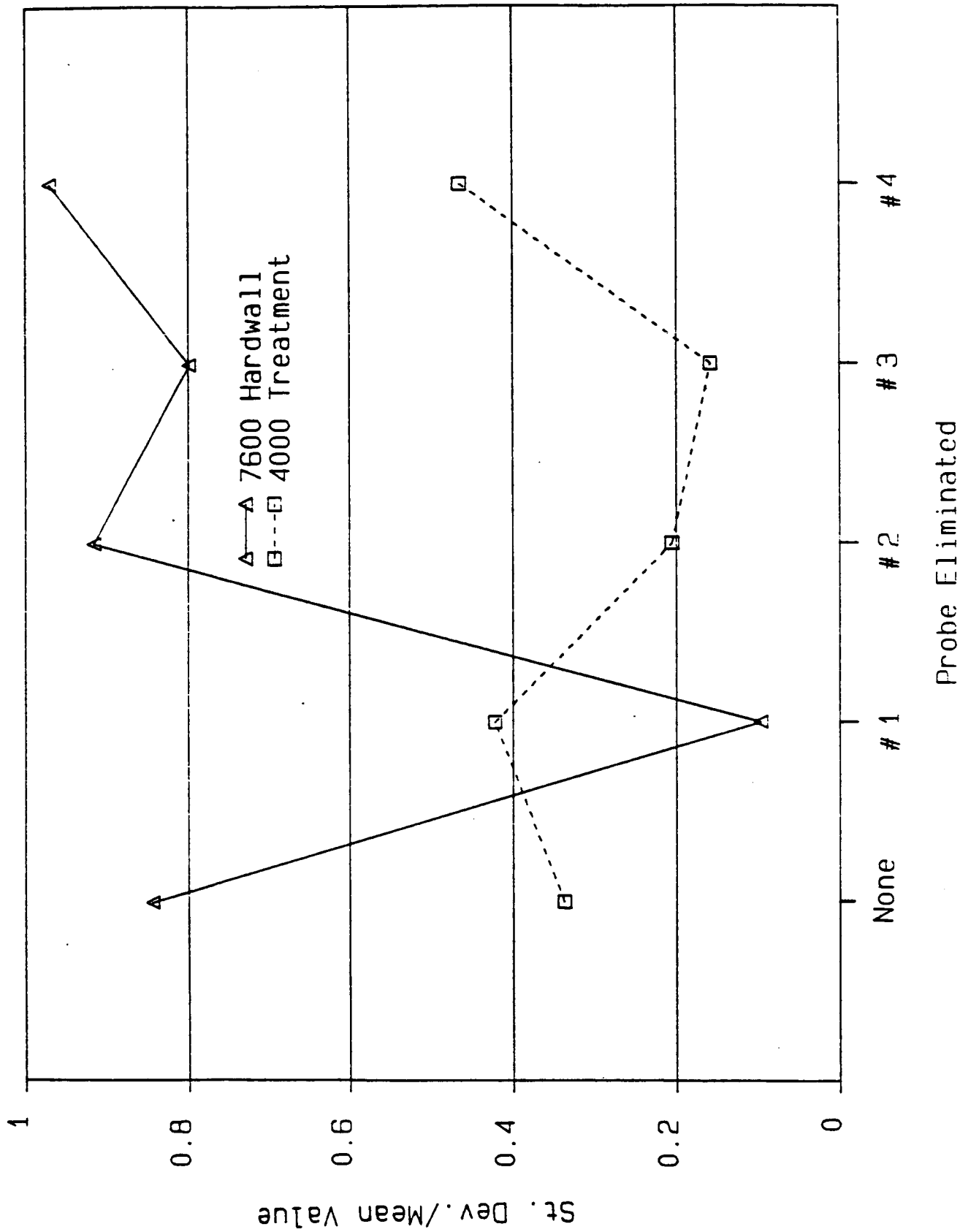
Figure A1. Scatter in the Modal Data Due to Probe Elimination at the Downstream Measurement Location

APPENDIX B

AN ASSESSMENT OF ERRORS IN THE IN-SITU MEASUREMENTS
OF THE ACOUSTIC IMPEDANCE

P_A (f) Signal at A

P_B (f) Signal at B
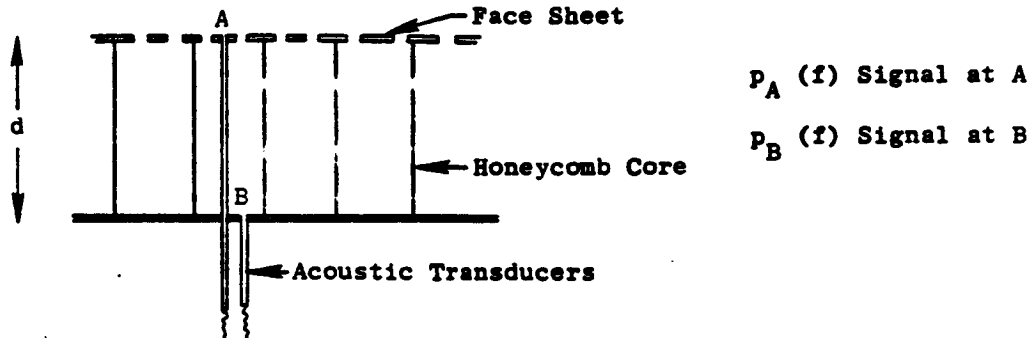
The sketch above shows two transducers sensing signals at the surface of the porous face sheet (A) and at the backwall of the cavity (B).

The Acoustic Impedance of the locally reacting SDOF panel in terms of the two signals, its thickness d and the frequency f is given by

$$\zeta(f) = -i \, H_{AB} \, \exp\{i \, \phi_{AB}(f)\} \, \csc(kd) \qquad (B1)$$

where k = 2πf/c, c is the speed of sound and

$$H_{AB} \, \exp\{i \, \phi_{AB}(f)\} = \overline{P_A(f) \, P_B^*(f)} \; / \; \overline{P_B(f) \, P_B^*(f)} \qquad (B2)$$

The transfer function $H_{AB}(f)$ and the phase difference $\phi_{AB}(f)$ are obtained from the analysis of the two signals; cosec(dk) is computed from specified values of the panel thickness d, and temperature T in the cavity. First consider the error in the measured impedance due to errors in the values

of d and T. It can be shown that an error in the impedance value $\delta\zeta_1(f)$
due to an error $\delta(kd)$ is given by

$$\delta\zeta_1(f) = (\delta R_1 + i\delta X_1)$$
$$= -(R+iX) \cot(kd) \cdot \delta(kd) \qquad (B3)$$

where

$$\delta(kd) = 0.000313 \; f \; \frac{\delta d}{\sqrt{T}} \; \frac{d \; \delta T}{T\sqrt{T}} \qquad (B4)$$

T is in $^\circ$K and d is in millimeters.

It is clear from (B3) that the error $\delta\zeta_1(f)$ is zero when cot(kd) is
zero, that is, close to the tuning frequency of the SDOF panel. Sample
calculations of the expected errors in the measured impedance of an SDOF panel
due to errors in the specified thickness and temperature are presented in
Table Bl. The errors in the resistance and reactance values due to errors in
the temperature and thickness are quite large near the antiresonance frequency
given by c/2d. Away from this frequency, these errors are quite small and may
be ignored. In practice the cavity thickness d may be measured with much
greater accuracy than specified in Table Bl. The accuracy of temperature may
be improved by accurate calibration of the thermocouples used in the
laboratory.

The other sources of error in the measured impedance are errors
$\delta H_{AB}(f)$ and $\delta\phi_{AB}(f)$ in the measurement of the transfer function and
the phase difference of the signals. These errors may be either of the bias
type or of random type as discussed in Reference 22. These types of errors
may be minimized by increasing the number of averages in the data analysis as
well as by reducing the bandwidth. However significant errors in the measured
values of $H_{AB}(f)$ and $\phi_{AB}(f)$ may exist due to the following:

1. Transducers not flush with the surfaces at A and B.

2. Leakages from the cavity other than through the porous sheet.

Table B1. In-Situ Measurements

- **Estimated Errors in the Measured Impedances Due to Errors in the Thickness (d) and Temperature (T)**

- $R = 0.4 \rho c$, $d = 46.48mm$, $T = 294°K$, $\delta d = 0.762$ mm, $\delta T = 1.1°K$

f, Hz	X, ρc	δR_{1_d}, ρc	δR_{1_T}, ρc	δX_{1_d}, ρc	δX_{1_T}, ρc
250.0	−4.604	0.006	0.001	−0.074	−0.009
500.0	−2.125	0.006	0.001	−0.033	−0.004
750.0	−1.217	0.006	0.001	−0.017	−0.002
1000.0	−0.698	0.005	0.001	−0.009	−0.001
1250.0	−0.330	0.004	0.000	−0.003	−0.000
1500.0	−0.031	0.003	0.000	−0.000	−0.000
1750.0	0.236	0.001	0.000	0.001	0.000
2000.0	0.495	−0.001	−0.000	−0.002	−0.000
2250.0	0.766	0.004	−0.001	−0.008	−0.001
2500.0	1.073	−0.008	−0.001	−0.023	−0.003
2750.0	1.459	−0.015	−0.002	−0.053	−0.006
3000.0	2.019	−0.024	−0.003	−0.123	−0.014
3250.0	3.050	−0.044	−0.005	−0.337	−0.039
3500.0	6.273	−0.109	−0.013	−1.716	−0.197
3750.0	−27.150	0.580	0.067	−39.381	−4.532
4000.0	−3.213	0.088	0.010	−0.706	−0.081
4250.0	−1.233	0.648	0.005	−0.147	−0.017
4500.0	−0.425	0.031	0.004	−0.033	−0.004
4750.0	0.058	0.022	0.002	0.003	0.000
5000.0	0.411	0.014	0.002	0.015	0.002
5250.0	0.702	0.008	0.001	0.014	0.002
5500.0	0.967	0.002	0.000	0.004	0.000
5750.0	1.226	−0.005	−0.001	−0.016	−0.002
6000.0	1.501	−0.013	−0.001	−0.049	−0.006
6250.0	1.818	−0.023	−0.003	−0.104	−0.012

R, X: Nominal values of resistance and reactance

δR_{1_d}, δX_{1_d}: Errors in resistance/reactance due to error δd (mm)

δR_{1_T}, δX_{1_T}: Error in resistance/reactance due to error δT (° K)

3. Inaccuracies in the calibration of transducers.

4. Inaccuracies due to insufficient signal-to-noise ratio.

Under conditions of grazing flow, the measurement of impedance is found to be extremely sensitive to the position of transducer A relative to the surface of the porous face sheet. Experience showed that for accurate measurement the face sheet transducer must be absolutely flush with it. Leakages were eliminated by constructing a single cavity with hard walls.

Inaccuracies in the calibrations of the transducers and insufficient signal-to-noise ratio are the most significant sources of error in the measured impedance. The calibrations of the transducers, the associated signal conditioning equipment and the A to D converter of the data analysis system are required because of significant differences in their response characteristics. The method used for the calibration of the transducers, the signal conditioning amplifiers and the analog-to-digital converters consisted of placing them at the end of a tube flush with a hard wall termination and exciting a broadband acoustic signal at the other end. Under these conditions, both the transducers were subjected to plane wave signals at all frequencies up to the cut-on frequency of the (1,0) mode. The transfer function and the phase difference measured under these conditions represented the calibration to be used when measuring impedance. Clearly, the accuracy of this calibration would depend on the signal-to-noise ratio during its measurement. Figure B1 shows the calibration of the transducer system used in the In-Situ measurements in the Grazing Flow Duct. The reliable part of this data lies roughly between 600 Hz and 2800 Hz. At frequencies outside this range, signal-to-noise ratio is a problem. The difficulty lies in poor coupling between the speaker and the tube at these frequencies and a relatively high level of electronic-system noise. A way to eliminate this problem would be to use discrete frequency signals for calibration.

From error analysis, it can be shown that the error $\delta \zeta_2$ in the measured impedance due to errors δH_{AB} and $\delta \phi_{AB}$ is given by
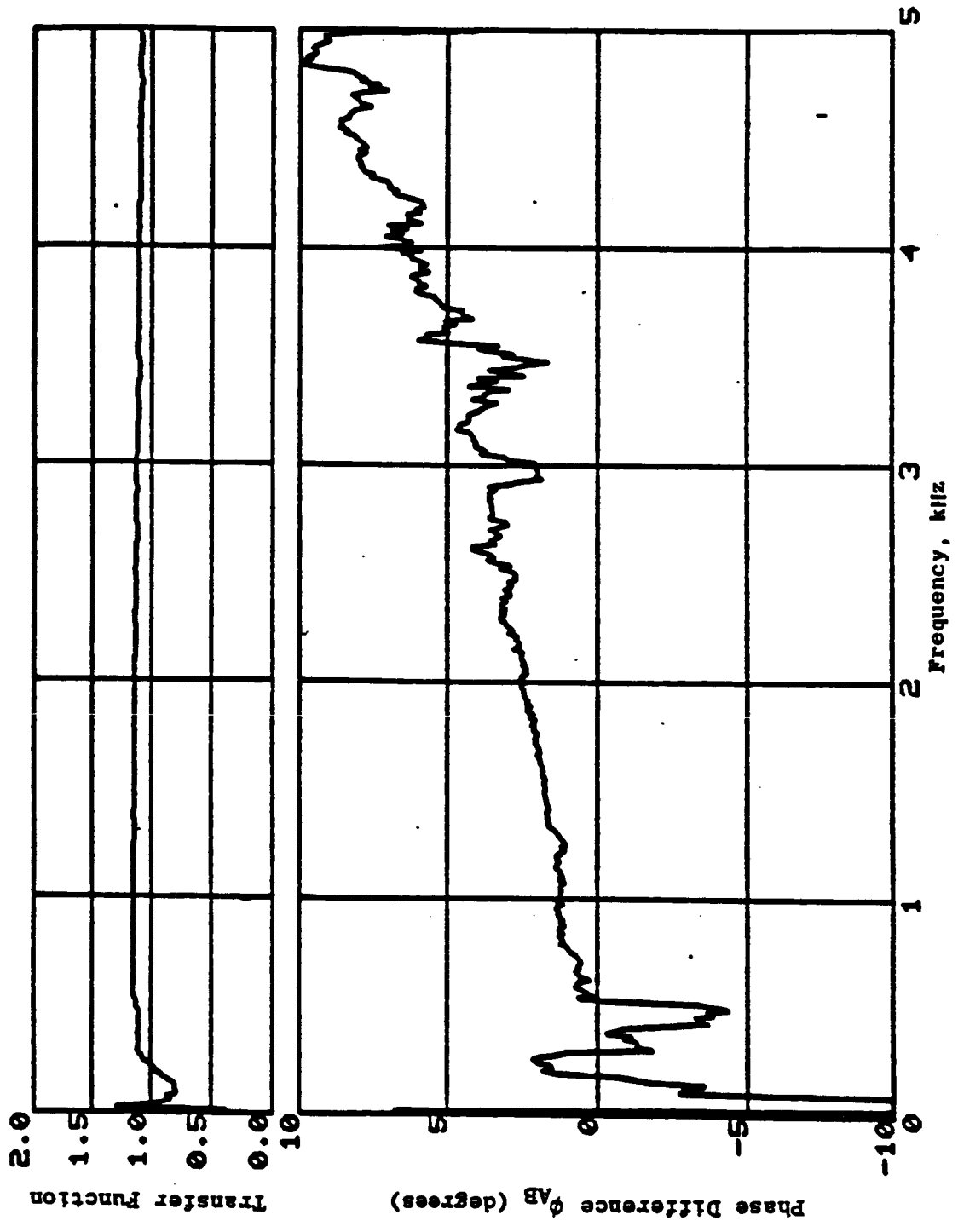
Figure B1. Typical Calibration of the Two Acoustic Transducers Used in the In-Situ Measurements.

175

$$\delta\zeta_2 = \delta R_2 + i\ \delta X_2$$

$$= -X\ \delta\phi_{AB} + R\ \frac{\delta H_{AB}}{H_{AB}} + i\left(R\delta\phi_{AB} + X\ \frac{\delta H_{AB}}{H_{AB}}\right) \qquad (B5)$$

where R and X are the acoustic resistance and reactance values respectively of the panel being tested. Table B2 shows sample calculations of the expected errors in the measured impedance due to given errors in the measured phase difference and the transfer function of the signals at A and B. A small error in phase has little effect on the measured reactance over the entire frequency range but gives rise to significant errors in the measured resistance at frequencies where the reactance is large. A small error in measured transfer function gives rise to a small error in both the measured resistance and reactance values.

Over the frequency range of interest in this study, the errors in the measured impedance due to errors in the measured values of $H_{AB}(f)$ and $\phi_{AB}(f)$ were considered to be insignificant.
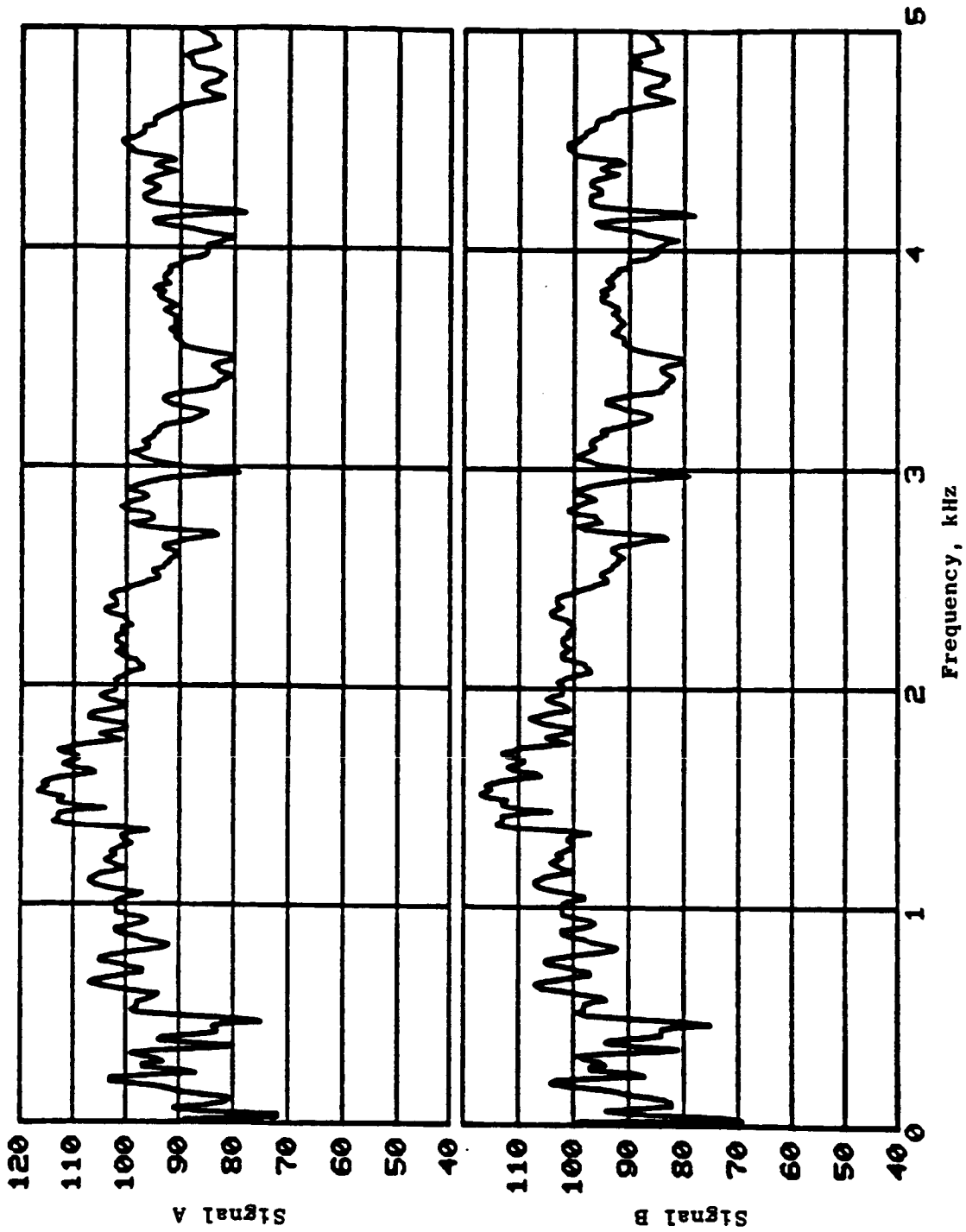
Figure B2. Autospectra of the Signal Used in the Calibration of Figure B1

177

Table B2. Expected Errors in Measured Impedance Due to Errors in the Measured Transfer Function (H_{AB}) and Phase Difference (ϕAB)

- $R = 0.4 \, \rho c$

- $\delta \phi_{AB} = 0.025$ radians (1.43°) error in phase difference $\phi_{AB}(f)$

- $\delta H_{AB}/H_{AB} = 0.05$

f, Hz	X, ρc	$\delta R_{2\phi}$, ρc	δX_{2H}, ρc
250.0	-4.604	-0.115	0.230
500.0	-2.125	-0.053	0.106
750.0	-1.217	-0.030	0.061
1000.0	-0.698	-0.017	0.035
1250.0	-0.330	-0.008	0.016
1500.0	-0.031	-0.001	0.002
1750.0	0.236	0.006	0.012
2000.0	0.495	0.012	0.025
2250.0	0.766	0.019	0.038
2500.0	1.073	0.027	0.054
2750.0	1.459	0.036	0.073
3000.0	2.019	0.050	0.101
3250.0	3.050	0.076	0.153
3500.0	6.273	0.157	0.314
3750.0	-27.150	-0.679	-1.357
4000.0	-3.213	-0.080	-0.161
4250.0	-1.233	-0.031	-0.062
4500.0	-0.425	-0.011	-0.021
4750.0	0.058	0.001	0.003
5000.0	0.411	0.010	0.021
5250.0	0.702	0.018	0.035
5500.0	0.967	0.024	0.048
5750.0	1.226	0.031	0.061
6000.0	1.501	0.038	0.075
6250.0	1.818	0.045	0.091

$\delta R_{2\phi}$, $\delta X_{2\phi}$: Errors due to $\delta \phi_{AB}$

δR_{2H}, δX_{2H}: Errors due to $\delta H_{AB}/H_{AB}$

APPENDIX C
EIGENVALUE EQUATIONS

The complete form of the eigenvalue equation (referred to in Section 4.1.1) for sound propagation in a lined duct carrying uniform flow is

$$F(\gamma) = \left\{ \frac{m^2}{\zeta} (1 - \zeta)^2 + i\beta kH\Lambda \frac{m(1 - \zeta)^2}{\zeta} + (\beta kH)^2\Lambda^2 \right\} T_1$$

$$- \gamma (1 - \zeta) \left\{ \frac{m(1 - \zeta)}{\zeta} - i\beta kH\Lambda \right\} T_2$$

$$- \gamma (1 - \zeta) \left\{ m(1 - \zeta) + i\beta kH\Lambda \right\} T_3$$

$$- \gamma^2 (1 - \zeta)^2 T_4 = 0 \qquad\qquad (C.1)$$

where β = acoustic admittance of the duct walls

$$\gamma = k_r r_2 \qquad\qquad (C.2)$$

$$\zeta = r_1/r_2$$

$$(C.3)$$

$$H = r_2 - r_1$$

$$T_1 = J_m (\zeta\gamma) Y_m(\gamma) - J_m (\gamma) Y_m (\zeta\gamma)$$

$$T_2 = J_m (\zeta\gamma) Y_{m+1} (\gamma) - J_{m+1} (\gamma) Y_m (\zeta\gamma)$$

$$(C.4)$$

$$T_3 = J_{m+1} (\zeta\gamma) Y_m (\gamma) - J_m (\gamma) Y_{m+1} (\zeta\gamma)$$

$$T_4 = J_{m+1}(\gamma) Y_{m+1}(\zeta\gamma) - J_{m+1}(\zeta\gamma) Y_{m+1}(\gamma)$$

$$\Lambda = (1 - \frac{K}{k} M)^2$$

$$(C.5)$$

$$\frac{K}{k} = \frac{-M \pm \sqrt{1 - (1 - M^2) \dfrac{\gamma^2(1 - \zeta)^2}{(kH)^2}}}{1 - M^2}$$

r_1 and r_2 are the inner and outer wall radii

and $J_m(\ )$ and $Y_m(\ )$ are Bessel functions of the first and

second kinds of order m.

As mentioned in Section 4.1.1, the eigenvalues can be determined by a
Newton-Raphson iteration of Equation (C.1).

Alternately, Equation (C.1) can be recast as the differential equation

$$\frac{d\gamma}{dx} = \frac{1}{D}\left[-\left\{ \frac{im(1-\zeta)^2}{\zeta} kH\Lambda + (kH)^2\Lambda^2 2\beta \right\} T_1 \right.$$

$$\left. - \gamma(1-\zeta)ikH\Lambda(T_2 - T_3) \right]\frac{d\beta}{dx} \qquad (C.6)$$

where

$$D = T_1 \left\{ \frac{m(1-\zeta)^2}{\zeta}\left[\frac{2m^2}{\gamma} - \gamma(1+\zeta^2) \right] \right.$$

$$+ i\beta kH(1-\zeta)^2\left[\frac{m}{\zeta}(A + \frac{2m}{\gamma}\Lambda) + \gamma\Lambda \right]$$

$$\left. + 2(\beta kH)^2\Lambda(A + \frac{m}{\gamma}\Lambda) \right\}$$

$$+ T_2 \left\{ (1-\zeta)^2(\zeta\gamma^2 - \frac{m^2}{\zeta}) + i\beta kH(1-\zeta)\left[\gamma A - \frac{m\Lambda(1-\zeta)}{\zeta} \right] - (\beta kH)^2\Lambda^2 \right\}$$

$$+ T_3 \left\{ (1-\zeta)^2(\gamma^2 - m^2) - i\beta kH(1-\zeta)\left[\gamma A + m\Lambda(1-\zeta) \right] - \zeta(\beta kH)^2\Lambda^2 \right\}$$

$$+ T_4 \left\{ (1-\zeta)^2 m(\gamma-1) + i\beta kH\Lambda(1-\zeta)(\zeta-\gamma) \right\} \qquad (C.7)$$

and T_1, T_2, T_3, and T_4 are represented in Equations (C.4).

Eigenvalues can be obtained by integrating Equation (C.6). Any variation
of admittance (β) with respect to the independent variable x can be pre-
scribed. For a linear variation $\beta = x\beta_w$ where β_w is the wall admittance,
Equation (C.6) and (C.7) reduced to

180

$$\frac{d\gamma}{dx} = -\frac{1}{D}\left[\left\{\frac{im(1-\zeta)^2}{\zeta}\beta_w kH\Lambda + 2(\beta_w kH)^2\Lambda^2 x\right\}T_1\right.$$
$$\left. + \gamma(1-\zeta)\,i\beta_w kH\Lambda(T_2 - T_3)\right] \tag{C.8}$$

and

$$D = T_1\left\{\frac{m(1-\zeta)^2}{\zeta}\left[\frac{2m^2}{\gamma} - \gamma(1+\zeta^2)\right] + i\beta_w kH(1-\zeta)^2\left[\frac{m}{\zeta}(A + \frac{2m}{\gamma}\Lambda) + \gamma\Lambda\right]x\right.$$

$$\left. + 2(\beta_w kH)^2\Lambda(A + \frac{m}{\gamma}\Lambda)\,x^2\right\}$$

$$+ T_2\left\{(1-\zeta)^2(\zeta\gamma^2 - \frac{m^2}{\zeta}) + i\beta_w kH(1-\zeta)\left[\gamma A - \frac{m\Lambda(1-\zeta)}{\zeta}\right]x - (\beta_w kH)^2\Lambda^2 x^2\right\}$$

$$+ T_3\left\{(1-\zeta)^2(\gamma^2 - m^2) - i\beta_w kH(1-\zeta)\left[\gamma A + m\Lambda(1-\zeta)\right]x - \zeta(\beta_w kH)^2\Lambda^2 x^2\right\}$$

$$+ T_4\left\{(1-\zeta)^2 m(\gamma - 1) + i\beta_w kH\Lambda(1-\zeta)(\zeta - \gamma)x\right\} \tag{C.9}$$

To find the softwall eigenvalues, Equation (C.8) must be integrated from $x = 0$ to $x = 1$. The initial values for γ (at $x = 0$) are the hardwall eigenvalues.

DISTRIBUTION LIST

CR 175067

NASA Lewis Research Center
21000 Brookpark Road
Cleveland, OH 44135

Attn:		No. of Copies
	Report Control Office, M.S. 60-1	1
	Library, M.S. 60-3	2
	John F. Groeneweg, M.S. 86-7	1
	Bruce J. Clark, M.S. 86-7	10
	Edward J. Rice, M.S. 5-7	1
	Marvin E. Goldstein, M.S. 5-2	1
	Leonard W. Schopen, M.S. 500-305	1

NASA Headquarters
Washington, DC 20546

Attn:	RP/J. Facey	1

NASA Scientific and Technical Information Facility
P. O. Box 8757
Baltimore Washington International Airport, MD 21240

Attn:	Accessioning Department	25

NASA Ames Research Center
Moffett Field, CA 94035

Attn:	D. Hickey, M.S. 247-1	1

NASA Langley Research Center
Hampton, VA 23665

Attn:	H. Morgan, M.S. 462	1
	R. Parrott, M.S. 460	1
	H. Lester, M.S. 463	1
	D. Chestnutt, M.S. 460A	1

Federal Aviation Administration
800 Independence Avenue, SW
Washington, D. C. 20591

Attn:	R. Koenig (CODE ARD-551)	1

U. S. Army Construction Engineering Research Laboratory
Box 4005
Champaign, IL 61820

Attn:	R. Raspet	1

Aeroacoustics Group
AFWAL/FIBDG
Wright-Patterson AFB, OH   45433

Attn: R. Shimovetz   1

Jet Propulsion Laboratory
4800 Oak Grove
Pasadena, CA   91103

Attn: T. Wang   1

AVCO Lycoming Division
550 South Main Street
Stratford, CT   06497

Attn: Craig Wilson   1

Boeing Commercial Airplane Company
P.O. Box 3707
Seattle, WA   98124

Attn: C. G. Hodge, M. S. 9W-65   1

Bolt, Beranek and Newman, Inc.
50 Moulton Street
Cambridge, MA   02138

Attn: Richard Hayden   1

Detroit Diesel/Allison Division
P. O. Box 894
Indianapolis, IN   46206

Attn: Mark Crelup   1
           Dr. Lynn E. Snyder   1

Garrett Turbine Engine Co.
111 S. 34th Street
P. O. Box 5217
Phoeniz, AZ   85010

Attn: Jack A. Mitchell   1

General Electric Company
One Neumann Way
Cincinnati, OH   45215

Attn: Dr. R. K. Majjigi, Mail Drop G-42   1

Hamilton Standard Division
United Technologies Corporation
Windsor Locks, CT 06096

Attn: Bernard Magliozzi, M.S. 1A 3-6   1
            F. Bruce Metzger   1

Hersh Acoustical Engineering
9545 Cozycraft Avenue
Chatworth, CA 91311

Attn: A. S. Hersh   1

Lockheed-Georgia Company
86 South Cobb Drive
Marietta, GA 30063

Attn: Krish Ahuja, M.S. B/72-74, Zone 403   1

McDonnell Douglas Aircraft
3855 Lakewood Blvd.
Long Beach, CA 90846

Attn: Dr. Daryl May   1

Nelson Industries
P. O. Box 428
Stoughton, WI 53589

Attn: P. Thawani   1

Northrop Corporation, ASD
8900 East Washington Blvd.
Pico Rivera, CA 90660-3737

Attn: R. E. Kraft, M.S. E122/3E   1

Pratt & Whitney Aircraft
400 Main Street
East Hartford, CT 06108

Attn: Douglas C. Mathews, M.S. 116-01   1
            Dr. Aldo Peracchio, M.S. 116-01   1

Sikorsky Aircraft Division
Dept. 4045 Aeromechanics Branch
North Main Street
Stratford, CT 06602

Attn: R. K. Shenoy   1

Southwest Research Institute
P. O. Drawer 28510
San Antonio, TX 78284

Attn: James F. Unruh   1

Tracoustics, Inc.
P. O. Box 3610
Austin, TX 78764

Attn: J. Schmitt   1

Wyle Labs
128 Maryland Street
El Segundo, CA 90245

Attn: Louis C. Sutherland   1

Embry-Riddle Aeronautical University
Regional Airport
Daytona Beach, FL 32014

Attn: Howard V. L. Patrick   1

Georgia Institute of Technology
School of Mechanical Engineering
Atlanta, GA 30332

Attn: A. D. Pierce   1

Massachusetts Institute of Technology
Department of Physics
Cambridge, MA 02139

Attn: K. U. Ingard   1

Penn State University
Aerospace Engineering Department
101 Engineering A Bldg.
University Park, PA 16802

Attn: Dr. B. Lakshminarayana   1
            J. Tichy   1

Purdue University
Department of Mechanical Engineering
West Lafayette, IN   47907

Attn: Dr. Sanford Fleeter   1

Texas A&M University
Aerospace Engineering Department
College Station, TX   77843

Attn: Kenneth Korkan   1

The University
Institute of Sound Vibration Research
Southampton 509 5NH
ENGLAND

Attn: C. L. Morfey   1

University of Arizona
Aerospace and Mechanical Engineering Department
Aero Building #16
Tucson, AZ   85721

Attn: Dr. E. Kerschen   1

University of California
Physics Department
Los Angeles, CA   90024

Attn: Isodore Rudnick   1

University of Leeds
Department of Applied Math Studies
Leeds L82 9JT
ENGLAND

Attn: David G. Crighton   1

University of Mississippi
Department of Physics and Astronomy
University, MS 38677

Attn: Henry E. Bass   1

University of Notre Dame
Department of Aerospace and Mechanical Engineering
Notre Dame, IN 46556

Attn: Professor H. Atassi   1